Conforming Discretizations of Mixed-Dimensional Partial Differential Equations

Wietse Marijn Boon

Thesis for the Degree of Philosophiae Doctor (PhD)
University of Bergen, Norway
2018

UNIVERSITY OF BERGEN

Conforming Discretizations of Mixed-Dimensional Partial Differential Equations

Wietse Marijn Boon

Thesis for the Degree of Philosophiae Doctor (PhD)
at the University of Bergen

2018

Date of defence: 01.06.2018

Year: 2018

Title: Conforming Discretizations of Mixed-Dimensional Partial Differential Equations

Name: Wietse Marijn Boon

Print: Skipnes Kommunikasjon / University of Bergen

Preface

This dissertation is submitted as a partial fulfillment of the requirements for the degree of Doctor Philosophy (PhD) at the University of Bergen. The advisory committee has consisted of Jan M. Nordbotten (University of Bergen), Inga Berre (University of Bergen), and Sarah Gasda (Uni Research CIPR).

The PhD project has been financially supported by Norwegian Research Council grant 233736.

Acknowledgments

> "... and these little frogs live their whole lives in the flowers right at the top of the trees and don't even know about the ground, and once you know the world is full of things like that, your life is never the same."
>
> *Terry Pratchett*

The above quote describes the road I have traveled while working on this dissertation. Although it was written by one of my favorite fantasy authors, the heart of the matter is all too real. Time and time again, I was reminded by just how little I know and several people helped me understand lessons of science and life in general, which always lead to eye-opening realizations. I would therefore like to express my gratitude to the following individuals and groups of people who were there for me these past years.

First, I thank Jan, whose advice and intuition have played a major part in this work. As the main advisor, he gave me a firsthand experience of his way of conducting research which has been an invaluable and inspiring adventure. Thank you for giving me so many opportunities to develop as a mathematician and to travel the world in order to work with the most incredible people. Moreover, thank you for providing support during setbacks and clear, honest assessments whenever I encountered non-trivial forks in the road.

Inga and Sarah have been unbelievably helpful. I thank them for always being eager to discuss, providing help wherever necessary, and pulling me back to Earth when my thoughts were losing touch with applicability.

As for the rest of the Porous Media Group, thank you for creating the amazing atmosphere in the department. I am especially grateful to Michael, with whom I shared an office and a large amount of days discussing science as well as life, the universe, and everything. Ana, Alessio, and Eren deserve special mentions as well, for reasons they are undoubtedly aware of. For the entire PMG, I feel incredibly lucky to have met you, worked with you, and experienced so many memorable times with you.

Uiteraard volgt er nog een bedankje aan al mijn geliefde Nederlanders. Pap en mam, dankjulliewel voor de steun die ik nodig had om dit project aan te gaan in het hoge noorden. Wouter, Femke en Nienke, bedankt voor jullie begrip tijdens het volgen van mijn avontuur en ik hoop dat die van jullie net zoveel plezier geven. Ik bedank verder nog mijn vrienden bestaande uit de boefjes van H.I.C. en de malle makkers uit Limmen. De willekeurige weekendjes en hilarische bezoekjes waren voor mij een onmisbare afleiding. Mariëlle, dankjewel

voor je steun. Voor iedereen geldt dat ik het geweldig vind dat we het gesprek (en de borrel) altijd weer kunnen oppakken alsof we elkaar nog wekelijks zien.

Finally, I would like to thank Ivan Yotov, for hosting my unforgettable stay at the University of Pittsburgh. I am grateful to him as well as all other collaborators for their help and contributions to this work.

Thank you.

Abstract

Mixed-dimensional partial differential equations (PDEs) are coupled equations defined on connected manifolds of different dimensionalities. Two main examples of mixed-dimensional PDEs are considered in this dissertation, namely flow in fractured porous media and mechanics of composite materials. We focus on the discretization of these examples using hierarchical finite elements defined on coupled manifolds of codimension one, successively. By uncovering their underlying structure, we use the corresponding tools to define, analyze and discretize mixed-dimensional partial differential equations.

Our first example concerning mixed-dimensional PDEs arises in the context of fracture flow. Here, the planar fractures, intersection lines, as well as intersection points are represented as lower-dimensional manifolds. In turn, the entire embedded fracture network forms a mixed-dimensional geometry. We continue by defining the conservation and constitutive laws on the mixed-dimensional geometry, leading to a hierarchically coupled system of partial differential equations. Next, we extend these concepts from flow to derive the governing equations concerning mechanics of materials with thin inclusions in an analogous manner. Together, the embedded features and their surroundings form the mixed-dimensional geometry and the behavior of the system can be captured by prescribing significantly different material parameters. The analysis of these systems introduces several new concepts including mixed-dimensional function spaces and semi-discrete differential operators.

With the aim of discretization, we use finite element exterior calculus to construct mixed finite element schemes on the mixed-dimensional geometry. We focus on two families of mixed-dimensional finite elements, hierarchically ordered by dimensionality. We refer to these families as the first and second kind and show that both are of interest in the context of fracture flow, with different behavior in terms of convergence and computational cost. On the other hand, the mixed formulation of the mechanics equations requires the family of elements of the second kind.

For fracture flow, stability and optimal convergence of the discretization method are shown with the use of weighted, mixed-dimensional Sobolev spaces. A novel way of incorporating the fracture aperture leads to a scheme capable of handling arbitrarily small and spatially varying apertures. In case of fractures pinching out, the degeneration of the equations eliminates the possibility for flow resulting in a natural termination of fractures.

In a benchmark study concerning flow through fractured porous media, the proposed scheme is compared to various other numerical methods. Four two-dimensional test cases of varying complexity are considered, specifically designed to highlight the typical difficulties

with modeling flow through fracture networks. With eight participating numerical schemes, a clear view is given of the performance and limitations of the state-of-the-art numerical schemes.

Finally, we consider the evolution of the water table and identify the water table itself as a lower-dimensional manifold. Its location is governed by a partial differential equation which is coupled to the underlying saturated region. To solve this problem, a numerical scheme is proposed which maps the problem to a stationary reference domain. We analyze the properties of this scheme and successfully apply it to a real world problem concerning ground flow patterns surrounding meandering streams.

Outline

This dissertation consists of two parts. The scientific background is introduced in Part I followed by the scientific results in Part II.

Part I consists of five chapters. Chapter 1 serves as an introduction to the subject of mixed-dimensional partial differential equations. A selection of applications is presented which serve as motivation for this study. These examples form a recurring theme throughout the subsequent chapters, starting with Chapter 2. There, the governing physical laws are presented and we provide the relevant background knowledge concerning conventional, or fixed-dimensional, partial differential equations. The mixed-dimensional framework is presented in Chapter 3. We first establish the geometrical conventions and continue with the implications this has on structures from functional analysis and the model problems. Afterwards, Chapter 4 is concerned with the use of conforming finite elements as a discretization technique. Here, the mixed-dimensional, conforming finite elements are presented in the form of two families. Finally, Chapter 5 summarizes the scientific contributions of the articles included in Part II and presents an outlook on future research. A table containing the notation used in this thesis is included at the end of Part I.

Part II contains the scientific results, which are grouped as main and related works. The main results consist of the following six scientific articles:

Paper A W.M. Boon, J.M. Nordbotten, I. Yotov, *Robust Discretization of Flow in Fractured Porous Media*, SIAM Journal of Numerical Analysis, in review. arXiv:1601.06977 [math.NA].

Paper B W.M. Boon, J.M. Nordbotten, *Stable Mixed Finite Elements for Linear Elasticity with Thin Inclusions*, in preparation.

Paper C J.M. Nordbotten, W.M. Boon, *Modeling, Structure and Discretization of Mixed-dimensional Partial Differential Equations*, Domain Decomposition Methods in Science and Engineering XXIV, Lecture Notes in Computational Science and Engineering, in review. arXiv:1705.06876 [math.NA].

Paper D B. Flemisch, I. Berre, W.M. Boon, A. Fumagalli, N. Schwenck, A. Scotti, I. Stefansson, A. Tatomir (2018), *Benchmarks for Single-phase Flow in Frac-*

tured Porous Media, Advances in Water Resources 111, 239–258.
doi: 10.1016/j.advwatres.2017.10.036.

Paper E J.M. Nordbotten, W.M. Boon, A. Fumagalli, E. Keilegavlen, *Unified Approach to Discretization of Flow in Fractured Porous Media*, Computational Geosciences, in review.
arXiv:1802.05961 [math.NA]

Paper F W.M. Boon, N. Balbarini, P.J. Binning, J.M. Nordbotten (2017), *Efficient Water Table Evolution Discretization using Domain Transformation*, Computational Geosciences 21(1), 3–11.
doi: 10.1007/s10596-016-9597-9

Additionally, the following two supplementary articles on related work are included:

Paper G N. Balbarini, W.M. Boon, P.L. Bjerg, J.M. Nordbotten, P.J. Binning (2017), *A 3-D Model of the Influence of Meanders on Groundwater Discharge to a Gaining Stream in an Unconfined Sandy Aquifer*, Journal of Hydrology 552, 168–181.
doi: 10.1016/j.jhydrol.2017.06.042.

Paper H W.M. Boon, J.M. Nordbotten, *An Adaptive Penalty Method for Constrained Minimization Problems*, Optimization Letters, in review.

Contents

Preface iii

Acknowledgments v

Abstract vii

Outline ix

I Scientific Background 1

1 Introduction 3
1.1 Motivation . . . 4
1.1.1 Flows in Fractured Porous Media . . . 5
1.1.2 Mechanics of Materials with Thin Inclusions . . . 6
1.1.3 Challenges Related to Safe CO_2 Storage . . . 7

2 Fixed-Dimensional Partial Differential Equations 9
2.1 Linear Conservation Laws . . . 9
2.1.1 Mass . . . 10
2.1.2 Momentum . . . 10
2.1.3 Poroelastic Stress . . . 11
2.2 Constitutive Laws . . . 11
2.2.1 Darcy's law . . . 12
2.2.2 Hooke's law . . . 12
2.2.3 Biot Theory . . . 13
2.3 Reminders on Functional Analysis . . . 14
2.3.1 The de Rham Complex . . . 16
2.3.2 Saddle Point Theory . . . 17
2.4 Variational Formulations . . . 19
2.4.1 Porous Media Flow . . . 19
2.4.2 Linear Mechanics . . . 20
2.4.3 Poroelasticity . . . 21

2.5 Remarks on Variational Inequalities 22

3 Mixed-Dimensional Partial Differential Equations 25
3.1 Geometrical Setting 25
3.2 Mixed-Dimensional Functional Analysis 27
3.2.1 Exterior Calculus 29
3.3 Generalized Governing Equations 31
3.3.1 Scaling the Dual Variable 31
3.3.2 Porous Media Flow 32
3.3.3 Linear Elasticity 33
3.3.4 Poroelasticity 34
3.3.5 Water Table Evolution 35

4 Conforming Discretization Techniques 37
4.1 Mixed Finite Elements 37
4.1.1 Conforming Elements 37
4.1.2 Dimensional Hierarchy 38
4.2 Stability Theory 40
4.2.1 The Inf-Sup Condition 41
4.2.2 Reduction through Quadrature 42

5 Summary and Outlook 43
5.1 Summary of the Papers 43
5.1.1 Main Results 43
5.1.2 Related Work 48
5.2 Outlook 50

Bibliography 53

II Scientific Results 61

A Robust Discretization of Flow in Fractured Porous Media

B Stable Mixed Finite Elements for Linear Elasticity with Thin Inclusions

C Modeling, Structure and Discretization of Mixed-dimensional Partial Differential Equations

D Benchmarks for Single-phase Flow in Fractured Porous Media

E Unified Approach to Discretization of Flow in Fractured Porous Media

F Efficient Water Table Evolution Discretization using Domain Transformation

G A 3-D Model of the Influence of Meanders on Groundwater Discharge to a Gaining Stream in an Unconfined Sandy Aquifer

H An Adaptive Penalty Method for Constrained Minimization Problems

Part I

Scientific Background

Chapter 1

Introduction

The language of mathematics has become ever more useful to describe the world around us. Ranging from the fundamental physical laws which were understood centuries ago to the modern observations made today, natural processes can often be related to equations constructed with the vocabulary of mathematics.

As with any language, its dictionary evolves over time through a constant editing of the existing entries whenever new insights emerge and additions to incorporate recent discoveries. This thesis, as the title suggests, is concerned with a specific part of that dictionary, namely the coupling of partial differential equations defined on manifolds of different dimensionalities. We refer to such equations, or systems of equations, as mixed-dimensional and aim to uncover the general, analytical framework to analyze such problems, with a specific focus on elliptic PDEs defined on manifolds of co-dimension one.

At first, it may seem that such a generalized framework is only appealing to the mathematician's eye, yet it turns out that these insights can serve a greater purpose. In the context of numerical methods, the analytical tools provided by the mixed-dimensional setting have a practical potential when constructing discretization schemes with favorable properties. In particular, important aspects of the physical problem can be identified and can consequently be preserved in a discretization setting. In this work, for instance, we focus on conservation of mass and momentum and construct numerical schemes which preserve these quantities locally. It is thus important to remember that although it may be interesting to present this framework for its own sake in a more abstract setting, our goal is to uncover the aspects which are useful with respect to the development, implementation, and analysis of numerical methods.

The main contributions of this thesis work are as follows:

1. **Rigorous analysis of mixed-dimensional partial differential equations.** By starting with the geometry containing manifolds of heterogeneous dimensionalities, a rigorous setting is made to define mixed-dimensional partial differential equations. In this work, we define analytical constructs including function spaces and differential operators as the natural analogues to their fixed-dimensional counterparts. In turn, these constructs are used in Papers A, B, and C to define and analyze specific mixed-dimensional PDEs.

2. **Constructing a robust discretization scheme by considering fracture flow as a mixed-dimensional PDE.** A numerical method is proposed based on the ideology of the mixed-dimensional framework to model flow in fractured porous media. With the use of mixed finite elements and a specific scaling of the flux variable, the scheme is locally mass conservative and can naturally handle arbitrarily small apertures, as well as fracture ends. Stability and optimal convergence of the scheme are shown in Paper A, using the newly developed tools from the mixed-dimensional framework. As a participant in the benchmark study presented in Paper D, the proposed scheme is shown to perform well in comparison with participating methods, especially in terms of flexibility and applicability.

3. **Establishing a systematic approach to constructing conforming discretization methods for mixed-dimensional problems.** By identifying the differential forms of interest in the problem, a corresponding choice of mixed finite elements is provided with the use of finite element exterior calculus. As shown in Paper C, two families of finite elements arise leading to discretization schemes with different properties. Those of the first kind are used in Paper A whereas the family of the second kind is considered for linear elasticity in Paper B.
   Moreover, the class of conforming discretization methods is not limited to mixed finite elements. As shown in Paper E, discretization methods such as finite volume and virtual element methods can be extended in a systematic way to mixed-dimensional problems.

4. **Using domain transformation to create an efficient numerical scheme for modeling water table evolution.** The water table evolution problem consists of a partial differential equation defined on a non-stationary domain. In this formulation, the height of the domain depends on the solution, leading to a complicated situation from a modeling perspective. By employing a coordinate transform to a stationary reference domain, we show that a computationally inexpensive scheme can be constructed which deals with these complexities. The stability of the scheme is shown in Paper F and the method is successfully applied to a real world application in Paper G.

1.1 Motivation

Applications of mixed-dimensional partial differential equations range from subsurface flows to elasticity of composite materials as well as certain biomedical problems. In this work, we mainly focus on mixed-dimensional equations arising in the following way. First, we consider a physical process and assume that thin inclusions present in the domain can be modeled as lower-dimensional manifolds. On these manifolds, we then impose different physical parameters or model alternative physical processes compared to the surroundings. The system of governing equations which couples the surroundings with the embedded features can then be classified as a mixed-dimensional PDE. Admittedly, this definition is not particularly precise and we therefore provide several occurrences to give a better illustration.

In principle, lower-dimensional manifolds can be distinguished in two categories. First, physically lower-dimensional features such as the interface between a liquid and a gas may be considered as a manifold in the domain. On this manifold, we may consider the surface tension as a physical process which is closely related to the physical processes in the neighboring liquid and gas regions. These interdependencies between equations defined on domains with different dimensionalities characterize the resulting system as mixed-dimensional.

On the other hand, lower-dimensional manifolds can be a result of modeling assumptions, which is the category on which this work focuses. In those cases, it is assumed that a feature has a negligibly small width or aperture in comparison to the domain of computation. By collapsing these thin features to lower-dimensional manifolds, reduced equations can be derived which are easier to solve both analytically and computationally. Moreover, from a discretization perspective, the construction of a shape-regular grids is a major challenge if the elements need to comply with the small widths or apertures. In fact, if we force the grid to respect the small width of these features, a significant refinement needs to be applied in the surroundings, leading to large numbers of elements. The reduction to a lower-dimensional feature greatly relieves these difficulties and allows for the use of grids with relatively fewer elements.

We consider two physical processes throughout this thesis. These are flow through fractures in a porous medium and elasticity of composite materials. At the intersection of these phenomena lies the theory of poroelasticity, which we refer to occasionally. In order to communicate the physical relevance before introducing the mathematical setting, we summarize the important aspects in terms of applications in the following two subsections.

1.1.1 Flows in Fractured Porous Media

Whether considering groundwater in the subsurface or blood flowing through biological tissue, flows through porous media can be found in a wide variety of scientific fields. In this work, we focus on single-phase flows of incompressible fluids such as water, brine, or oil through subsurface rock. With this starting point, many alleys of investigation are possible, including multiphase flows or the coupling of flow with chemical processes and thermal effects. Here, however, our interest lies in mixed-dimensional partial differential equations and therefore consider the incorporation of fractures within the rock.

Fractures are ever-present in the subsurface, ranging from small fractures on the centimeter scale to faults slicing through several rock layers. Since liquids flow more easily through fractures than the surrounding, porous rock, they play an important role in stimulating fluid flows [2]. In turn, engineering applications concerning geothermal energy as well as oil recovery aim to use these flow paths to their advantage. Therefore, a proper understanding of flows through fractures is essential in order to optimize in terms of technology and exploit the fracture network to its fullest extent.

Due to their high density and varying orientations, fractures frequently intersect to form complex networks [24]. It is therefore problematic from a modeling perspective to keep track of all fractures in a network. However, the effect a fracture has on a system strongly depends on its size. In our models, therefore assume that homogenization has been applied to fractures

below a certain length scale and only larger fractures are incorporated explicitly.

In the context of mixed-dimensional PDEs, we consider the fractures as lower-dimensional manifolds. Thus, in a three-dimensional rock, the fractures are represented as two-dimensional planes. For simplicity, the curvature is neglected and we incorporate fractures as either ellipsoids or polygonal surfaces. Aside from the advantages this assumption adds with respect to mesh generation in the discretization step, it is also useful in the modeling stage. Most notably, the separation of the manifold from its surrounding allows us to easily introduce different material properties on each manifold such as the permeability or, more drastically, impose more sophisticated governing flow equations. We may, for example, consider Stokes flow in the fractures and Darcy flow in the matrix.

The representation of fractures as lower-dimensional features was introduced by [3, 4] and is frequently used in fracture flow modeling. The resulting models are referred to as Discrete Fracture Models, or DFM, and a variety of methods have been developed over the years. Notable contributions include the mortar approach [28, 40], the use of X-FEM and unfitted grids [23, 29, 38], and several finite volume schemes, see e.g. [46, 50]. Further references to key contributions in this field can be found in Papers A and D.

The key concept in this work which separates it from other DFM methods is the introduction of a mixed-dimensional PDE and the use of semi-discrete operators to construct the model. This allows us to analyze the problem on a continuous level before introduction of the mesh, and results in a natural incorporation of intersection lines and points, as well as fracture ends. Moreover, through the mixed-dimensional geometry, the inside of the fracture is considered a separate entity from the interfaces with the surrounding matrix. This allows for a distinct treatment of coupling conditions, more advanced reduced equations, and even varying discretization approaches between dimensions, as shown in Paper E.

1.1.2 Mechanics of Materials with Thin Inclusions

Our second application is concerned with elasticity. One of the most accessible examples in this context is to consider plate-reinforced concrete. The composition of these two materials combines the light weight of concrete with the strength of steel, thus using the advantages of each component. This constitutes a typical example of thin inclusions, namely the plates, with significantly different material properties compared to its surroundings. In this case, we can consider a mechanical process defined on the plates which is fully coupled to the mechanical process active in the surrounding concrete. By making modeling assumptions to represent the plates as lower-dimensional manifolds, we can describe this process mathematically using coupled differential equations. Due to the interaction between the mechanical process in the three-dimensional surroundings with a similar process defined on a lower-dimensional manifold, we arrive at a mixed-dimensional partial differential equation.

Alternatively, we could remain in the context of subsurface rock and consider fractures cemented due to a chemical reaction. In this setting, the fractures are filled with a material which is assumed to act as an elastic medium. The material properties remain to be defined and we can consider either weak or strong inclusions relative to the surroundings, depending on the context. For weak inclusions, however, possible contact between the sides of the frac-

tures significantly increases the complexity of the model. Such contact problems typically lead to variational inequalities, and Paper H is related to this field.

The setting considered herein differs slightly from the conventional theory of thin shells, see e.g. [21]. Here, we always assume that the lower-dimensional manifold is fully coupled to a surrounding medium. We are thus interested in the elastic behavior of the material as a whole with respect to the material properties of the thin inclusions, similar to [18].

By imposing appropriate conditions on the boundary of the domain or inside the fractures, circumstances can be mimicked which stimulate fracture propagation. This is an essential process for geothermal energy applications, for example, since a generated fracture network enables fluid flow between an injection and an extraction well. The models related to rock failure form a scientific field of their own (see e.g. [26, 35] and references therein) which is beyond the scope of this work. Nevertheless, we note that the main ingredient for fracture propagation is the stress field and we are therefore interested in models which explicitly incorporate the stress as a variable. Here, and particularly in Paper B, we focus on mixed finite elements to accomplish this rather than conventional finite elements since the latter require post-processing procedures to reconstruct the stress.

1.1.3 Challenges Related to Safe CO_2 Storage

CO_2 capture and storage is a modern technique proposed to tackle the atmospheric carbon problem [43]. The idea is to capture CO_2 instead of releasing it in the atmosphere and use subsurface formations as storage sites for large quantities. The formation needs to be sufficiently permeable to accommodate the injected CO_2 and overlain by a low permeable layer to keep it in place. This sealing formation is referred to as the caprock and its properties are of vital importance in the study of storage capacity and leakage risks.

This application unifies the different mixed-dimensional problems considered in this work. In particular, two aspects related to this technology can be described by mixed-dimensional PDEs, namely the integrity of the caprock and the separated flow through the aquifer of CO_2 and brine.

First, let us consider the mechanical response of the caprock to the injection of CO_2 which greatly influences its integrity. Here, we can consider two different scales. At the large scale, we can consider the aquifer in which the injection takes place as a lower-dimensional manifold. This is due to the fact that an aquifer typically has a horizontal extent which is much greater than its vertical height [12, 43]. A mixed-dimensional approach is then still capable of capturing the different material properties of the aquifer and caprock and in turn, can describe the response of the caprock to increased pressures in the aquifer during and after injection.

At a smaller scale, fractures present in the caprock could be hazardous. The highly conductive fractures may stimulate leakage of the injected CO_2 to unwanted locations or worse, back to the surface. The modeling of flow through such fractured media could provide valuable insight into the leakage pathways out of the storage site.

Secondly, the flow of the more buoyant CO_2 through the aquifer is typically modeled using sharp interface equations [22, 30]. Such models are structurally similar to the water

table evolution equations considered in Papers F and G. The sharp interface is represented as a lower-dimensional manifold and its location is determined by the surrounding flow processes, leading to a coupled, dynamical system.

Thirdly, the mathematical models applied to these problems need to respect physical constraints in order to produce sensible solutions. In the context of CO_2 storage, it would for example, not be sensible to have negative saturations in multiphase flows. On the other hand, in sharp interface models, the location of the interface is bounded by the impermeable caprock. These constraints can be incorporated in the mathematical model with the use of variational inequalities, which we consider in Paper H.

In short, the mathematical theory proposed in this dissertation are directly related to a range of physical processes. As is explained in this work, the proper understanding of mixed-dimensional problems greatly benefits the development of solution strategies for its related problems. These results can therefore be considered an example of how the development of mathematics in an abstract form is not only important for its own sake, but also for its implications in various real-world applications.

Chapter 2

Fixed-Dimensional Partial Differential Equations

To become acquainted with the mathematical formulations of the examples mentioned in Chapter 1, this chapter starts with a single domain of interest and describes the relevant physical processes with the use of mathematical concepts. These descriptions lead to fixed-dimensional, or conventional, partial differential equations. The theory on PDEs is rich (see e.g. [25, 33]) and we restrict this exposition to the topics of interest for the subsequent chapters. In short, this chapter shows how certain physical processes can be translated to mathematical systems of equations and how to arrive at the weak or variational formulation of these problems.

This section presents the derivation using the following steps: First, the physical conservation laws of interest are introduced in Section 2.1. Then, in Section 2.2, we consider the associated constitutive law and boundary conditions which close the system. The necessary tools from functional analysis are introduced in Section 2.3 with which the variational formulations are derived in Section 2.4. The generalization to variational inequalities is considered in Section 2.5.

2.1 Linear Conservation Laws

At the cornerstone of all models considered here is the physical concept of conservation. Conservation laws arise in several different fields of physics and include, but are not limited to, conservation of energy, conservation of electric charge, and conservation of linear and angular momentum. The mathematical description of these laws follows a certain structure, which we explain in this section using the conservation of mass as an example. The analogous conservation laws relevant to linear elasticity and poroelasticity are considered afterwards.

2.1.1 Mass

In order to describe mass conservation as a mathematical equation, we consider a porous medium saturated by an incompressible fluid and follow the derivation presented in [43]. Let us consider a given volume Ω in n dimensions with boundary $\partial\Omega$. Typically, choosing $n = 2$ or $n = 3$ suffices for practical applications. On this volume, we introduce the function m to represent the mass per unit volume at a certain point, as is conventional in continuum models. Secondly, the flux $\boldsymbol{q}$ is defined as a vector function on Ω representing the discharge of a fluid per unit area. The third ingredient is a source or sink of mass denoted by f_q, which can be related to a production or injection well, for example.

The total change in mass over time $\dot{m}$ in the volume Ω is then given by the mass entering through the boundary $\partial\Omega$ and mass entering or leaving due to the source (or sink) f_q. This relationship can be expressed mathematically by the following integral equation

$$\int_\Omega \dot{m}\mathrm{d}x = -\int_{\partial\Omega} \boldsymbol{q}\cdot\boldsymbol{n}\mathrm{d}s + \int_\Omega f_q\mathrm{d}x.$$

Here, $\boldsymbol{n}$ is the outward normal vector to $\partial\Omega$ with unit length. Using the divergence theorem, the first term on the right-hand side is rewritten as a volume integral leading to the following equation

$$\int_\Omega \dot{m} + \nabla\cdot\boldsymbol{q} - f_q\mathrm{d}x = 0,$$

with $\nabla\cdot$ denoting the divergence. The examples which follow in this work mainly concern incompressible fluids, or finding a steady state solution. In either case, the first term is zero since there will be no changes in mass in the given, stationary volume Ω. We may therefore simplify this equation to

$$\int_\Omega \nabla\cdot\boldsymbol{q} - f_q\mathrm{d}x = 0. \tag{2.1.1}$$

The final step is to note that the integral (2.1.1) is zero for any arbitrary volume Ω. In turn, the integrand is identically zero and we arrive at the differential equation

$$\nabla\cdot\boldsymbol{q} = f_q. \tag{2.1.2}$$

In the remainder, we will refer to equation (2.1.2) as the description of the law of mass conservation. Note that it is a simple relationship involving only the divergence as a differential operator. Naturally this equation does not suffice to model subsurface flows and we will consider an additional, constitutive law relating the flux $\boldsymbol{q}$ to the pressure p in Section 2.2.1.

2.1.2 Momentum

The second example we consider is related to elasticity. The conservation laws of interest then concern linear and angular momentum [34]. For its derivation, we first translate from the flow terminology above to the counterparts in the context of mechanics. First, the analogue of the flux is the Cauchy stress tensor, which we denote by σ. It represents a force per unit area.

Secondly, a body force, denoted by $\boldsymbol{f}_\sigma$ can be interpreted as a vector-valued source term. We are once again interested in equilibrium states, thus all terms concerning derivatives in time are eliminated. Following an analogous derivation as in Section 2.1.1, we obtain the following conservation law, commonly referred to as the conservation of linear momentum:

$$\nabla \cdot \sigma = \boldsymbol{f}_\sigma. \tag{2.1.3}$$

For the purpose of this section, conservation of linear momentum can thus be seen as the tensorial equivalent of (2.1.2).

On the other hand, equilibrium implies that angular momentum is conserved as well. This is related to the symmetry of the stress tensor σ, which can be mathematically described by

$$\operatorname{asym} \sigma := \frac{1}{2}\left(\sigma - \sigma^T\right) = 0. \tag{2.1.4}$$

Here, the superscript T denotes the transpose. Together, these two equations describe the linear conservation laws for mechanics considered in this work.

2.1.3 Poroelastic Stress

Thirdly, the coupled process of porous media flow and mechanics is known as poromechanics. In terms of the relevant conservation laws, which is central to this subsection, the key is to find the conserved, physical quantities. For that purpose, we first focus on the conservation of linear momentum from (2.1.3). The pressure p of the fluid influences this stress balance by acting as an isotropic stress. In turn, the conserved quantity is the poroelastic (or total) stress σ_p, given by

$$\sigma_p = \sigma - \alpha p I, \tag{2.1.5}$$

where α is the Biot-Willis constant and I is the identity tensor. In turn, the conservation of linear momentum (2.1.3) in a poroelastic medium is given by

$$\nabla \cdot \sigma_p = \boldsymbol{f}_\sigma. \tag{2.1.6}$$

Note that the modification to the stress tensor in (2.1.5) only affects the diagonal terms. Therefore, the equilibrium equation describing conservation of angular momentum remains unchanged

$$\operatorname{asym} \sigma_p = \operatorname{asym} \sigma = 0.$$

As for the law of conservation of mass, this expression changes due to the deformation of the material. This modification will be considered with the constitutive laws in Section 2.2.3.

2.2 Constitutive Laws

The second ingredient in modeling the physical processes of interest in this work is to supplement the conservation equation from the previous section with a constitutive law and appropriate boundary conditions. The constitutive law is usually derived through a simplification

of the true physical law by using convenient assumptions. Following the same structure as Section 2.1, we first look at porous media flow, followed by linear elasticity and poromechanics.

2.2.1 Darcy's law

The pressure p is a scalar quantity which, in continuum models, represents the force per area exerted by the fluid. Fluids flow from high to low pressure regions, which can easily be described by the linear relationship known as Darcy's law [43]. This law can be derived rigorously through homogenization of the Navier-Stokes equations with the assumption of creeping flow [52]. Here, however, it suffices to introduce this law by defining a symmetric, positive-definite permeability tensor K as the coefficient in the following linear equation:

$$\boldsymbol{q} = -K(\nabla p - \rho \boldsymbol{g}). \tag{2.2.1}$$

The density of the fluid is represented by ρ and $\boldsymbol{g}$ is the force of gravity. In the following, we will neglect gravity effects.

Finally, appropriate boundary conditions are required in order to make the problem well-posed. For this, we assume that the boundary is decomposed disjointly as $\partial\Omega = \partial_p\Omega \cup \partial_q\Omega$. We prescribe the normal flux on $\partial_q\Omega$ and the pressure on $\partial_p\Omega$. In order to obtain a unique solution, $\partial_p\Omega$ is assumed to have positive measure, i.e. the pressure is prescribed on a section of the boundary, not merely at distinct points. The boundary data is denoted as g_q for the normal flux and g_p for the pressure.

The system of equations describing porous media flow is then given by Darcy's law, the law of mass conservation, and the imposed boundary conditions:

$$\boldsymbol{q} = -K\nabla p \tag{2.2.2a}$$

$$\nabla \cdot \boldsymbol{q} = f_q \qquad \text{in } \Omega, \tag{2.2.2b}$$

$$p = g_p \qquad \text{on } \partial_p\Omega, \tag{2.2.2c}$$

$$\boldsymbol{q} \cdot \boldsymbol{n} = g_q \qquad \text{on } \partial_q\Omega. \tag{2.2.2d}$$

2.2.2 Hooke's law

Similar to the pressure introduced for the flow equations, we consider the vector-valued displacement $\boldsymbol{u}$ in the context of mechanics. Again, we remain within the linear regime and introduce the relationship between stress and displacement using the theory of infinitesimal strain. Thus, our first assumption is that the deformation and its gradient are small with respect to the size of the domain. The linearized strain $\varepsilon(\boldsymbol{u})$ can then be introduced as

$$\varepsilon(\boldsymbol{u}) = \operatorname{sym}(\nabla \boldsymbol{u}) = \frac{1}{2}\left(\nabla \boldsymbol{u} + (\nabla \boldsymbol{u})^T\right). \tag{2.2.3}$$

In turn, the constitutive law relates the stress σ with the strain $\varepsilon(\boldsymbol{u})$. The stress-strain relationship considered in this work is given by Hooke's law. In isotropic materials, we can use the Lamé parameters μ and λ to describe this law as

$$\sigma = 2\mu\varepsilon(\boldsymbol{u}) + \lambda \operatorname{Tr}(\varepsilon(\boldsymbol{u}))I, \tag{2.2.4}$$

where we use Tr to denote the trace of a tensor and I once again denotes the identity tensor. Since we aim to retain the strong sense of conservation with respect to momentum as introduced in Section 2.1.2, our preference is to keep the stress as one of our variables. Therefore, it is more preferable to write the strain as a function of the stress rather than vice versa. Therefore, we invert the linear relationship (2.2.4) to obtain

$$\varepsilon(\boldsymbol{u}) = A\sigma := \frac{1}{2\mu}\left(\sigma - \frac{\lambda}{2\mu + n\lambda}\operatorname{Tr}(\sigma)I\right). \tag{2.2.5}$$

Note that n, the dimensionality of the domain, plays a role in this equation. In fact, in case of $n = 2$, then the third dimension is simply not a part of our model. As such, the model does not formally correspond to either plane-stress or plane-strain assumptions, but rather to both since all variables are defined in the plane.

Finally, appropriate boundary conditions are required to close the system. The boundary of the domain is assumed to be decomposable in the disjoint union $\partial\Omega = \partial_u\Omega \cup \partial_\sigma\Omega$. The displacement is prescribed as $\boldsymbol{g}_u$ on $\partial_u\Omega$, which is assumed to have positive measure. On the other hand, $\partial_\sigma\Omega$ denotes the section of the boundary on which the normal stress is given, which may be empty. The given value for the normal stress is denoted by $\boldsymbol{g}_\sigma$.

The full system of equations governing linear elasticity is then given by the constitutive law, the two conservation equations form Section 2.1.2 and the given boundary conditions:

$$A\sigma = \varepsilon(\boldsymbol{u}) \tag{2.2.6a}$$

$$\nabla \cdot \sigma = \boldsymbol{f}_\sigma \tag{2.2.6b}$$

$$\operatorname{asym}\sigma = 0 \qquad \text{in } \Omega, \tag{2.2.6c}$$

$$\boldsymbol{u} = \boldsymbol{g}_u \qquad \text{on } \partial_u\Omega, \tag{2.2.6d}$$

$$\sigma \cdot \boldsymbol{n} = \boldsymbol{g}_\sigma \qquad \text{on } \partial_\sigma\Omega. \tag{2.2.6e}$$

The attentive reader will notice that (2.2.6c) is superfluous since it follows directly from (2.2.6a). Nevertheless, it is presented here to ease the translation towards the variational formulation with relaxed symmetry in Section 2.4.2.

Remark 2.2.1 *The conventional approach to linear elasticity is to eliminate the stress σ by substituting* (2.2.4) *into* (2.2.6b) *and consider only the primal variable, the displacement. This leads to a much simpler system but the explicit imposition of momentum conservation is lost.*

2.2.3 Biot Theory

In a poroelastic medium, the flow through the pores and the mechanical properties of the matrix form a coupled process. Thus, in the study of poromechanics, we combine the governing equations for flow with those for mechanics to arrive at Biot consolidation theory [11].

Here, we restrict the mathematical description to the linearized, quasi-static system. That is, we assume that the inertial effects are negligible and may therefore consider the equilibrium equations from Section 2.1.2.

The constitutive laws in this case consist of the coupling between the flow and mechanics. First, as we have seen in section 2.1.3, the pressure acts as an isotropic stress. The pressure is included in the definition of the conserved quantity, known as the poroelastic stress, as shown in (2.1.5). On the other hand, the influence of mechanics on the flow is incorporated by modifying the conservation equation (2.1.2). Changes in volume are directly related to the divergence of the displacement over time. The mass conservation equation is then modified with a second instance of Biot-Willis constant α:

$$S_0\dot{p} + \alpha\nabla\cdot\dot{\boldsymbol{u}} + \nabla\cdot\boldsymbol{q} = f_q. \tag{2.2.7}$$

Here, S_0 denotes the specific storativity, which is included for generality, in case compressible fluids are considered. Combining this equation with the flow and mechanics systems from this section, the quasi-static, linear Biot system is formed:

$$\begin{aligned} A(\sigma_p + \alpha p I) &= \varepsilon(\boldsymbol{u}) && && \text{(2.2.8a)}\\ S_0\dot{p} + \alpha\nabla\cdot\dot{\boldsymbol{u}} + \nabla\cdot\boldsymbol{q} &= f_q, && && \text{(2.2.8b)}\\ \boldsymbol{q} &= -K\nabla p && && \text{(2.2.8c)}\\ \nabla\cdot\sigma_p &= \boldsymbol{f}_\sigma && && \text{(2.2.8d)}\\ \operatorname{asym}\sigma_p &= 0 && \text{in } \Omega. && \text{(2.2.8e)} \end{aligned}$$

Just as this system of equations is a combination of the flow and elasticity equations, the relevant boundary conditions are given by combinations as well. Using the same notation for the parts of the boundary with specific boundary conditions, we impose

$$\begin{aligned} \boldsymbol{u} &= \boldsymbol{g}_u \text{ on } \partial_u\Omega, & \sigma_p\cdot\boldsymbol{n} &= \boldsymbol{g}_\sigma \text{ on } \partial_\sigma\Omega, && \text{(2.2.9a)}\\ p &= g_p \text{ on } \partial_p\Omega, & \boldsymbol{q}\cdot\boldsymbol{n} &= g_q \text{ on } \partial_q\Omega. && \text{(2.2.9b)} \end{aligned}$$

In this case, the boundary of the domain is decomposed in two, possibly different ways, given by $\partial\Omega = \partial_p\Omega \cup \partial_q\Omega = \partial_u\Omega \cup \partial_\sigma\Omega$. Again, we assume that the boundaries $\partial_p\Omega$ and $\partial_u\Omega$ have positive measure for solvability purposes. Note that the boundary condition imposed on $\partial_\sigma\Omega$ concerns the poroelastic stress, which is natural since this is the conserved quantity.

Again, the system can be simplified by substituting equations into each other. We refer to this formulation as the five-field formulation and the system of equations formed after elimination of the stress is known as the three-field formulation. This has been investigated numerically in [31, 45], among others. Further elimination of the flux then leads to the two-field formulation, see e.g. [37]. In this work, we prefer the five-field formulation due to the explicit imposition of mass and momentum conservation.

2.3 Reminders on Functional Analysis

A detailed introduction to the elegant field of functional analysis is not within the scope of this dissertation. Rather, we will pick up the theory at the point where the definitions and theorems start to be of relevance to the problems at hand. We thereby emphasize the key tools

used in the subsequent chapters and articles rather than the formal, underlying details. For a more thorough explanation of the concepts introduced here, we refer the reader to [1, 13, 20].

We start by defining the function space $L^2(\Omega;\mathbb{F})$, of square-integrable functions defined on Ω which map to $\mathbb{F}$. In the fixed-dimensional case in n dimensions, $\mathbb{F}$ is typically either the space of real numbers $\mathbb{R}$, vectors $\mathbb{V} = \mathbb{R}^n$, or $n \times n$ matrices $\mathbb{V}^n$. For two elements $f, g \in L^2(\Omega;\mathbb{F})$, the inner product and induced norm are then given by

$$(f,g)_\Omega = \int_\Omega f \cdot g \mathrm{d}x, \qquad \|f\|^2_{L^2(\Omega)} = (f,f)_\Omega . \tag{2.3.1}$$

Here, the dot-product is the inner product associated with $\mathbb{F}$. The space $L^2(\Omega;\mathbb{F})$ can thus be defined as

$$L^2(\Omega;\mathbb{F}) = \left\{ f : \Omega \to \mathbb{F} : \|f\|_{L^2(\Omega)} < \infty \right\}. \tag{2.3.2}$$

In terms of analysis, the restriction to square-integrable functions and the associated inner product is advantageous. However, we typically require a few more properties in order to consider a partial differential equations. As we have seen, most conservation principles are stated using the divergence operator. In order for such a statement to be well-defined, the function in question needs to have sufficient regularity to apply the divergence. Therefore, we will next consider certain subspaces of L^2 based on regularity properties.

The following three function spaces will play a dominant role in this work:

$$H^1(\Omega;\mathbb{R}) = \left\{ f \in L^2(\Omega;\mathbb{R}) : \ \nabla f \in L^2(\Omega;\mathbb{V}) \right\}, \tag{2.3.3a}$$

$$H(\mathrm{curl},\Omega;\mathbb{V}) = \left\{ \boldsymbol{f} \in L^2(\Omega;\mathbb{V}) : \ \nabla \times \boldsymbol{f} \in L^2(\Omega;\mathbb{V}) \right\}, \tag{2.3.3b}$$

$$H(\mathrm{div},\Omega;\mathbb{V}) = \left\{ \boldsymbol{f} \in L^2(\Omega;\mathbb{V}) : \ \nabla \cdot \boldsymbol{f} \in L^2(\Omega;\mathbb{R}) \right\}. \tag{2.3.3c}$$

These are Hilbert spaces in their own right and therefore endowed with inner products. These inner products induce the following norms, on which we omit the field $\mathbb{F}$ for notational convenience:

$$\|f\|^2_{H^1(\Omega)} = \|f\|^2_{L^2(\Omega)} + \|\nabla f\|^2_{L^2(\Omega)}, \tag{2.3.4a}$$

$$\|\boldsymbol{f}\|^2_{H(\mathrm{curl},\Omega)} = \|\boldsymbol{f}\|^2_{L^2(\Omega)} + \|\nabla \times \boldsymbol{f}\|^2_{L^2(\Omega)}, \tag{2.3.4b}$$

$$\|\boldsymbol{f}\|^2_{H(\mathrm{div},\Omega)} = \|\boldsymbol{f}\|^2_{L^2(\Omega)} + \|\nabla \cdot \boldsymbol{f}\|^2_{L^2(\Omega)}. \tag{2.3.4c}$$

In order to incorporate boundary conditions, we use a subscript zero to indicate the subspaces containing functions with zero trace on $\partial\Omega$. In other words, let us define

$$H^1_0(\Omega;\mathbb{R}) = \left\{ f \in H^1(\Omega;\mathbb{R}) : \ f|_{\partial\Omega} = 0 \right\}, \tag{2.3.5a}$$

$$H_0(\mathrm{curl},\Omega;\mathbb{V}) = \left\{ \boldsymbol{f} \in H(\mathrm{curl},\Omega;\mathbb{V}) : \ \boldsymbol{n} \times \boldsymbol{f}|_{\partial\Omega} = 0 \right\}, \tag{2.3.5b}$$

$$H_0(\mathrm{div},\Omega;\mathbb{V}) = \left\{ \boldsymbol{f} \in H(\mathrm{div},\Omega;\mathbb{V}) : \ \boldsymbol{n} \cdot \boldsymbol{f}|_{\partial\Omega} = 0 \right\}. \tag{2.3.5c}$$

To finalize this section, we recall the algebraic identities which are commonly used in our analysis. First, let us consider $\boldsymbol{f} \in H(\mathrm{div},\Omega;\mathbb{V})$ and $g \in H^1(\Omega;\mathbb{R})$. Integration by parts and the divergence theorem then give us the following equation

$$(\nabla \cdot \boldsymbol{f}, g)_\Omega + (\boldsymbol{f}, \nabla g)_\Omega = \int_\Omega \nabla \cdot (\boldsymbol{f} g) \mathrm{d}x = (\boldsymbol{f} \cdot \boldsymbol{n}, g)_{\partial\Omega}, \tag{2.3.6}$$

where $\boldsymbol{n}$ is the outward normal vector to the boundary $\partial\Omega$ with unit length.

Remark 2.3.1 *A word of caution is in order with respect to the right-hand side of* (2.3.6)*. Technically speaking, this term represents a duality pairing and not an L^2 inner product. This is due to the fact that the normal trace of $\boldsymbol{f} \in H(\mathrm{div}, \Omega; \mathbb{V})$ is generally not in $L^2(\partial\Omega)$, but in the dual of $H^{\frac{1}{2}}(\partial\Omega)$ [13]. In the subsequent chapters, this is rarely encountered since we often impose higher regularity assumptions on the functions $\boldsymbol{f}$ and g.*

Finally, we introduce another important building block in functional analysis, namely the dual space. For a given function space F, we define its dual space F^* as the space of linear, continuous functionals acting on F. The dual space, denoted with a superscript asterisk, is a normed space with its norm given by

$$\|g\|_{F^*} = \sup_{f \in F \setminus \{0\}} \frac{\langle g, f \rangle_{F^* \times F}}{\|f\|_F}, \tag{2.3.7}$$

with angled brackets denoting the duality pairing.

2.3.1 The de Rham Complex

The function spaces introduced thus far are intimately related by the de Rham complex. Again, the theory surrounding this complex is much richer than what can be considered here and we refer the interested reader to the works of Bott and Tu [14] and Spivak [48] for more comprehensive introductions. Herein, we restrict the exposition to the concepts which resurface in the subsequent chapters.

On a smooth domain Ω in three dimensions, let us arrange the introduced function spaces from (2.3.3) in the following sequence.

$$\mathbb{R} \hookrightarrow H^1(\Omega; \mathbb{R}) \xrightarrow{\nabla} H(\mathrm{curl}, \Omega; \mathbb{V}) \xrightarrow{\nabla\times} H(\mathrm{div}, \Omega; \mathbb{V}) \xrightarrow{\nabla\cdot} L^2(\Omega; \mathbb{R}) \to 0. \tag{2.3.8}$$

Two important properties are represented in this diagram. First, each differential operator maps into the next function space with the far left and right arrows corresponding to an inclusion and zero operator, respectively. Secondly, we note that two consecutive steps in this diagram corresponds to mapping to zero. In particular, using elementary results from calculus, we see that the gradient of a constant function is zero and moreover, that the gradient of a scalar function has zero curl. Finally, taking the divergence of the curl of a vector function leads to zero as well.

On the other hand, for the imposition of boundary conditions, we concern ourselves with the subspaces consisting of functions with zero trace from (2.3.5). Again, a sequence arises:

$$0 \hookrightarrow H_0^1(\Omega; \mathbb{R}) \xrightarrow{\nabla} H_0(\mathrm{curl}, \Omega; \mathbb{V}) \xrightarrow{\nabla\times} H_0(\mathrm{div}, \Omega; \mathbb{V}) \xrightarrow{\nabla\cdot} L^2(\Omega; \mathbb{R}) \to \mathbb{R}. \tag{2.3.9}$$

Here, the rightmost arrow corresponds to integration over the domain.

For applications to the mechanics equations, we are interested in the vector-valued de Rham complex which can be formed by applying the differential operators in a row-wise

manner. We repeat it here for convenience:

$$\begin{aligned}
&\mathbb{R}^n \hookrightarrow H^1(\Omega;\mathbb{R}^n) \xrightarrow{\nabla} H(\mathrm{curl},\Omega;\mathbb{V}^n) \xrightarrow{\nabla\times} H(\mathrm{div},\Omega;\mathbb{V}^n) \xrightarrow{\nabla\cdot} L^2(\Omega;\mathbb{R}^n) \to 0\\
&0 \hookrightarrow H_0^1(\Omega;\mathbb{R}^n) \xrightarrow{\nabla} H_0(\mathrm{curl},\Omega;\mathbb{V}^n) \xrightarrow{\nabla\times} H_0(\mathrm{div},\Omega;\mathbb{V}^n) \xrightarrow{\nabla\cdot} L^2(\Omega;\mathbb{R}^n) \to \mathbb{R}^n.
\end{aligned} \tag{2.3.10}$$

Remark 2.3.2 *By intention, the complex* (2.3.10) *remains silent on the presence of symmetry for matrices in $\mathbb{V}^n$. The asymmetry mapping can be included, which leads to the more sophisticated elasticity complex as introduced by Arnold et al. [8].*

In the language of exterior calculus, the complex (2.3.8) is considered a representation of a more general structure. Let $\Lambda^k(\Omega)$ denote the space of smooth differential k-forms on an n-dimensional domain Ω. Let d denote the exterior derivative which maps differential k-forms to differential $(k+1)$-forms. Thus, a sequence of spaces is formed with an increasing index k and an operator d which maps each space to the next.

$$0 \longrightarrow \Lambda^0(\Omega) \xrightarrow{\mathrm{d}} \Lambda^1(\Omega) \xrightarrow{\mathrm{d}} \Lambda^2(\Omega) \dashrightarrow^{\mathrm{d}} \Lambda^n(\Omega) \longrightarrow 0. \tag{2.3.11}$$

Since two consecutive applications of the exterior derivative d maps to zero, i.e.

$$\mathrm{dd} = 0, \tag{2.3.12}$$

the sequence (2.3.11) is called a co-chain complex and is referred to as the de Rham complex. A form $a \in \Lambda^k(\Omega)$ is called closed if $\mathrm{d}a = 0$ and exact if a form $b \in \Lambda^{k-1}$ exists such that $\mathrm{d}b = a$. Thus, all exact forms are closed. On the other hand, if Ω is contractible, then all closed forms are exact as well [48].

Next, we fit the Sobolev spaces from Section 2.3 into this setting, which explains the similarities in the norms given by (2.3.4). Let us consider the norm

$$\|v\|^2_{H\Lambda^k(\Omega)} = \|v\|^2_{L^2(\Omega)} + \|\mathrm{d}v\|^2_{L^2(\Omega)}, \tag{2.3.13}$$

and the corresponding Hilbert space

$$H\Lambda^k(\Omega) = \left\{ v \in \Lambda^k(\Omega) : \|v\|_{H\Lambda^k(\Omega)} < \infty \right\}. \tag{2.3.14}$$

By identifying the exterior derivative as a gradient, curl, divergence or zero operator depending on the value of k, we can identify the central four spaces in sequence (2.3.8) with the sequence given by $H\Lambda^k(\Omega)$ with k ranging from 0 to $n = 3$.

2.3.2 Saddle Point Theory

As we have seen in the examples from Section 2.1, we treat the conservation law explicitly while putting less emphasis on the constitutive law. To that effect, the primary variable, i.e. the pressure or displacement, will act as a Lagrange multiplier which enforces this conservation law locally. As is often the case after the introduction of Lagrange multipliers, the problems we arrive at can be identified as saddle point problems.

In order to make this identification, we use the structure of saddle point problems to rewrite the problem to a standardized form [13]. To consider a general problem of this form, we need two spaces $\boldsymbol{Q}$ and P as well as linear, continuous operators $A : \boldsymbol{Q} \to \boldsymbol{Q}^*$ and $B : \boldsymbol{Q} \to P^*$. The transpose of B is denoted by $B^T : P \to \boldsymbol{Q}^*$. The standard form of a saddle point problem is then given by:
Given $\boldsymbol{g} \in \boldsymbol{Q}^*$ and $f \in P^*$, find $\boldsymbol{q} \in \boldsymbol{Q}$ and $p \in P$ such that

$$\begin{bmatrix} A & B^T \\ B & 0 \end{bmatrix} \begin{bmatrix} \boldsymbol{q} \\ p \end{bmatrix} = \begin{bmatrix} \boldsymbol{g} \\ f \end{bmatrix}. \tag{2.3.15}$$

The first step in analyzing saddle point problems is therefore to identify the associated function spaces and the operators A and B. As we then consider the continuous setting, we introduce the bilinear forms a and b associated with A and B. Using angled brackets to denote duality pairings, these are defined by

$$a(\boldsymbol{q}, \tilde{\boldsymbol{q}}) = \langle A\boldsymbol{q}, \tilde{\boldsymbol{q}} \rangle_{\boldsymbol{Q}^* \times \boldsymbol{Q}}, \tag{2.3.16a}$$

$$b(\boldsymbol{q}, \tilde{p}) = \langle B\boldsymbol{q}, \tilde{p} \rangle_{P^* \times P} = \langle \boldsymbol{q}, B^T \tilde{p} \rangle_{\boldsymbol{Q} \times \boldsymbol{Q}^*}. \tag{2.3.16b}$$

With the use of these bilinear forms, we can rewrite (2.3.15) to the following, equivalent formulation:
Given $\boldsymbol{g} \in \boldsymbol{Q}^*$ and $f \in P^*$, find $\boldsymbol{q} \in \boldsymbol{Q}$ and $p \in P$ such that

$$a(\boldsymbol{q}, \tilde{\boldsymbol{q}}) + b(\tilde{\boldsymbol{q}}, p) = \langle \boldsymbol{g}, \tilde{\boldsymbol{q}} \rangle_{\boldsymbol{Q}^* \times \boldsymbol{Q}} \qquad \forall \tilde{\boldsymbol{q}} \in Q, \tag{2.3.17a}$$

$$b(\boldsymbol{q}, \tilde{p}) = \langle f, \tilde{p} \rangle_{P^* \times P} \qquad \forall \tilde{p} \in P. \tag{2.3.17b}$$

The formulation of the model problems from Section 2.2 correspond to (2.3.15) and it is referred to as the strong formulation. The derivation of equivalent problems in the form (2.3.17) is presented in Section 2.4. These problems will be referred to as the variational, or weak formulation.

In order for the problem to be well-posed, we require that a unique solution exists and that this solution depends continuously on the given boundary data. To prove this in the context of saddle-point problems, we consider two conditions, one concerning the bilinear form a and one concerning b:

1. ElKer: A constant $C_a > 0$ exists such that for all $\boldsymbol{q} \in \operatorname{Ker} B$, it holds that

$$a(\boldsymbol{q}, \boldsymbol{q}) \geq C_a \|\boldsymbol{q}\|_Q^2. \tag{2.3.18}$$

2. Inf-Sup: A constant $C_b > 0$ exists such that for any $p \in P$, a function $\boldsymbol{q} \in \boldsymbol{Q} \setminus \{0\}$ exists such that

$$b(\boldsymbol{q}, p) \geq C_b \|\boldsymbol{q}\|_Q \|p\|_P. \tag{2.3.19}$$

Here, $\operatorname{Ker} B$ denotes the kernel of B, defined by all functions $\boldsymbol{q} \in \boldsymbol{Q}$ with $B\boldsymbol{q} = 0$. These two conditions are sufficient to prove existence and uniqueness of a solution which

depends continuously on the data. To be more precise, if the ElKer and Inf-Sup conditions are satisfied, then a constant C exists such that

$$\|\boldsymbol{q}\|_Q + \|p\|_P \leq C(\|\boldsymbol{q}\|_{Q^*} + \|f\|_{P^*}) \tag{2.3.20}$$

By showing that (2.3.20) is satisfied, the problem is proven to be well-posed. For more details, we refer to the exposition given by Boffi et al. [13].

Remark 2.3.3 *The conditions, as specified above, are* sufficient *but not* necessary *conditions to obtain well-posedness. In order to derive the necessary conditions, we can weaken the ElKer condition* (2.3.18) *to the following condition:*
A constant $C_a' > 0$ exists such that

$$\inf_{\boldsymbol{q}\in K} \sup_{\tilde{\boldsymbol{q}}\in K} \frac{a(\boldsymbol{q},\tilde{\boldsymbol{q}})}{\|\boldsymbol{q}\|_Q \|\boldsymbol{q}\|_Q} \geq C_a' \qquad \inf_{\boldsymbol{q}\in K} \sup_{\tilde{\boldsymbol{q}}\in K} \frac{a(\tilde{\boldsymbol{q}},\boldsymbol{q})}{\|\boldsymbol{q}\|_Q \|\boldsymbol{q}\|_Q} \geq C_a'$$

with $K = \operatorname{Ker} B$. However, since the ElKer condition is generally satisfied for the bilinear forms and norms considered herein, we can usually simply consider (2.3.18)*.*

2.4 Variational Formulations

The next step towards a numerically solvable system of equations is to derive the variational (or weak) form of the problems presented in Section 2.2. Due to the similar structure found in all the problems we consider, the derivations are to a certain extent alike. Namely, we first multiply the conservation equation with a suitable test function and integrate over the domain. The second step is to test the constitutive law and apply integration by parts where needed.

2.4.1 Porous Media Flow

The first system we consider are the flow equations described in Section 2.2.1. In order to describe its variational formulation, we first define the relevant function spaces. By choosing the spaces of functions with the minimal required regularity properties, we arrive at

$$\boldsymbol{Q} = H(\operatorname{div}, \Omega; \mathbb{V}), \qquad \boldsymbol{Q}_0 = \left\{\boldsymbol{q} \in \boldsymbol{Q} : \boldsymbol{q}\cdot\boldsymbol{n}|_{\partial_q\Omega} = 0\right\},$$
$$P = L^2(\Omega; \mathbb{R}).$$

The space $\boldsymbol{Q}_0$ is defined in order to properly incorporate the flux boundary condition.

We test the constitutive law and conservation law with functions from $\boldsymbol{Q}_0$ and P respectively. After applying the integration by parts formula (2.3.6) on the constitutive law, we arrive at the variational problem:
Find $(\boldsymbol{q}, p) \in \boldsymbol{Q} \times P$ such that

$$\left(K^{-1}\boldsymbol{q}, \tilde{\boldsymbol{q}}\right)_\Omega - (p, \nabla\cdot\tilde{\boldsymbol{q}})_\Omega = \left(g_p, \tilde{\boldsymbol{q}}\cdot\boldsymbol{n}\right)_{\partial_p\Omega} \qquad \forall \tilde{\boldsymbol{q}} \in \boldsymbol{Q}_0, \tag{2.4.1a}$$

$$(\nabla\cdot\boldsymbol{q}, \tilde{p})_\Omega = \left(f_q, \tilde{p}\right)_\Omega \qquad \forall \tilde{p} \in P. \tag{2.4.1b}$$

Note that in this formulation, the pressure boundary condition is naturally included in the system of equations. On the other hand, the flux boundary condition needs to be incorporated separately, which is known as an essential boundary condition:

$$\boldsymbol{q} \cdot \boldsymbol{n} = g_q \qquad \text{on } \partial_q \Omega.$$

We can easily fit (2.4.1) in the standardized form given by (2.3.17). For that, we identify the bilinear forms a and b by

$$a(\boldsymbol{q}, \tilde{\boldsymbol{q}}) = \left(K^{-1}\boldsymbol{q}, \tilde{\boldsymbol{q}}\right)_\Omega, \qquad b(\boldsymbol{q}, \tilde{p}) = -(\tilde{p}, \nabla \cdot \boldsymbol{q})_\Omega. \tag{2.4.2}$$

This identification will be apparent in all following examples, and we therefore omit it in the subsequent sections.

2.4.2 Linear Mechanics

As we have observed in Section 2.2.2, the equations describing linear elasticity are close to being the vector-valued analogue of the porous media flow equations. In turn, the relevant function space follow naturally from the observations in the previous subsection

$$\Sigma = H(\mathrm{div}, \Omega; \mathbb{V}^n), \qquad \Sigma_0 = \left\{\boldsymbol{\sigma} \in \Sigma : \boldsymbol{\sigma} \cdot \boldsymbol{n}|_{\partial_\sigma \Omega} = 0\right\},$$
$$U = L^2(\Omega; \mathbb{R}^n).$$

Note that the symmetry of the stress tensor is not included in the definition of Σ. This is because we are already aiming for a viable mixed finite element discretization. If we were to enforce the symmetry inside the space, thus considering only symmetric stress tensors, we run into difficulty constructing a finite element for the stress. These finite elements are necessarily of higher order, see e.g. [10], and are difficult to construct in three dimensions [7].

Instead, we enforce the symmetry on σ in an integrated sense with the use of a Lagrange multiplier, hence the name weak (or relaxed) symmetry. This approach has been investigated by [8], among others. Let us denote the Lagrange multiplier space as R which we define as

$$R = L^2(\Omega; \mathbb{K}). \tag{2.4.3}$$

Since this space is used to compare off-diagonal terms in an $n \times n$ tensor, $\mathbb{K}$ depends on the dimensionality n. If $n = 3$, three rotations are possible and we have $\mathbb{K} = \mathbb{R}^3$. On the other hand, only one rotation is possible on a planar domain ($n = 2$) which leads to $\mathbb{K} = \mathbb{R}$. In general, we have $\mathbb{K} = \mathbb{R}^{k_n}$ with $k_n = \binom{n}{2} = n(n-1)/2$.

The asymmetry operator introduced before maps matrices to matrices, and thus we need a different operator to map from Σ into R. Let us therefore introduce $\mathrm{skw} : \mathbb{M} \to \mathbb{K}$ for an $n \times n$ matrix M with components m_{ij} as

$$\mathrm{skw}\, M = \begin{cases} [m_{23} - m_{32},\ m_{31} - m_{13},\ m_{12} - m_{21}], & n = 3, \\ m_{12} - m_{21}, & n = 2. \end{cases} \tag{2.4.4}$$

The operator is then naturally lifted to skw : $\Sigma \to R$.

Having the function spaces and operators defined, we are ready to give the variational formulation of the linear elasticity equations in a mixed form:
Find $(\sigma, \boldsymbol{u}, r) \in \Sigma \times \boldsymbol{U} \times R$ such that

$$(A\sigma, \tilde{\sigma})_\Omega + (\boldsymbol{u}, \nabla \cdot \tilde{\sigma})_\Omega - (r, \operatorname{skw} \tilde{\sigma})_\Omega = (g_u, \tilde{\sigma} \cdot \boldsymbol{n})_{\partial_u \Omega} \qquad \forall \tilde{\sigma} \in \Sigma_0, \tag{2.4.5a}$$

$$(\nabla \cdot \sigma, \tilde{\boldsymbol{u}})_\Omega = (\boldsymbol{f}_\sigma, \tilde{\boldsymbol{u}})_\Omega \qquad \forall \tilde{\boldsymbol{u}} \in \boldsymbol{U}, \tag{2.4.5b}$$

$$(\operatorname{skw} \sigma, \tilde{r})_\Omega = 0 \qquad \forall \tilde{r} \in R, \tag{2.4.5c}$$

subject to the essential boundary condition

$$\sigma_p \cdot \boldsymbol{n} = \boldsymbol{g}_\sigma \qquad \text{on } \partial_\sigma \Omega. \tag{2.4.6}$$

2.4.3 Poroelasticity

In the examples considered thus far, the process of poromechanics is the only case which leads to time-dependent equations. Although this time dependency can be reflected by introducing Bochner spaces [25], we limit the exposition to the equations at a given moment in time t for sake of simplicity. In turn, we may inherit the five function spaces $\Sigma \times P \times \boldsymbol{Q} \times \boldsymbol{U} \times R$ from the previous sections for $t \in [0, T]$.

The symmetry in the system of equations for poroelasticity is not apparent at first sight, but can easily be shown after a few manipulations. After testing the conservation equation (2.2.8b) with a test function $\tilde{p}$, we obtain

$$(S_0 \dot{p}, \tilde{p})_\Omega + (\nabla \cdot \boldsymbol{u}, \tilde{p})_\Omega + (\nabla \cdot \boldsymbol{q}, \tilde{p})_\Omega = \left(f_q, \tilde{p}\right)_\Omega \qquad \forall \tilde{p} \in P. \tag{2.4.7}$$

The problematic term in this equation is $(\nabla \cdot \boldsymbol{u}, \tilde{p})_\Omega$. As we have seen in the previous sections, both the pressure and displacement spaces are assumed to be in $L^2(\Omega)$ for the separate problems. In this exposition we do not wish to assume any more regularity on these functions a priori. Thus, we cannot take the divergence of $\boldsymbol{u}$ since it is only square-integrable and we may be tempted to apply integration by parts. However, this leads to a term which includes the gradient of the merely square integrable pressure which is just as nonsensical.

To get us out of this sticky situation, we use the manipulation from Lee [36] to rewrite this term. Using the strong formulation, we derive:

$$(\nabla \cdot \boldsymbol{u}, \tilde{p})_\Omega = (\operatorname{Tr} \varepsilon(\boldsymbol{u}), \tilde{p})_\Omega = \left(\operatorname{Tr} A(\sigma_p + \alpha p I), \tilde{p}\right)_\Omega = \left(A(\sigma_p + \alpha p I), \tilde{p} I\right)_\Omega. \tag{2.4.8}$$

Including the Biot-Willis constant α and the time derivative on the appropriate terms, we obtain the five-field formulation of the Biot equations at time $t \in [0, T]$:
Find $(\sigma_p, p, \boldsymbol{q}, \boldsymbol{u}, r) \in \Sigma \times P \times \boldsymbol{Q} \times \boldsymbol{U} \times R$ such that

$$\begin{aligned}
\left(A(\sigma_p + \alpha p I), \tilde{\sigma}_p\right)_\Omega + \left(\boldsymbol{u}, \nabla \cdot \tilde{\sigma}_p\right)_\Omega - \left(r, \operatorname{skw} \tilde{\sigma}_p\right)_\Omega &= \left(g_u, \tilde{\sigma}_p \cdot \boldsymbol{n}\right)_{\partial_u \Omega} && \forall \tilde{\sigma}_p \in \Sigma_0, \\
(S_0 \dot{p}, \tilde{p})_\Omega + \left(A(\dot{\sigma}_p + \alpha \dot{p} I), \alpha \tilde{p} I\right)_\Omega + (\nabla \cdot \boldsymbol{q}, \tilde{p})_\Omega &= \left(f_q, \tilde{p}\right)_\Omega && \forall \tilde{p} \in P, \\
\left(K^{-1} \boldsymbol{q}, \tilde{\boldsymbol{q}}\right)_\Omega - (p, \nabla \cdot \tilde{\boldsymbol{q}})_\Omega &= \left(g_p, \tilde{\boldsymbol{q}} \cdot \boldsymbol{n}\right)_{\partial_p \Omega} && \forall \tilde{\boldsymbol{q}} \in \boldsymbol{Q}_0, \\
\left(\nabla \cdot \sigma_p, \tilde{\boldsymbol{u}}\right)_\Omega &= (\boldsymbol{f}_\sigma, \tilde{\boldsymbol{u}})_\Omega && \forall \tilde{\boldsymbol{u}} \in \boldsymbol{U}, \\
\left(\operatorname{skw} \sigma_p, \tilde{r}\right)_\Omega &= 0 && \forall \tilde{r} \in R.
\end{aligned}$$

In this formulation, the essential boundary conditions are given by

$$\sigma_p \cdot \boldsymbol{n} = \boldsymbol{g}_\sigma \text{ on } \partial_\sigma \Omega, \qquad \boldsymbol{q} \cdot \boldsymbol{n} = g_q \text{ on } \partial_q \Omega.$$

Remark 2.4.1 *The above system relies heavily on the trick given by equation* (2.4.8) *and the use of the poroelastic stress. If, instead, one chooses to use the elastic stress σ as the main variable, a different strategy is needed to treat the term $(\alpha \nabla p, \tilde{\boldsymbol{u}})_\Omega$ which arises in the fourth equation.*

We may approximate the gradient of pressure or the divergence of the displacement using a discrete differential, denoted by D_h. The second and fourth equations of the system are then rewritten as

$$\begin{aligned} (S_0 \dot{p}, \tilde{p})_\Omega + (\alpha D_h \cdot \dot{\boldsymbol{u}}, \tilde{p})_\Omega + (\nabla \cdot \boldsymbol{q}, \tilde{p})_\Omega &= \left(f_q, \tilde{p}\right)_\Omega && \forall \tilde{p} \in P, \\ (\nabla \cdot \sigma, \tilde{\boldsymbol{u}})_\Omega - (\alpha D_h p, \tilde{\boldsymbol{u}})_\Omega &= (\boldsymbol{f}_\sigma, \tilde{\boldsymbol{u}})_\Omega && \forall \tilde{\boldsymbol{u}} \in \boldsymbol{U}. \end{aligned}$$

Using techniques from Discontinuous Galerkin methods for example, an appropriate operator D_h can be constructed resulting in a symmetric system. Such a scheme may perform well in one sense or another, but the use of discrete differential operators alters the system of equations. Therefore, this strategy does not fit well within the spirit of conformity we aim for and we will not continue further down this path.

2.5 Remarks on Variational Inequalities

In each variational formulation from the previous section, we search for a function in a function space. Although this strategy works for the problems considered above, it is unfeasible if more constraints are added to the problem. In particular, if the solution needs to satisfy additional, physical constraints given by inequalities, then the solution space needs to be restricted to a specific set of functions. By imposing these constraints, the problem becomes a variational inequality.

A common instance of this arises in the context of obstacle problems and contact mechanics. A classic example is to consider the deformation of an elastic sphere resting on a rigid surface [32]. Depending on the magnitude of gravity, a certain area of the sphere will be in contact with the surface. Since this area will depend on the solution, it is non-trivial to prescribe conventional boundary conditions to the sphere using a decomposition of the boundary. With the use of inequalities, however, boundary conditions can be formulated for the displacement and the normal stress such that the sphere does not penetrate the surface and the surface only generates a normal force.

Similarly, in the modeling of fracture mechanics, the behavior of the system before fractures are closed is very different before and after the two sides of the fracture touch. This contact condition can be described as an inequality constraint on the displacement and stress fields to disallow penetration and to mimic the correct behavior once the fracture is open.

As is apparent in the above examples, we thus search the solution in an admissible set which is a subset of the more general function space. To give a general example of variational inequalities, we follow [32]. Let V be a function space and V_a a nonempty closed convex

subset of V. Given a mapping $A : V_a \to V^*$ and a functional $f \in V^*$, we find $u \in V_a$ such that

$$\langle Au - f, v - u \rangle_{V^* \times V} \geq 0, \qquad \forall v \in V_a. \tag{2.5.1}$$

Note that variational equalities including those from the previous section can be seen as the special case where $V_a = V$. In that sense, variational inequalities are thus a generalization.

Variational inequalities form an important class of related non-linear problems both in the context of contact dynamics, as well as in multiphase flows to ensure that saturations remain within physical bounds, for example. Related work on solution methods for variational inequalities in a fixed-dimensional setting is presented in Paper H. Their extension to mixed-dimensional problems has interesting potential, yet this is reserved for future research and the remaining chapters will focus on variational equalities.

Chapter 3

Mixed-Dimensional Partial Differential Equations

With the goal of a mixed-dimensional PDE in mind, we continue by incorporating of thin inclusions in the domain. Due to their large aspect ratios, we make the modeling choice to represent these features as lower-dimensional objects. It important to note that we make the modeling assumption at this point instead of during the discretization later in Chapter 4. This allows us to analyze the problem in a continuous setting, which is the subject of this chapter. By establishing the analytical tools beforehand, we gain a solid background to derive a conforming discretization scheme afterwards.

In this chapter, we first introduce the geometrical setting and the way in which we consider the lower-dimensional, embedded manifolds. On the created geometry, we then define the key concepts from functional analysis which can be used to define mixed-dimensional partial differential equation. After a short detour towards the underlying structure with respect to exterior calculus, several concrete examples are provided using the model problems from previous chapters.

3.1 Geometrical Setting

The manner in which the geometry of the problem is incorporated is of crucial importance. Different interpretations inevitably lead to widely varying methods and a faulty assumption at this stage may result in issues or limitations for the resulting scheme.

Let us start by introducing the open domain as $D \subset \mathbb{R}^n$ with n typically equal to two or three. As assumed, thin inclusions are present inside D which form $(n-1)$-dimensional manifolds. The key idea is then to consider these features as lower-dimensional manifolds on which a separate differential equation can be defined. Moreover, when multiple manifolds cross each other, the intersection is considered an $(n-2)$-dimensional manifold. This process can be repeated until a zero-dimensional manifold is reached which we refer to as an intersection point. In this way, a hierarchy of manifolds with different dimensionalities is created which forms the cornerstone of the mixed-dimensional framework. In this work, we assume

all manifolds to be smooth.

For notational convenience, we use a superscript to keep track of the dimensionality of a manifold and a subscript to denote its index. Thus, Ω_i^d represents an open d-dimensional manifold with index i contained in D. Omission of these sub- and superscripts then implies the union or summation over all indices:

$$\Omega^d = \bigcup_i \Omega_i^d, \qquad \Omega = \bigoplus_{d=0}^{n} \Omega^d. \tag{3.1.1}$$

We use the direct sum notation to emphasize the summation of manifolds with different dimensionalities.

A key attribute of the decomposition of the domain D according to dimension is that we assume each d-dimensional manifold is removed from Ω^{d+1}. For example, Ω^n is the open domain describing the region surrounding the inclusions and contains none of the points in Ω^d for $d < n$. Moreover, it means that two lines intersecting in a point Ω_1^0 are decomposed into four lines with ends meeting at Ω_1^0. An illustration of the dimensional decomposition in three dimensions is given in Figure 3.1.

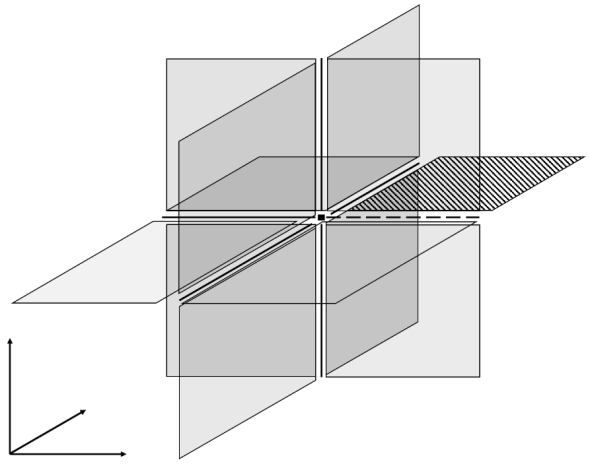

Figure 3.1: The decomposition of a three-dimensional domain D with three intersecting planes. Here, the ambient domain Ω^3 is given by eight cubes, the two-dimensional domain Ω^2 consists of twelve planes, the one-dimensional Ω^1 is composed of six lines, and Ω^0 comprises the single point at the center.

The interface between domains of codimension one is referred to using a separate notation. Let Γ_{ij}^d denote the d-dimensional interface between Ω_i^d and Ω_j^{d+1}. Here, we keep in mind that if Ω_i^d is embedded in Ω_j^{d+1}, then Γ_{ij}^d is defined on both sides of Ω_i^d. This interface can thus be alternatively described by

$$\Gamma_{ij}^d = \partial_i \Omega_j^{d+1} \tag{3.1.2}$$

where ∂_i denotes the boundary of a domain corresponding to a lower-dimensional manifold with index i.

Once more, we omit indices to imply union or direct summation in the following way:

$$\Gamma_i^d = \bigcup_j \Gamma_{ij}^d, \qquad \Gamma^d = \bigcup_i \Gamma_i^d, \qquad \Gamma = \bigoplus_{d=0}^{n-1} \Gamma^d. \tag{3.1.3}$$

Each Γ_{ij}^d is equipped with a unit normal vector $\boldsymbol{n}$ pointing from Ω^{d+1} towards Ω^d. The only part of the domain which remains unaccounted for is the boundary of Ω^d which is not adjacent to a lower-dimensional manifold and does not touch the boundary. These immersed sections of $\partial\Omega^d$ are denoted by $\partial_0\Omega^d$.

The open domain D can then be decomposed in the following way

$$D = \Omega \cup \partial_0\Omega \tag{3.1.4}$$

Each manifold may touch the boundary of the full domain. Let us take, as an example, the boundary $\partial_p\Omega$ on which the pressure is defined for the flow equations. The $(d-1)$-dimensional boundary $\partial_p\Omega^d$ is then denoted by $\partial_p\Omega^d \cap \partial_p\Omega$. In turn, the boundary $\partial_p\Omega$ is decomposed as

$$\partial_p\Omega = \bigoplus_{d=0}^{n} \partial_p\Omega^d. \tag{3.1.5}$$

With these definitions in place, a decomposition of the boundary of each d-dimensional submanifold arises. With the notation from the previous section to refer to boundaries with specified boundary condition for flow and mechanics, this decomposition is given by

$$\partial\Omega^d = \partial_p\Omega^d \cup \partial_q\Omega^d \cup \partial_0\Omega^d \cup \Gamma^{d-1} = \partial_u\Omega^d \cup \partial_\sigma\Omega^d \cup \partial_0\Omega^d \cup \Gamma^{d-1}. \tag{3.1.6}$$

3.2 Mixed-Dimensional Functional Analysis

In order to define differential equations on the mixed-dimensional geometry, we first require the correct notions of inner products, norms, and function spaces. Analogous to Section 2.3, we start with square-integrable functions, followed by the spaces of functions with more regularity similar to (2.3.3). We then introduce integration by parts and end with the mixed-dimensional de Rham complex.

The notion of square-integrable functions is arguably the most readily extendable concept to the mixed-dimensional framework. Let us start with the inner product and the respectively induced L^2 norm:

$$(f, g)_\Omega = \sum_{d=0}^{n} (f, g)_{\Omega^d}, \qquad \|f\|^2_{L^2(\Omega)} = \sum_{d=0}^{n} \|f\|^2_{L^2(\Omega^d)} = (f, f)_\Omega. \tag{3.2.1}$$

Hidden within these definitions is the matter of measures. For $d \geq 1$, we assume that integration over a d-dimensional manifold is performed using the standard Lebesgue measure in d dimensions. Integration in zero dimensions is then defined as point evaluation.

At this stage, we may define $L^2(\Omega, \mathbb{F})$ as the space of functions which are square-integrable on the mixed-dimensional geometry given by Ω:

$$L^2(\Omega; \mathbb{F}) = \prod_{d=0}^{n} L^2(\Omega^d; \mathbb{F}^d). \tag{3.2.2}$$

In this work, we choose field $\mathbb{F}$ to be either scalars in all dimensions, denoted by $\mathbb{R}$, n-vectors denoted by $\mathbb{R}^n$, d-vectors denoted by $\mathbb{V}$ or $d \times d$-matrices which we denote by $\mathbb{V}^d$. For the asymmetry multiplier in elasticity problems, we use $\mathbb{K}$ to denote $\mathbb{R}^{d(d-1)/2}$ in Ω^d.

In the previous section, we have taken care to introduce the interface between manifolds of codimension one as Γ. In the mixed-dimensional setting, we will be interested in functions defined on Ω with well-defined traces on Γ. Since Ω^d will coincide geometrically with Γ^d, we employ the hat and check notation as short-hand to distinguish the two function values. For a sufficiently regular function $\boldsymbol{g}$ defined on Ω, let the notation $\hat{\boldsymbol{g}} \cdot \boldsymbol{n}$ denote its normal trace on Γ and let a check denote its restriction to the lower-dimensional domain:

$$\begin{aligned} \hat{\boldsymbol{g}} \cdot \boldsymbol{n} &= \boldsymbol{g}^{d+1} \cdot \boldsymbol{n}, && \text{on } \Gamma^d \text{ with } 0 \leq d \leq n-1, \\ \check{\boldsymbol{g}} &= \boldsymbol{g}^d, && \text{on } \Omega^d \text{ with } 1 \leq d \leq n. \end{aligned}$$

This allows us to define the jump operator $[\![\cdot]\!] : L^2(\Gamma) \to L^2(\Omega)$ as

$$[\![\hat{\boldsymbol{g}} \cdot \boldsymbol{n}]\!]|_{\Omega_i^d} = \sum_j \left(\hat{\boldsymbol{g}} \cdot \boldsymbol{n}|_{\Gamma_{ij}^d} \right), \qquad 0 \leq d \leq n-1. \tag{3.2.3}$$

The jump operator will play an important role in the definition of differential operators in the mixed-dimensional framework. The model problems introduced in Chapter 2 only concern the divergence and its dual and we will therefore limit the exposition here to these differential operators.

Using $\nabla_\parallel$ as the del operator in the tangential directions and the jump operator from (3.2.3), we define the mixed-dimensional divergence as

$$\mathfrak{D} \cdot \boldsymbol{f} = \nabla_\parallel \cdot \check{\boldsymbol{f}} - [\![\hat{\boldsymbol{f}} \cdot \boldsymbol{n}]\!]. \tag{3.2.4}$$

This divergence operator arises naturally in the derivation for the reduced equations after an integration across all directions normal to the manifold.

With this definition in place, we can consider functions, defined on the mixed-dimensional geometry which have sufficient regularity to apply this divergence operator to. We thereby define the function space

$$H(\mathfrak{D}\cdot, \Omega; \mathbb{V}) = \prod_{d=1}^{n} \left\{ \boldsymbol{f}^d \in H(\mathrm{div}, \Omega^d; \mathbb{V}) : \hat{\boldsymbol{f}} \cdot \boldsymbol{n}|_{\Gamma^{d-1}} \in L^2(\Gamma^{d-1}; \mathbb{R}) \right\} \tag{3.2.5}$$

Since This space will be used for the dual variables, i.e. the tangential flux and stress. By the properties of this space, we have for $\boldsymbol{f} \in H(\mathfrak{D}\cdot, \Omega; \mathbb{V})$:

$$\mathfrak{D} \cdot \boldsymbol{f} \in L^2(\Omega; \mathbb{R}) \tag{3.2.6}$$

Since two functions $\boldsymbol{f}, \boldsymbol{g} \in H(\mathfrak{D}\cdot, \Omega; \mathbb{V})$ have well-defined components on both Ω and Γ, we introduce a compound inner product as

$$\langle \boldsymbol{f},\, \boldsymbol{g} \rangle_{\Omega\times\Gamma} = \sum_{d=1}^{n} \left((\boldsymbol{f}^d, \boldsymbol{g}^d)_{\Omega^d} + (\boldsymbol{f}^d \cdot \boldsymbol{n}, \boldsymbol{g}^d \cdot \boldsymbol{n})_{\Gamma^{d-1}} \right). \tag{3.2.7}$$

This inner product is then used to derive the dual to the mixed-dimensional divergence. For that purpose, we consider $\boldsymbol{f} \in H(\mathfrak{D}\cdot, \Omega; \mathbb{V})$ and $g \in \prod_{d=0}^{n} H^1(\Omega^d)$ and denote the mixed-dimensional codivergence of g by $-\mathfrak{D}g$. Here, we inherit the sign convention from the fixed-dimensional case where the dual to the divergence is the negative gradient. Through a notion of integration by parts, we derive

$$\begin{aligned}
\langle \boldsymbol{f},\, \mathfrak{D}g \rangle_{\Omega\times\Gamma} &= \left(\hat{\boldsymbol{f}} \cdot \boldsymbol{n}, \hat{g} \right)_{\partial\Omega\setminus\Gamma} - (\mathfrak{D} \cdot \boldsymbol{f}, \breve{g})_{\Omega} \\
&= \left(\hat{\boldsymbol{f}} \cdot \boldsymbol{n}, \hat{g} \right)_{\partial\Omega\setminus\Gamma} - \left(\nabla_{\parallel} \cdot \breve{\boldsymbol{f}}, \breve{g} \right)_{\Omega} + \left([\![\hat{\boldsymbol{f}} \cdot \boldsymbol{n}]\!], \breve{g} \right)_{\Omega} \\
&= \left(\hat{\boldsymbol{f}} \cdot \boldsymbol{n}, \hat{g} \right)_{\partial\Omega\setminus\Gamma} - \left(\nabla_{\parallel} \cdot \breve{\boldsymbol{f}}, \breve{g} \right)_{\Omega} + \left(\hat{\boldsymbol{f}} \cdot \boldsymbol{n},\, \breve{g} \right)_{\Gamma} + \left(\hat{\boldsymbol{f}} \cdot \boldsymbol{n},\, \hat{g} \right)_{\Gamma} - \left(\hat{\boldsymbol{f}} \cdot \boldsymbol{n},\, \hat{g} \right)_{\Gamma} \\
&= \left(\breve{\boldsymbol{f}}, \nabla_{\parallel} \breve{g} \right)_{\Omega} + \left(\hat{\boldsymbol{f}} \cdot \boldsymbol{n},\, \breve{g} - \hat{g} \right)_{\Gamma}.
\end{aligned}$$

Thus, the negated mixed-dimensional co-divergence of g is given by

$$\mathfrak{D}g = [\nabla_{\parallel} \breve{g},\ \breve{g} - \hat{g}], \tag{3.2.8}$$

with square brackets indicating that the first component is defined as a function on Ω and the second on Γ. Note that g has sufficiently regularity for the trace $\hat{g}$ on Γ to be well-defined.

Remark 3.2.1 *We consistently refer to the operator in equation* (3.2.8) *as the co-divergence instead of the gradient. This is because, formally, the mixed-dimensional gradient would act on differential 0-forms which are only defined in the top dimension (See Section 3.2.1). In turn, the co-divergence plays a more important role in the models considered herein.*

3.2.1 Exterior Calculus

With the mixed-dimensional divergence and co-divergence defined in the previous section, the question arises whether these definitions can be generalized to differential operators defined on the mixed-dimensional geometry. Indeed, this is possible in the context of exterior calculus as explored on simplicial complexes by Licht [39]. We provide a short introduction to these ideas in this section.

The key observation is to note the structure of the mixed-dimensional divergence as introduced in (3.2.4). It is given by the composition of a continuous operator which preserves dimensionality with a discrete operator which maps to manifolds of lower dimension. Turning towards the language of exterior calculus, recall d as the exterior derivative presented in Section 2.3.1. A similar generalization can be constructed for the jump operator which we denote by $\mathbb{d}$. For its exact definition, we refer to Paper C. The two operators are then defined

with the following domains and codomains:

$$\Lambda^k(\Omega^d) \xrightarrow{\mathrm{d}} \Lambda^{k+1}(\Omega^d) \qquad\qquad \Lambda^k(\Omega^d) \xrightarrow{\mathbb{d}} \Lambda^k(\Omega^{d-1}) \tag{3.2.9}$$

Note that the operator $\mathbb{d}$ consists of an appropriate sum of traces, thus mapping between dimensions. It therefore provides the building block to considering mixed-dimensional differential forms. For that purpose, we introduce the mixed-dimensional differential k-forms as

$$\mathfrak{Q}^k(\Omega) = \prod_{d=0}^{n} \Lambda^{d-(n-k)}(\Omega^d), \tag{3.2.10}$$

with $\Lambda^k(\Omega^d) = 0$ if $k \notin [0, d]$.

The composition of the continuous differential d and the discrete operator $\mathbb{d}$ leads to the definition of the mixed-dimensional exterior derivative $\mathfrak{d}$:

$$\mathfrak{d} = \mathrm{d} + \mathbb{d}, \qquad\qquad \mathfrak{Q}^k(\Omega) \xrightarrow{\mathfrak{d}} \mathfrak{Q}^{k+1}(\Omega). \tag{3.2.11}$$

One of the most important observations is that the newly defined exterior derivative creates a cochain complex in its own right, given by

$$0 \hookrightarrow \mathfrak{Q}^0(\Omega) \xrightarrow{\mathfrak{d}} \mathfrak{Q}^1(\Omega) \xrightarrow{\mathfrak{d}} \mathfrak{Q}^2(\Omega) \dashrightarrow^{\mathfrak{d}} \mathfrak{Q}^n(\Omega) \longrightarrow 0. \tag{3.2.12}$$

The fact that two consecutive applications of $\mathfrak{d}$ maps to zero follows from the properties of the differential operators d and $\mathbb{d}$ and the anticommutative relationship between them:

$$\mathfrak{d}^2 = (\mathrm{d} + \mathbb{d})^2 = \mathrm{dd} + \mathrm{d}\mathbb{d} + \mathbb{d}\mathrm{d} + \mathbb{d}\mathbb{d} = \mathrm{d}\mathbb{d} - \mathrm{d}\mathbb{d} = 0. \tag{3.2.13}$$

Returning to the notation of fixed-dimensional exterior calculus, this chain can be represented as a triangle by decomposing $\mathfrak{d}$:

$$\begin{array}{ccccccccc}
\mathfrak{Q}^0(\Omega) & & \Lambda^0(\Omega^n) & & & & & & \\
\downarrow{\scriptstyle \mathfrak{d}} & & \downarrow{\scriptstyle \mathrm{d}} & \searrow^{\mathbb{d}} & & & & & \\
\mathfrak{Q}^1(\Omega) & & \Lambda^1(\Omega^n) & & \Lambda^0(\Omega^{n-1}) & & & & \\
\downarrow{\scriptstyle \mathfrak{d}} & & \downarrow{\scriptstyle \mathrm{d}} & \searrow^{\mathbb{d}} & \downarrow{\scriptstyle \mathrm{d}} & \searrow^{\mathbb{d}} & & & \\
\mathfrak{Q}^2(\Omega) & & \Lambda^2(\Omega^n) & & \Lambda^1(\Omega^{n-1}) & & \Lambda^0(\Omega^{n-2}) & & \\
\vdots{\scriptstyle \mathfrak{d}} & & \vdots{\scriptstyle \mathrm{d}} & \searrow^{\mathbb{d}} & \vdots{\scriptstyle \mathrm{d}} & \searrow^{\mathbb{d}} & \vdots{\scriptstyle \mathrm{d}} & \searrow^{\mathbb{d}} & \\
\mathfrak{Q}^n(\Omega) & & \Lambda^n(\Omega^n) & & \Lambda^{n-1}(\Omega^{n-1}) & & \Lambda^{n-2}(\Omega^{n-2}) & & \Lambda^0(\Omega^0)\ .
\end{array} \tag{3.2.14}$$

In this representation, each row corresponds to $\mathfrak{Q}^k(\Omega)$ for a value of k and each column corresponds to a de Rham sequence on Ω^d for a given dimensionality d. The extension from simplicial complexes to the geometrical setting from Section 3.1 and the analysis of the corresponding Hilbert complexes are currently in development.

3.3 Generalized Governing Equations

The geometry and analytical tools introduced in the previous sections give us sufficient background to define mixed-dimensional partial differential equations. This section uses these concepts to generalize the problems defined in Section 2.4. Before we consider the explicit problems, though, we first make a short note on the choice of dual variable in Section 3.3.1.

3.3.1 Scaling the Dual Variable

The derivation of the reduced equations typically involves either integrating or averaging the governing equations across the lower-dimensional manifold. In both cases, a symmetric system is obtained, which leads to a freedom in the choice of variables. In particular, we can choose the dual variable to be either the averaged or the integrated quantity. For the flow equations, this corresponds to the flux tangential to a manifold. Similarly for the elasticity problem, the tangential stresses may be considered either in an averaged or integrated form. Although both choices of the dual variable are valid, each has a drawback when considering manifolds with arbitrarily small apertures or widths.

To illustrate this, let us consider an example of porous media flow in a single two-dimensional manifold Ω^2 with aperture γ embedded in a three-dimensional, impermeable domain. We furthermore assume that the pressure is prescribed by g_p along the entire boundary, i.e. $\partial\Omega^2 = \partial_p\Omega^2$. The function spaces of relevance to this model problem are given by

$$\boldsymbol{Q}^2 = H(\mathrm{div}, \Omega^2; \mathbb{V}), \qquad P^2 = L^2(\Omega^2; \mathbb{R}).$$

Choosing $\boldsymbol{q}_{avg}$ as the average, tangential flux, we obtain the following system:

$$\begin{aligned} \left(K^{-1}\boldsymbol{q}_{avg}, \tilde{\boldsymbol{q}}\right)_{\Omega^2} - \left(p, \nabla_\parallel \cdot \tilde{\boldsymbol{q}}\right)_{\Omega^2} &= \left(g_p, \tilde{\boldsymbol{q}} \cdot \boldsymbol{n}\right)_{\partial_p\Omega^2} && \forall \tilde{\boldsymbol{q}} \in \boldsymbol{Q}_0^2, \\ \left(\nabla_\parallel \cdot \gamma\boldsymbol{q}_{avg}, \tilde{p}\right)_{\Omega^2} &= \left(\gamma f_q, \tilde{p}\right)_{\Omega^2} && \forall \tilde{p} \in P^2. \end{aligned}$$

In order to symmetrize this system, the test functions can be chosen as $\gamma\tilde{\boldsymbol{q}}$. However, if we consider $\gamma \downarrow 0$, then the entire system deteriorates and there is nothing left to solve. Alternatively, if γ is constant, we may rescale the second equation by dividing by γ. This leads to a system which is independent of γ and the effects of zero aperture will not be incorporated correctly.

Alternatively, a natural choice is to introduce $\boldsymbol{q}_{int}$ as the flux integrated over the direction normal to Ω^2. The variational formulation then takes on the following form

$$\begin{aligned} \left((\gamma K)^{-1}\boldsymbol{q}_{int}, \tilde{\boldsymbol{q}}\right)_{\Omega^2} - \left(p, \nabla_\parallel \cdot \tilde{\boldsymbol{q}}\right)_{\Omega^2} &= \left(g_p, \tilde{\boldsymbol{q}} \cdot \boldsymbol{n}\right)_{\partial_p\Omega^2} && \forall \tilde{\boldsymbol{q}} \in \boldsymbol{Q}_0^2, \\ \left(\nabla_\parallel \cdot \boldsymbol{q}_{int}, \tilde{p}\right)_{\Omega^2} &= \left(\gamma f_q, \tilde{p}\right)_{\Omega^2} && \forall \tilde{p} \in P^2. \end{aligned}$$

Our interest lies once more in the case where $\gamma \downarrow 0$, and thus we are forced to assume that the permeability K scales as γ^{-1}. In the limiting case, this implies that the tangential permeability tends to infinity and flow in these directions will always be possible even if the

aperture is zero. Since this is unphysical, we would need to separately consider the case of $\gamma = 0$. A scaling with γ does not solve all issues, since the second equation would have to be scaled as well. This leads to a scaled conservation law, which we prefer to avoid.

A third option, and the preferred method within this thesis, is to employ a scaled flux inspired by Arbogast and Taicher [6]. In that work, the scaling is used to capture regions of zero porosity whereas here we aim to handle zero aperture. Let us introduce the scaling factor ϵ as the square root of the aperture. The scaled flux $\boldsymbol{q}$ is then defined such that

$$\epsilon \boldsymbol{q}_{avg} = \boldsymbol{q} = \epsilon^{-1} \boldsymbol{q}_{int}. \tag{3.3.1}$$

With this choice of flux, the following symmetric system of equations is obtained

$$\begin{aligned} \left(K^{-1}\boldsymbol{q}, \tilde{\boldsymbol{q}}\right)_{\Omega^2} - \left(p, \nabla_{\parallel} \cdot \epsilon \tilde{\boldsymbol{q}}\right)_{\Omega^2} &= \left(g_p, \epsilon \tilde{\boldsymbol{q}} \cdot \boldsymbol{n}\right)_{\partial_p \Omega^2} && \forall \tilde{\boldsymbol{q}} \in \boldsymbol{Q}_0^2, \\ \left(\nabla_{\parallel} \cdot \epsilon \boldsymbol{q}, \tilde{p}\right)_{\Omega^2} &= \left(\epsilon^2 f_q, \tilde{p}\right)_{\Omega^2} && \forall \tilde{p} \in P^2. \end{aligned}$$

Note that the dependency on the aperture is now completely inside the coupling terms. In turn, the system will naturally handle the limiting case of $\gamma \downarrow 0$. In fact, setting ϵ to zero, we see that the only possible solution for the flux is $\boldsymbol{q} = 0$ from the first equation. This corresponds with the physical interpretation that no flow is possible in the tangential directions if the aperture is zero.

The generalization of this scaling to multiple reductions is to define ϵ such that ϵ^2 equals the volume of the intersection point if $n - d = 3$, the cross-sectional area if $n - d = 2$ and aperture if $n - d = 1$. In other words, ϵ satisfies the following scaling:

$$\epsilon \sim \gamma^{\frac{n-d}{2}}. \tag{3.3.2}$$

In the (poro)mechanics equations from Sections 2.4.2 and 2.2.3, the dual variable is the (poro)elastic stress. Using the same arguments regarding robustness of the model to small widths of manifolds, we therefore employ a scaled (poro)elastic stress instead of averaged or integrated quantities.

3.3.2 Porous Media Flow

As we have seen in Section 2.1, a linear conservation law can be described using the divergence operator. This remains valid in the mixed-dimensional setting and we can express mass conservation, using the scaled flux $\boldsymbol{q}$ from the previous section, as

$$\mathfrak{D} \cdot \epsilon \boldsymbol{q} = \epsilon^2 f_q, \tag{3.3.3}$$

with f_q the source term averaged over the directions normal to the submanifold. Recall from the previous section that $\epsilon \boldsymbol{q}$ represents the flux integrated over the cross-section of the lower-dimensional feature.

With mass conservation defined and Darcy flow inside the manifolds, we are missing one vital ingredient, namely the coupling condition. In this case, we impose that the flow

across Γ is governed by Darcy's law as well, with a permeability constant K_n. In particular, we impose

$$\epsilon^{-1}\boldsymbol{q}\cdot\boldsymbol{n} = -K_n\gamma^{-1}(\check{p}-\hat{p}), \qquad \text{on } \Gamma. \tag{3.3.4}$$

In order to have all dependency on γ in the terms concerning $\boldsymbol{q}$, we incorporate γ in the permeability tensor. The resulting, scaled flux and the permeability are then given the short-hand notation

$$\boldsymbol{q} = [\check{\boldsymbol{q}}, \hat{\boldsymbol{q}}\cdot\boldsymbol{n}], \qquad \mathfrak{K} = [K, K_n\gamma^{-1}], \tag{3.3.5}$$

where we once more use square brackets to denote components in Ω and Γ, respectively. The structure of Darcy's law familiar from (2.2.1) then reemerges with the codivergence from (3.2.8):

$$\epsilon^{-1}\boldsymbol{q} = -\mathfrak{K}\mathfrak{D}p. \tag{3.3.6}$$

Starting with the function spaces for the fixed-dimensional representation of porous media flow (2.4.1), we can define the relevant function spaces as

$$\boldsymbol{Q} = \left\{\boldsymbol{q}\in H(\mathfrak{D}\cdot,\Omega;\mathbb{V}) :\ \boldsymbol{q}\cdot\boldsymbol{n}|_{\partial_0\Omega} = 0\right\}, \qquad \boldsymbol{Q}_0 = \left\{\boldsymbol{q}\in\boldsymbol{Q} : \boldsymbol{q}\cdot\boldsymbol{n}|_{\partial_q\Omega} = 0\right\},$$
$$P = L^2(\Omega;\mathbb{R}).$$

The variational formulation for mixed-dimensional Darcy flow, as derived in Paper A, is then compactly described by:
Find $(\boldsymbol{q}, p)\in\boldsymbol{Q}\times P$ such that

$$\langle\mathfrak{K}^{-1}\boldsymbol{q},\ \tilde{\boldsymbol{q}}\rangle_{\Omega\times\Gamma} - (p, \mathfrak{D}\cdot\epsilon\tilde{\boldsymbol{q}})_\Omega = \left(g_p, \epsilon\tilde{\boldsymbol{q}}\cdot\boldsymbol{n}\right)_{\partial_p\Omega} \qquad \forall\tilde{\boldsymbol{q}}\in\boldsymbol{Q}_0, \tag{3.3.7a}$$
$$(\mathfrak{D}\cdot\epsilon\boldsymbol{q}, \tilde{p})_\Omega = \left(f_q, \tilde{p}\right)_\Omega \qquad \forall\tilde{p}\in P, \tag{3.3.7b}$$

subject to the essential boundary condition

$$\boldsymbol{q}\cdot\boldsymbol{n} = g_q \qquad \text{on } \partial_q\Omega.$$

Structurally, the system of equations (3.3.7) is identical to (2.4.1). This is one of the advantages of the mixed-dimensional framework, since the same steps can be followed in the well-posedness analysis of this system as in the fixed-dimensional case.

This analysis can be found in Paper A, using weighted spaces and norms to handle arbitrarily small values for ϵ. Since this is significantly more involved, we assume ϵ bounded away from zero in this introduction and refer to Paper A for further details.

3.3.3 Linear Elasticity

The similarities between the equations for linear elasticity and porous media flow are directly inherited to the mixed-dimensional setting. The relevant function spaces can therefore once again be considered as the tensorial analogues of the flux and pressure spaces from the

previous section, including the use of a dual variable scaled with ϵ. With the addition of the space R, we consider the function spaces

$$\Sigma = \left\{\sigma \in H(\mathfrak{D}\cdot, \Omega; \mathbb{V}^n) : \ \sigma \cdot \boldsymbol{n}|_{\partial_0\Omega} = 0\right\}, \qquad \Sigma_0 = \left\{\sigma \in \Sigma : \sigma \cdot \boldsymbol{n}|_{\partial_\sigma\Omega} = 0\right\},$$
$$\boldsymbol{U} = L^2(\Omega; \mathbb{R}^n),$$
$$R = L^2(\Omega; \mathbb{K}).$$

Secondly, we use a scaled stress because of the arguments discussed in Section 3.3.1. The influence between dimensions is assumed as a Robin condition on Γ in Paper B which gives a generalization of the operator A from (2.2.5). Moreover, we let the skw operator test symmetry of the tangential components of the stress tensor, which only exist for $2 \leq d \leq 3$. We then obtain the following system of equations for the mixed-dimensional generalization of linear elasticity:
Find $(\sigma, \boldsymbol{u}, r) \in \Sigma \times \boldsymbol{U} \times R$ such that

$$\langle A\sigma, \ \tilde{\sigma}\rangle_{\Omega\times\Gamma} + (\boldsymbol{u}, \mathfrak{D} \cdot \epsilon\tilde{\sigma})_\Omega - (r, \operatorname{skw} \epsilon\tilde{\sigma})_\Omega = (g_u, \tilde{\sigma} \cdot \boldsymbol{n})_{\partial_u\Omega} \qquad \forall \tilde{\sigma} \in \Sigma_0, \tag{3.3.8a}$$
$$(\mathfrak{D} \cdot \epsilon\sigma, \tilde{\boldsymbol{u}})_\Omega = (\boldsymbol{f}_\sigma, \tilde{\boldsymbol{u}})_\Omega \qquad \forall \tilde{\boldsymbol{u}} \in \boldsymbol{U}, \tag{3.3.8b}$$
$$(\operatorname{skw} \epsilon\sigma, \tilde{r})_\Omega = 0 \qquad \forall \tilde{r} \in R, \tag{3.3.8c}$$

subject to the essential boundary condition

$$\sigma \cdot \boldsymbol{n} = \boldsymbol{g}_\sigma \qquad \text{on } \partial_\sigma\Omega. \tag{3.3.9}$$

Remark 3.3.1 *Well-posedness of problem* (3.3.8) *is shown in Paper B. Interestingly, this proof requires several additional tools when compared to the mixed-dimensional flow problem* (3.3.7) *due to the presence of the symmetry multiplier. The key is to use the mixed-dimensional curl, which we obtain from [39] and Paper C.*

3.3.4 Poroelasticity

In Section 2.4.3, we have presented the five-field formulation for the linear Biot system in a conventional, n-dimensional domain. The analogue in the mixed-dimensional setting can be derived using the same techniques as described for the flow and elasticity problems in the previous sections. Here, the thin inclusions are thus assumed to be poroelastic entities as well.

Combining the mixed-dimensional flow and elasticity equations, we immediately arrive at the following formulation at each time $t \in [0, T]$:
Find $(\sigma_p, p, \boldsymbol{q}, \boldsymbol{u}, r) \in \Sigma \times P \times \boldsymbol{Q} \times \boldsymbol{U} \times R$ such that

$$\langle A(\sigma_p + \alpha p I), \ \tilde{\sigma}_p\rangle_{\Omega\times\Gamma} + \left(\boldsymbol{u}, \mathfrak{D} \cdot \epsilon\tilde{\sigma}_p\right)_\Omega - \left(r, \operatorname{skw} \epsilon\tilde{\sigma}_p\right)_\Omega = \left(g_u, \tilde{\sigma}_p \cdot \boldsymbol{n}\right)_{\partial_u\Omega}, \tag{3.3.10a}$$
$$(S_0\dot{p}, \tilde{p})_\Omega + \langle A(\dot{\sigma}_p + \alpha\dot{p}I), \ \alpha\tilde{p}I\rangle_{\Omega\times\Gamma} + (\mathfrak{D} \cdot \epsilon\boldsymbol{q}, \tilde{p})_\Omega = \left(f_q, \tilde{p}\right)_\Omega, \tag{3.3.10b}$$
$$\langle \mathfrak{K}^{-1} 1_\gamma \boldsymbol{q}, \ \tilde{\boldsymbol{q}}\rangle_{\Omega\times\Gamma} - (p, \mathfrak{D} \cdot \epsilon\tilde{\boldsymbol{q}})_\Omega = \left(g_p, \epsilon\tilde{\boldsymbol{q}} \cdot \boldsymbol{n}\right)_{\partial_p\Omega}, \tag{3.3.10c}$$
$$\left(\mathfrak{D} \cdot \epsilon\sigma_p, \tilde{\boldsymbol{u}}\right)_\Omega = (\boldsymbol{f}_\sigma, \tilde{\boldsymbol{u}})_\Omega, \tag{3.3.10d}$$
$$\left(\operatorname{skw} \epsilon\sigma_p, \tilde{r}\right)_\Omega = 0, \tag{3.3.10e}$$

For all $(\tilde{\sigma}_p, \tilde{p}, \tilde{\boldsymbol{q}}, \tilde{\boldsymbol{u}}, \tilde{r}) \in \Sigma \times P \times \boldsymbol{Q} \times \boldsymbol{U} \times R$. The essential boundary conditions in this case are the prescribed flux and poroelastic stress on the corresponding parts of the boundary:

$$\sigma_p \cdot \boldsymbol{n} = \boldsymbol{g}_\sigma \text{ on } \partial_\sigma \Omega, \qquad \boldsymbol{q} \cdot \boldsymbol{n} = g_q \text{ on } \partial_q \Omega.$$

3.3.5 Water Table Evolution

Sharp interface problems form a distinct, but closely related class of problems. Let us consider the evolution of the water table through time. The water table is defined as the height ζ below which the medium is fully saturated with water. In this setting, we consider it as a sharp interface and thus a lower-dimensional manifold. The height ζ varies in time and space, and is therefore included as a variable, defined on the top boundary $\partial_\zeta \Omega$ of the domain of computation Ω.

The evolution of the water table through time is governed by the following differential equation

$$\phi \dot{\zeta} = f_I + \boldsymbol{q} \cdot \boldsymbol{n} \qquad \text{on } \partial_\zeta \Omega. \tag{3.3.11}$$

where ϕ denotes the porosity, f_I is the (time-dependent) source term due to infiltration and $\boldsymbol{q} \cdot \boldsymbol{n}$ is the normal flux from the saturated region. Note that this is a differential equation defined on a lower-dimensional manifold, thus it can be considered a mixed-dimensional partial differential equation. The process, however does not fit perfectly with the examples above, since a mixed-dimensional differential operator is lacking.

For this problem, it is more convenient to use the hydraulic head as the primary variable instead of the pressure. Therefore, let p_H denote the hydraulic head. The hydraulic head at the water table is equal to the elevation of the water table. Mathematically speaking, this means that the following boundary condition is imposed

$$p_H = \zeta \qquad \text{on } \partial_\zeta \Omega.$$

The system of equations is then formed by Darcy's law and mass conservation with a storativity term:

$$\boldsymbol{q} = -K \nabla p_H \tag{3.3.12a}$$

$$S_0 \dot{p}_H + \nabla \cdot \boldsymbol{q} = f_q \qquad \text{in } \Omega. \tag{3.3.12b}$$

After a disjoint decomposition of the boundary as $\partial\Omega = \partial_\zeta \Omega \cup \partial_p \Omega \cup \partial_q \Omega$, the boundary conditions are given by

$$\phi \dot{\zeta} = f_I + \boldsymbol{q} \cdot \boldsymbol{n}, \tag{3.3.13a}$$

$$p_H = \zeta \qquad \text{on } \partial_\zeta \Omega, \tag{3.3.13b}$$

$$p_H = g_p \qquad \text{on } \partial_p \Omega, \tag{3.3.13c}$$

$$\boldsymbol{q} \cdot \boldsymbol{n} = g_q \qquad \text{on } \partial_q \Omega. \tag{3.3.13d}$$

The difficulty in this problem lies in the fact that the domain of computation depends on the solution. To remedy this situation, we employ a domain transformation Φ which maps

the physical, time-dependent domain to a stationary reference domain $\tilde{\Omega}$ as illustrated by Figure 3.2. The advantage of this strategy is that it is relatively easy to implement, since we do not need to consider a moving mesh.

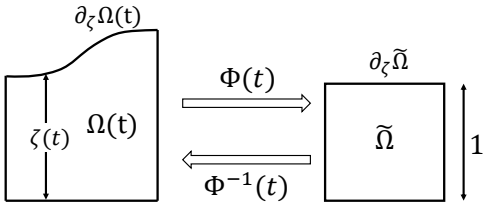

Figure 3.2: Transformation from the physical to a reference domain. The top boundary corresponds to the time-dependent water table.

The most straightforward choice of the transformation Φ is a linear scaling in the vertical direction. This transformation inevitably depends on ζ and this dependency appears in the permeability tensor in the reference domain. In turn, the problem is non-linear and we propose a Picard iterative scheme to obtain a solution in Paper F.

For this problem, it is less important to impose local mass conservation. We will therefore consider the primal formulation of Darcy flow by substituting Darcy's law into the conservation equation. This primal formulation includes the gradient of the hydraulic head and thus the relevant function space is as follows:

$$P_H = H^1(\tilde{\Omega}; \mathbb{R}).$$

In the reference domain, the weak formulation of the problem is then given by

$$S_s(\dot{p}_H, \tilde{p}_H)_{\tilde{\Omega}} + (K(p_H)\nabla p_H, \nabla \tilde{p}_H)_{\tilde{\Omega}} + \phi\,(\dot{p}_H, \tilde{p}_H)_{\partial_\zeta \tilde{\Omega}} = (f_I, \tilde{p}_H)_{\partial_\zeta \tilde{\Omega}}, \qquad \forall \tilde{p}_H \in P_H,$$

for each time $t \in [0, T]$.

The application of this scheme to a physical problem is presented in Paper G, where we investigate groundwater discharge to gaining streams and the influence of meanders in the stream.

Chapter 4

Conforming Discretization Techniques

The mixed-dimensional partial differential equations described in the previous section are amenable to rigorous analysis. With the tools presented in Section 3.2, well-posedness of these problems can typically be proven which gives us existence and uniqueness of the solution. However, in an attempt to derive an analytical solution, the situation becomes significantly more involved.

To overcome this issue, we approximate the solution to the continuous problems using a discretization technique. In this process, the continuous problem is converted to a finite-dimensional, discrete system which has a computable solution. We classify a discretization technique as conforming if the discrete solution is searched within the function space to which the continuous solution belongs. In this work, we focus on finite element methods which arise after a tessellation of the domain into shape-regular simplices conforming to the mixed-dimensional geometry. Other discretization techniques for mixed-dimensional problems, not presented in this introduction, appear in Papers D and E.

Section 4.1 introduces the standard mixed finite elements and their extensions to the mixed-dimensional framework. Afterwards, we comment on the analysis of the discretization scheme with an emphasis on stability in Section 4.2.

4.1 Mixed Finite Elements

In this work, the discretization method of preference is mixed finite elements. The main reason for this choice is that, in this case, the concepts introduced in the previous sections related to mixed-dimensional PDEs are readily translated to their discrete counterparts. The most important of these are the discretized analogues of the function spaces from Sections 2.3 and 3.2.

4.1.1 Conforming Elements

In the fixed-dimensional setting, recall the spaces H^1, $H(\mathrm{div})$, $H(\mathrm{curl})$, and L^2 from Section 2.3. The idea behind conforming finite elements is to create discrete function spaces

which form subspaces of their continuous counterparts. This means that if we aim to create an approximation of a function $\boldsymbol{q} \in \boldsymbol{Q}$, we look for a discrete function $\boldsymbol{q}_h \in \boldsymbol{Q}_h \subseteq \boldsymbol{Q}$.

This may seem like a natural place to start, yet it can be rather technical to create finite elements which preserve all the properties of their continuous analogues. In the context of mixed finite elements, one typically aims to construct stable pairs of finite element spaces, and these may not be trivial to find without the proper tools. Here, the results from finite element exterior calculus come to our aid. Here, we limit the exposition to the most relevant concepts and we refer the reader to [9] for more details.

On a simplicial mesh, conforming to the geometry, two families of finite elements arise. Here, we inherit the nomenclature of Nédélec by referring to these families as either of the first or the second kind. Moreover, we use the notation from [9] to and let $P_r^-\Lambda^k$ be the discretization of differential k-forms of polynomial order r of the first kind. On the other hand, its discretization of the second kind will be denoted by $P_r\Lambda^k$. The following co-chains of spaces then arise, as described by Arnold et al. [9]:

$$P_r^-\Lambda^k(\Omega^d) \xrightarrow{\mathrm{d}} P_r^-\Lambda^{k+1}(\Omega^d), \qquad P_r\Lambda^k(\Omega^d) \xrightarrow{\mathrm{d}} P_{r-1}\Lambda^{k+1}(\Omega^d). \tag{4.1.1}$$

In the literature, the family of the first kind is occasionally referred to as the reduced finite elements.

Remark 4.1.1 *The two families as presented here are not strictly separate categories of finite elements. The well-known Lagrange elements, for example, can be described by $P_r\Lambda^0(\Omega^d)$ as well as $P_r^-\Lambda^0(\Omega^d)$. Moreover, the mapping defined above is generally not surjective and the following two relationships hold as well*

$$P_r^-\Lambda^k(\Omega^d) \xrightarrow{\mathrm{d}} P_{r-1}\Lambda^{k+1}(\Omega^d), \qquad P_r\Lambda^k(\Omega^d) \xrightarrow{\mathrm{d}} P_r^-\Lambda^{k+1}(\Omega^d). \tag{4.1.2}$$

In this work, we focus on the mappings given in (4.1.1)*, as these remain within each family.*

4.1.2 Dimensional Hierarchy

By choosing the conforming finite elements from the previous section, a second relationship between these elements is uncovered, as we map to lower-dimensional manifolds. Let us consider the jump operator $\mathbb{d}$ and apply it to a discrete function. We then observe that the image of this operator is a conforming finite element space on the lower-dimensional manifold. In fact, the finite elements of the first and second kind possess the following relationship:

$$P_r^-\Lambda^k(\Omega^d) \xrightarrow{\mathbb{d}} P_r^-\Lambda^k(\Omega^{d-1}), \qquad P_r\Lambda^k(\Omega^d) \xrightarrow{\mathbb{d}} P_r\Lambda^k(\Omega^{d-1}). \tag{4.1.3}$$

The two families of finite elements are generalized by introducing the discretization of the mixed-dimensional k-form $\mathfrak{Q}^k$. Using P_r and P_r^- to denote elements of the first and second kind, respectively, we define

$$P_r^-\mathfrak{Q}^k(\Omega) = \prod_{d=0}^{n} P_r^-\Lambda^{d-(n-k)}(\Omega^d), \qquad P_r\mathfrak{Q}^k(\Omega) = \prod_{d=0}^{n} P_{r+n-d}\Lambda^{d-(n-k)}(\Omega^d). \tag{4.1.4}$$

Together with equation (4.1.1), we uncover that the finite elements are related to one another within each family by the differential operator $\mathfrak{d}$ in the following way:

$$P_r^- \mathfrak{L}^k(\Omega) \xrightarrow{\mathfrak{d}} P_r^- \mathfrak{L}^{k+1}(\Omega), \qquad P_r \mathfrak{L}^k(\Omega) \xrightarrow{\mathfrak{d}} P_{r-1} \mathfrak{L}^{k+1}(\Omega). \tag{4.1.5}$$

To make this more concrete, let us describe these relationships by considering the different components of $\mathfrak{L}^k(\Omega)$. In particular, we note that the polynomial order is preserved for the finite elements of the first (or reduced) kind. The conforming finite elements of lowest order are thus related according to the following diagram

$$\begin{array}{ccccccccc}
P_1^- \mathfrak{L}^0(\Omega) & & P_1(\Omega^3) & & & & & & \\
\downarrow \mathfrak{d} & & \downarrow \mathrm{d} & \searrow \mathbb{d} & & & & & \\
P_1^- \mathfrak{L}^1(\Omega) & & N1_0^e(\Omega^3) & & P_1(\Omega^2) & & & & \\
\downarrow \mathfrak{d} & & \downarrow \mathrm{d} & \searrow \mathbb{d} & \downarrow \mathrm{d} & \searrow \mathbb{d} & & & \\
P_1^- \mathfrak{L}^2(\Omega) & & N1_0^f(\Omega^3) & & RT_0(\Omega^2) & & P_1(\Omega^1) & & \\
\downarrow \mathfrak{d} & & \downarrow \mathrm{d} & \searrow \mathbb{d} & \downarrow \mathrm{d} & \searrow \mathbb{d} & \downarrow \mathrm{d} & \searrow \mathbb{d} & \\
P_1^- \mathfrak{L}^3(\Omega) & & P_0(\Omega^3) & & P_0(\Omega^2) & & P_0(\Omega^1) & & P_0(\Omega^0)
\end{array} \tag{4.1.6}$$

Here, P_r denotes Lagrange elements of order r if $r > 0$ and discontinuous Lagrange elements of order r for $r \leq 0$. The Nédélec elements of the first kind [41] are denoted by $N1_r^e$ and $N1_r^f$ with degrees of freedom defined on the edges or faces of an element, respectively. Finally, RT_r denotes the Raviart-Thomas space of polynomial order r [44]. The spaces given on the bottom two rows are used in Paper A to discretize Darcy flow through fractured porous media, given by the system of equations (3.3.7).

This diagram of elements of the first kind has been analyzed for simplicial complexes by Licht [39].

On the other hand, the finite elements of the second kind form a similar diagram with a few different properties. Most notably, the order of the polynomial space is reduced by each application of the differential d, yet remains constant under application of $\mathbb{d}$. Thus, a different pattern emerges, as shown in the diagram

$$\begin{array}{ccccccccc}
P_3 \mathfrak{L}^0(\Omega) & & P_3(\Omega^3) & & & & & & \\
\downarrow \mathfrak{d} & & \downarrow \mathrm{d} & \searrow \mathbb{d} & & & & & \\
P_2 \mathfrak{L}^1(\Omega) & & N2_2^e(\Omega^3) & & P_3(\Omega^2) & & & & \\
\downarrow \mathfrak{d} & & \downarrow \mathrm{d} & \searrow \mathbb{d} & \downarrow \mathrm{d} & \searrow \mathbb{d} & & & \\
P_1 \mathfrak{L}^2(\Omega) & & N2_1^f(\Omega^3) & & BDM_2(\Omega^2) & & P_3(\Omega^1) & & \\
\downarrow \mathfrak{d} & & \downarrow \mathrm{d} & \searrow \mathbb{d} & \downarrow \mathrm{d} & \searrow \mathbb{d} & \downarrow \mathrm{d} & \searrow \mathbb{d} & \\
P_0 \mathfrak{L}^3(\Omega) & & P_0(\Omega^3) & & P_{-1}(\Omega^2) & & P_{-2}(\Omega^1) & & P_{-3}(\Omega^0)
\end{array} \tag{4.1.7}$$

Here $N2_r$ denotes Nédélec elements of the second kind [42] and BDM_r represents the Brezzi-Douglas-Marini element of order r [15]. The polynomial order on $P_r(\Omega^0)$ is redundant since all finite element spaces reduce to point evaluation in zero dimensions.

It is important to note that in this family, degree of polynomial depends increases with the amount of reductions from the ambient space, or $n - d$. If we were to consider a two-dimensional problem, fewer reductions are possible and we may therefore consider a family with a lower polynomial order.

$$\begin{array}{ccccccc}
P_2\mathfrak{L}^0(\Omega) & & P_2(\Omega^2) & & & & \\
\downarrow \mathfrak{d} & & \downarrow \mathrm{d} & \searrow^{\mathbb{d}} & & & \\
P_1\mathfrak{L}^1(\Omega) & & BDM_1(\Omega^2) & & P_2(\Omega^1) & & \\
\downarrow \mathfrak{d} & & \downarrow \mathrm{d} & \searrow^{\mathbb{d}} & \downarrow \mathrm{d} & \searrow^{\mathbb{d}} & \\
P_0\mathfrak{L}^2(\Omega) & & P_0(\Omega^2) & & P_{-1}(\Omega^1) & & P_{-2}(\Omega^0)
\end{array} \tag{4.1.8}$$

In comparison, the finite elements of the second kind have more degrees of freedom than those of the first kind. Unfortunately, the added computational cost of using such elements does not necessarily increase the accuracy of the method. For example, for the Poisson equation in mixed form, the use of BDM_1 elements produces the same solution as that given by Raviart-Thomas elements of lowest order. Since the BDM space has twice as many degrees of freedom, its usefulness is not immediately apparent in that case.

However, since the order of the spaces depends on the number of reductions, this family of finite elements allows for more accurate representations inside the lower-dimensional manifolds. This is shown in Paper C, where a comparison in two dimensions between elements of the first and second kind shows that higher rates of convergence are obtained in the fractures, due to these higher-order elements. The computational cost of this improved accuracy is marginal, because of the lower dimensionality of the manifold.

Moreover, the family of finite elements of the second kind play an important role when considering the mixed formulation of elasticity with relaxed symmetry. In that case, the $H(\mathrm{div})$-conforming finite elements of the first kind do not have enough degrees of freedom to form stable triplets with the corresponding L^2-conforming displacement and rotation spaces. We therefore turn to this family when we construct the discrete spaces for the elasticity problem in Paper B.

Finally, recall that the water table evolution problem from Section 3.3.5 is solved in a primal formulation. The corresponding function space can be identified as a space of differential 0-forms, which means that the conforming discretization in that case is given by Lagrange elements. In order to provide a computationally efficient scheme, we have therefore chosen the lowest-order, i.e. linear, Lagrange elements in Papers F and G.

4.2 Stability Theory

The use of conforming finite elements has several advantages, especially in the context of analysis of the resulting scheme. Since the discrete spaces are contained in the solution space,

the mathematical structure is kept intact and the analytical tools from the continuous problem are available to determine the properties of the numerical scheme. To see this, let us consider the discretized version of the fixed-dimensional Darcy system (2.4.1) after a choice of conforming finite element spaces $\boldsymbol{Q}_h^n \times P_h^n$ as presented in the previous section:
Find $(\boldsymbol{q}_h, p_h) \in \boldsymbol{Q}_h^n \times P_h^n$ such that

$$\left(K^{-1}\boldsymbol{q}_h, \tilde{\boldsymbol{q}}_h\right)_\Omega - (p_h, \nabla \cdot \tilde{\boldsymbol{q}}_h)_\Omega = \left(g_p, \tilde{\boldsymbol{q}}_h \cdot \boldsymbol{n}\right)_{\partial_p \Omega} \qquad \forall \tilde{\boldsymbol{q}}_h \in \boldsymbol{Q}_{0,h}^n, \tag{4.2.1a}$$

$$(\nabla \cdot \boldsymbol{q}_h, \tilde{p_h})_\Omega = \left(f_q, \tilde{p_h}\right)_\Omega \qquad \forall \tilde{p_h} \in P_h^n. \tag{4.2.1b}$$

Recall that in Section 4.1.2, we have identified finite elements which conform to the mixed-dimensional spaces defined for all problems considered herein. We therefore omit mentioning the different discrete systems, since they can easily be constructed by considering the restriction to these discrete, conforming function spaces.

A desirable, if not essential, property a method can have is convergence, or how well the true solution is approximated with respect to the mesh size. Convergence can be shown by proving two ingredients: consistency and stability. Consistency implies that the true solution to the continuous problem satisfies the discretized system of equations. In the context of conforming methods, this is always the case. For example, the solution $(\boldsymbol{q}, p) \in \boldsymbol{Q}^n \times P^n$ to the Darcy flow problem (2.4.1) satisfies the discrete equations (4.2.1) since $\boldsymbol{Q}_h^n \times P_h^n \subseteq \boldsymbol{Q}^n \times P^n$.

Stability, on the other hand, means that the solution depends continuously on the data in the given norms, irrespective of the mesh size. Before considering all mesh sizes, let us start with a given mesh. The discretized system is then a saddle point problem which can be written in the standardized form (2.3.15). As such, we use the saddle-point theory explained in Section 2.3.2 to show well-posedness of the corresponding system. Once we prove that norm of the solution is bounded by the norm of the data with a bounding constant independent of the mesh size, we have shown that the scheme is stable.

For that purpose, we turn to the two (sufficient) conditions introduced in Section 2.3.2. These state that the bilinear form a is elliptic on the kernel of B and that the inf-sup condition holds for b in the appropriate norms. As we encounter in Papers A and B, the ElKer condition is readily satisfied after choosing the correct norms for the function spaces. We will therefore lay the focus on the inf-sup condition in the following section.

4.2.1 The Inf-Sup Condition

Analogous to the condition introduced in Section 2.3.2, the inf-sup condition in the discrete setting is given by:
There exists a constant $C_b > 0$, independent of the mesh size such that for any $p_h \in P_h$, a function $\boldsymbol{q}_h \in \boldsymbol{Q}_h \setminus \{0\}$ exists such that

$$b(\boldsymbol{q}_h, p_h) \geq C_b \|\boldsymbol{q}_h\|_Q \|p_h\|_P. \tag{4.2.2}$$

This condition is equivalent to stating that a function $\boldsymbol{q}_h \in \boldsymbol{Q}_h \setminus \{0\}$ exists such that

$$b(\boldsymbol{q}_h, p_h) = \|p_h\|_P^2 \qquad \text{with } \|\boldsymbol{q}_h\|_Q \leq C_b \|p_h\|_P. \tag{4.2.3}$$

The proofs in Papers A and B therefore assume that the primal variable is given, and the key is to construct a viable dual variable, from the correct space, such that these conditions are satisfied. In the context of conforming finite elements, it is therefore very useful if the dual variable is mapped into the space of the primal variable by the operator B. For example, in case of the fixed-dimensional flow problem, we choose our finite element spaces $\boldsymbol{Q}_h^n \times P_h^n$ such that

$$\nabla \cdot \boldsymbol{Q}_h^n \subseteq P_h^n. \tag{4.2.4}$$

In the mixed-dimensional setting, the pair of finite element spaces is chosen in order to satisfy

$$\mathfrak{D} \cdot \boldsymbol{Q}_h \subseteq P_h. \tag{4.2.5}$$

Here, the results from exterior calculus and the dimensional hierarchy given in Section 4.1.2 provide a suggestion to choosing finite elements which have this property.

4.2.2 Reduction through Quadrature

A major drawback of using mixed finite elements is the computational cost. The introduction of the dual variable, besides adding a large amount of degrees of freedom, typically changes the structure of the problem to a saddle point problem, which may be challenging to solve.

In order to overcome this problem, a promising solution can be found by introducing a quadrature rule on one of the inner products. As explored by [16, 51], a multi-point flux mixed finite element method is obtained. Starting with the variational formulation concerning fixed-dimensional Darcy flow (2.4.1), we use the subscript QR to denote that the quadrature rule has been applied. The augmented, discrete problem then becomes:
Given $\boldsymbol{g} \in \boldsymbol{Q}_h^{n*}$ and $f \in P_h^{n*}$, find $\boldsymbol{q} \in \boldsymbol{Q}_h^n$ and $p \in P_h^n$ such that

$$\left(K^{-1}\boldsymbol{q}, \tilde{\boldsymbol{q}}\right)_{QR} - (p, \nabla \cdot \tilde{\boldsymbol{q}})_\Omega = \left(g_p, \tilde{\boldsymbol{q}} \cdot \boldsymbol{n}\right)_{\partial_p \Omega} \qquad \forall \tilde{\boldsymbol{q}} \in \boldsymbol{Q}_{0,h}^n, \tag{4.2.6a}$$

$$(\nabla \cdot \boldsymbol{q}, \tilde{p})_\Omega = \left(f_q, \tilde{p}\right)_\Omega \qquad \forall \tilde{p} \in P_h^n. \tag{4.2.6b}$$

If $\boldsymbol{Q}$ is discretized using BDM_1 elements, then the quadrature rule can be chosen to be the trapezoid rule. In turn, the operator A_{QR} corresponding to $a(\cdot, \cdot)$ in this system become easily invertible. The flux can then be eliminated and we directly compute the pressure

$$BA_{QR}^{-1}B^T p = BA_{QR}^{-1}g_p - f_q \qquad \text{in } P_h^*. \tag{4.2.7}$$

Note that in this system, we are only concerned with the pressure space, which has fewer degrees of freedom. Moreover, this system is positive-definite and can therefore be solved more easily than the original, large saddle point problem. Even though the flux is eliminated, it remains readily available through the reconstruction

$$\boldsymbol{q} = A_{QR}^{-1}(g_p - B^T p). \tag{4.2.8}$$

Finally, we emphasize that even though a quadrature rule is used, the rate of convergence remains intact. In conclusion, a computationally inexpensive scheme is constructed which is provably convergent. Similar techniques are expected to be applicable to the proposed mixed-dimensional discretizations.

Chapter 5

Summary and Outlook

In this chapter, we summarize the scientific results presented in the form of eight scientific articles in Part II. The first six papers, presented in Section 5.1.1, comprise the main results. This section starts with Paper A in which Darcy flow in fractured porous media is considered followed by its analogues for linear elasticity in Paper B. A more general framework in terms of mixed-dimensional exterior calculus is discussed in Paper C. Paper D presents a benchmark study for numerical schemes solving flow in fractured media in which the method from Paper A is a participant. In Paper E, we introduce the mixed-dimensional analogues of different discretization schemes such as finite volume and virtual methods for fracture flow. Finally, the water table evolution problem is considered in Papers F, in which a numerical scheme based domain transformation is proposed and analyzed.

Section 5.1.2 contains two papers on related work. In Paper G, the domain transformation method from Paper F is applied to a real-world test case concerning gaining streams. Finally, Paper H proposes an adaptive penalty method for solving inequality constrained minimization problems.

5.1 Summary of the Papers

5.1.1 Main Results

Paper A: Robust Discretization of Flow in Fractured Porous Media

This paper is the first concrete example of how the mixed-dimensional framework can be used in practice. Many of the concepts introduced in this thesis have their origin with this work, including the domain decomposition according to dimension and the use of conforming mixed finite elements in different dimensions, among others.

The main contribution of this work is fourfold. First, the dimensional decomposition provides a novel insight in the consideration of fracture intersections. The representation of fractures as lower-dimensional manifolds has become a common concept in the fracture modeling, see e.g. [23, 28]. However, a general consensus on the interpretation of fracture intersections was lacking, and these were often included using ad hoc assumptions. In this paper,

the dimensional decomposition naturally provides the tools to define differential equations on the fracture intersection lines, therewith allowing flow to occur along these intersection lines. In this paper, we consider Darcy flow in manifolds of all dimensionalities and exploit the resulting similarities in the equations.

Secondly, the majority of existing fracture flow discretization schemes assume that the fractures have a spatially constant aperture, see e.g. [27, 40]. This assumption allows for a straightforward derivation of the reduced model, yet it has one important drawback. Fracture tips under this assumption are incorporated as abrupt endings and a boundary condition is imposed, which is typically a no-flow condition [5]. However, such an abrupt ending implies that the fracture has a rectangular shape at the end, while it is usually more physical to consider a fracture pinching out. In this paper, the reduced equations are derived by assuming spatially varying apertures. In turn, fracture pinch-outs can be included in the model, at the expense of a more involved analysis. With the use of a numerical example, the behavior of the solution is shown to be noticeably different compared to abrupt fracture endings in certain cases.

Thirdly, the incorporation of spatially varying apertures leads to a more involved analysis of the problem. The aperture shows up as a scaling factor which, in turn, raises the need for weighted Sobolev spaces. Well-posedness of the continuous problem is then shown with respect to these function spaces, always considering the aperture as spatially varying and arbitrarily small, including the limiting case of zero aperture. To discretize, familiar mixed finite elements are chosen for the flux and pressure variables, which provides local mass conservation.

Finally, the proposed scheme can be considered as a mortar method, with one significant distinction. Conventional mortar methods employ the pressure as the mortar variable whereas here, the flux is used. This results in a stronger notion of mass conservation, at the expense of a more involved analysis of the scheme. Moreover, the close connection to mortar methods allows for the use of non-matching grids along fractures and fracture intersections. Although the mesh is still required to conform to the fracture network geometrically, the meshing difficulties are relieved by allowing for independent grid generation on different sides of fractures and intersections.

The method proposed in this paper resurfaces in several other works. First, it is a participant in the benchmark study included as Paper D. Secondly, the applicability of the scheme to transport problems has been investigated by Stefansson [49]. Finally, Paper E generalizes the choice of mixed finite elements in each dimension to other choices of stable discretization methods.

Paper B: Stable Mixed Finite Elements for Linear Elasticity with Thin Inclusions

As shown in the previous sections, a natural analogue to the mixed-dimensional flow problem from Paper A is to consider the mechanics equations on the mixed-dimensional geometry. Applications of this work include composite materials, fractured media, and certain root systems. Again, the interest lies in developing a locally conservative scheme and mixed finite

elements are employed. As explored by [8], the relaxation of symmetry on the stress tensor allows the use of familiar, low-order finite elements and we employ this strategy in each dimension.

This work includes the following two contributions. First, it is observed that the choice of finite elements is not as trivial as for the mixed-dimensional flow problem. In the ambient space, the stable triplet of elements presented by [8] is chosen, given by BDM_1 for the stress and piecewise constants for the displacement and rotation variables. This space contains piecewise functions of polynomial order one or less and the initial guess for the analogues in fewer dimensions would be to choose linear Lagrange elements for the stress and piecewise constants for the displacement and rotation. However, to have a truly conforming mixed finite element scheme where the divergence operator maps from the stress into the displacement space, one needs to employ a higher-order triplet inside the lower-dimensional domains. This naturally improves the approximation properties in the lower dimensions while the added computational cost is marginal.

Secondly, the well-posedness analysis in this paper contains an application of the mixed-dimensional de Rham complex, with the mixed-dimensional curl in particular. This is due to the fact that the structure of the equations is the same compared to the fixed-dimensional case. The aim is then to use similar techniques in the analysis and an important part of the analysis of elasticity problems with relaxed symmetry is to use the curl, which maps to the kernel of the divergence. In our setting, the image of the conventional curl is not contained in the kernel of the mixed-dimensional divergence and therefore does not suffice. The mixed-dimensional curl, presented in Paper C, does have this property and is exploited to show the well-posedness of the problem.

Paper C: Modeling, Structure and Discretization of Mixed-dimensional Partial Differential Equations

Paper C introduces a generalizing framework in the context of exterior calculus for mixed-dimensional partial differential equations. With the use of finite element exterior calculus, we immediately obtain choices of conforming finite elements in all dimensions. These finite elements are used in Papers A and B for flow and elasticity, respectively.

After introducing the geometrical setting, the paper starts with the derivation of the mixed-dimensional divergence. Its generalization in terms of the semi-discrete exterior derivative is then presented followed by the structure for mixed-dimensional partial differential equations. Several results are summarized, without rigorous proofs, to provide insight into the tools available for the consequent analysis.

A useful observation in this proceedings paper is the translation of the results from exterior calculus to finite-dimensional spaces. After the appropriate identification of the differential forms, a conforming finite element scheme is readily available. With the use of an elliptic example concerning fracture flow, the discretization of the primal formulation leads to choosing Lagrange elements in each dimension. Alternatively, the mixed formulation gives rise to the reduced mixed finite elements as used in Paper A and the less trivial family of elements of the second kind used in Paper B.

The paper concludes by testing these three conforming discretization schemes in a numerical experiment. A model problem is presented corresponding to flow through two intersecting fractures in a two-dimensional domain. The observed rates of convergence are as expected with a notably improved order of convergence in the fractures for the mixed finite elements of the second kind due to the higher order elements used there.

Paper D: Benchmarks for Single-phase Flow in Fractured Porous Media

As the title suggests, Paper D is a comparison study of a selection of discretization schemes for single-phase flow in fractured porous media. The motivation for such a study is twofold. First, the development of these numerical methods was mostly performed independently and an objective comparison of these schemes was lacking thus far. The aim was therefore to collect these methods and test how well each performs in terms of applicability, accuracy, computational cost and convergence with respect to each other.

Secondly, the model problems considered in this are constructed to serve as benchmarks for the development of future schemes. These case studies were therefore chosen to reflect all the challenges which arise in the modeling of flow through fracture networks. The problems considered are two-dimensional, ranging from regular fracture networks with few, perpendicular fractures to a realistic, complex case with over a hundred fractures intersecting at random angles. A second test of flexibility was conducted by varying the permeabilities of the fractures. This way, the performance of the methods was explored with respect to both conductive fractures and blocking features.

The methodology of comparison is as follows. Accuracy and convergence of the solution was tested by comparing both the matrix and fracture pressures to a fine-scale solution obtained using a mimetic finite difference method. In terms of computational cost, each method provided the generated matrix from which the condition number was estimated, the number of degrees of freedom was observed and the degree of sparsity was calculated.

The most notable distinction between the methods is the way that fractures are incorporated with respect to the mesh. Three methods required grids which completely conform to the fracture network while three other methods were able to mesh independently and have the fractures cross through the elements. As noted in the summary of Paper A, our proposed method requires the grid to conform to the geometry of the fracture network, yet the grid is permitted to be non-matching along the fractures.

Finally, we make a short remark on the performance of the discretization method proposed in Paper A. Our method was one of only two methods which showed convergence in all test cases. The remaining six schemes exhibited stagnation in the convergence rates whenever a blocking and a conducting fracture intersect. Moreover, although all methods could theoretically solve all model problems, our method was one of three which was able to run all test cases without encountering implementation restrictions or limitations with respect to permeabilities.

On the other hand, the method requires more degrees of freedom than the schemes based on primal formulations. Furthermore, the condition numbers were among the highest in test cases with conductive fractures and relatively low if the model problem contained blocking

features. This dependency of the condition number lends itself as a subject for future investigation.

Paper E: Unified Approach to Discretization of Flow in Fractured Porous Media

The observation that fracture flow can be described as a mixed-dimensional elliptic problem raises the question on how existing discretization techniques designed for fixed-dimensional elliptic problems can be applied. In this paper, we explore this question by showing how different numerical methods can be coupled between domains of heterogeneous dimensions with the use of a flux mortar variable. The established approach is termed the Mixed-Dimensional Flux Coupling (MDFC) scheme and this work both analyzes the approach in a general setting and presents numerical results for five choices of numerical schemes.

The MDFC approach is formulated without relying on a specific choice of numerical schemes in each dimension. The only requirement is that the chosen numerical method acts as a stable Neumann to Dirichlet map. In turn, the internal workings of these methods are not called upon and the approach is therefore well-suited for use in existing code. The most intrusive modifications necessary to implement the scheme concern the incorporation of flux boundary conditions and appropriate source terms.

An abstract analysis of the approach is presented under mild conditions regarding the underlying methods. We show that the linear system can be reduced to a Schur complement system in terms of the introduced flux mortar variable. In turn, well-posedness of the discrete system of equations is shown independent of the mesh size given that the permeabilities do not degenerate. A disadvantage of this general approach is that the results are likely to be suboptimal. More nuanced results such as convergence rates or a priori error estimates require details specific to the chosen method. Nonetheless, the analysis shows that the resulting MDFC scheme is stable depending only on the stability of the underlying discretization schemes.

Numerical examples in two and three dimensions highlight the large degree of flexibility of the proposed coupling scheme. The five numerical schemes tested consist of linear Lagrange elements, reduced mixed finite elements of lowest order, dual virtual elements, and two finite volume schemes employing two-point and multi-point flux approximation, respectively. The results confirm that the MDFC scheme is stable for all choices methods and the majority of methods exhibit linear convergence. The MDFC is thus shown to be a viable coupling strategy for a wide range of numerical methods.

Finally, a discussion on grid ratios and permeabilities which arose in the analysis is tested. By varying the normal permeabilities and the coarseness of the mortar grid, we show how the smallest eigenvalues of the Schur complement system behaves for all five methods. Once more, the results are in line with the theory and stability is shown in all cases with a weak dependency on the ratio between the mortar and outer grid.

Paper F: Efficient Water Table Evolution Discretization using Domain Transformation

In this paper, the evolution of the water table through time is considered. In the subsurface, the water table is represented as the lower-dimensional interface separating a fully saturated region below from the unsaturated soil above. The location of this interface fluctuates due to changes in flows from natural causes such as rainfall or from anthropological structures such as wells and dams. The focus is therefore on the flows within the saturated region, which gives rise to the main difficulty in this problem. In particular, since the height of the water table is governed by saturated flows, the domain of computation depends on the solution.

The most important observation in this work is the introduction and exploitation of a domain transformation. In particular, the physical domain is scaled in the vertical direction to create a reference domain with a fixed height. The coordinate transformation is then used to rewrite the problem to a non-linear partial differential equation defined on the stationary domain. Here, the equation governing the water table evolution is defined at the top boundary. By using the hydraulic head as the only unknown variable in a primal formulation, this equation is incorporated as a natural boundary condition. To solve this non-linear problem, a fixed point iterative scheme is proposed which we show to be convergent under mild assumptions.

Compared to alternatives such as moving mesh methods or saturated-unsaturated flow models, the proposed method is significantly less computationally demanding, as experienced in Paper G. In contrast to moving mesh methods, no re-meshing is required and the scheme performs well in the presence of steep gradients. On the other hand, saturated-unsaturated models which use the Richards equation are computationally demanding and convergence of iterative schemes is generally not guaranteed [47].

Two model problems are considered in two and three dimensions, respectively, corresponding to the region near an extraction well. The numerical experiments show the quadratic convergence inherent to the linear Lagrange elements used. Finally, a short numerical experiment with respect to heterogeneities in permeability is performed in two dimensions. Due to the coordinate transformation, the heterogeneities are not stationary in the reference domain and a degradation in the convergence rates can be observed. In special cases, however, a modified domain transformation can be applied which saves the convergence rates.

5.1.2 Related Work

Paper G: A 3-D Model of the Influence of Meanders on Groundwater Discharge to a Gaining Stream in an Unconfined Sandy Aquifer

In this interdisciplinary work, the spatial variability of groundwater flows in the vicinity of gaining, meandering streams is considered. The aim is to map water fluxes in an aquifer with the use of numerical simulations in order to investigate the effect of stream meanders on the regional flow paths. This way, insight is provided into these three-dimensional flows at the reach scale for applications such as transport of contaminants in the groundwater.

To separate the influence of meanders in the stream from other factors, a synthetic test

case is presented consisting of a stream in a three-dimensional aquifer which varies from straight to highly sinuous. The model problem is an extension of the two-dimensional steady state model presented in [19]. A short investigation into alternative effects is performed by varying the stream width, meander amplitude, magnitude of the hydraulic gradient, the hydraulic conductivity, and the aquifer thickness. The computed groundwater flow patterns are then investigated with a specific focus on the groundwater discharge to the stream. In addition to these model problems, the same methodology is used to simulate a real stream using data from a field site in Grindsted, Denmark.

The numerical results show a significant influence of the meander geometry on the spatial distribution of groundwater flows to streams. Several observations are made which are impossible to achieve with a two-dimensional model. The groundwater discharge is shown to be highest at the meander extremes, with fluxes from the upper section of the aquifer entering the stream at the outward pointing bank. On the other hand, groundwater from deeper sections of the aquifer is often observed to flow beneath the stream to enter at the inward bank. These patterns were observed for both the synthetic cases and the Grindsted field study.

The computations were performed using the discretization scheme proposed in Paper F. The efficiency of this method is most apparent when compared to the saturated-unsaturated flow model, reducing the computational time by a factor of approximately 32 for the time-dependent real case. Moreover, the domain transformation scheme showed no instabilities or oscillations in contrast to the moving-mesh method.

Paper H: An Adaptive Penalty Method for Constrained Minimization Problems

Before contact problems can be considered in a mixed-dimensional setting, a generalization is necessary extending the theory from this dissertation towards variational inequalities. With this goal in mind, Paper H considers inequality constrained minimization problems and proposes an iterative solution method. The

The construction of the proposed method is based on two well-known methods, namely the penalty and the active set method. The penalty method includes a term into the formulation which penalizes the solution if it lies outside the admissible set. Although this allows for the use of the Newton method, thus leading to a locally convergent method, the converged solution is not guaranteed to satisfy the imposed constraints exactly. The active set method, on the other hand, does lead to a feasible solution. Its disadvantage, however, is that a warm start is often required to achieve fast convergence.

The adaptive penalty method proposed in this work is designed to combine the advantages of these two methods. Starting as a penalty method, the penalty parameter is iteratively set as a spatially varying function depending on the residual. As the solution converges, the penalty parameter tends to zero and the scheme behaves as the active set method. In turn, the converged solution satisfies the constraints imposed in the original problem. Similar to the penalty method, the Newton method can be applied at each iteration step.

The spatially dependent penalty parameter is obtained by solving a synthetic diffusion equation. This equation has no physical relevance and we may therefore approximate its solution using a coarse solve thus reducing computational cost. We remark that different

interpretations of the adaptive penalty method are possible, including an identification with a quasi-Newton method or with a regularized active set method.

To test the method, a one-dimensional obstacle problem is considered. Comparing to the active set method, the scheme converges in fewer iterations in the range of tested parameters. Moreover, the variant of the method using a coarse solve performs equally well.

5.2 Outlook

The mixed-dimensional framework opens numerous paths for future investigation. We summarize a selection of these in this section, in order of relevance to the scientific papers included in Part II.

First, the combination of mixed-dimensional flow from Paper A with elasticity from Paper B deserves further investigation. In Section 2.4.3, we have shown how this leads to the five-field formulation of the linearized Biot equations. The same lines of reasoning found throughout this thesis can be used to find a suitable choice of finite elements and to establish the corresponding analysis. By choosing mixed finite elements, stability can be obtained from the separate equations corresponding to flow and elasticity. However, the cost of choosing a discretization conforming to the five-field formulation, is in the amount of degrees of freedom which inevitably leads to large linear systems. Elimination of several variables through static condensation may be key, yet a further understanding of such manipulations in the mixed-dimensional setting is necessary.

Secondly, more advanced physics can be included for the models described in both Papers A and B. Here, we have only considered Darcy's law and linear elasticity, yet the theory is not limited to this choice. Stokes' flow inside the fractures or finite strain assumptions on the inclusions would be welcome additions, at the cost of requiring a more technical analysis.

Third, the problems considered in this work correspond to differential d-forms, namely pressures and displacements, and $(d-1)$-forms given by fluxes and stresses. An interesting continuation of these ideas is to consider differential $(d-2)$-forms in the mixed-dimensional setting. The resulting equations would be of interest in the context of Maxwell's equations for electromagnetism on a mixed-dimensional geometry. Possibly, this line of reasoning is then closely related to the work by Buffa and Christiansen [17] in which non-conductive screens are considered.

Fourth, a second comparison project in the spirit of Paper D can be designed to provide new insights. The discretization techniques can then be tested when more advanced physical processes such as transport, deformation and chemical reactions are added to the single-phase fracture flow problem. Then, a more important role will be played by the flux field, which has not been considered in the current work. Moreover, it would be interesting to consider three-dimensional problems and investigate the performance of the schemes capable of solving those cases.

Fifth, the flux coupling scheme presented in Paper E is open to more exotic combinations of discretization schemes. In this work, we have chosen the same discretization scheme in each dimension, yet the framework allows for the coupling of independently chosen methods per dimension and even per individual fracture. In turn, the computational cost can be

weighed against the desired accuracy for the surrounding matrix, the fractures and the intersection lines independently. On the other hand, the similarities between flow and mechanics highlighted throughout this thesis may be applicable in this setting as well, possibly leading to a mixed-dimensional stress coupling scheme. The advantages of primal and mixed finite elements can then be combined for the setting of elastic materials with thin inclusions. However, it is likely that further development of the theory in Paper B is necessary beforehand.

As for the domain transformation method constructed in Paper F, several variations and extensions are possible. For instance, the use of mixed finite elements would give the method local mass conservation, which is essential for applications involving transport. The analysis will change drastically since the water table itself changes from a natural to an essential boundary condition. On the other hand, in the context of CO_2-storage, the use of domain transformations may prove fruitful as well. In order to model the evolution of the CO_2 plume after injection in a confined aquifer, for example, it would be interesting to use a coordinate mapping depending on the interface between CO_2 and brine. The major obstacle that needs to be addressed, however, is the degeneracy of the coordinate transformation at the tip of the plume.

Seventh, the exploration of contact problems in the mixed-dimensional framework requires a proper understanding of variational inequalities. Applying the adaptive penalty method from Paper H to these problems may be very fruitful. Especially for problems with a large amount of degrees of freedom, we may then investigate whether the adaptive penalty method converges faster than the active set method and whether a more satisfying solution than conventional penalty methods is produced.

Finally, a further analysis of the de Rham complex and its properties when considered on the mixed-dimensional geometry may yield interesting results. The focus in this work has been on the implications for discretization schemes, but this mixed-dimensional structure may hold secrets for other applications, yet undiscovered.

Bibliography

[1] Adams, R. and Fournier, J. (2008). Sobolev Spaces. Acad. Press. ISBN 9780123958419.

[2] Adler, P. and Thovert, J. (1999). Fractures and Fracture Networks. Theory and Applications of Transport in Porous Media. Springer. ISBN 9780792356479.

[3] Alboin, C., Jaffré, J., Roberts, J., and Serres, C. (1999). Domain Decomposition for Flow in Porous Media with Fractures. In Lai, C., Bjorstad, P., Cross, M., and Widlund, O. (editors), *Domain Decomposition Methods in Sciences and Engineering*, pages 365–373. Domain Decomposition Press, Bergen, Norway.

[4] Alboin, C., Jaffré, J., Roberts, J. E., and Serres, C. (2002). Modeling Fractures as Interfaces for Flow and Transport. In Chen, Z. and Ewing, R. (editors), *Fluid Flow and Transport in Porous Media: Mathematical and Numerical Treatment (South Hadley, MA, 2001)*, volume 295 of *Contemp. Math.*, pages 13–24. Amer. Math. Soc., Providence, RI USA. ISBN 9780821828076.

[5] Angot, P., Boyer, F., and Hubert, F. (2009). Asymptotic and numerical modelling of flows in fractured porous media. *ESAIM: Mathematical Modelling and Numerical Analysis 23*, 239–275.

[6] Arbogast, T. and Taicher, A. L. (2016). A Linear Degenerate Elliptic Equation Arising from Two-Phase Mixtures. *SIAM Journal on Numerical Analysis 54*(5), 3105–3122.

[7] Arnold, D. N. and Falk, R. S. (1988). A new mixed formulation for elasticity. *Numerische Mathematik 53*(1-2), 13–30.

[8] Arnold, D. N., Falk, R. S., and Winther, R. (2006). Differential complexes and stability of finite element methods II: The elasticity complex. *IMA Volumes in Mathematics and its Applications 142*, 47.

[9] Arnold, D. N., Falk, R. S., and Winther, R. (2006). Finite element exterior calculus, homological techniques, and applications. *Acta Numerica 15*, 1–155.

[10] Arnold, D. N. and Winther, R. (2002). Mixed finite elements for elasticity. *Numerische Mathematik 92*(3), 401–419.

[11] Biot, M. A. (1941). General theory of three-dimensional consolidation. *Journal of applied physics 12*(2), 155–164.

[12] Bjørnarå, T. I., Nordbotten, J. M., and Park, J. (2016). Vertically integrated models for coupled two-phase flow and geomechanics in porous media. *Water Resources Research 52*(2), 1398–1417.

[13] Boffi, D., Fortin, M., and Brezzi, F. (2013). Mixed finite element methods and applications. Springer series in computational mathematics. Springer, Berlin, Heidelberg. ISBN 978-3-642-36518-8.

[14] Bott, R. and Tu, L. W. (2013). Differential forms in algebraic topology, volume 82. Springer Science & Business Media.

[15] Brezzi, F., Douglas, J., and Marini, L. D. (1985). Two families of mixed finite elements for second order elliptic problems. *Numerische Mathematik 47*(2), 217–235.

[16] Brezzi, F., Fortin, M., and Marini, L. (2006). Error analysis of piecewise constant pressure approximations of Darcy's law. *Computer methods in applied mechanics and engineering 195*(13), 1547–1559.

[17] Buffa, A. and Christiansen, S. (2003). The electric field integral equation on Lipschitz screens: definitions and numerical approximation. *Numerische Mathematik 94*(2), 229–267.

[18] Caillerie, D. and Nedelec, J. (1980). The effect of a thin inclusion of high rigidity in an elastic body. *Mathematical Methods in the Applied Sciences 2*(3), 251–270.

[19] Cardenas, M. B. (2009). Stream-aquifer interactions and hyporheic exchange in gaining and losing sinuous streams. *Water Resources Research 45*(6), n/a–n/a. doi: 10.1029/2008WR007651. W06429.

[20] Cheney, W. (2013). Analysis for Applied Mathematics. Graduate Texts in Mathematics. Springer New York. ISBN 9781475735598.

[21] Ciarlet, P. G. (1997). Mathematical Elasticity Volume II: Theory of Plates. Elsevier, Amsterdam.

[22] Class, H., Ebigbo, A., Helmig, R., Dahle, H. K., Nordbotten, J. M., Celia, M. A., Audigane, P., Darcis, M., Ennis-King, J., Fan, Y., et al. (2009). A benchmark study on problems related to CO2 storage in geologic formations. *Computational Geosciences 13*(4), 409.

[23] D'Angelo, C. and Scotti, A. (2011). A mixed finite element method for Darcy flow in fractured porous media with non-matching grids. *ESAIM: Mathematical Modelling and Numerical Analysis 46*(2), 465–489.

[24] Dietrich, P., Helmig, R., Sauter, M., Hötzl, H., Köngeter, J., and Teutsch, G. (2005). Flow and Transport in Fractured Porous Media. Springer-Verlag Berlin Heidelberg. ISBN 9783540232704.

[25] Evans, L. (1998). Partial Differential Equations. Orient Longman. ISBN 9780821848593.

[26] Fjar, E., Holt, R. M., Raaen, A., Risnes, R., and Horsrud, P. (2008). Petroleum related rock mechanics, volume 53. Elsevier.

[27] Formaggia, L., Fumagalli, A., Scotti, A., and Ruffo, P. (2014). A reduced model for Darcy's problem in networks of fractures. *ESAIM: Mathematical Modelling and Numerical Analysis 48*(4), 1089–1116. doi: 10.1051/m2an/2013132.

[28] Frih, N., Martin, V., Roberts, J., and Saâda, A. (2012). Modeling fractures as interfaces with nonmatching grids. *Computational Geosciences 16*(4), 1043–1060. doi: 10.1007/s10596-012-9302-6.

[29] Fumagalli, A. and Scotti, A. (2014). An Efficient XFEM Approximation of Darcy Flows in Arbitrarily Fractured Porous Media. *Oil Gas Sci. Technol. âĂŞ Rev. IFP Energies nouvelles 69*(4), 555–564. doi: 10.2516/ogst/2013192.

[30] Gasda, S., Nordbotten, J., and Celia, M. (2011). Vertically averaged approaches for CO2 migration with solubility trapping. *Water Resources Research 47*(5).

[31] Gaspar, F., Lisbona, F., and Vabishchevich, P. (2003). A finite difference analysis of Biot's consolidation model. *Applied numerical mathematics 44*(4), 487–506.

[32] Grossmann, C., Roos, H., and Stynes, M. (2007). Numerical Treatment of Partial Differential Equations. Universitext. Springer Berlin Heidelberg. ISBN 9783540715849.

[33] Haberman, R. (2004). Applied Partial Differential Equations: With Fourier Series and Boundary Value Problems. Pearson Prentice Hall. ISBN 9780130652430.

[34] Holzapfel, G. (2000). Nonlinear Solid Mechanics: A Continuum Approach for Engineering. Wiley. ISBN 9780471823193.

[35] Jaeger, J. C., Cook, N. G., and Zimmerman, R. (2009). Fundamentals of rock mechanics. John Wiley & Sons.

[36] Lee, J. J. (2016). Robust error analysis of coupled mixed methods for Biot's consolidation model. *Journal of Scientific Computing 69*(2), 610–632.

[37] Lewis, R. W. and Schrefler, B. A. (1998). The finite element method in the static and dynamic deformation and consolidation of porous media. John Wiley.

[38] Li, L., Lee, S. H., et al. (2006). Efficient field-scale simulation for black oil in a naturally fractured reservoir via discrete fracture networks and homogenized media. In *International Oil & Gas Conference and Exhibition in China*. Society of Petroleum Engineers.

[39] Licht, M. W. (2016). Complexes of discrete distributional differential forms and their homology theory. *Foundations of Computational Mathematics* doi: 10.1007/s10208-016-9315-y.

[40] Martin, V., Jaffré, J., and Roberts, J. E. (2005). Modeling Fractures and Barriers As Interfaces for Flow in Porous Media. *SIAM J. Sci. Comput. 26*(5), 1667–1691. doi: 10.1137/S1064827503429363.

[41] Nédélec, J.-C. (1980). Mixed finite elements in $\mathbb{R}^3$. *Numerische Mathematik 35*(3), 315–341. doi: 10.1007/BF01396415.

[42] Nédélec, J.-C. (1986). A new family of mixed finite elements in R3. *Numerische Mathematik 50*(1), 57–81.

[43] Nordbotten, J. and Celia, M. (2011). Geological Storage of CO2: Modeling Approaches for Large-Scale Simulation. Wiley. ISBN 9781118137079.

[44] Raviart, P. and Thomas, J. (1977). A mixed finite element method for 2-nd order elliptic problems. In Galligani, I. and Magenes, E. (editors), *Mathematical Aspects of Finite Element Methods*, volume 606 of *Lecture Notes in Mathematics*, pages 292–315. Springer Berlin Heidelberg. ISBN 978-3-540-08432-7. doi: 10.1007/BFb0064470.

[45] Rodrigo, C., Gaspar, F., Hu, X., and Zikatanov, L. (2016). Stability and monotonicity for some discretizations of the Biot's consolidation model. *Computer Methods in Applied Mechanics and Engineering 298*, 183–204.

[46] Sandve, T. H., Berre, I., and Nordbotten, J. M. (2012). An Efficient Multi-point Flux Approximation Method for Discrete Fracture-Matrix Simulations. *J. Comput. Phys. 231*(9), 3784–3800. doi: 10.1016/j.jcp.2012.01.023.

[47] Short, D., Dawes, W. R., and White, I. (1995). The practicability of using Richards' equation for general purpose soil-water dynamics models. *Environment International 21*(5), 723–730.

[48] Spivak, M. (1965). Calculus on Manifolds. Addison-Wesley, Reading, Massachusetts.

[49] Stefansson, I. (2016). A Comparison of Two Numerical Models for Flow in Fractured Porous Media and the Impact of Fracture Intersection Cell Removal. Master's thesis, The University of Bergen.

[50] Tunc, X., Faille, I., Gallouët, T., Cacas, M., and Havé, P. (2012). A model for conductive faults with non-matching grids. *Computational Geosciences 16*(2), 277–296. doi: 10.1007/s10596-011-9267-x.

[51] Wheeler, M. F. and Yotov, I. (2006). A Multipoint Flux Mixed Finite Element Method. *SIAM J. Numer. Anal. 44*(5), 2082–2106. doi: 10.1137/050638473.

[52] Whitaker, S. (1986). Flow in porous media I: A theoretical derivation of Darcy's law. *Transport in porous media 1*(1), 3–25.

Notation

In Part I of this thesis, we use a consistent notation as much as possible. This appendix provides a short summary of the most common conventions with respect to accents as well as two tables describing the meaning of different letters and symbols.

Super- and subscripts are commonly employed in the mixed-dimensional setting. We use a superscript d to denote dimensionality and a subscript i to indicate the index of a manifold. A subscript zero on a function space denotes that the functions have zero normal trace. The subscript h refers to the discretized version of the object, usually a function or function space.

In terms of accents, we use the hat and check notation to distinguish variables within a manifold and the traces of variables from one dimension higher. A tilde on a function implies that it is a test function whereas a dot is used to represent the derivative in time. In case of the water table evolution problem, the tilde notation on a domain refers to the reference domain after coordinate transformation.

Bold script implies that the variable is vector-valued. Two tables of commonly used letters and symbols follow below.

Table of Notation: Symbols and Greek Letters

Symbol	Description
α	Biot-Willis constant
γ	Aperture
Γ	Interface
∂	Boundary
ϵ	Scaling parameter depending on γ
ε	Strain
ζ	Height of the water table
λ	Lamé parameter
Λ^k	Space of differential k-forms
μ	Lamé parameter
σ	Elastic Stress
σ_p	Poroelastic Stress
Ω	Subdomain or manifold
∇	Del operator

Table of Notation: Latin Letters

Symbol	Description
a	Bilinear form
A	Inverse stress-strain relationship
b	Bilinear form
C	A positive constant
d	Dimensionality of manifold
d	Exterior derivative
$\mathfrak{d}$	Mixed-dimensional exterior derivative
$\mathbb{d}$	Jump operator
$\mathfrak{D}$	Mixed-dimensional analogue of ∇
f	Source function, bold for vector-valued functions
g	Boundary data
h	Typical mesh size
	As subscript: discrete analogue
H	Sobolev space equipped with an L^2-norm
i, j, k	Counting indices
K	Tangential permeability
K_n	Normal permeability
$\mathbb{K}$	Vector space of dimension $d(d-1)/2$
$\mathfrak{K}$	Mixed-dimensional permeability
L^2	Function space of square-integrable functions
$\mathfrak{Q}^k$	Space of mixed-dimensional differential k-forms
m	Mass
n	Dimensionality of surrounding medium
$\boldsymbol{n}$	Normal vector
p	Pressure
p_H	Hydraulic head
P_r	Polynomial approximation of degree r
$\boldsymbol{q}$	Flux
r	Rotation
$\mathbb{R}$	Space of real numbers
S_0	Storativity
t	Time
T	End time
$\boldsymbol{u}$	Displacement
$\mathbb{V}$	Space of d-vectors

Part II

Scientific Results

Paper A

Robust Discretization of Flow in Fractured Porous Media

W.M. Boon, J.M. Nordbotten, I. Yotov

SIAM Journal of Numerical Analysis. In review.

arXiv:1601.06977 [math.NA]

ROBUST DISCRETIZATION OF FLOW IN FRACTURED POROUS MEDIA

WIETSE M. BOON[†], JAN M. NORDBOTTEN[†‡], AND IVAN YOTOV [§]

Abstract. Flow in fractured porous media represents a challenge for discretization methods due to the disparate scales and complex geometry. Herein we propose a new discretization, based on the mixed finite element method and mortar methods. Our formulation is novel in that it employs the normal fluxes as the mortar variable within the mixed finite element framework, resulting in a formulation that couples the flow in the fractures with the surrounding domain with a strong notion of mass conservation. The proposed discretization handles complex, non-matching grids, and allows for fracture intersections and termination in a natural way, as well as spatially varying apertures. The discretization is applicable to both two and three spatial dimensions. A priori analysis shows the method to be optimally convergent with respect to the chosen mixed finite element spaces, which is sustained by numerical examples.

Key words. mixed finite element, mortar finite element, fracture flow

1. Introduction. Fractures are ubiquitous in natural rocks, and in many cases have a leading order impact on the structure of fluid flow [1, 12]. Due to great differences in permeability, the fractures may either conduct the flow or act as blocking features. Due to their significant impact, detailed and robust modeling of coupled flow between fractures and a permeable rock is essential in applications spanning from enhanced geothermal systems, to CO_2 storage and petroleum extraction.

Because of the complex structure of natural fracture networks [12], it remains a challenge to provide robust and flexible discretization methods. Here, we identify a few distinct features which are attractive from the perspective of applications. The method formulated in this work is specifically designed to meet these goals.

First, we emphasize the importance of mass conservative discretizations. This is of particular significance when the flow field is coupled to transport (of e.g. heat or composition), as transport schemes are typically very sensitive to non-conservative flow fields [22]. The second property of interest is grid flexibility. This is important both in order to accommodate the structure of the fracture network, but also in order to honor other properties of the problem, such as material heterogeneities or anthropogenic features such as wells [24]. Third, it is necessary that discretization methods are robust in the physically relevant limits. In the case of fractures, it is imperative to allow for arbitrarily large aspect ratios, that is to say, thin fractures with arbitrarily small apertures, including the aperture going to zero as fractures terminate. Finally, our interest is in provably stable and convergent methods.

Since their aspect ratios frequently range as high as 100-1000, it is appealing to consider fractures as lower-dimensional features, as was first explored in [2, 3]. In this setting, we consider a three-dimensional domain of permeable rock, within which (multiple) fractures will be represented by (multiple) two-dimensional manifolds. In the case where two or more fractures intersect, we will naturally also be interested in the intersection lines and points. Our approach handles such manifolds, lines, and points in a unified manner.

[†]Department of Mathematics, University of Bergen, Postbox 7803, 5020 Bergen, Norway (wietse.boon@uib.no, jan.nordbotten@uib.no) This work was supported in part by Norwegian Research Council grants 233736 and 228832.

[‡]Department of Civil and Environmental Engineering, Princeton University, Princeton, NJ 08544, USA.

[§]Department of Mathematics, University of Pittsburgh, Pittsburgh, PA, USA.

Several methods have been proposed to discretize fractured porous media, some of which are reviewed below. However, to our knowledge, no method has been presented which fulfills the four design goals outlined above.

A natural discretization approach to obtain conservative discretizations is to consider finite volume methods adapted to fracture networks (see e.g. [21, 31]). Here, the fractures are added as hybrid cells between the matrix cells. The small cells which are formed at the intersections are then excluded with the use of transformations in order to save condition numbers and computational cost. However, the formulation requires the grids to match along the fractures. The incorporation of non-matching grids along faults was analyzed by Tunc et al. [33]. While the presented finite volume formulations are formally consistent methods, convergence analyses of these methods are lacking.

Alternatively, the extended finite element (XFEM) approach [11, 15, 32] is a method in which the surroundings are meshed independently from the fractures. The fracture meshes are then added afterwards, crossing through the domain and cutting the elements. Although this may be attractive from a meshing perspective, the cut elements may become arbitrarily small such that special constructions are needed to ensure stability. Such constructions are typically introduced whenever multiple fractures, intersections, and fracture endings are considered in the model. Our aim is to develop a method with a unified approach to such features and a different approach is therefore chosen. Admittedly, the construction of meshes will be more involved for complicated cases but we aim to relieve this by allowing for non-matching grids.

The Mixed Finite Element (MFE) method [9, 10] is employed in this work, since it provides two important advantages. The method defines the flux as a separate variable and mass conservation can therefore be imposed locally. Furthermore, the tools necessary to perform rigorous analysis can be adapted from those available in the literature.

Mortar methods, as introduced in [8], form an appealing framework for fracture modeling, since both non-matching grids and intersections are naturally handled. The combination with MFE has since been explored extensively (see e.g. [5, 28]). The idea of conductive fractures was first exploited in [16, 25], where Darcy flow is allowed inside the mortar space based on the pressure variable. However, in previously developed mortar MFE methods, the choice of using the pressure variable in the mortar space does not allow for strong flux continuity.

Herein we propose a new method, based on the structure of mortar MFE methods. Our formulation is novel in that it employs the fluxes as the mortar variable within the mixed finite element framework. Thus, the proposed method couples the flow in fractures with the surrounding domain using a stronger notion of mass conservation. For domain decomposition with matching grids, flux Lagrange multiplier for MFE methods was proposed in [20]. To the best of our knowledge, this technique has not been explored in the context of mortar MFE methods on non-matching grids. The method is designed with the four goals outlined above in mind.

We formulate the method hierarchically, which allows for a unified treatment of the permeable domain, the fractures, intersection lines, and intersection points in arbitrary dimensions. We show through rigorous analysis that the method is robust with respect to the aspect ratio, however we exclude the case of degenerate normal permeability from our analysis. The numerical results verify all the analytical results, and furthermore indicate stability also in the case of degenerate normal permeability.

The paper is organized as follows. Section 2 introduces the model in a continuous

setting and explains the concept of composite function spaces formed by function spaces with different dimensions. Section 3 is devoted to the discretized problem and the analytical proofs of properties such as stability and convergence. Finally, results of numerical experiments confirming the theory in two and three dimensions are presented in Section 4. We point out that a full numerical comparison to the alternative discretization methods discussed above has been conducted separately as part of a benchmark study [14].

2. Model Formulation. In this section, we first describe the notion of working with subdomains with different dimensions and introduce the notation used in this paper. Next, the governing equations for the continuous problem are derived and presented. The section is concluded with the derivation of the weak formulation of the problem.

2.1. Geometric Representation. Consider an n-dimensional domain Ω, which is decomposed into subdomains with different dimensionalities. Setting the ambient dimension of the problem n equal to 2 or 3 will suffice for most practical purposes, but the theory allows for n to be arbitrary. The subdomains of dimension $n-1$ then represent fractures, while the lower-dimensional domains represent intersection lines and points.

We start by establishing notation. Let N^d denote the total number of d-dimensional subdomains and let each open, d-dimensional subdomain be denoted by Ω_i^d with $0 \leq d \leq n$ and counting index $i \in \{1, 2, \dots N^d\}$. For notational simplicity, the union of all d-dimensional subdomains is denoted by Ω^d:

$$\Omega^d = \bigcup_{i=1}^{N^d} \Omega_i^d.$$

A key concept in the decomposition is that all intersections of d-dimensional subdomains are considered as $(d-1)$-dimensional domains. In turn, the domain Ω^{d-1} is excluded from Ω^d. For example, the point at the intersection between two lines becomes a new, lower-dimensional subdomain Ω^0 which is removed from Ω^1. An illustration of the decomposition in two dimensions is given in Figure 1 (Left). The procedural decomposition by dimension applies equally well to problems in three dimensions.

Physically, the flow between domains of different dimension (e.g. between fracture and matrix) is of particular interest. We are thus careful with the interfaces between subdomains of successive dimension. For each subdomain Ω_i^d with $d \leq n-1$, we define $\mathcal{J}_i^d$ as a set of local counting indices which enumerates its adjacent d-interfaces. In turn, each interface is denoted by Γ_{ij}^d with $j \in \mathcal{J}_i^d$. Analogous to the notation as employed above, we define the following geometric entities as

$$\Gamma_i^d = \bigcup_{j \in \mathcal{J}_i^d} \Gamma_{ij}^d, \qquad \Gamma^d = \bigcup_{i=1}^{N^d} \Gamma_i^d, \qquad \Gamma = \bigcup_{d=0}^{n-1} \Gamma^d.$$

The interface Γ_i^d coincides spatially with Ω_i^d, but its importance lies in being a subset of the boundary of the adjacent $(d+1)$-dimensional domains. An illustration of Γ^1 in a two-dimensional setting is given in Figure 1 (Right).

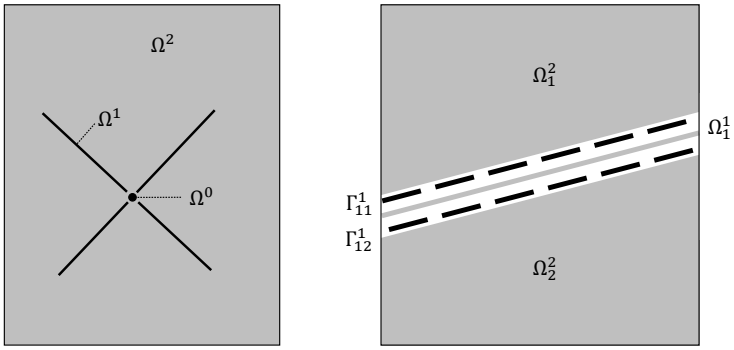

FIGURE 1. *(Left) The domain is decomposed into subdomains where the dimensionality of each subdomain is given by the superscript. This decomposition allows us to model fractures and intersections as lower-dimensional features in the domain. In this particular illustration, we have four fracture segments, thus* $N^1 = 4$. *(Right) The interface* Γ^1 *in case of a single fracture. We define* Γ *as the union of interfaces between domains of codimension one.*

At this point, we have the necessary entities to introduce the dimensional decomposition of the domain Ω and its boundary:

$$\Omega \cup \partial\Omega = \left(\bigcup_{d=0}^{n} \Omega^d \right) \cup \left(\bigcup_{d=1}^{n} \partial\Omega^d \backslash \Gamma^{d-1} \right). \tag{2.1}$$

Let $\boldsymbol{\nu}$ denote the outward unit normal to Ω^d, defined on $\partial\Omega^d$. By definition, $\boldsymbol{\nu}$ on Γ^d is thus directed from Ω^{d+1} to Ω^d, i.e. towards the lower-dimensional subdomain.

The boundary of the model domain will enter naturally with the governing equations below. We emphasize that domains of any dimension may contact the domain boundary. Also, the case of subdomains with codimension two will not be considered in this work (e.g. line wells in 3D or two planar fractures meeting at a point). Nevertheless, it is possible to fit those cases into this framework by introducing specifically constructed subdomains of intermediate dimension.

As a minor comment we note that the geometric representation, as well as much of the analysis below, can be generalized to calculus on manifolds. However, while the framework of manifolds does increase the mathematical elegance, and in some places simplifies and makes the exposition more precise, we believe that the current presentation is accessible to a wider readership. As an immediate consequence of this choice, we will from here on assume that all domains Ω_i^d are flat.

2.2. Governing equations. The model considered in this work is governed by two physical relationships, namely mass conservation and Darcy's law. In particular, it is assumed that Darcy's law holds not just in the porous material, but also in all lower-dimensional subdomains. This corresponds to the physical situation of either thin open fractures (Poiseulle flow), or fractures filled with some material. The mathematical representations of these relationships have been well established and employed by several models [4, 5, 11, 16]. Here, we will introduce these relationships within

the dimensional decomposition framework. Starting with the governing equations in the surrounding regions, we then continue with their analogues in lower-dimensional subdomains and finish with the coupling equations.

First, let us consider the surroundings Ω^n. We aim to find the flux $\boldsymbol{u}^n$ and pressure p^n satisfying

$$\boldsymbol{u}^n = -K\nabla p^n \qquad \text{in } \Omega^n, \tag{2.2a}$$

$$\nabla \cdot \boldsymbol{u}^n = f \qquad \text{in } \Omega^n, \tag{2.2b}$$

$$p^n = g \qquad \text{on } \partial\Omega_D^n, \tag{2.2c}$$

$$\boldsymbol{u}^n \cdot \boldsymbol{\nu} = 0 \qquad \text{on } \partial\Omega_N^n. \tag{2.2d}$$

Here, we assume that the boundary of Ω can be parititioned as $\partial\Omega = \partial\Omega_D \cup \partial\Omega_N$, with $\partial\Omega_D \cap \partial\Omega_N = \emptyset$ and $\partial\Omega_D$ with positive measure. We assume that each subdomain Ω_i^n of Ω^n has a non-empty Dirichlet boundary, i.e. $|\partial\Omega_i^n \cap \partial\Omega_D| > 0$. The following notation is then employed within the dimensional decomposition framework:

$$\partial\Omega_D^d = \partial\Omega^d \cap \partial\Omega_D, \qquad \partial\Omega_N^d = \partial\Omega^d \cap \partial\Omega_N, \qquad 1 \le d \le n.$$

Furthermore, K is a bounded, symmetric, positive definite, $n \times n$ tensor representing the material permeability. Equation (2.2a) is known as Darcy's law and equation (2.2b) is conservation of mass in the case of incompressible fluids.

We continue with the governing equations defined on the lower-dimensional subdomains. In order to derive these equations with the correct scaling, two physical parameters are introduced, inherent to the geometry of the problem. First, on each Γ_{ij}^d, $0 \le d \le n-1$, let γ_{ij}^d denote the length from Γ_{ij}^d to the center of Ω_i^d. For brevity, we will generally omit the indices on γ and all other parameters

Secondly, on each subdomain Ω_i^d with $0 \le d \le n-1$, let ϵ represent the square root of the cross-sectional length if $d = n-1$, area if $d = n-2$, or volume if $d = n-3$. Ergo, ϵ scales as $\gamma^{\frac{n-d}{2}}$ by definition. We assume that both ϵ and γ are bounded and known a priori and extended to the surroundings by setting $\epsilon = \gamma = 1$ in Ω^n.

In general, we allow ϵ and γ to vary spatially. As such, we are particularly interested in the case of closing fractures, i.e. where ϵ and γ decrease to zero. Regarding the rate at which this is possible, we assume that the following holds almost everywhere in the sense of the Lebesgue measure:

$$|\nabla \epsilon| \lesssim \epsilon^{\frac{1}{2}}, \tag{2.3}$$

with $|\cdot|$ denoting the Euclidean norm.

Here, and onwards, the notation $a \lesssim b$ is used to imply that a constant $C > 0$ exists, independent of ϵ, γ, and later h such that $a \le Cb$. The relations $\gtrsim$ and $\eqsim$ have analogous meaning.

The hat-notation $\hat{\epsilon}$ is used to denote the trace of ϵ onto Γ_{ij}^d from one level higher, i.e. ϵ defined on Ω^{d+1}:

$$\hat{\epsilon}_{ij}^d := \epsilon_j^{d+1}|_{\Gamma_{ij}^d}, \qquad j \in \mathcal{J}_i^d, \qquad d \le n-1.$$

We set $\hat{\epsilon} = 1$ in Ω^n. Due to the construction of the dimensional decomposition, we assume that Ω_i^d borders on a subdomain Ω_j^{d+1} with positive aperture for at least one index $j_{\max} \in \mathcal{J}_i^d$. The parameter $\hat{\epsilon}$ corresponding to this index is referred to as follows

$$\hat{\epsilon}_{\max}(x) := \hat{\epsilon}_{i,j_{\max}}^d(x) > 0, \qquad x \in \Omega_i^d, \qquad 0 \le d \le n-1. \tag{2.4}$$

The relationship between ϵ and $\hat{\epsilon}_{\max}$ is then assumed to satisfy

$$\|\epsilon^{\frac{1}{2}}\|_{L^\infty(\Omega_i^d)}\|\hat{\epsilon}_{\max}^{-1}\|_{L^\infty(\Omega_i^d)} \lesssim 1, \qquad 1 \leq d \leq n. \tag{2.5}$$

To justify this property, we derive for $d \geq 1$ and $n \leq 3$ that

$$\hat{\epsilon}_{\max}^{-1}\epsilon^{\frac{1}{2}} \eqsim \hat{\gamma}^{-\frac{n-(d+1)}{2}}\gamma^{\frac{n-d}{4}} \lesssim \gamma^{-\frac{n-d}{4}+\frac{1}{2}} \lesssim \gamma^0 = 1.$$

Since this relationship will later be used for the fluxes in Ω^d, (2.5) is not necessarily imposed for $d = 0$.

With the defined ϵ, the scaled flux $\boldsymbol{u}^d$, $1 \leq d \leq n$, is introduced such that

$$\boldsymbol{u}^d := \epsilon\tilde{\boldsymbol{u}}^d, \tag{2.6}$$

with $\tilde{\boldsymbol{u}}^d$ as the average, tangential flux in Ω^d. In other words, $\boldsymbol{u}^d$ can be described as an intermediate definition between the average flux $\tilde{\boldsymbol{u}}^d$ and the integrated flux (given by $\epsilon\boldsymbol{u}^d$). It is reminiscent of the scaled flux presented in [6].

In order to derive the conservation equation on a lower-dimensional surface, the fluxes entering through the boundary Γ^d must be accounted for [27]. Let λ^d, $0 \leq d \leq n-1$, denote $\boldsymbol{u}^{d+1} \cdot \boldsymbol{\nu}$ on Γ^d. Here $\boldsymbol{\nu}$ is the normal vector associated with Γ^d as defined in Subsection 2.1.

Mass may enter the fracture from one side and continue tangentially through the fracture creating a (pointwise) difference in normal fluxes. To capture this jump, λ^d will consist of multiple components λ_{ij}^d, each representing a scaled flux across Γ_{ij}^d.

Recall the set $\mathcal{J}_i^d$ of local indices at Ω_i^d as defined in Subsection 2.1. The jump operator is then given by

$$[\![\cdot]\!] : L^2(\Gamma^d) \to L^2(\Omega^d), \qquad [\![\lambda]\!]|_{\Omega_i^d} = -\sum_{j\in\mathcal{J}_i^d}\lambda_{ij}^d, \qquad 0 \leq d \leq n-1. \tag{2.7}$$

The definitions introduced in this section allow us to deduce the mass conservation equation for the lower-dimensional domains. Let us consider Ω^1 with $n = 2$ and integrate the mass conservation equation (2.2b) over a quadrilateral region ω illustrated in Figure 2.

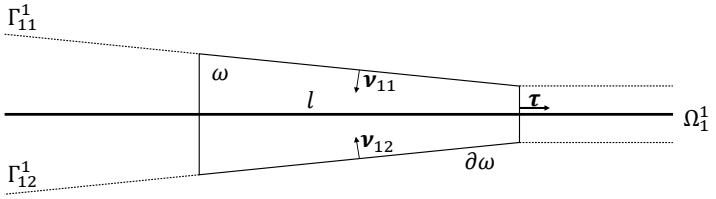

FIGURE 2. *Local geometry for derivation of the conservation law.* Ω^1 *represents the reduced, lower-dimensional manifold whereas the boundary between the fracture and matrix is given by* Γ.

We apply the divergence theorem on ω to derive

$$\int_\omega \nabla\cdot\boldsymbol{u} = \int_{\partial\omega_r}\boldsymbol{u}\cdot\boldsymbol{\tau} - \int_{\partial\omega_l}\boldsymbol{u}\cdot\boldsymbol{\tau} - \int_{\partial\omega\cap\Gamma}\boldsymbol{u}\cdot\boldsymbol{\nu}. \tag{2.8}$$

Next, we let the width of ω, given by l, decrease to zero. The definition of the scaled fluxes from (2.6) and the factor $\hat{\epsilon} = 1$ gives us

$$\begin{aligned} \lim_{l\to 0} l^{-1} \int_{\omega} \nabla \cdot \boldsymbol{u} &= \nabla_\tau \cdot \epsilon \boldsymbol{u}^1 + [\![\big(1 + \big|\nabla_\tau \frac{\gamma}{2}\big|^2\big)^{\frac{1}{2}} \hat{\epsilon} \boldsymbol{u}^2 \cdot \boldsymbol{\nu}]\!] \\ &= \nabla_\tau \cdot \epsilon \boldsymbol{u}^1 + [\![\big(1 + \big|\nabla_\tau \frac{\gamma}{2}\big|^2\big)^{\frac{1}{2}} \hat{\epsilon} \lambda^1]\!], \end{aligned} \tag{2.9}$$

with ∇_τ the nabla operator tangential to Ω^1. Note that the term $\big(1 + \big|\nabla_\tau \frac{\gamma}{2}\big|^2\big)^{\frac{1}{2}}$ is close to unity since the changes in aperture are small by (2.3). We will therefore omit this factor for simplicity of exposition, while understanding that it can be subsumed into the definition of $\hat{\epsilon}$ at no additional theoretical complexity, and thus state the resulting conservation law as

$$\nabla \cdot \epsilon \boldsymbol{u}^d + [\![\hat{\epsilon} \lambda^d]\!] = \epsilon^2 f^d \qquad \text{in } \Omega^d,\ 1 \le d \le n-1. \tag{2.10}$$

Here, f^d represents the averaged source terms within Ω^d. From here on, we denote ∇ as the d-dimensional vector differential operator in Ω^d. The case $d = 0$ deserves additional attention since there is no tangential direction in which flow is possible. In turn, the mass conservation equation is reduced to

$$[\![\hat{\epsilon} \lambda^0]\!] = \epsilon^2 f^0 \qquad \text{in } \Omega^0. \tag{2.11}$$

Equation (2.10) is simplified by introducing the semi-discrete differential operator D:

$$D \cdot [\boldsymbol{u}^d, \lambda^d] := \nabla \cdot \boldsymbol{u}^d + [\![\lambda^d]\!]. \tag{2.12}$$

Continuing with the constitutive relationships, we consider Darcy's law in lower dimensions as described by the following linear expression:

$$\epsilon^{-1} \boldsymbol{u}^d = -K \nabla p^d \qquad \text{in } \Omega^d,\ 1 \le d \le n-1. \tag{2.13}$$

Note that we abuse notation once more by defining the permeability K as a $d \times d$ tensor when used in Ω^d.

The required boundary conditions for the lower-dimensional problems are chosen in the following way. First, the fracture may cross the domain and end on the boundary $\partial\Omega$. In that case, the imposed boundary condition in Ω^d is chosen to coincide with the boundary condition defined for the corresponding portion of $\partial\Omega$. In other words, if the fracture ends on $\partial\Omega_N$, a no-flux condition is imposed. On the other hand, if it ends on $\partial\Omega_D$, the pressure value is set to the average of g across the cross section of Ω^d, which we denote by g^d.

$$\begin{aligned} p^d &= g^d && \text{on } \partial\Omega_D^d, \\ \boldsymbol{u}^d \cdot \boldsymbol{\nu} &= 0 && \text{on } \partial\Omega_N^d, \qquad 1 \le d \le n-1. \end{aligned}$$

The remainder of $\partial\Omega^d$ either borders on a lower-dimensional domain or represents an immersed tip. In the former case, a flux boundary condition is imposed on Γ^{d-1} using the previously defined variable λ^{d-1}. In case of immersed tips, we assume that the mass transfer through the tip is negligible due to the large ratio between the fracture

aperture and length. Therefore, in accordance with [4], a no-flux boundary condition is imposed. The boundary conditions are summarized as

$$\begin{aligned} \boldsymbol{u}^d \cdot \boldsymbol{\nu} &= \lambda^{d-1} && \text{on } \Gamma^{d-1},\ 1 \le d \le n, \\ \boldsymbol{u}^d \cdot \boldsymbol{\nu} &= 0 && \text{on } \partial\Omega^d \backslash (\Gamma^{d-1} \cup \partial\Omega),\ 1 \le d \le n-1. \end{aligned}$$

We will also allow for $\epsilon \downarrow 0$ at fracture tips, leading to a degenerate equation wherein the boundary condition is mute.

Analogous to [4, 25], Darcy's law is assumed to describe the flow normal to the fracture. For this, we introduce the normal permeability K_ν^d in Ω^d and impose the following relationship between the scaled, normal flux λ^d and the pressure difference on Γ_{ij}^d:

$$\hat{\epsilon}^{-1}\lambda_{ij}^d = -K_\nu \frac{p_i^d - p^{d+1}|_{\Gamma_{ij}^d}}{\gamma}, \qquad 0 \le d \le n-1, \tag{2.14}$$

where we use the notation $p_i^d = p^d|_{\Omega_i^d}$. Moreover, sufficient regularity of p is assumed in order to take such traces.

The above represents the full description of the model equations considered herein, and is the setting in which the numerical method is constructed and validated. However, the analysis of both the continuous and discrete settings is restricted to the case where we have two further constants c_0 and c_1 such that the normal permeability is not degenerate in the following sense:

$$0 < c_0 \le \gamma K_\nu^{-1} \le c_1 < \infty, \tag{2.15}$$

similar to [25]. We note in particular that the lower bound is needed for the completeness of the solution space under the chosen norms, see Lemma 2.2.

The above equations comprise our model problem for flow in fractured porous media.

2.3. Weak Formulation. Let us continue by deriving the weak formulation of the problem. For this, we introduce the function spaces associated with the dimensional decomposition introduced in Subsection 2.1. For each value of d denoting the dimensionality, let the function space $\boldsymbol{V}^d$ contain the (tangential) flux, let Λ^d contain the flux across subdomain interfaces, and let Q^d contain the pressure. For the continuous weak formulation, we define these function spaces as

$$\begin{aligned} \boldsymbol{V}^d &= \left\{ \boldsymbol{v} \in (L^2(\Omega^d))^d : \nabla \cdot \epsilon\boldsymbol{v} \in L^2(\Omega^d),\ (\epsilon\boldsymbol{v} \cdot \boldsymbol{\nu})|_{\partial\Omega^d \backslash (\Gamma^{d-1} \cup \partial\Omega_D)} = 0 \right\}, && 1 \le d \le n, \\ \Lambda^d &= L^2(\Gamma^d), && 0 \le d \le n-1, \\ Q^d &= L^2(\Omega^d), && 0 \le d \le n. \end{aligned}$$

The key tool used to create a succinct method, is to create dimensionally structured function spaces by applying the direct sum over all different dimensionalities. Particularly, we define the composite function spaces

$$\mathscr{V} = \bigoplus_{d=1}^{n} \boldsymbol{V}^d, \qquad \mathit{\Lambda} = \bigoplus_{d=0}^{n-1} \Lambda^d, \qquad \mathscr{Q} = \bigoplus_{d=0}^{n} Q^d. \tag{2.16}$$

The dimensionally structured space $\mathit{\Lambda}$ will contain the normal flux across Γ and act as a mortar space. To avoid doubly defining the normal fluxes across Γ with

functions from $\mathscr{V}$ and Λ, a final function space is defined containing functions with zero normal flux across Γ:

$$\boldsymbol{V}_0^d = \left\{ \boldsymbol{v} \in \boldsymbol{V}^d : \epsilon \boldsymbol{v} \cdot \boldsymbol{\nu} = 0 \text{ on } \Gamma^{d-1} \right\}, \qquad 1 \leq d \leq n,$$

$$\mathscr{V}_0 = \bigoplus_{d=1}^{n} \boldsymbol{V}_0^d. \tag{2.17}$$

To rigorously impose the essential boundary condition on Γ, a linear extension operator $\mathcal{R}$ is introduced for functions belonging to Λ. The construction of this operator is done using the dimensional decomposition. For $0 \leq d \leq n-1$, let the operator $\mathcal{R}^d : \Lambda^d \to \boldsymbol{V}^{d+1}$ be defined such that

$$\mathcal{R}^d \lambda^d \cdot \boldsymbol{\nu} = \begin{cases} \lambda^d \text{ on } \Gamma^d \\ 0 \text{ on } \partial\Omega^{d+1} \backslash \Gamma^d, \end{cases} \tag{2.18}$$

in which $\boldsymbol{\nu}$ represents the unit normal vector associated with Γ^d. The image of $\mathcal{R}^d$ has slightly higher regularity than $H(\mathrm{div}; \Omega^{d+1})$ with normal trace in $L^2(\partial\Omega^{d+1})$. Now, let us define the operator $\mathcal{R} : \Lambda \to \mathscr{V}$ as

$$\mathcal{R}\lambda = \bigoplus_{d=0}^{n-1} \mathcal{R}^d \lambda^d.$$

At this point, some freedom remains in the choice of $\mathcal{R}$. Even though the resulting method is not affected by the eventual choice, a specific extension operator is constructed later in (2.24) which has favorable properties for the sake of the analysis.

Due to this construction, the flux will always be composed of a pair $(\boldsymbol{u}_0, \lambda)$ which gives rise to the space $\mathscr{X}$ given by

$$\mathscr{X} = \mathscr{V}_0 \times \Lambda. \tag{2.19}$$

With the appropriate function spaces and operators defined, we continue with the derivation of the weak form of the problem. The derivation is standard for all equations except for (2.14), which requires some additional attention. For a given Ω_i^d, $0 \leq d \leq n-1$, let us test (2.14) with a function $\mu^d \in \Lambda^d$. After summation over $j \in \mathcal{J}_i^d$, we obtain

$$\sum_{j \in \mathcal{J}_i^d} \langle \frac{\gamma}{K_\nu} \lambda_{ij}^d, \mu_{ij}^d \rangle_{\Gamma_{ij}^d} = \sum_{j \in \mathcal{J}_i^d} \langle p^{d+1}, \hat{\epsilon} \mu_{ij}^d \rangle_{\Gamma_{ij}^d} + (p_i^d, [\![\hat{\epsilon} \mu^d]\!])_{\Omega_i^d}, \tag{2.20}$$

where $\langle \cdot, \cdot \rangle_{\Gamma_{ij}^d}$ and $(\cdot, \cdot)_{\Omega_i^d}$ denote the L^2-inner products on Γ_{ij}^d and Ω_i^d, respectively. A useful aspect of this relationship is that the first term on the right-hand side is exactly the boundary term which appears in the weak form of Darcy's law (2.13) after partial integration. The notation is simplified by introducing the inner products and the associated norms in the dimensional decomposition framework:

$$(\cdot, \cdot)_\Omega = \sum_{d=0}^{n} (\cdot, \cdot)_{\Omega^d} = \sum_{d=0}^{n} \sum_{i=1}^{N^d} (\cdot, \cdot)_{\Omega_i^d}, \qquad \| \cdot \|_{L^2(\Omega)}^2 = \sum_{d=0}^{n} \| \cdot \|_{L^2(\Omega^d)}^2,$$

$$\langle \cdot, \cdot \rangle_\Gamma = \sum_{d=0}^{n-1} \langle \cdot, \cdot \rangle_{\Gamma^d} = \sum_{d=0}^{n-1} \sum_{i=1}^{N^d} \sum_{j \in \mathcal{J}_i^d} \langle \cdot, \cdot \rangle_{\Gamma_{ij}^d}, \qquad \| \cdot \|_{L^2(\Gamma)}^2 = \sum_{d=0}^{n-1} \| \cdot \|_{L^2(\Gamma^d)}^2.$$

We are now ready to state the variational form of the problem:

The weak solution $(\boldsymbol{u}_0, \lambda, p) \in \mathscr{V}_0 \times \Lambda \times \mathscr{Q}$ satisfies

$$(K^{-1}(\boldsymbol{u}_0 + \mathcal{R}\lambda), \boldsymbol{v}_0)_\Omega - (p, \nabla \cdot \epsilon \boldsymbol{v}_0)_\Omega = -\langle g, \epsilon \boldsymbol{v}_0 \cdot \boldsymbol{\nu} \rangle_{\partial\Omega_D} \qquad \forall \boldsymbol{v}_0 \in \mathscr{V}_0, \tag{2.21a}$$

$$(K^{-1}(\boldsymbol{u}_0 + \mathcal{R}\lambda), \mathcal{R}\mu)_\Omega - (p, \nabla \cdot \epsilon \mathcal{R}\mu)_\Omega$$

$$+\langle \frac{\gamma}{K_\nu}\lambda, \mu \rangle_\Gamma - (p, [\![\hat{\epsilon}\mu]\!])_\Omega = 0 \qquad \forall \mu \in \Lambda, \tag{2.21b}$$

$$-(\nabla \cdot \epsilon(\boldsymbol{u}_0 + \mathcal{R}\lambda), q)_\Omega - ([\![\hat{\epsilon}\lambda]\!], q)_\Omega = -(\epsilon^2 f, q)_\Omega \qquad \forall q \in \mathscr{Q}. \tag{2.21c}$$

We set all functions not defined for certain indexes (such as $\boldsymbol{u}_0^0$ and λ^n) to zero such that the unified presentation is well-defined. Equation (2.21a) follows from (2.2a) and (2.13), whereas equation (2.21b) follows additionally from (2.20). Finally, equation (2.21c) follows from equations (2.2b), (2.10) and (2.11). In the above, we assume that $g \in H^{\frac{1}{2}}(\partial\Omega_D)$ and $f \in L^2(\Omega)$ which guarantees that the right-hand side terms in (2.21a) and (2.21b) are well-posed. In particular, since $\epsilon \boldsymbol{v}_{\boldsymbol{0}}^d \in H(\mathrm{div}; \Omega^d)$ and $\epsilon \boldsymbol{v}_{\boldsymbol{0}}^d \cdot \boldsymbol{\nu} = 0$ on $\partial\Omega^d \backslash \partial\Omega_D^d$, then $\epsilon \boldsymbol{v}_{\boldsymbol{0}}^d \cdot \boldsymbol{\nu} \in H^{-\frac{1}{2}}(\partial\Omega_D^d)$, see e.g. [18].

We note that for fractures which have $\epsilon = \gamma = 0$ uniformly, this model reduces to a domain decomposition method which uses λ as a flux mortar to impose continuity of pressure in a weak sense.

The next step is to observe that the system (2.21) can be classified as a saddle point problem. For this purpose, we rewrite the problem into a different format by using the divergence operator D from (2.12) and the bilinear forms a and b given by

$$a(\boldsymbol{u}_0, \lambda;\ \boldsymbol{v}_0, \mu) = (K^{-1}(\boldsymbol{u}_0 + \mathcal{R}\lambda), \boldsymbol{v}_0 + \mathcal{R}\mu)_\Omega + \langle \frac{\gamma}{K_\nu}\lambda, \mu \rangle_\Gamma, \tag{2.22a}$$

$$b(\boldsymbol{v}_0, \mu;\ p) = -(p, D \cdot [\epsilon(\boldsymbol{v}_0 + \mathcal{R}\mu), \hat{\epsilon}\mu])_\Omega. \tag{2.22b}$$

These definitions allows us to rewrite system (2.21) to the following, equivalent problem:
Find the functions $(\boldsymbol{u}_0, \lambda, p) \in \mathscr{V}_0 \times \Lambda \times \mathscr{Q}$ such that

$$a(\boldsymbol{u}_0, \lambda;\ \boldsymbol{v}_0, \mu) + b(\boldsymbol{v}_0, \mu;\ p) - b(\boldsymbol{u}_0, \lambda;\ q) = -\langle g, \epsilon \boldsymbol{v}_0 \cdot \boldsymbol{\nu} \rangle_{\partial\Omega_D} + (\epsilon^2 f, q)_\Omega, \tag{2.23}$$

for all $(\boldsymbol{v}_0, \mu, q) \in \mathscr{V}_0 \times \Lambda \times \mathscr{Q}$.

2.4. Well-posedness. Before proceeding to the discretization, it is important to analyze the variational problem (2.23) in the continuous sense. To that end, we present a proof of the well-posedness of this problem within the dimensional hierarchy setting.

For the purpose of the analysis, let us introduce a specific extension operator $\mathcal{R} : \Lambda \to \mathscr{V}$. For $1 \leq d \leq n$, let $\mathcal{R}^{d-1}\lambda^{d-1} \in \boldsymbol{V}^d$ and an auxiliary variable $p_\lambda^d \in Q^d$ be defined as the solution to the following problem:

$$(K^{-1}\mathcal{R}^{d-1}\lambda^{d-1}, \boldsymbol{v}_0^d)_{\Omega^d} - (p_\lambda^d, \nabla \cdot \epsilon \boldsymbol{v}_0^d)_{\Omega^d} = 0 \qquad \forall \boldsymbol{v}_0^d \in \boldsymbol{V}_0^d, \tag{2.24a}$$

$$(\nabla \cdot \epsilon \mathcal{R}^{d-1}\lambda^{d-1}, q^d)_{\Omega^d} + (\epsilon p_\lambda^d, q^d)_{\Omega^d} = 0 \qquad \forall q^d \in Q^d, \tag{2.24b}$$

$$\mathcal{R}^{d-1}\lambda^{d-1} \cdot \boldsymbol{\nu} = \lambda^{d-1} \qquad \text{on } \Gamma^{d-1}, \tag{2.24c}$$

$$\mathcal{R}^{d-1}\lambda^{d-1} \cdot \boldsymbol{\nu} = 0 \qquad \text{on } \partial\Omega^d \backslash \Gamma^{d-1}. \tag{2.24d}$$

Note that the boundary conditions are chosen such that $\mathcal{R}^{d-1}\lambda^{d-1}$ is a suitable extension compliant with equation (2.18).

LEMMA 2.1. *The solution* $(\mathcal{R}^{d-1}\lambda^{d-1}, p_\lambda^d) \in \boldsymbol{V}^d \times Q^d$ *to problem* (2.24) *satisfies the following bounds:*

$$\|K^{-\frac{1}{2}}\mathcal{R}^{d-1}\lambda^{d-1}\|_{L^2(\Omega^d)} + \|\epsilon^{\frac{1}{2}}p_\lambda^d\|_{L^2(\Omega^d)} \lesssim \|\lambda^{d-1}\|_{L^2(\Gamma^{d-1})}, \tag{2.25a}$$

$$\|\nabla\cdot\epsilon\mathcal{R}^{d-1}\lambda^{d-1}\|_{L^2(\Omega^d)} \lesssim \|\epsilon_{\max}^{\frac{1}{2}}\lambda^{d-1}\|_{L^2(\Gamma^{d-1})}, \tag{2.25b}$$

where $\epsilon_{\max}|_{\Omega_i^d} = \|\epsilon\|_{L^\infty(\Omega_i^d)}$.

Proof. Let us introduce the function $\boldsymbol{v}_\lambda^d$ as the $H(\mathrm{div})$-extension of λ^{d-1} described in [29] (Section 4.1.2). In particular, $\boldsymbol{v}_\lambda^d\cdot\nu = \lambda^{d-1}$ and it satisfies the following bound:

$$\|\boldsymbol{v}_\lambda^d\|^2_{L^2(\Omega^d)} + \|\nabla\cdot\boldsymbol{v}_\lambda^d\|^2_{L^2(\Omega^d)} \lesssim \|\lambda^{d-1}\|^2_{L^2(\Gamma^{d-1})}. \tag{2.26}$$

Inequality (2.25a) is formed by setting the test functions in (2.24) as $\boldsymbol{v}_0^d = \mathcal{R}^{d-1}\lambda^{d-1} - \boldsymbol{v}_\lambda^d$ and $q^d = p_\lambda^d$. After summation of the equations, we obtain

$$\begin{aligned}\|K^{-\frac{1}{2}}\mathcal{R}^{d-1}\lambda^{d-1}\|^2_{L^2(\Omega^d)} + \|\epsilon^{\frac{1}{2}}p_\lambda^d\|^2_{L^2(\Omega^d)} &= (K^{-1}\mathcal{R}^{d-1}\lambda^{d-1}, \boldsymbol{v}_\lambda^d)_{\Omega^d} + (p_\lambda^d, \nabla\cdot\epsilon\boldsymbol{v}_\lambda^d)_{\Omega^d}\\ &= (K^{-1}\mathcal{R}^{d-1}\lambda^{d-1}, \boldsymbol{v}_\lambda^d)_{\Omega^d} + (p\nabla\epsilon, \boldsymbol{v}_\lambda^d)_{\Omega^d} + (\epsilon p_\lambda^d, \nabla\cdot\boldsymbol{v}_\lambda^d)_{\Omega^d}.\end{aligned}$$

The Cauchy-Schwarz inequality is then used followed by the positive-definiteness of K, the bound on $\nabla\epsilon$ from (2.3), and (2.26) to give:

$$\begin{aligned}&\|K^{-\frac{1}{2}}\mathcal{R}^{d-1}\lambda^{d-1}\|^2_{L^2(\Omega^d)} + \|\epsilon^{\frac{1}{2}}p_\lambda^d\|^2_{L^2(\Omega^d)}\\ &\qquad\lesssim \left(\|K^{-\frac{1}{2}}\mathcal{R}^{d-1}\lambda^{d-1}\|_{L^2(\Omega^d)} + \|\epsilon^{\frac{1}{2}}p_\lambda^d\|_{L^2(\Omega^d)}\right)\|\lambda^{d-1}\|_{L^2(\Gamma^{d-1})}.\end{aligned} \tag{2.27}$$

Secondly, we obtain (2.25b) by setting $q^d = \nabla\cdot\epsilon\mathcal{R}^{d-1}\lambda^{d-1}$ in equation (2.24b):

$$\|\nabla\cdot\epsilon\mathcal{R}^{d-1}\lambda^{d-1}\|_{L^2(\Omega^d)} \le \|\epsilon p_\lambda^d\|_{L^2(\Omega^d)} \le \|\epsilon_{\max}^{\frac{1}{2}}\epsilon^{\frac{1}{2}}p_\lambda^d\|_{L^2(\Omega^d)} \lesssim \|\epsilon_{\max}^{\frac{1}{2}}\lambda^{d-1}\|_{L^2(\Gamma^{d-1})}.$$

□

The constructed extension operator $\mathcal{R}$ allows us to form the norms as used in the subsequent analysis:

$$\begin{aligned}\|[\boldsymbol{v}_0,\mu]\|^2_{\mathscr{X}_\mathcal{R}} &= \|K^{-\frac{1}{2}}(\boldsymbol{v}_0+\mathcal{R}\mu)\|^2_{L^2(\Omega)} + \|\gamma^{\frac{1}{2}}K_\nu^{-\frac{1}{2}}\mu\|^2_{L^2(\Gamma)}\\ &\quad + \|\hat{\epsilon}_{\max}^{-1}D\cdot[\epsilon(\boldsymbol{v}_0+\mathcal{R}\mu), \hat{\epsilon}\mu]\|^2_{L^2(\Omega)},\end{aligned} \tag{2.28a}$$

$$\|q\|_\mathscr{Q} = \|\hat{\epsilon}_{\max}q\|_{L^2(\Omega)}. \tag{2.28b}$$

Here, $\hat{\epsilon}_{\max}$ is used as defined in (2.4). The energy norm is created as the combination of these norms:

$$|||(\boldsymbol{u}_0,\lambda,p)|||^2 = \|[\boldsymbol{u}_0,\lambda]\|^2_{\mathscr{X}_\mathcal{R}} + \|p\|^2_\mathscr{Q}. \tag{2.29}$$

In order to show well-posedness of the problem in this energy norm, we present three lemmas, which provide the necessary tools to invoke standard saddle-point theory.

LEMMA 2.2 (Completeness). *With the extension operator* $\mathcal{R}$ *from* (2.24)*, the space* $\mathscr{X}$ *from* (2.19) *is a Hilbert space with inner product*

$$\begin{aligned}([\boldsymbol{u}_0,\lambda],[\boldsymbol{v}_0,\mu])_{\mathscr{X}_\mathcal{R}} &= (K^{-1}(\boldsymbol{u}_0+\mathcal{R}\lambda), \boldsymbol{v}_0+\mathcal{R}\mu)_{L^2(\Omega)} + (\gamma K_\nu^{-1}\lambda,\mu)_{L^2(\Gamma)}\\ &\quad + (\hat{\epsilon}_{\max}^{-1}D\cdot[\epsilon(\boldsymbol{u}_0+\mathcal{R}\lambda), \hat{\epsilon}\lambda], \hat{\epsilon}_{\max}^{-1}D\cdot[\epsilon(\boldsymbol{v}_0+\mathcal{R}\mu), \hat{\epsilon}\mu])_{L^2(\Omega)},\end{aligned} \tag{2.30}$$

which induces the norm from (2.28a).

Proof. $\mathscr{X}$ is a linear space and $(\cdot,\cdot)_{\mathscr{X}_\mathcal{R}}$ is an inner product. In order to show completeness of $\mathscr{X}$ with respect to the induced norm (2.28a), we consider a Cauchy sequence $\{[\boldsymbol{v}_{0,k},\mu_k]\}_{k=0}^{\infty}\subset\mathscr{X}$. In other words, as $l,k\to\infty$, we have

$$\|[\boldsymbol{v}_{0,k}-\boldsymbol{v}_{0,l},\mu_k-\mu_l]\|^2_{\mathscr{X}_\mathcal{R}}\to 0. \tag{2.31}$$

By completeness of the L^2-spaces, there exists a $\boldsymbol{v}\in L^2(\Omega)$ such that $\boldsymbol{v}_{0,k}+\mathcal{R}\mu_k\to\boldsymbol{v}$ and a $\mu\in L^2(\Gamma)$ such that $\mu_k\to\mu$, using (2.15) for the latter. Thus, we can define $\boldsymbol{v}_0=\boldsymbol{v}-\mathcal{R}\mu\in L^2(\Omega)$. Using the same argumentation, $\xi\in L^2(\Omega)$ exists such that $\hat{\epsilon}_{\max}^{-1}D\cdot[\epsilon(\boldsymbol{v}_{0,k}+\mathcal{R}\mu_k),\hat{\epsilon}\mu_k]\to\xi$. It remains to show how ξ is connected to $[\boldsymbol{v}_0,\mu]$.

Let us consider a test function ψ with $\psi^0\in L^2(\Omega^0)$ and $\psi^d\in C_0^\infty(\Omega^d)$ for $d\geq 1$ and derive

$$\begin{aligned}
(\hat{\epsilon}_{\max}^{-1}D\cdot[\epsilon(\boldsymbol{v}_{0,k}+\mathcal{R}\mu_k),\hat{\epsilon}\mu_k],\psi)_\Omega &= (\hat{\epsilon}_{\max}^{-1}\nabla\cdot\epsilon(\boldsymbol{v}_{0,k}+\mathcal{R}\mu_k),\psi)_\Omega+(\hat{\epsilon}_{\max}^{-1}[\![\hat{\epsilon}\mu_k]\!],\psi)_\Omega\\
&= -(\epsilon(\boldsymbol{v}_{0,k}+\mathcal{R}\mu_k),\nabla\hat{\epsilon}_{\max}^{-1}\psi)_\Omega+(\hat{\epsilon}_{\max}^{-1}[\![\hat{\epsilon}\mu_k]\!],\psi)_\Omega\\
&= -(\boldsymbol{v}_{0,k}+\mathcal{R}\mu_k,-\epsilon\hat{\epsilon}_{\max}^{-2}(\nabla\hat{\epsilon}_{\max})\psi+\epsilon\hat{\epsilon}_{\max}^{-1}(\nabla\psi))_\Omega+(\hat{\epsilon}_{\max}^{-1}[\![\hat{\epsilon}\mu_k]\!],\psi)_\Omega\\
&\xrightarrow{k\to\infty} -(\boldsymbol{v}_0+\mathcal{R}\mu,-\epsilon\hat{\epsilon}_{\max}^{-2}(\nabla\hat{\epsilon}_{\max})\psi+\epsilon\hat{\epsilon}_{\max}^{-1}(\nabla\psi))_\Omega+(\hat{\epsilon}_{\max}^{-1}[\![\hat{\epsilon}\mu]\!],\psi)_\Omega\\
&= (\hat{\epsilon}_{\max}^{-1}D\cdot[\epsilon\boldsymbol{v}_0,\hat{\epsilon}\mu],\psi)_\Omega
\end{aligned} \tag{2.32}$$

Hence, we have shown that $\xi=\hat{\epsilon}_{\max}^{-1}D\cdot[\epsilon\boldsymbol{v}_0,\hat{\epsilon}\mu]$. Moreover, since $\mu\in L^2(\Gamma)$, it follows that $[\![\mu]\!]\in L^2(\Omega)$. With $\xi\in L^2(\Omega)$, we obtain $\nabla\cdot\epsilon\boldsymbol{v}_0\in L^2(\Omega)$ and therewith $\boldsymbol{v}_0\in\mathscr{V}_0$. Thus, $\mathscr{X}$ is complete. □

Remark 2.1. *The above proof exploits the lower bound on γK_ν^{-1} stated in* (2.15). *In order to avoid this restriction, weighted Sobolev spaces need to be considered similar to e.g. [19].*

Lemma 2.3 (Continuity and Ellipticity). *The bilinear forms a and b from* (2.22) *are continuous with respect to the norms given in* (2.28). *Moreover, if the pair $(\boldsymbol{u}_0,\lambda)\in\mathscr{X}$ satisfies*

$$b(\boldsymbol{u}_0,\lambda;\ q)=0 \text{ for all } q\in\mathscr{Q}, \tag{2.33}$$

then a constant $C_a>0$ exists such that

$$a(\boldsymbol{u}_0,\lambda;\ \boldsymbol{u}_0,\lambda)\geq C_a|||(\boldsymbol{u}_0,\lambda,0)|||^2. \tag{2.34}$$

Proof. Continuity of the bilinear forms follows directly from the Cauchy-Schwarz inequality. Let us continue with assumption (2.33), which translates to

$$(q,D\cdot[\epsilon(\boldsymbol{u}_0+\mathcal{R}\lambda),\hat{\epsilon}\lambda])_\Omega=0, \qquad \text{for all } q\in\mathscr{Q}.$$

Since $D\cdot\mathscr{X}\subseteq\mathscr{Q}$, it follows that

$$\|D\cdot[\epsilon(\boldsymbol{u}_0+\mathcal{R}\lambda),\hat{\epsilon}\lambda]\|^2_{L^2(\Omega)}=0.$$

Using the definition of a from (2.22a) and $\hat{\epsilon}_{\max}>0$ from (2.4), we obtain:

$$\begin{aligned}
a(\boldsymbol{u}_0,\lambda;\ \boldsymbol{u}_0,\lambda) &= (K^{-1}(\boldsymbol{u}_0+\mathcal{R}\lambda),\boldsymbol{u}_0+\mathcal{R}\lambda)_\Omega+\langle\frac{\gamma}{K_\nu}\lambda,\lambda\rangle_\Gamma\\
&= \|K^{-\frac{1}{2}}(\boldsymbol{u}_0+\mathcal{R}\lambda)\|^2_{L^2(\Omega)}+\|\gamma^{\frac{1}{2}}K_\nu^{-\frac{1}{2}}\lambda\|^2_{L^2(\Gamma)}+\|\hat{\epsilon}_{\max}^{-1}D\cdot[\epsilon(\boldsymbol{u}_0+\mathcal{R}\lambda),\hat{\epsilon}\lambda]\|^2_{L^2(\Omega)}\\
&= |||(\boldsymbol{u}_0,\lambda,0)|||^2.
\end{aligned}$$

Thus, the result is shown with $C_a = 1$. ∎

LEMMA 2.4 (Inf-Sup). *Let the bilinear form b be defined by equation* (2.22b). *Then there exists a constant $C_b > 0$ such that for any given function $p \in \mathscr{Q}$,*

$$\sup_{(\boldsymbol{v}_0,\mu)\in\mathscr{X}} \frac{b(\boldsymbol{v}_0,\mu;\ p)}{|||(\boldsymbol{v}_0,\mu,0)|||} \geq C_b |||(0,0,p)|||. \tag{2.35}$$

Proof. Assume $p \in \mathscr{Q}$ given. We aim to construct a pair $(\boldsymbol{v}_0, \mu) \in \mathscr{X}$ such that the inequality holds. The construction is done by sequentially ascending through the dimensional hierarchy. For convenience, we recall the definition of b:

$$-b(\boldsymbol{v}_0,\mu;\ p) = (p, \nabla\cdot\epsilon(\boldsymbol{v}_0 + \mathcal{R}\mu))_\Omega + (p, [\![\hat{\epsilon}\mu]\!])_\Omega.$$

The function $\mu \in \Lambda$ is constructed in a hierarchical manner. Let us start by choosing μ^0 such that the following is satisfied:

$$[\![\hat{\epsilon}\mu^0]\!] = \hat{\epsilon}^2_{\max} p^0, \qquad \|\mu^0\|_{L^2(\Gamma^0)} \lesssim \|\hat{\epsilon}_{\max} p^0\|_{L^2(\Omega^0)}. \tag{2.36}$$

We construct a suitable μ^0 for a given index i by finding $j_{\max}$ where $\hat{\epsilon}_{ij_{\max}} = \hat{\epsilon}_{\max}$ and setting $\mu^0_{ij_{\max}} = \hat{\epsilon}_{\max} p^0$ while choosing $\mu^0_{ik} = 0$ for $k \neq j_{\max}$.

The next step is to generalize this strategy to $1 \leq d \leq n-1$. In this, we need to counteract the contribution of the extension operator. Let us construct μ^d such that it satisfies:

$$[\![\hat{\epsilon}\mu^d]\!] = \hat{\epsilon}^2_{\max} p^d - \nabla\cdot\epsilon\mathcal{R}^{d-1}\mu^{d-1}. \tag{2.37}$$

Again, only $\mu^d_{ij_{\max}}$ is non-zero. We now have

$$\begin{aligned}
\|\mu^d\|_{L^2(\Gamma^d)} &\lesssim \|\hat{\epsilon}_{\max} p^d\|_{L^2(\Omega^d)} + \|\hat{\epsilon}^{-1}_{\max}\nabla\cdot\epsilon\mathcal{R}^{d-1}\mu^{d-1}\|_{L^2(\Omega^d)} \\
&\lesssim \|\hat{\epsilon}_{\max} p^d\|_{L^2(\Omega^d)} + \|\hat{\epsilon}^{-1}_{\max}\epsilon^{\frac{1}{2}}_{\max}\mu^{d-1}\|_{L^2(\Omega^d)} \\
&\lesssim \|\hat{\epsilon}_{\max} p^d\|_{L^2(\Omega^d)} + \|\mu^{d-1}\|_{L^2(\Gamma^{d-1})},
\end{aligned} \tag{2.38}$$

where we used Lemma 2.1 and property (2.5).

Next, we set the functions $\boldsymbol{v}_0^d$ with $1 \leq d \leq n-1$ to zero and continue with $d = n$. Let us construct $\boldsymbol{v}_0^n \in \boldsymbol{V}_0^n$ and a supplementary variable $p_v^n \in Q^n$ using the following auxiliary problem :

$$\begin{aligned}
(K^{-1}\boldsymbol{v}_0^n, \boldsymbol{w}_0^n)_{\Omega^n} - (p_v^n, \nabla\cdot\boldsymbol{w}_0^n)_{\Omega^n} &= 0 && \forall \boldsymbol{w}_0^n \in \boldsymbol{V}_0^n, \\
(\nabla\cdot\boldsymbol{v}_0^n, q^n)_{\Omega^n} &= (p^n - \nabla\cdot\mathcal{R}^{n-1}\mu^{n-1}, q^n)_{\Omega^n} && \forall q^n \in Q^n.
\end{aligned}$$

This problem is well-posed since $|\partial\Omega_i^n \cap \partial\Omega_D| > 0$ for each i and thus each subdomain borders on a homogeneous, Dirichlet boundary condition. Standard stability arguments for this mixed formulation combined with the estimate from Lemma 2.1 and the defined $\epsilon = 1$ in Ω^n then give us

$$\begin{aligned}
\|K^{-\frac{1}{2}}\boldsymbol{v}_0^n\|^2_{L^2(\Omega^n)} + \|\nabla\cdot\epsilon\boldsymbol{v}_0^n\|^2_{L^2(\Omega^n)} &\lesssim \|p^n\|_{L^2(\Omega^n)} + \|\nabla\cdot\mathcal{R}^{n-1}\mu^{n-1}\|_{L^2(\Omega^n)} \\
&\lesssim \|p^n\|_{L^2(\Omega^n)} + \|\mu^{n-1}\|_{L^2(\Gamma^{n-1})}.
\end{aligned} \tag{2.39}$$

The choice $(\boldsymbol{v}_0, \mu) \in \mathscr{V}_0 \times \Lambda$ is now finalized and two key observations can be made. First, we recall the positive-definiteness of K_ν and the boundedness of $\mathcal{R}$ given

by Lemma 2.1. Combined with the bounds (2.36), (2.38), and (2.39), we derive using (2.5):

$$\begin{aligned}
\|[\boldsymbol{v}_0,\mu]\|^2_{\mathscr{X}_\mathcal{R}} &\lesssim \|K^{-\frac{1}{2}}(\boldsymbol{v}_0+\mathcal{R}\mu)\|^2_{L^2(\Omega)} + \|\mu\|^2_{L^2(\Gamma)} + \|\hat{\epsilon}^{-1}_{\max} D\cdot[\epsilon(\boldsymbol{v}_0+\mathcal{R}\mu),\hat{\epsilon}\mu]\|^2_{L^2(\Omega)}\\
&\lesssim \|p^n\|_{L^2(\Omega^n)} + \|\mu\|^2_{L^2(\Gamma)} + \|K^{-\frac{1}{2}}\mathcal{R}\mu\|^2_{L^2(\Omega)}\\
&\quad + \|\hat{\epsilon}^{-1}_{\max}\nabla\cdot\epsilon\mathcal{R}\mu\|^2_{L^2(\Omega)} + \|\hat{\epsilon}^{-1}_{\max}[\![\hat{\epsilon}\mu]\!]\|^2_{L^2(\Omega)}\\
&\lesssim \|p^n\|^2_{L^2(\Omega^n)} + \|\mu\|^2_{L^2(\Gamma)}\\
&\lesssim \|p^n\|^2_{L^2(\Omega^n)} + \textstyle\sum_{d=0}^{n-1}\|\hat{\epsilon}_{\max}p^d\|^2_{L^2(\Omega^d)} = |\!|\!|(0,0,p)|\!|\!|^2. \qquad (2.40)
\end{aligned}$$

Moreover, substitution of the constructed $(\boldsymbol{v}_0,\mu)$ in the form b gives us

$$(p^d,\nabla\cdot\epsilon(\boldsymbol{v}_0^d+\mathcal{R}^{d-1}\mu^{d-1}))_{\Omega^d} + (p^d,[\![\hat{\epsilon}\mu^d]\!])_{\Omega^d} = \|\hat{\epsilon}_{\max}p^d\|^2_{L^2(\Omega^d)}, \qquad 0\le d\le n.$$

Thus, after summation over all dimensions, we obtain

$$b(\boldsymbol{v}_0,\mu;\ p) = |\!|\!|(0,0,p)|\!|\!|^2. \qquad (2.41)$$

The proof is concluded by combining (2.40) and (2.41). ∎

We emphasize that the constants used in the previous lemmas are independent of γ and ϵ. In fact, the dependency on the aperture is completely reflected in the definition of the norms.

THEOREM 2.5. *Problem* (2.23) *is well-posed with respect to the energy norm* (2.29)*, i.e. there exists a unique solution such that*

$$|\!|\!|(\boldsymbol{u}_0,\lambda,p)|\!|\!| \lesssim \|\epsilon^{\frac{3}{2}}f\|_{L^2(\Omega)} + \|g\|_{H^{\frac{1}{2}}(\partial\Omega_D)}. \qquad (2.42)$$

Proof. We firstshow the continuity of the right-hand side of (2.23). We consider each term separately:

$$\begin{aligned}
-\langle g,\epsilon\boldsymbol{v}_0\cdot\boldsymbol{\nu}\rangle_{\partial\Omega_D} &= -\langle g,\epsilon(\boldsymbol{v}_0+\mathcal{R}\mu)\cdot\boldsymbol{\nu}\rangle_{\partial\Omega_D}\\
&\lesssim \|g\|_{H^{\frac{1}{2}}(\partial\Omega_D)}\|\epsilon(\boldsymbol{v}_0+\mathcal{R}\mu)\|_{H(\mathrm{div},\Omega)}\\
&\lesssim \|g\|_{H^{\frac{1}{2}}(\partial\Omega_D)}(\|\epsilon(\boldsymbol{v}_0+\mathcal{R}\mu)\|_{L^2(\Omega)} + \|D\cdot[\epsilon(\boldsymbol{v}_0+\mathcal{R}\mu),\hat{\epsilon}\mu]\|_{L^2(\Omega)}\\
&\quad + \|[\![\hat{\epsilon}\mu]\!]\|_{L^2(\Omega)})\\
&\lesssim \|g\|_{H^{\frac{1}{2}}(\partial\Omega_D)}\|[\boldsymbol{v}_0,\mu]\|_{\mathscr{X}_\mathcal{R}}. \qquad (2.43)
\end{aligned}$$

Here, we used assumption (2.15) and $\hat{\epsilon}_{\max}>0$ in the final step. For the second term, we use (2.5) to derive:

$$(\epsilon^2 f,q)_\Omega \le \|\hat{\epsilon}^{-1}_{\max}\epsilon^2 f\|_{L^2(\Omega)}\|\hat{\epsilon}_{\max}q\|_{L^2(\Omega)} \le \|\epsilon^{\frac{3}{2}}f\|_{L^2(\Omega)}\|q\|_{\mathscr{Q}}. \qquad (2.44)$$

Using Lemmas 2.2 to 2.4, the well-posedness of problem (2.23) follows from saddle-point problem theory, see e.g. [9]. ∎

3. Discretization. In this section, the discretization of problem (2.23) is considered. First, the requirements on the choice of discrete function spaces are stated. We then continue by showing stability for the discrete problem and end the section with a priori error estimates.

3.1. Discrete Spaces. In order to properly define the discrete equivalent of (2.23), we start by introducing the mesh. Let $\mathcal{T}_\Omega^d$ with $0 \leq d \leq n$ be a finite element partition of Ω^d made up of d-dimensional, shape-regular, simplicial elements. Secondly, let $\mathcal{T}_\Gamma^d$ with $0 \leq d \leq n-1$ be a partition of Γ^d consisting of d-dimensional simplices. We will commonly refer to $\mathcal{T}_\Gamma^d$ as the mortar mesh. Furthermore, let h denote the mesh size.

The discrete analogues of the function spaces are constructed using the dimensional hierarchy. Let us introduce $\boldsymbol{V}_h^d \subset \boldsymbol{V}^d$ and $\boldsymbol{V}_{0,h}^d \subset \boldsymbol{V}_0^d$ for $1 \leq d \leq n$ and $Q_h^d \subset Q^d$ with $0 \leq d \leq n$. Finally, the mortar space is given by

$$\Lambda_{ij,h}^d \subset L^2(\Gamma_{ij}^d), \qquad \Lambda_h^d = \bigoplus_{i=1}^{N^d} \bigoplus_{j \in \mathcal{J}_i^d} \Lambda_{ij,h}^d, \qquad 0 \leq d \leq n-1.$$

The discrete, dimensionally composite function spaces are then defined in analogy to (2.16) as

$$\mathscr{V}_h = \bigoplus_{d=1}^{n} \boldsymbol{V}_h^d, \qquad \mathscr{V}_{0,h} = \bigoplus_{d=1}^{n} \boldsymbol{V}_{0,h}^d, \qquad \mathit{\Lambda}_h = \bigoplus_{d=0}^{n-1} \Lambda_h^d, \qquad \mathscr{Q}_h = \bigoplus_{d=0}^{n} Q_h^d.$$

Finally, the combined space containing the fluxes is given by

$$\mathscr{X}_h = \mathscr{V}_{0,h} \times \mathit{\Lambda}_h.$$

Before we continue with the analysis in Subsection 3.2, let us present a total of four conditions on the discrete function spaces. The first is necessary, while the remaining conditions provide attractive features of the numerical method.

First, it is essential that the pair $\mathscr{V}_h \times \mathscr{Q}_h$ is chosen such that

$$Q_h^d = \nabla \cdot V_h^d, \qquad 1 \leq d \leq n. \tag{3.1}$$

This can be satisfied by choosing any of the usual mixed finite element pairs [5, 9].

The second condition concerns the space $\mathit{\Lambda}_h$. For simplicity, we assume that the function spaces defined on different sides bordering Ω_i^d are the same. In other words, we have

$$\Lambda_{ij,h}^d = \Lambda_{ik,h}^d, \qquad j,k \in \mathcal{J}_i^d.$$

Third, conventional mortar methods (e.g. [5]) require that the mortar mesh $\mathcal{T}_\Gamma^d$ is a sufficiently coarse partition of Γ^d when compared to $\mathcal{T}_\Omega^{d+1}$. Let us define $\hat{\Pi}_h^d : \Lambda_h^d \to \boldsymbol{V}_h^{d+1} \cdot \boldsymbol{\nu}|_{\Gamma^d}$ as the L^2-projection from the mortar mesh onto the trace of the bordering, higher-dimensional mesh. In the unified setting, the projection $\hat{\Pi}_h$ is then given by $\bigoplus_{d=0}^{n-1} \hat{\Pi}_h^d$ and the mortar condition can be described for $\mu_h \in \mathit{\Lambda}_h$ as

$$\|\hat{\Pi}_h \mu_h\|_{L^2(\Gamma)} \gtrsim \|\mu_h\|_{L^2(\Gamma)}. \tag{3.2}$$

This can easily be satisfied in case of matching grids by aligning the mortar grid with the trace of the surrounding mesh. Otherwise, it suffices to choose $\mathcal{T}_\Gamma^d$ as slightly coarser.

As shown in [16], the introduction of a flow problem inside the fracture guarantees a unique solution even if the mortar mesh is finer, thus removing the need for (3.2).

The same principle applies here. However, in this work we choose the mortar variable as the normal flux, instead of the fracture pressure, in order to have a stronger notion of mass conservation. Due to this choice, the control on the L^2-norm of the mortar variable is weighted with γ, as is apparent from (2.28a). Since γ is typically small, the main control on μ comes from $\mathcal{R}_h\mu$, which only sees $\hat{\Pi}_h\mu_h$ as boundary data. Thus, in order to eliminate the possible non-zero kernel of $\hat{\Pi}_h$, which may result in numerical oscillations of the mortar flux, it is advantageous to satisfy (3.2) in practice.

Fourth, we let all lower-dimensional meshes match with the corresponding mortar mesh, such that

$$[\![\Lambda_h]\!] = \mathscr{Q}_h. \tag{3.3}$$

In the discretized setting, we have need of a discrete extension operator $\mathcal{R}_h : \Lambda_h \to \mathscr{V}_h$. In accordance with (2.18), the function $\mathcal{R}_h\mu$ is such that $\mathcal{R}_h\mu\cdot\boldsymbol{\nu}|_\Gamma = \hat{\Pi}_h\mu$ and has zero normal trace on the remaining boundaries. A particularly attractive choice is to construct $\mathcal{R}_h\mu$ with a predefined support near the boundary. The bounded support then results in a beneficial sparsity pattern.

To finish the section, we explicitly state a family of discrete function spaces which satisfy all conditions on simplicial elements for $n = 3$ and polynomial order k. Any choice of stable mixed spaces is valid and our choice is given by

$$\mathscr{V}_h = \bigoplus_{d=1}^{3}\mathbb{RT}_k(\mathcal{T}_\Omega^d), \qquad \mathscr{Q}_h = \bigoplus_{d=0}^{3}\mathbb{P}_k(\mathcal{T}_\Omega^d), \qquad \Lambda_h = \bigoplus_{d=0}^{2}\mathbb{P}_k(\mathcal{T}_\Gamma^d). \tag{3.4}$$

Here, $\mathbb{RT}_k$ represents the k-th order Raviart-Thomas(-Nedelec) space [26, 30] which corresponds with continuous Lagrange elements of order $k+1$ for $d = 1$. The space $\mathbb{P}_k$ then represents k-th order discontinuous Lagrange elements. As is required, we choose $\mathscr{V}_{0,h} = \mathscr{V}_0 \cap \mathscr{V}_h$ with zero normal trace on Γ. The function spaces corresponding to $k = 0$ will be referred to as the lowest-order choice.

With the chosen discrete spaces, we are ready to define the discrete functionals. In the remainder, we will omit the index h in most places for notational simplicity.

$$a_h(\boldsymbol{u}_0, \lambda;\ \boldsymbol{v}_0, \mu) = (K^{-1}(\boldsymbol{u}_0 + \mathcal{R}_h\lambda), \boldsymbol{v}_0 + \mathcal{R}_h\mu)_\Omega + \langle \frac{\gamma}{K_\nu}\lambda, \mu\rangle_\Gamma, \tag{3.5a}$$

$$b_h(\boldsymbol{v}_0, \mu;\ p) = -(p, D\cdot[\epsilon(\boldsymbol{v}_0 + \mathcal{R}_h\mu), \hat{\epsilon}\mu])_\Omega. \tag{3.5b}$$

The finite element problem associated with (2.23) is now formulated as follows: Find $(\boldsymbol{u}_0, \lambda, p) \in \mathscr{V}_{0,h} \times \Lambda_h \times \mathscr{Q}_h$ such that

$$a_h(\boldsymbol{u}_0, \lambda;\ \boldsymbol{v}_0, \mu) + b_h(\boldsymbol{v}_0, \mu;\ p) - b_h(\boldsymbol{u}_0, \lambda;\ q) = -\langle g, \epsilon\boldsymbol{v}_0\cdot\boldsymbol{\nu}\rangle_{\partial\Omega_D} + (\epsilon^2 f, q)_\Omega, \tag{3.6}$$

for all $(\boldsymbol{v}_0, \mu, q) \in \mathscr{V}_{0,h} \times \Lambda_h \times \mathscr{Q}_h$.

3.2. Stability and Convergence. With the choice of discrete function spaces and the formulation of the finite element problem (3.6) in Subsection 3.1, we continue to study the stability of the scheme. The analysis is similar to that presented in Subsection 2.4 and we particularly emphasize the issues arising from the discretization in this separate presentation.

First, the incorporation of varying apertures requires some additional attention. For this purpose, we introduce the maximum value of ϵ on each element of the grid. More specifically, let us define ϵ_e as a piecewise constant function such that

$$\epsilon_e = \sup_{x\in e_\Omega} \epsilon(x) \qquad \text{on each } e_\Omega \in \mathcal{T}_\Omega. \tag{3.7}$$

By definition, this parameter equals one in Ω^n.

Secondly, for the purpose of the analysis, a specific discrete extension operator $\mathcal{R}_h : \Lambda_h \to \mathscr{V}_h$ is constructed similar to $\mathcal{R}$ from (2.24). In particular, let the pair $(\mathcal{R}_h^{d-1}\lambda^{d-1}, p_\lambda^d) \in \boldsymbol{V}_h^d \times Q_h^d$ with $1 \leq d \leq n$ be the solution to the following problem:

$$(K^{-1}\mathcal{R}_h^{d-1}\lambda^{d-1}, \boldsymbol{v}_0^d)_{\Omega^d} - (p_\lambda^d, \nabla \cdot \epsilon \boldsymbol{v}_0^d)_{\Omega^d} = 0 \qquad \forall \boldsymbol{v}_0^d \in \boldsymbol{V}_{0,h}^d \tag{3.8a}$$

$$(\nabla \cdot \epsilon \mathcal{R}_h^{d-1}\lambda^{d-1}, q^d)_{\Omega^d} + (\epsilon_e p_\lambda^d, q^d)_{\Omega^d} = 0 \qquad \forall q^d \in Q_h^d. \tag{3.8b}$$

The corresponding boundary conditions are chosen to comply with the desired condition given in equation (2.18), namely:

$$\mathcal{R}_h^{d-1}\lambda^{d-1} \cdot \boldsymbol{\nu} = \hat{\Pi}_h^{d-1}\lambda^{d-1} \qquad \text{on } \Gamma^{d-1}, \tag{3.9a}$$

$$\mathcal{R}_h^{d-1}\lambda^{d-1} \cdot \boldsymbol{\nu} = 0 \qquad \text{on } \partial\Omega^d \backslash \Gamma^{d-1}. \tag{3.9b}$$

The estimates on $\mathcal{R}_h^{d-1}\lambda^{d-1}$, analogous to Lemma 2.1 are given by the following lemma.

LEMMA 3.1. *The solution* $(\mathcal{R}_h^{d-1}\lambda^{d-1}, p_\lambda^d) \in \boldsymbol{V}_h^d \times Q_h^d$ *to problem* (3.8) *with boundary conditions given by* (3.9) *satisfies the following bounds:*

$$\|K^{-\frac{1}{2}}\mathcal{R}_h^{d-1}\lambda^{d-1}\|_{L^2(\Omega^d)} + \|\epsilon_e^{\frac{1}{2}} p_\lambda^d\|_{L^2(\Omega^d)} \lesssim \|\lambda^{d-1}\|_{L^2(\Gamma^{d-1})} \tag{3.10a}$$

$$\|\Pi_{Q_h}^d \nabla \cdot \epsilon \mathcal{R}_h^{d-1}\lambda^{d-1}\|_{L^2(\Omega^d)} \lesssim \|\epsilon_{\max}^{\frac{1}{2}}\lambda^{d-1}\|_{L^2(\Gamma^{d-1})}. \tag{3.10b}$$

with $\epsilon_{\max}|_{\Omega_i^d} = \|\epsilon\|_{L^\infty(\Omega_i^d)}$ *and* $\Pi_{Q_h}^d$ *the* L^2*-projection onto* Q_h^d.

Proof. Let $\Pi_{V_h}^d$ be the Fortin interpolator related to $\boldsymbol{V}_h^d$ [9]. Moreover, let $\boldsymbol{v}_{\lambda,h}^d = \Pi_{V_h}^d \boldsymbol{v}_\lambda^d$ with $\boldsymbol{v}_\lambda^d \in \boldsymbol{V}^d$ such that

$$\boldsymbol{v}_\lambda^d \cdot \boldsymbol{\nu} = \hat{\Pi}_h^{d-1}\lambda^{d-1} \qquad \text{on } \Gamma^{d-1},$$
$$\boldsymbol{v}_\lambda^d \cdot \boldsymbol{\nu} = 0 \qquad \text{on } \partial\Omega^d \backslash \Gamma^{d-1},$$

while also satisfying for some $s > 0$ (see [29])

$$\|\boldsymbol{v}_\lambda^d\|_{H^s(\Omega^d)} + \|\nabla \cdot \boldsymbol{v}_\lambda^d\|_{L^2(\Omega^d)} \lesssim \|\lambda^{d-1}\|_{L^2(\Gamma^{d-1})}.$$

It follows that

$$\boldsymbol{v}_{\lambda,h}^d \cdot \boldsymbol{\nu} = (\Pi_{V_h}^d \boldsymbol{v}_\lambda^d) \cdot \boldsymbol{\nu} = \hat{\Pi}_h^{d-1}(\boldsymbol{v}_\lambda^d \cdot \boldsymbol{\nu}) = \hat{\Pi}_h^{d-1}\lambda^{d-1} \qquad \text{on } \Gamma^{d-1}.$$

Hence, we may set the test function $\boldsymbol{v}_0^d = \mathcal{R}_h^{d-1}\lambda^{d-1} - \boldsymbol{v}_{\lambda,h}^d \in \boldsymbol{V}_{0,h}$. By continuity of the interpolator $\Pi_{V_h}^d$, see [5],

$$\|\boldsymbol{v}_{\lambda,h}^d\|_{L^2(\Omega^d)} = \|\Pi_{V_h}^d \boldsymbol{v}_\lambda^d\|_{L^2(\Omega^d)} \lesssim \|\boldsymbol{v}_\lambda^d\|_{H^s(\Omega^d)} + \|\nabla \cdot \boldsymbol{v}_\lambda^d\|_{L^2(\Omega^d)} \lesssim \|\lambda^{d-1}\|_{L^2(\Gamma^{d-1})} \tag{3.11}$$

Furthermore, the interpolator has the property $\nabla \cdot \Pi_{V_h}^d \boldsymbol{v}_\lambda^d = \Pi_{Q_h}^d \nabla \cdot \boldsymbol{v}_\lambda^d$, with $\Pi_{Q_h}^d$ the L^2-projection onto Q_h^d. From this, we obtain

$$\|\nabla \cdot \boldsymbol{v}_{\lambda,h}^d\|_{L^2(\Omega^d)} = \|\nabla \cdot \Pi_{V_h}^d \boldsymbol{v}_\lambda^d\|_{L^2(\Omega^d)} \leq \|\nabla \cdot \boldsymbol{v}_\lambda^d\|_{L^2(\Omega^d)} \lesssim \|\lambda^{d-1}\|_{L^2(\Gamma^{d-1})} \tag{3.12}$$

Now, let us set the test functions in (3.8) as $\boldsymbol{v}_0^d = \mathcal{R}_h^{d-1}\lambda^{d-1} - \boldsymbol{v}_{\lambda,h}^d$ and $q^d = p_\lambda^d$. This gives us, as in equation (2.27):

$$\begin{aligned}\|K^{-\frac{1}{2}}\mathcal{R}_h^{d-1}\lambda^{d-1}\|^2_{L^2(\Omega^d)} + \|\epsilon_e^{\frac{1}{2}} p_\lambda^d\|^2_{L^2(\Omega^d)} &= (K^{-1}\mathcal{R}_h^{d-1}\lambda^{d-1}, \boldsymbol{v}_{\lambda,h}^d)_{\Omega^d} - (p_\lambda^d, \nabla\cdot\epsilon\boldsymbol{v}_{\lambda,h}^d)_{\Omega^d} \\ &\lesssim (\|K^{-\frac{1}{2}}\mathcal{R}_h^{d-1}\lambda^{d-1}\|_{L^2(\Omega^d)} + \|\epsilon_e^{\frac{1}{2}} p_\lambda^d\|_{L^2(\Omega^d)})\ \|\lambda^{d-1}\|_{L^2(\Gamma^{d-1})}.\end{aligned}$$

Here, we have used (3.11), (3.12), and the fact that $\epsilon(x) \leq \epsilon_e(x)$ for all $x \in \Omega$. The first bound (3.10a) is now shown. Secondly, (3.10b) follows by setting $q^d = \Pi_{Q_h}^d \nabla\cdot\epsilon\mathcal{R}_h^{d-1}\lambda^{d-1}$ and using (3.10a):

$$\|\Pi_{Q_h}^d \nabla\cdot\epsilon\mathcal{R}_h^{d-1}\lambda^{d-1}\|_{L^2(\Omega^d)} \leq \|\epsilon_e p_\lambda^d\|_{L^2(\Omega^d)} = \|\epsilon_e^{\frac{1}{2}}\epsilon_e^{\frac{1}{2}} p_\lambda^d\|_{L^2(\Omega^d)} \leq \|\epsilon_{\max}^{\frac{1}{2}}\lambda^{d-1}\|_{L^2(\Gamma^{d-1})}.$$

□

We emphasize once more that this extension operator is only constructed for the sake of the analysis. Since we are continually interested in the combined flux $\boldsymbol{u}_0 + \mathcal{R}_h\lambda$ instead of the individual parts, it is generally more practical to choose $\mathcal{R}_h$ as any preferred extension operator which incorporates the essential boundary conditions.

Let us continue by defining the norms in the discrete setting, which differ only slightly from the norms defined in (2.28). For $[\boldsymbol{v}_0, \mu] \in \mathscr{X}_h$, let us introduce the following norm:

$$\begin{aligned}\|[\boldsymbol{v}_0,\mu]\|^2_{\mathscr{X}_{\mathcal{R},h}} &= \|K^{-\frac{1}{2}}(\boldsymbol{v}_0 + \mathcal{R}_h\mu)\|^2_{L^2(\Omega)} + \|\gamma^{\frac{1}{2}}K_\nu^{-\frac{1}{2}}\mu\|^2_{L^2(\Gamma)} \\ &\quad + \|\Pi_{\mathscr{Q}_h} D\cdot[\epsilon(\boldsymbol{v}_0 + \mathcal{R}_h\mu), \hat{\epsilon}\mu]\|^2_{L^2(\Omega)}.\end{aligned} \tag{3.13}$$

Here, $\Pi_{\mathscr{Q}_h}$ is the L^2-projection onto $\mathscr{Q}_h$. The flexibility in the choice of $\mathcal{R}_h$ is apparent in this norm by noting that it depends on the combined flux, instead of its separate parts $\boldsymbol{u}_0$ and $\mathcal{R}_h\lambda$. The norm on the pressure $q \in \mathscr{Q}_h$ remains unchanged, and we recall it for convenience:

$$\|q\|_{\mathscr{Q}_h} = \|q\|_{\mathscr{Q}} = \|\hat{\epsilon}_{\max} q\|_{L^2(\Omega)}. \tag{3.14}$$

The discrete energy norm is formed as the combination of (3.13) and (3.14):

$$|||(\boldsymbol{u}_0,\lambda,p)|||_h^2 = \|[\boldsymbol{u}_0,\lambda]\|^2_{\mathscr{X}_{\mathcal{R},h}} + \|p\|^2_{\mathscr{Q}_h}. \tag{3.15}$$

Next, this energy norm is used to prove an inf-sup condition on b_h, as shown in the following Lemma.

LEMMA 3.2 (Inf-Sup). *Let the bilinear form b_h be defined by equation* (3.5b) *and let the function spaces $\mathscr{V}_{0,h}$, Λ_h, and $\mathscr{Q}_h$ comply with the restrictions from Subsection 3.1. Then there exists a constant $C_{b_h} > 0$, independent of γ, ϵ, and h such that for any given function $p \in \mathscr{Q}_h$,*

$$\sup_{(\boldsymbol{v}_0,\mu)\in\mathscr{X}_h} \frac{b_h(\boldsymbol{v}_0,\mu;\ p)}{|||(\boldsymbol{v}_0,\mu,0)|||_h} \geq C_{b_h}|||(0,0,p)|||_h. \tag{3.16}$$

Proof. A similar strategy to that used in Lemma 2.4 is employed. First, the function $\mu^0 \in \Lambda_h^0$ is constructed. For each index i, recall that $j_{\max}$ denotes the index for which $\hat{\epsilon}_{i,j_{\max}} = \hat{\epsilon}_{\max}$. We then set $\mu_{ik}^0 = 0$ for $k \neq j_{\max}$ and choose

$$\mu_{i,j_{\max}}^0 = -\hat{\epsilon}_{\max} p^0.$$

The following two properties then follow readily:

$$(\llbracket \hat{\epsilon}\mu^0 \rrbracket, p^0)_{\Omega^0} = (-\hat{\epsilon}_{\max}\mu^0_{i,j_{\max}}, p^0)_{\Omega^0} = (-\mu^0_{i,j_{\max}}, \hat{\epsilon}_{\max}p^0)_{\Omega^0} = \|\hat{\epsilon}_{\max}p^0\|^2,$$
$$\|\mu^0\|^2_{L^2(\Gamma^0)} = \|\hat{\epsilon}_{\max}p^0\|^2_{L^2(\Omega^0)}.$$

Using a similar strategy, we construct μ^d with $1 \leq d \leq n-1$ such that $\mu^d_{ik} = 0$ for $k \neq j_{\max}$. The remaining function $\mu^d_{i,j_{\max}}$ is defined such that

$$(\hat{\epsilon}_{\max}\mu^d_{i,j_{\max}}, \varphi_k)_{\Omega^d_i} = (-\hat{\epsilon}^2_{\max}p^d + \nabla\cdot\epsilon\mathcal{R}^{d-1}_h\mu^{d-1}, \varphi_k)_{\Omega^d_i}. \tag{3.17}$$

for all basis functions $\varphi_k \in \Lambda^d_{ij,h}$. We show that $\mu^d_{i,j_{\max}}$ is well-defined by rewriting it as the linear combination $\mu^d_{i,j_{\max}} = \sum_k \alpha_k\varphi_k$. The matrix for solving α_k is then given by $A_{kl} = (\hat{\epsilon}_{\max}\varphi_l, \varphi_k)_{\Omega^d_i}$ which is symmetric and positive definite given $\hat{\epsilon}_{\max} > 0$ by (2.4).

Moreover, the chosen μ^d has the following properties where we use (3.3) and the bounds (2.5) and (3.10b).

$$(\llbracket \hat{\epsilon}\mu^d \rrbracket, p^d)_{\Omega^d} = \|\hat{\epsilon}_{\max}p^d\|^2_{L^2(\Omega^d)} - (\nabla\cdot\epsilon\mathcal{R}^{d-1}_h\mu^{d-1}, p^d)_{\Omega^d}, \tag{3.18a}$$

$$\|\mu^d\|_{L^2(\Gamma^d)} \lesssim \|\hat{\epsilon}_{\max}p^d\|_{L^2(\Omega^d)} + \|\mu^{d-1}\|_{L^2(\Gamma^{d-1})}. \tag{3.18b}$$

The functions $\boldsymbol{v}^d_0$ with $1 \leq d \leq n$ now remain to be constructed in order to obtain additional control on the pressure. As in Lemma 2.4, we set

$$\boldsymbol{v}^d_0 = 0 \qquad \text{for } 1 \leq d \leq n-1. \tag{3.19}$$

For the final case $d = n$, we recall that $Q^n_h \times V^n_{0,h}$ is a stable mixed finite element pair as given by (3.1). Keeping this in mind, $\boldsymbol{v}^n_0$ is constructed such that it forms the following solution together with $p^n_v \in Q^n_h$

$$\begin{aligned}
(K^{-1}\boldsymbol{v}^n_0, \boldsymbol{w}^n_0)_{\Omega^n} - (p^n_v, \nabla\cdot\boldsymbol{w}^n_0)_{\Omega^n} &= 0 && \boldsymbol{w}^n_0 \in \boldsymbol{V}^n_{0,h}\\
(\nabla\cdot\boldsymbol{v}^n_0, q^n)_{\Omega^n} &= (p^n - \nabla\cdot\mathcal{R}^{n-1}_h\mu^{n-1}, q^n)_{\Omega^n}, && q^n \in Q^n_h\\
\boldsymbol{v}^n_0\cdot\nu &= 0, && \text{on } \partial\Omega^n\backslash\partial\Omega_D.
\end{aligned}$$

We note that $\epsilon = \hat{\epsilon}_{\max} = 1$ in Ω^n and it follows by construction that

$$\begin{aligned}
-b_h(\boldsymbol{v}_0, \mu;\ p) &= (p, \nabla\cdot\epsilon(\boldsymbol{v}_0 + \mathcal{R}_h\mu))_\Omega + (p, \llbracket\hat{\epsilon}\mu\rrbracket)_\Omega\\
&= \|\hat{\epsilon}_{\max}p\|^2_{L^2(\Omega)} = \|p\|^2_{\mathscr{Q}_h}.
\end{aligned} \tag{3.20}$$

The corresponding bounds on $\boldsymbol{v}^n_0$ are derived using standard mixed finite element arguments and (3.10b):

$$\begin{aligned}
\|K^{-\frac{1}{2}}\boldsymbol{v}^n_0\|_{L^2(\Omega^n)} + \|\Pi^n_{Q_h}\nabla\cdot\epsilon\boldsymbol{v}^n_0\|_{L^2(\Omega^n)} &= \|K^{-\frac{1}{2}}\boldsymbol{v}^n_0\|_{L^2(\Omega^n)} + \|\nabla\cdot\boldsymbol{v}^n_0\|_{L^2(\Omega^n)}\\
&\lesssim \|p^n\|_{L^2(\Omega^n)} + \|\nabla\cdot\mathcal{R}^{n-1}_h\mu^{n-1}\|_{L^2(\Gamma^{n-1})}\\
&\lesssim \|p^n\|_{L^2(\Omega^n)} + \|\mu^{n-1}\|_{L^2(\Gamma^{n-1})}
\end{aligned} \tag{3.21}$$

The construction of $(\boldsymbol{v}_0, \mu)$ is now complete and the bounds (3.18b) and (3.21) in combination with (3.10) give us

$$\begin{aligned}
|||(\boldsymbol{v}_0, \mu, 0)|||^2_h &\lesssim \|K^{-\frac{1}{2}}\boldsymbol{v}_0\|^2_{L^2(\Omega)} + \|K^{-\frac{1}{2}}\mathcal{R}_h\mu\|^2_{L^2(\Omega)} + \|\gamma^{\frac{1}{2}}K_\nu^{-\frac{1}{2}}\mu\|^2_{L^2(\Gamma)}\\
&\quad + \|\Pi_{\mathscr{Q}_h}(\nabla\cdot\epsilon(\boldsymbol{v}_0 + \mathcal{R}_h\mu) + \llbracket\hat{\epsilon}\mu\rrbracket)\|^2_{L^2(\Omega)}\\
&\lesssim \|\hat{\epsilon}_{\max}p\|^2_{L^2(\Omega)} = \|p\|^2_{\mathscr{Q}_h}.
\end{aligned} \tag{3.22}$$

The proof is concluded by combining (3.20) and (3.22). ∎

With the previous lemma, we are ready to present the stability result, given by the following theorem.

THEOREM 3.3 (Stability). *Let the mesh and function spaces $\mathscr{V}_{0,h}$, Λ_h, and $\mathscr{Q}_h$ be chosen such that they comply with the restrictions from Subsection 3.1. Then the discrete problem* (3.6) *has a unique solution satisfying the stability estimate*

$$\|\!|(\boldsymbol{u}_0,\lambda,p)|\!\|_h \lesssim \|\epsilon^{\frac{3}{2}} f\|_{L^2(\Omega)} + \|g\|_{H^{\frac{1}{2}}(\partial\Omega_D)}. \tag{3.23}$$

Proof. Starting with Lemma 3.2, let $(\boldsymbol{u}_{0,p},\lambda_p)$ be the constructed pair based on the pressure distribution p with the following two properties

$$-(p, D\cdot[\epsilon(\boldsymbol{u}_{0,p}+\mathcal{R}_h\lambda_p),\hat{\epsilon}\lambda_p])_\Omega = \|p\|^2_{\mathscr{Q}_h}, \tag{3.24a}$$

$$\|[\boldsymbol{u}_{0,p},\lambda_p]\|_{\mathscr{X}_{\mathcal{R},h}} \lesssim \|p\|_{\mathscr{Q}_h}. \tag{3.24b}$$

We then introduce the following test functions with $\delta_1>0$ a constant to be determined later:

$$\boldsymbol{v}_0 = \boldsymbol{u}_0+\delta_1\boldsymbol{u}_{0,p}, \qquad \mu=\lambda+\delta_1\lambda_p, \qquad q = p+\Pi_{\mathscr{Q}_h} D\cdot[\epsilon(\boldsymbol{u}_0+\mathcal{R}_h\lambda),\hat{\epsilon}\lambda].$$

Substitution of these test functions in (3.6) gives us

$$\begin{aligned}
&\|K^{-\frac{1}{2}}(\boldsymbol{u}_0+\mathcal{R}_h\lambda)\|^2_{L^2(\Omega)} + \|\gamma^{\frac{1}{2}}K_\nu^{-\frac{1}{2}}\lambda\|^2_{L^2(\Gamma)} + \|\Pi_{\mathscr{Q}_h} D\cdot[\epsilon(\boldsymbol{u}_0+\mathcal{R}_h\lambda),\hat{\epsilon}\lambda]\|^2_{L^2(\Omega)}\\
&\quad + \delta_1\|p\|^2_{\mathscr{Q}_h}\\
&= -\langle g,\epsilon(\boldsymbol{u}_0+\delta_1\boldsymbol{u}_{0,p})\cdot\boldsymbol{\nu}\rangle_{\partial\Omega_D} + (\epsilon^2 f, p+\Pi_{\mathscr{Q}_h} D\cdot[\epsilon(\boldsymbol{u}_0+\mathcal{R}_h\lambda),\hat{\epsilon}\lambda])_\Omega\\
&\quad - (K^{-1}(\boldsymbol{u}_0+\mathcal{R}_h\lambda),\delta_1(\boldsymbol{u}_{0,p}+\mathcal{R}_h\lambda_p))_\Omega - \langle\frac{\gamma}{K_\nu}\lambda,\delta_1\lambda_p\rangle_\Gamma\\
&\le \frac{1}{2\delta_2}\|g\|^2_{H^{\frac{1}{2}}(\partial\Omega_D)} + \frac{\delta_2}{2}\|\epsilon(\boldsymbol{u}_0+\delta_1\boldsymbol{u}_{0,p})\cdot\boldsymbol{\nu}\|^2_{H^{-\frac{1}{2}}(\partial\Omega_D)} + \big(\frac{1}{2(\delta_1\hat{\epsilon}_{\max})^2}+\frac{1}{2}\big)\|\epsilon^2 f\|^2_{L^2(\Omega)}\\
&\quad + \frac{\delta_1^2}{2}\|\hat{\epsilon}_{\max}p\|^2_{L^2(\Omega)} + \frac{1}{2}\|\Pi_{\mathscr{Q}_h} D\cdot[\epsilon(\boldsymbol{u}_0+\mathcal{R}_h\lambda),\hat{\epsilon}\lambda]\|^2_{L^2(\Omega)}\\
&\quad + \frac{1}{2}\|K^{-\frac{1}{2}}(\boldsymbol{u}_0+\mathcal{R}_h\lambda)\|^2_{L^2(\Omega)} + \frac{\delta_1^2}{2}\|K^{-\frac{1}{2}}(\boldsymbol{u}_{0,p}+\mathcal{R}_h\lambda_p)\|^2_{L^2(\Omega)})\\
&\quad + \frac{1}{2}\|\gamma^{\frac{1}{2}}K_\nu^{-\frac{1}{2}}\lambda\|^2_{L^2(\Gamma)} + \frac{\delta_1^2}{2}\|\gamma^{\frac{1}{2}}K_\nu^{-\frac{1}{2}}\lambda_p\|^2_{L^2(\Gamma)},
\end{aligned}$$

with $\delta_2>0$ a constant.

Let us consider the second term after the inequality. The fact that the extension operator $\mathcal{R}_h$ has zero normal trace on $\partial\Omega^d$, the positive definiteness of K, and the trace theorem give us

$$\begin{aligned}
\|\epsilon(\boldsymbol{u}_0+\delta_1\boldsymbol{u}_{0,p})\cdot\boldsymbol{\nu}\|_{H^{-\frac{1}{2}}(\partial\Omega_D)} &\le \|\epsilon(\boldsymbol{u}_0+\mathcal{R}_h\lambda)\cdot\boldsymbol{\nu}\|_{H^{-\frac{1}{2}}(\partial\Omega_D)} + \delta_1\|\epsilon(\boldsymbol{u}_{0,p}+\mathcal{R}_h\lambda_p)\cdot\boldsymbol{\nu}\|_{H^{-\frac{1}{2}}(\partial\Omega_D)}\\
&\lesssim \|K^{-\frac{1}{2}}(\boldsymbol{u}_0+\mathcal{R}_h\lambda)\|_{L^2(\Omega)} + \|\nabla\cdot\epsilon(\boldsymbol{u}_0+\mathcal{R}_h\lambda)\|_{L^2(\Omega)}\\
&\quad + \delta_1\|K^{-\frac{1}{2}}(\boldsymbol{u}_{0,p}+\mathcal{R}_h\lambda_p)\|_{L^2(\Omega)} + \delta_1\|\nabla\cdot\epsilon(\boldsymbol{u}_{0,p}+\mathcal{R}_h\lambda_p)\|_{L^2(\Omega)}.
\end{aligned} \tag{3.25}$$

Considering the second term, let ϵ_h be the piecewise constant approximation of ϵ. We then use $\nabla\cdot\mathscr{V}_h\subseteq\mathscr{Q}_h$ from (3.1) and the L^∞ approximation property of ϵ_h from [13]

to obtain

$$\begin{aligned}
\|\nabla\cdot\epsilon(\boldsymbol{u}_0+\mathcal{R}_h\lambda)\|_{L^2(\Omega)} \leq\ & \|(\nabla\epsilon)\cdot(\boldsymbol{u}_0+\mathcal{R}_h\lambda)\|_{L^2(\Omega)}+\|\epsilon\nabla\cdot(\boldsymbol{u}_0+\mathcal{R}_h\lambda)\|_{L^2(\Omega)}\\
\lesssim\ & \|\epsilon^{\frac{1}{2}}\|_{L^\infty(\Omega)}\|\boldsymbol{u}_0+\mathcal{R}_h\lambda\|_{L^2(\Omega)}+\|(\epsilon-\epsilon_h)\nabla\cdot(\boldsymbol{u}_0+\mathcal{R}_h\lambda)\|_{L^2(\Omega)}\\
&+\|\Pi_{\mathscr{Q}_h}\epsilon_h\nabla\cdot(\boldsymbol{u}_0+\mathcal{R}_h\lambda)\|_{L^2(\Omega)}\\
\lesssim\ & \|\boldsymbol{u}_0+\mathcal{R}_h\lambda\|_{L^2(\Omega)}+\|(\epsilon-\epsilon_h)\nabla\cdot(\boldsymbol{u}_0+\mathcal{R}_h\lambda)\|_{L^2(\Omega)}\\
&+\|\Pi_{\mathscr{Q}_h}(\epsilon_h-\epsilon)\nabla\cdot(\boldsymbol{u}_0+\mathcal{R}_h\lambda)\|_{L^2(\Omega)}+\|\Pi_{\mathscr{Q}_h}\epsilon\nabla\cdot(\boldsymbol{u}_0+\mathcal{R}_h\lambda)\|_{L^2(\Omega)}\\
\lesssim\ & \|\boldsymbol{u}_0+\mathcal{R}_h\lambda\|_{L^2(\Omega)}+h\|\nabla\epsilon\|_{L^\infty(\Omega)}\|\nabla\cdot(\boldsymbol{u}_0+\mathcal{R}_h\lambda)\|_{L^2(\Omega)}\\
&+\|\Pi_{\mathscr{Q}_h}\epsilon\nabla\cdot(\boldsymbol{u}_0+\mathcal{R}_h\lambda)\|_{L^2(\Omega)}\\
\lesssim\ & \|\boldsymbol{u}_0+\mathcal{R}_h\lambda\|_{L^2(\Omega)}+\|\Pi_{\mathscr{Q}_h}\epsilon\nabla\cdot(\boldsymbol{u}_0+\mathcal{R}_h\lambda)\|_{L^2(\Omega)}, \qquad (3.26)
\end{aligned}$$

using an inverse inequality. Finally, we use assumption (2.15) and the positive definiteness of K to derive

$$\begin{aligned}
\|\Pi_{\mathscr{Q}_h}\epsilon\nabla\cdot(\boldsymbol{u}_0+\mathcal{R}_h\lambda)\|_{L^2(\Omega)} \lesssim\ & \|\Pi_{\mathscr{Q}_h}(\nabla\epsilon)\cdot(\boldsymbol{u}_0+\mathcal{R}_h\lambda)\|_{L^2(\Omega)}+\|\Pi_{\mathscr{Q}_h}\nabla\cdot\epsilon(\boldsymbol{u}_0+\mathcal{R}_h\lambda)\|_{L^2(\Omega)}\\
\lesssim\ & \|\boldsymbol{u}_0+\mathcal{R}_h\lambda\|_{L^2(\Omega)}+\|\Pi_{\mathscr{Q}_h}\nabla\cdot\epsilon(\boldsymbol{u}_0+\mathcal{R}_h\lambda)\|_{L^2(\Omega)}\\
\lesssim\ & \|\boldsymbol{u}_0+\mathcal{R}_h\lambda\|_{L^2(\Omega)}+\|\Pi_{\mathscr{Q}_h}D\cdot[\epsilon(\boldsymbol{v}_0+\mathcal{R}_h\mu),\hat{\epsilon}\mu]\|_{L^2(\Omega)}\\
&+\|\Pi_{\mathscr{Q}_h}[\![\hat{\epsilon}\mu]\!]\|_{L^2(\Omega)}\\
\lesssim\ & \|[\boldsymbol{u}_0,\lambda]\|_{\mathscr{X}_{\mathcal{R},h}}. \qquad (3.27)
\end{aligned}$$

The steps from (3.26) and (3.27) are then repeated for $\boldsymbol{u}_{0,p}+\mathcal{R}_h\lambda_p$ and we conclude

$$\|\epsilon(\boldsymbol{u}_0+\delta_1\boldsymbol{u}_{0,p})\cdot\boldsymbol{\nu}\|^2_{H^{-\frac{1}{2}}(\partial\Omega_D)}\lesssim\|[\boldsymbol{u}_0,\lambda]\|^2_{\mathscr{X}_{\mathcal{R},h}}+\delta_1^2\|[\boldsymbol{u}_{0,p},\lambda_p]\|^2_{\mathscr{X}_{\mathcal{R},h}}. \qquad (3.28)$$

By setting δ_2 sufficiently small and using the properties of $(\boldsymbol{u}_{0,p},\lambda_p)$ from (3.24), we obtain

$$\|[\boldsymbol{u}_0,\lambda]\|^2_{\mathscr{X}_{\mathcal{R},h}}+\delta_1\|p\|^2_{\mathscr{Q}_h}\lesssim\|\epsilon^{\frac{3}{2}}f\|^2_{L^2(\Omega)}+\|g\|^2_{H^{\frac{1}{2}}(\partial\Omega_D)}+\delta_1^2\|p\|^2_{\mathscr{Q}_h} \qquad (3.29)$$

Choosing a sufficiently small value for δ_1 then concludes the stability estimate. Since we are considering a square linear system, this estimate implies existence and uniqueness of the solution. ∎

With the stability result from Theorem 3.3, we continue with the basic error estimates. The true solution, i.e. the unique solution to (2.23), will be denoted by $(\boldsymbol{u}_0,\lambda,p)$ and the finite element solution will be called $(\boldsymbol{u}_{0,h},\lambda_h,p_h)$. Since we are interested in the combined fluxes, we re-introduce

$$\boldsymbol{u}=\boldsymbol{u}_0+\mathcal{R}\lambda,\qquad\qquad \boldsymbol{u}_h=\boldsymbol{u}_{0,h}+\mathcal{R}_h\lambda_h.$$

These definitions show the flexibility in the choice of extension operator. In fact, for a given $\boldsymbol{u}$ with normal trace λ on Γ, the above decomposition is possible for an arbitrary choice of $\mathcal{R}$ satisfying (2.18). In turn, the goal of the analysis which follows is not to prove that $\boldsymbol{u}_{0,h}$ converges to $\boldsymbol{u}_0$ since this depends completely on the choice of extension operator. Rather, we aim to show that the combined flux $\boldsymbol{u}_h$ converges to $\boldsymbol{u}$. To emphasize this nuance, we introduce the norm:

$$\|[\boldsymbol{v},\mu]\|^2_{\mathscr{X}_h}=\|K^{-\frac{1}{2}}\boldsymbol{v}\|^2_{L^2(\Omega)}+\|\gamma^{\frac{1}{2}}K_\nu^{-\frac{1}{2}}\mu\|^2_{L^2(\Gamma)}+\|\Pi_{\mathscr{Q}_h}D\cdot[\epsilon\boldsymbol{v},\hat{\epsilon}\mu]\|^2_{L^2(\Omega)}. \qquad (3.30)$$

Let $\Pi_{\Lambda_h} : \Lambda \to \Lambda_h$ and $\Pi_{\mathscr{Q}_h} : \mathscr{Q} \to \mathscr{Q}_h$ be L^2-projection operators to the corresponding discrete spaces. Additionally, let $\Pi^d_{V_h} : V^d \cap (L^{2+s})^d \to V_h^d$ for $1 \leq d \leq n$ and $s > 0$ denote the standard Fortin interpolator associated with the chosen flux space V^d. The direct sum of $\Pi^d_{V_h}$ over all dimensions $1 \leq d \leq n$ gives us $\Pi_{\mathscr{V}_h}$.

Let k represent the order of the polynomials in the pressure space. The following interpolation estimates hold for the operators $\Pi_{\mathscr{V}_h}$, Π_{Λ_h}, and $\Pi_{\mathscr{Q}_h}$ and a chosen value of k (see e.g. [5, 9]):

$$\|\boldsymbol{u} - \Pi_{\mathscr{V}_h}\boldsymbol{u}\|_{0,\Omega} \lesssim \|\boldsymbol{u}\|_{r,\Omega}\, h^r, \qquad 1 \leq r \leq k+1, \tag{3.31a}$$

$$\|\nabla \cdot (\boldsymbol{u} - \Pi_{\mathscr{V}_h}\boldsymbol{u})\|_{0,\Omega} \lesssim \|\nabla \cdot \boldsymbol{u}\|_{r,\Omega}\, h^r, \qquad 1 \leq r \leq k+1, \tag{3.31b}$$

$$\|\lambda - \Pi_{\Lambda_h}\lambda\|_{0,\Gamma} \lesssim \|\lambda\|_{r,\Gamma}\, h^r, \qquad 1 \leq r \leq k+1, \tag{3.31c}$$

$$\|p - \Pi_{\mathscr{Q}_h}p\|_{0,\Omega} \lesssim \|p\|_{r,\Omega}\, h^r, \qquad 1 \leq r \leq k+1. \tag{3.31d}$$

Here, $\|\cdot\|_{r,\Sigma}$ is short-hand for the $H^r(\Sigma)$-norm.

We are now ready to continue with the error estimates. For this, we employ the same strategy as in [7]. First, the test functions are chosen from the discrete function spaces and we subtract the systems (2.23) and (3.6) to obtain

$$\begin{aligned}(K^{-1}(\boldsymbol{u} - \boldsymbol{u}_h), \boldsymbol{v}_h)_\Omega + \langle \frac{\gamma}{K_\nu}(\lambda - \lambda_h), \mu_h\rangle_\Gamma - (p - p_h, D \cdot [\epsilon\boldsymbol{v}_h, \hat{\epsilon}\mu_h])_\Omega \\ + (q_h, D \cdot [\epsilon(\boldsymbol{u} - \boldsymbol{u}_h), \hat{\epsilon}(\lambda - \lambda_h)])_\Omega = 0.\end{aligned} \tag{3.32}$$

An immediate consequence of choosing $q_h = \Pi_{\mathscr{Q}_h} D \cdot [\epsilon(\boldsymbol{u} - \boldsymbol{u}_h), \hat{\epsilon}(\lambda - \lambda_h)]$ is that

$$\Pi_{\mathscr{Q}_h} D \cdot [\epsilon(\boldsymbol{u} - \boldsymbol{u}_h), \hat{\epsilon}(\lambda - \lambda_h)] = 0. \tag{3.33}$$

Turning back to (3.32), we introduce the projections of the true solution onto the corresponding spaces and manipulate the equation to

$$\begin{aligned}&(K^{-1}(\Pi_{\mathscr{V}_h}\boldsymbol{u} - \boldsymbol{u}_h), \boldsymbol{v}_h)_\Omega + \langle \frac{\gamma}{K_\nu}(\Pi_{\Lambda_h}\lambda - \lambda_h), \mu_h\rangle_\Gamma - (\Pi_{\mathscr{Q}_h}p - p_h, D \cdot [\epsilon\boldsymbol{v}_h, \hat{\epsilon}\mu_h])_\Omega \\ &\quad + (q_h, \Pi_{\mathscr{Q}_h} D \cdot [\epsilon(\Pi_{\mathscr{V}_h}\boldsymbol{u} - \boldsymbol{u}_h), \hat{\epsilon}(\Pi_{\Lambda_h}\lambda - \lambda_h)])_\Omega \\ &= (K^{-1}(\Pi_{\mathscr{V}_h}\boldsymbol{u} - \boldsymbol{u}), \boldsymbol{v}_h)_\Omega + \langle \frac{\gamma}{K_\nu}(\Pi_{\Lambda_h}\lambda - \lambda), \mu_h\rangle_\Gamma - (\Pi_{\mathscr{Q}_h}p - p, D \cdot [\epsilon\boldsymbol{v}_h, \hat{\epsilon}\mu_h])_\Omega \\ &\quad + (q_h, \Pi_{\mathscr{Q}_h} D \cdot [\epsilon(\Pi_{\mathscr{V}_h}\boldsymbol{u} - \boldsymbol{u}), \hat{\epsilon}(\Pi_{\Lambda_h}\lambda - \lambda)])_\Omega.\end{aligned}$$

We continue by making the following explicit choice of test functions. For that, we first introduce the pair $(\boldsymbol{u}_{p,h}, \lambda_{p,h})$ from the inf-sup condition in Lemma 3.2 based on the pressure distribution $\Pi_{\mathscr{Q}_h}p - p_h$. Let us recall the following two properties

$$-(\Pi_{\mathscr{Q}_h}p - p_h, D \cdot [\epsilon\boldsymbol{u}_{p,h}, \hat{\epsilon}\lambda_{p,h}])_\Omega = \|\Pi_{\mathscr{Q}_h}p - p_h\|^2_{\mathscr{Q}_h}, \tag{3.34a}$$

$$\|[\boldsymbol{u}_{p,h}, \lambda_{p,h}]\|_{\mathscr{X}_h} \lesssim \|\Pi_{\mathscr{Q}_h}p - p_h\|_{\mathscr{Q}_h}. \tag{3.34b}$$

Under the assumption that the solution has sufficient regularity, we are ready to set the test functions as

$$\begin{aligned}\boldsymbol{v}_h &= \Pi_{\mathscr{V}_h}\boldsymbol{u} - \boldsymbol{u}_h + \delta_1\boldsymbol{u}_{p,h},\\ \mu_h &= \Pi_{\Lambda_h}\lambda - \lambda_h + \delta_1\lambda_{p,h},\\ q_h &= \Pi_{\mathscr{Q}_h}p - p_h,\end{aligned}$$

with $\delta_1 > 0$ to be determined later. Substitution in the above system and applying Cauchy-Schwarz and Young inequalities multiple times (with parameters $\delta_1, \delta_2, \delta_3 > 0$) and (3.34a) then gives us

$$\begin{aligned}
&\left(1 - \frac{\delta_2}{2} - \frac{\delta_3}{2}\right)\left(\|K^{-\frac{1}{2}}(\Pi_{\mathscr{V}_h}\boldsymbol{u} - \boldsymbol{u}_h)\|^2_{L^2(\Omega)} + \|\gamma^{\frac{1}{2}}K_\nu^{-\frac{1}{2}}(\Pi_{\Lambda_h}\lambda - \lambda_h)\|^2_{L^2(\Gamma)}\right) \\
&\qquad + \delta_1\|\Pi_{\mathscr{Q}_h}p - p_h\|^2_{\mathscr{Q}_h} \\
&\qquad \leq \left(\frac{1}{2\delta_3} + \frac{1}{2}\right)\left(\|K^{-\frac{1}{2}}(\Pi_{\mathscr{V}_h}\boldsymbol{u} - \boldsymbol{u})\|^2_{L^2(\Omega)} + \|\gamma^{\frac{1}{2}}K_\nu^{-\frac{1}{2}}(\Pi_{\Lambda_h}\lambda - \lambda)\|^2_{L^2(\Gamma)}\right) \\
&\qquad\quad + \frac{1}{2\delta_1}\|\hat{\epsilon}^{-1}_{\max}\Pi_{\mathscr{Q}_h}D\cdot[\epsilon(\Pi_{\mathscr{V}_h}\boldsymbol{u} - \boldsymbol{u}), \hat{\epsilon}(\Pi_{\Lambda_h}\lambda - \lambda)]\|^2_{L^2(\Omega)} \\
&\qquad\quad + \frac{\delta_1}{2}\|\hat{\epsilon}_{\max}(\Pi_{\mathscr{Q}_h}p - p_h)\|^2_{L^2(\Omega)} \\
&\qquad\quad + \left(\frac{1}{2\delta_2} + \frac{1}{2}\right)\delta_1^2\left(\|K^{-\frac{1}{2}}\boldsymbol{u}_{p,h}\|^2_{L^2(\Omega)} + \|\gamma^{\frac{1}{2}}K_\nu^{-\frac{1}{2}}\lambda_{p,h}\|^2_{L^2(\Gamma)}\right) \\
&\qquad\quad + (p - \Pi_{\mathscr{Q}_h}p, D\cdot[\epsilon(\Pi_{\mathscr{V}_h}\boldsymbol{u} - \boldsymbol{u}_h + \delta_1\boldsymbol{u}_{p,h}), \hat{\epsilon}(\Pi_{\Lambda_h}\lambda - \lambda_h + \delta_1\lambda_{p,h})])_\Omega. \qquad (3.35)
\end{aligned}$$

We continue to form a bound on the last term in (3.35). For brevity, we briefly revert to the notation of $\boldsymbol{v}_h$ and μ_h. The definition of the operator $D\cdot$ and the product rule give us

$$\begin{aligned}
&(p - \Pi_{\mathscr{Q}_h}p, D\cdot[\epsilon\boldsymbol{v}_h, \hat{\epsilon}\mu_h])_\Omega = (p - \Pi_{\mathscr{Q}_h}p, \nabla\cdot\epsilon\boldsymbol{v}_h + [\![\hat{\epsilon}\mu_h]\!])_\Omega \\
&\qquad = (p - \Pi_{\mathscr{Q}_h}p, \nabla\epsilon\cdot\boldsymbol{v}_h)_\Omega + (p - \Pi_{\mathscr{Q}_h}p, \epsilon\nabla\cdot\boldsymbol{v}_h)_\Omega + (p - \Pi_{\mathscr{Q}_h}p, [\![\hat{\epsilon}\mu_h]\!])_\Omega. \qquad (3.36)
\end{aligned}$$

Let us consider the three terms on the right-hand side one at a time. For the first term, we use Cauchy-Schwarz, (2.3), and the positive-definiteness of K to derive

$$\begin{aligned}
(p - \Pi_{\mathscr{Q}_h}p, \nabla\epsilon\cdot\boldsymbol{v}_h)_\Omega &\leq \|p - \Pi_{\mathscr{Q}_h}p\|_{L^2(\Omega)}\|\nabla\epsilon\|_{L^\infty(\Omega)}\|\boldsymbol{v}_h\|_{L^2(\Omega)} \\
&\lesssim \|p - \Pi_{\mathscr{Q}_h}p\|_{L^2(\Omega)}\|\boldsymbol{v}_h\|_{L^2(\Omega)} \\
&\lesssim \|p - \Pi_{\mathscr{Q}_h}p\|_{L^2(\Omega)}\|K^{-\frac{1}{2}}\boldsymbol{v}_h\|_{L^2(\Omega)}. \qquad (3.37)
\end{aligned}$$

Let us continue with the second term. Let ϵ_h be the piecewise constant approximation of ϵ. Since $\nabla\cdot\boldsymbol{v}_h \in \mathscr{Q}_h$, we have $\epsilon_h\nabla\cdot\boldsymbol{v}_h \in \mathscr{Q}_h$. We use this in combination with the L^∞ approximation property of ϵ_h from [13] and an inverse inequality to derive

$$\begin{aligned}
(p - \Pi_{\mathscr{Q}_h}p, \epsilon\nabla\cdot\boldsymbol{v}_h)_\Omega &= ((I - \Pi_{\mathscr{Q}_h})p, (\epsilon - \epsilon_h)\nabla\cdot\boldsymbol{v}_h)_\Omega \\
&\lesssim \|p - \Pi_{\mathscr{Q}_h}p\|_{L^2(\Omega)}h\|\nabla\epsilon\|_{L^\infty(\Omega)}\|\nabla\cdot\boldsymbol{v}_h\|_{L^2(\Omega)} \\
&\lesssim \|p - \Pi_{\mathscr{Q}_h}p\|_{L^2(\Omega)}\|\boldsymbol{v}_h\|_{L^2(\Omega)} \\
&\lesssim \|p - \Pi_{\mathscr{Q}_h}p\|_{L^2(\Omega)}\|K^{-\frac{1}{2}}\boldsymbol{v}_h\|_{L^2(\Omega)}. \qquad (3.38)
\end{aligned}$$

Next, we consider the final term in (3.36). With the exception of $d = 1$ and $n = 3$, this term is zero since $[\![\Lambda_h]\!] = \mathscr{Q}_h$ by (3.3) and $\hat{\epsilon}$ is constant. Thus, let us consider a Ω^d with $d = 1$ and $n = 3$. In this case, we derive

$$\begin{aligned}
(p - \Pi_{\mathscr{Q}_h}p, [\![\hat{\epsilon}\mu_h]\!])_{\Omega^d} &\lesssim \|p - \Pi_{\mathscr{Q}_h}p\|_{L^2(\Omega^d)}\|\hat{\epsilon}\mu_h\|_{L^2(\Omega^d)} \\
&\lesssim \|p - \Pi_{\mathscr{Q}_h}p\|_{L^2(\Omega^d)}\|\gamma^{\frac{1}{2}}K_\nu^{-\frac{1}{2}}\mu_h\|_{L^2(\Omega^d)}. \qquad (3.39)
\end{aligned}$$

The final equality follows by noting that $\hat{\epsilon}^1 \eqsim \epsilon^2 \eqsim \gamma^{\frac{3-2}{2}}$ and that there is no extension of the one-dimensional domain beyond the point where $\gamma = 0$.

For the final term in (3.35), we then obtain from (3.36)-(3.39):

$$
\begin{aligned}
&(p - \Pi_{\mathscr{Q}_h} p,\, D \cdot [\epsilon \boldsymbol{v}_h, \hat{\epsilon} \mu_h])_\Omega \\
&\qquad \lesssim \|p - \Pi_{\mathscr{Q}_h} p\|_{L^2(\Omega)} (\|K^{-\frac{1}{2}} \boldsymbol{v}_h\|_{L^2(\Omega)} + \|\gamma^{\frac{1}{2}} K_\nu^{-\frac{1}{2}} \mu_h^1\|_{L^2(\Gamma^1)}) \\
&\qquad \leq \|p - \Pi_{\mathscr{Q}_h} p\|_{L^2(\Omega)} (\|K^{-\frac{1}{2}} (\Pi_{\mathscr{V}_h} \boldsymbol{u} - \boldsymbol{u}_h)\|_{L^2(\Omega)} + \|K^{-\frac{1}{2}} \delta_1 \boldsymbol{u}_{p,h}\|_{L^2(\Omega)} \\
&\qquad\quad + \|\gamma^{\frac{1}{2}} K_\nu^{-\frac{1}{2}} (\Pi_{\Lambda_h}^1 \lambda^1 - \lambda_h^1)\|_{L^2(\Gamma^1)} + \|\gamma^{\frac{1}{2}} K_\nu^{-\frac{1}{2}} \delta_1 \lambda_{p,h}^1\|_{L^2(\Gamma^1)}) \\
&\qquad \leq \left(\frac{1}{2\delta_4} + \frac{1}{2\delta_5} + 1 \right) \|p - \Pi_{\mathscr{Q}_h} p\|_{L^2(\Omega)}^2 \\
&\qquad\quad + \frac{\delta_4}{2} \|K^{-\frac{1}{2}} \Pi_{\mathscr{V}_h} \boldsymbol{u} - \boldsymbol{u}_h\|_{L^2(\Omega)}^2 + \frac{1}{2} \delta_1^2 \|K^{-\frac{1}{2}} \boldsymbol{u}_{p,h}\|_{L^2(\Omega)}^2 \\
&\qquad\quad + \frac{\delta_5}{2} \|\gamma^{\frac{1}{2}} K_\nu^{-\frac{1}{2}} (\Pi_{\Lambda_h}^1 \lambda^1 - \lambda_h^1)\|_{L^2(\Gamma^1)}^2 + \frac{1}{2} \delta_1^2 \|\gamma^{\frac{1}{2}} K_\nu^{-\frac{1}{2}} \lambda_{p,h}^1\|_{L^2(\Gamma^1)}^2).
\end{aligned}
$$

We collect the above and set the parameters δ_2 to δ_5 sufficiently small. In turn, (3.34b) and a sufficiently small δ_1 then give us the estimate

$$
\begin{aligned}
\|K^{-\frac{1}{2}} (\Pi_{\mathscr{V}_h} \boldsymbol{u} - \boldsymbol{u}_h)\|_{L^2(\Omega)}^2 + \|\gamma^{\frac{1}{2}} K_\nu^{-\frac{1}{2}} (\Pi_{\Lambda_h} \lambda - \lambda_h)\|_{L^2(\Gamma)}^2 + \|\Pi_{\mathscr{Q}_h} p - p_h\|_{\mathscr{Q}_h}^2 \\
\lesssim \|[\boldsymbol{u} - \Pi_{\mathscr{V}_h} \boldsymbol{u}, \lambda - \Pi_{\Lambda_h} \lambda]\|_{\mathscr{X}_h}^2 + \|p - \Pi_{\mathscr{Q}_h} p\|_{L^2(\Omega)}^2.
\end{aligned}
$$

Thus, with (3.33), the triangle inequality, and the properties from (3.31), we have shown convergence of order $k+1$ as stated in the following theorem.

THEOREM 3.4 (Convergence). *Let* $(\boldsymbol{u}_0, \lambda, p)$ *solve* (2.23) *and denote* $\boldsymbol{u} = \boldsymbol{u}_0 + \mathcal{R}\lambda$. *Analogously, let* $(\boldsymbol{u}_{0,h}, \lambda_h, p_h)$ *solve* (3.6) *and denote* $\boldsymbol{u}_h = \boldsymbol{u}_{0,h} + \mathcal{R}_h \lambda_h$. *Then, given a quasi-uniform grid, the norms from* (3.14) *and* (3.30)*, and the Fortin interpolators from* (3.31)*, the following error estimate holds*

$$
\begin{aligned}
\|[\boldsymbol{u} - \boldsymbol{u}_h, \lambda - \lambda_h]\|_{\mathscr{X}_h} + \|p - p_h\|_{\mathscr{Q}_h} \\
\lesssim \|[\boldsymbol{u} - \Pi_{\mathscr{V}_h} \boldsymbol{u}, \lambda - \Pi_{\Lambda_h} \lambda]\|_{\mathscr{X}_h} + \|p - \Pi_{\mathscr{Q}_h} p\|_{L^2(\Omega)} \\
\lesssim h^{k+1} (\|\boldsymbol{u}\|_{k+1,\Omega} + \|\nabla \cdot \boldsymbol{u}\|_{k+1,\Omega} + \|\lambda\|_{k+1,\Gamma} + \|p\|_{k+1,\Omega}).
\end{aligned} \tag{3.40}
$$

4. Numerical Results.

To confirm the theory derived in the previous sections, we show two sets of numerical results using test cases designed to highlight some of the typical challenges associated with fracture flow simulation. First, we introduce a setup in two dimensions and describe the included features with their associated parameters, followed by an evaluation of the results. This example includes a fracture tip gradually decreasing to zero, thus indicating that (2.15) may not be a necessary condition. Next, a three-dimensional problem is considered which provides an accessible illustration of the dimensional decomposition full dimensional decomposition.

4.1. Two-Dimensional Problem.

For the two-dimensional test case, the domain Ω is the unit square. A unit pressure drop is simulated by imposing a Dirichlet boundary condition for the pressure at the top and bottom boundaries of Ω. On the remaining sides, a no-flow boundary condition is imposed. For simplicity, the source function f is set to zero.

Multiple fractures with different properties are added to Ω to show the extent of the capabilities of the method. Figure 3 (Left) gives an illustration of these fractures. First, the domain contains a fracture intersection. Modeling intersections is non-trivial for a variety of fracture flow schemes and typically calls for special considerations (see e.g. [15, 17, 31, 32]). In contrast, for the method we present, the implementation of an intersection follows naturally due to the dimensional decomposition. Although the test case merely contains a single intersection, this can easily be extended.

In addition to the intersection, a second aspect is the termination of fractures. The method is designed to handle these endings well, which is investigated by introducing immersed and half-immersed fractures as well as fractures crossing through the boundary as shown in Figure 3 (Left). As suggested in Subsection 2.2, a fracture ending can either be modeled by ending the feature and setting a zero-flux boundary condition or letting the aperture decrease to zero. Both models are included here, applied to the lower and upper horizontal fractures, respectively.

By setting the aperture to zero, a virtual extension is created which may be desirable for computational reasons. Due to the close relation to mortar methods, a virtual fracture can serve as an interface between two subdomains with non-matching grids, thus creating a domain decomposition method. By setting the aperture to zero, tangential flow is naturally eliminated and the method simplifies to a mortar scheme with the normal flux as the mortar variable. For our test case, the region where this occurs is illustrated by a dashed line in Figure 3.

Furthermore, we investigate the handling of non-matching grids by independently meshing the two sides of all fractures, illustrated by Figure 3 (Right). The mortar mesh is then chosen sufficiently coarse in order to meet requirement (3.2).

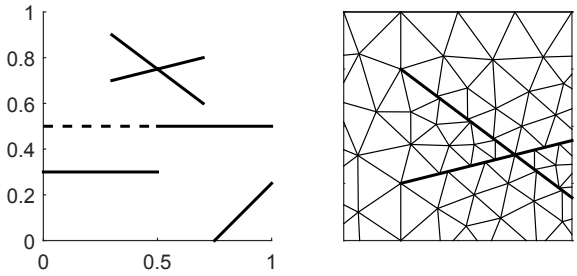

FIGURE 3. *(Left) The domain contains an intersection, multiple fracture endings, a fracture passing through the domain and a virtual extension of a fracture represented by the dashed line. (Right) The grid is non-matching along all fractures, including the sections with zero aperture.*

Let us continue by defining the parameters for the test cases. First, we assume isotropic permeability in Ω^2 and set K^2 as the 2×2 identity tensor. The different included fractures are given different material properties, given in Table 1. The aperture γ is chosen as a constant in all fractures except for the central horizontal feature Ω^1_7, which has zero aperture for $x_1 \leq 0.5$ and we let the aperture increase for $x_1 > 0.5$ subject to the constraint on the gradient from (2.3). The precise formula is given in Table 1. Fractures with high permeabilities are expected to stimulate flow whereas a low permeability leads to blocking features.

For this example, we assume that K_ν^0, i.e. the permeability in the intersection point, is given. It is possible to define this permeability differently on each interface between fracture and intersection depending on the permeabilities of the attached fractures. Alternatively, a single value can be prescribed, yet this will rely heavily on the modeling assumptions. Here, we omit such procedures in order to present the scheme in the most general setting.

TABLE 1
The coordinates and parameters associated with the lower-dimensional domains.

	x_{start}	x_{end}	K, K_ν	γ
Ω_1^0	(0.5, 0.75)		100	0.01
Ω_1^1	(0.5, 0.75)	(0.7, 0.8)	100	0.01
Ω_2^1	(0.5, 0.75)	(0.3, 0.9)	100	0.01
Ω_3^1	(0.5, 0.75)	(0.3, 0.7)	100	0.01
Ω_4^1	(0.5, 0.75)	(0.7, 0.6)	100	0.01
Ω_5^1	(0.75, 0)	(0.5, 0.75)	100	0.01
Ω_6^1	(0, 0.3)	(0.5, 0.3)	0.01	0.01
Ω_7^1	(0, 0.5)	(1, 0.5)	0.01	$0.01(2\max(x_1 - 0.5, 0))^4$

4.1.1. Qualitative Results. The results for the two-dimensional test case introduced above are shown in Figure 4 with the use of lowest order Raviart-Thomas elements for the flux and piecewise constants for the mortar and pressure variables (see (3.4)). As expected, the results are free of oscillations and neither the fracture endings, intersection, or non-matching grid cause problems for the scheme. Moreover, the solution is qualitatively in accordance with the physically expected results.

Most notably, we observe the effects on the pressure distribution related to the prescribed permeabilities and apertures. High permeabilities enforce a nearly continuous pressure, which is clearly shown both between the fracture and matrix pressures, but similarly between the fracture and intersection pressure, represented by a dot. On the other hand, the two regions with low permeabilities result in a pressure discontinuity across the fracture. Recall that the abrupt fracture ending calls for a no-flux boundary condition, whereas a gradual decrease in aperture naturally stops the flow beyond the closure point of the fracture. From the pressure and flux distributions in Figure 4, it is clear that these two different models for fracture endings lead to different behavior of the solution. In particular, the solution is visibly less regular around the abrupt fracture ending compared to the region where a fracture pinches out. Thus, the result emphasizes the impact of abrupt fracture endings relative to gradual pinch-outs for low permeabilities.

As an additional comment, we have also investigated fracture pinch-outs which violate (2.3). In this case, minor oscillations are seen near the fracture tip, verifying that inequality (2.3) is a necessary condition not just for the analysis, but also for the method.

4.1.2. Convergence. According to the theory, we expect to see linear convergence in all variables for the lowest order choice of spaces described by (3.4) with $k = 0$. To verify this, numerical experiments were performed on five consecutively refined grids. All solutions were then compared to the solution on the finest grid.

Let us continue by describing the norms used in this comparison, starting with the flux variables. These fluxes have irregular behavior around fracture tips resulting in a loss of convergence rates in these regions. For that reason, we exclude balls with some small radius $\rho > 0$ centered at the fracture tips, denoted by $\mathfrak{B}_\rho$. For this test

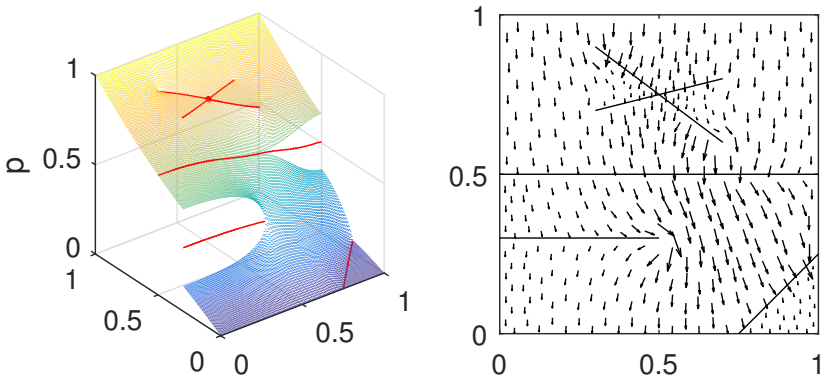

FIGURE 4. *(Left) The pressure distribution for the two-dimensional test case. The effects of abrupt fracture endings as opposed to gradual closure of fractures is apparent around the tips of the blocking features. Continuity of the solution is visible where the aperture equals zero. (Right) The flow uses conducting fractures as preferential flow paths whereas it is forced around the features with low permeability.*

case, it has been found sufficient to set $\rho = 0.02$. We emphasize that the flux variable is given by $\boldsymbol{u}_h = \boldsymbol{u}_{0,h} + \mathcal{R}_h \lambda_h$, i.e. the full flux is compared in accordance with the theory from Subsection 3.2. Moreover, (3.33) shows there is no error in the divergence of the flux when comparing the discrete to the continuous solution using the norms from (3.30). Therefore, we consider convergence in the following, appropriately scaled norms:

$$|\boldsymbol{v}|_{\mathscr{V}} = \|K^{-1/2}\boldsymbol{v}\|_{L^2(\Omega\setminus\mathfrak{B}_\rho)}, \qquad \boldsymbol{v} \in \mathscr{V}, \tag{4.1a}$$

$$|\mu|_{\Lambda} = \|\gamma^{\frac{1}{2}} K_\nu^{-\frac{1}{2}} \mu\|_{L^2(\Gamma)}, \qquad \mu \in \Lambda, \tag{4.1b}$$

$$|q|_{\mathscr{Q}} = \|\hat{\epsilon}_{\max} q\|_{L^2(\Omega)}, \qquad q \in \mathscr{Q}. \tag{4.1c}$$

The errors and convergence results are shown in Table 2. On average, we observe linear convergence in all variables, confirming the theory. For $d = 0$, which corresponds to a point evaluation of the solution, the accuracy becomes dependent on the particular grid near the intersection, and while the general trend is first-order convergence, the particular rates for this example appear erratic.

4.2. Three-Dimensional Problem. The model problem presented in this section is specifically chosen to illustrate the dimensional decomposition in three dimensions. The domain Ω is constructed by starting with the unit cube and introducing three planar fractures defined by $x_1 = 0.5$, $x_2 = 0.5$, and $x_3 = 0.5$, respectively.

The dimensional decomposition of Ω as described in Section 2.1 is then performed as follows. The fractures split the domain into 8 smaller cubes whose union defines Ω^3. The domain Ω^2 is defined as the union of the fractures excluding the intersection lines (i.e. Ω^2 consists of 12 planes). Next, the union of the 6 intersection lines, after exclusion of the intersection point, forms Ω^1. Finally, the single intersection point with coordinates $(0.5, 0.5, 0.5)$ defines Ω^0. To conclude, Γ is defined as the union of all interfaces between subdomains of codimension one.

To close the problem, the following boundary conditions are introduced. The pressure is given at the top and bottom by the function $g(\boldsymbol{x}) = x_3\left(x_1^2 + x_2\right)$. A

TABLE 2
Relative errors and convergence rates on a grid with typical mesh size h_{coarse} and consecutively refined grids.

		d=0		d=1		d=2	
	h/h_{coarse}	Error	Rate	Error	Rate	Error	Rate
$\boldsymbol{u}_h$	2^0			1.40e-01		1.10e-01	
	2^{-1}			6.84e-02	1.04	7.07e-02	0.64
	2^{-2}			3.17e-02	1.11	3.19e-02	1.15
	2^{-3}			1.21e-02	1.39	1.39e-02	1.19
λ_h	2^0	5.46e-02		1.56e-01			
	2^{-1}	1.47e-02	1.90	8.36e-02	0.90		
	2^{-2}	3.74e-03	1.97	4.32e-02	0.95		
	2^{-3}	1.94e-03	0.95	2.06e-02	1.07		
p_h	2^0	9.63e-05		1.04e-02		2.44e-02	
	2^{-1}	4.43e-06	4.44	4.96e-03	1.07	1.21e-02	1.01
	2^{-2}	1.40e-05	-1.66	2.40e-03	1.05	5.87e-03	1.04
	2^{-3}	5.88e-06	1.26	1.04e-03	1.21	2.59e-03	1.18

no-flux condition is set on the remaining boundaries. All fracture planes and lines touching the boundary $\partial\Omega$ naturally inherit these conditions.

The parameters for this test case are chosen such that the problem reflects conducting fractures. Specifically, we set $K^3 = 1$ as the matrix permeability, $K^d = K^d_\nu = 100$ for $0 \leq d \leq 2$, and the aperture as $\gamma = 0.01$ for all lower-dimensional domains. The simplicial meshes generated for this problem are matching along all intersections and thus, a matching mortar mesh is employed. The discretized problem is implemented with the use of FEniCS [23].

Due to the lack of immersed fracture tips in the proposed domain, no special considerations are needed and each variable is expected to converge linearly for all values of d. The numerical results displayed by Table 3 confirm these expectations. Once again, the solution on a finer grid is used to serve as the true solution.

TABLE 3
Relative errors and convergence rates for the 3D problem. The results show that each variable has (at least) first order convergence in each dimension.

		d=0		d=1		d=2		d=3	
	h	Error	Rate	Error	Rate	Error	Rate	Error	Rate
$\boldsymbol{u}_h$	2^{-1}			1.46e-01		3.50e-01		2.76e-01	
	2^{-2}			4.62e-02	1.66	1.97e-01	0.83	1.56e-01	0.83
	2^{-3}			1.31e-02	1.81	9.76e-02	1.02	7.76e-02	1.00
λ_h	2^{-1}	2.24e-01		2.15e-01		1.94e-01			
	2^{-2}	1.71e-02	3.71	9.93e-02	1.12	1.07e-01	0.86		
	2^{-3}	5.96e-03	1.52	4.30e-02	1.21	5.60e-02	0.93		
p_h	2^{-1}	4.51e-02		1.55e-01		1.50e-01		1.36e-01	
	2^{-2}	7.11e-03	2.67	7.40e-02	1.07	7.15e-02	1.07	6.69e-02	1.02
	2^{-3}	1.49e-03	2.25	3.29e-02	1.17	3.17e-02	1.17	3.06e-02	1.13

To visualize the solution obtained in this test case, Figure 5 shows the pressure distribution and the two-dimensional fluxes, i.e. the fluxes tangential to the fractures. Due to the parameters and boundary conditions, the solution exhibits a dominant flow through the conductive fractures from top to bottom.

5. Conclusion. In this work, we proposed a mixed finite element method for Darcy flow problems in fractured porous media. The use of flux mortars in a mixed method results in a mass conservative scheme which is able to handle non-matching

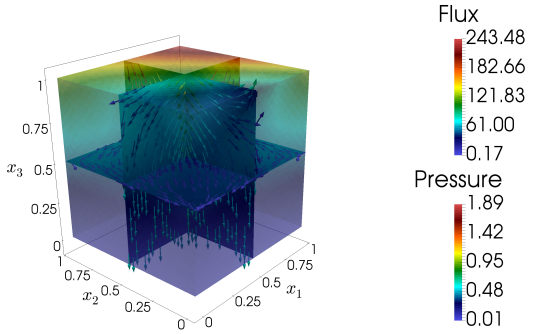

FIGURE 5. *The pressure distribution in the regular three-dimensional case superimposed on the two-dimensional flux field. The solution is qualitatively consistent with expectations for a problem with conducting fractures.*

grids. The key novel components of the method are the hierarchical approach obtained after subdividing the domain in a dimensional manner, as well as the use of dimensionally composite function spaces to analyze the problem with respect to stability and a priori error estimates. Our analysis shows the method is robust and convergent allowing for varying, and arbitrary small apertures. Numerical results confirm the theory, and furthermore show that the constraint on the degeneracy of the normal permeability used in the analysis may not be needed in practice.

Acknowledgments. The authors wish to thank Inga Berre, Sarah Gasda, and Eirik Keilegavlen for valuable comments and discussions on this topic. The research is funded in part by the Norwegian Research Council grants: 233736, 250223. The third author was partially supported by the US DOE grant DE-FG02-04ER25618 and NSF grant DMS 1418947.

REFERENCES

[1] P.M. ADLER AND J.F. THOVERT, *Fractures and Fracture Networks*, Theory and Applications of Transport in Porous Media, Springer, (1999).

[2] C. ALBOIN, J. JAFFRÉ, J.E. ROBERTS, AND C. SERRES, *Domain decomposition for flow in porous media with fractures*, in Domain Decomposition Methods in Sciences and Engineering, C.H. Lai, P.E. Bjorstad, M. Cross, and O.B Widlund, eds., Domain Decomposition Press, Bergen, Norway, (1999), pp. 365–373.

[3] C. ALBOIN, J. JAFFRÉ, J. E. ROBERTS, AND C. SERRES, *Modeling fractures as interfaces for flow and transport*, in Fluid Flow and Transport in Porous Media: Mathematical and Numerical Treatment (South Hadley, MA, 2001), Z. Chen and R.E. Ewing, eds., vol. 295 of Contemp. Math., Amer. Math. Soc., Providence, RI USA, (2002), pp. 13–24.

[4] P. ANGOT, F. BOYER, AND F. HUBERT, *Asymptotic and numerical modelling of flows in fractured porous media*, ESAIM: Mathematical Modelling and Numerical Analysis, 23 (2009), pp. 239–275.

[5] T. ARBOGAST, L. C. COWSAR, M. F. WHEELER, AND I. YOTOV, *Mixed finite element methods on non-matching multiblock grids*, SIAM Journal on Numerical Analysis, 37 (2000), pp. 1295–1315.

[6] T. ARBOGAST, M.A. HESSE, AND A.L. TAICHER, *Mixed methods for two-phase Darcy–Stokes mixtures of partially melted materials with regions of zero porosity*, SIAM Journal on Scientific Computing, 39 (2017), pp. B375–B402.

[7] T. ARBOGAST AND A. L. TAICHER, *A linear degenerate elliptic equation arising from two-phase mixtures*, SIAM Journal on Numerical Analysis, 54 (2016), pp. 3105–3122.

[8] C. Bernardi, Y. Maday, and A. T. Patera, *A new nonconforming approach to domain decomposition: the mortar element method*, Nonliner Partial Differential Equations and Their Applications, (1994).
[9] D. Boffi, M. Fortin, and F. Brezzi, *Mixed finite element methods and applications*, Springer series in computational mathematics, Springer, Berlin, Heidelberg, (2013).
[10] F. Brezzi and M. Fortin, *Mixed and hybrid finite elements methods*, Springer series in computational mathematics, Springer-Verlag, 1991.
[11] C. D'Angelo and A. Scotti, *A mixed finite element method for Darcy flow in fractured porous media with non-matching grids*, ESAIM: Mathematical Modelling and Numerical Analysis, 46 (2011), pp. 465–489.
[12] P. Dietrich, R. Helmig, M. Sauter, H. Hötzl, J. Köngeter, and G. Teutsch, *Flow and Transport in Fractured Porous Media*, Springer-Verlag Berlin Heidelberg, (2005).
[13] J. Douglas jr., T. Dupont, and L. Wahlbin, *The stability in L^q of the L^2-projection into finite element function spaces.*, Numerische Mathematik, 23 (1975), pp. 193–198.
[14] B. Flemisch, I. Berre, W. Boon, A. Fumagalli, N. Schwenck, A. Scotti, I. Stefansson, and A. Tatomir, *Benchmarks for single-phase flow in fractured porous media*, arXiv preprint arXiv:1701.01496, (2017).
[15] L. Formaggia, A. Fumagalli, A. Scotti, and P. Ruffo, *A reduced model for Darcys problem in networks of fractures*, ESAIM: Mathematical Modelling and Numerical Analysis, 48 (2014), pp. 1089–1116.
[16] N. Frih, V. Martin, J.E. Roberts, and A. Saâda, *Modeling fractures as interfaces with nonmatching grids*, Computational Geosciences, 16 (2012), pp. 1043–1060.
[17] A. Fumagalli and A. Scotti, *An efficient XFEM approximation of Darcy flows in arbitrarily fractured porous media*, Oil Gas Sci. Technol. Rev. IFP Energies nouvelles, 69 (2014), pp. 555–564.
[18] J. Galvis and M. Sarkis, *Non-matching mortar discretization analysis for the coupling Stokes–Darcy equations*, Electron. Trans. Numer. Anal, 26 (2007), p. 07.
[19] V. Girault, M. F. Wheeler, B. Ganis, and M. E. Mear, *A lubrication fracture model in a poro-elastic medium*, Mathematical Models and Methods in Applied Sciences, 25 (2015), pp. 587–645.
[20] R. Glowinski and M. F. Wheeler, *Domain decomposition and mixed finite element methods for elliptic problems*, in First International Symposium on Domain Decomposition Methods for Partial Differential Equations, R. Glowinski, G. H. Golub, G. A. Meurant, and J. Periaux, eds., SIAM, Philadelphia, 1988, pp. 144–172.
[21] M. Karimi-Fard, L.J. Durlofsky, and K. Aziz, *An efficient discrete-fracture model applicable for general-purpose reservoir simulators*, SPE Journal, 9 (2004), pp. 227–236.
[22] R.J. LeVeque, *Finite Volume Methods for Hyperbolic Problems*, Cambridge Texts in Applied Mathematics, Cambridge University Press, (2002).
[23] A. Logg, K.-A. Mardal, G. N. Wells, et al., *Automated Solution of Differential Equations by the Finite Element Method*, Springer, (2012).
[24] B. T. Mallison, M.H. Hui, and W. Narr, *Practical gridding algorithms for discrete fracture modeling workflows*, in 12th European Conference on the Mathematics of Oil Recovery, (2010).
[25] V. Martin, J. Jaffré, and J. E. Roberts, *Modeling fractures and barriers as interfaces for flow in porous media*, SIAM J. Sci. Comput., 26 (2005), pp. 1667–1691.
[26] J.C. Nedelec, *Mixed finite elements in $\mathbb{R}^3$*, Numerische Mathematik, 35 (1980), pp. 315–341.
[27] J.M. Nordbotten and M.A. Celia, *Geological Storage of CO2: Modeling Approaches for Large-Scale Simulation*, Wiley, (2011).
[28] G. Pencheva and I. Yotov, *Balancing domain decomposition for mortar mixed finite element methods*, Numerical linear algebra with applications, 10 (2003), pp. 159–180.
[29] A. Quarteroni and A. Valli, *Domain decomposition methods for partial differential equations*, no. CMCS-BOOK-2009-019, Oxford University Press, (1999).
[30] P.A. Raviart and J.M. Thomas, *A mixed finite element method for 2-nd order elliptic problems*, in Mathematical Aspects of Finite Element Methods, Ilio Galligani and Enrico Magenes, eds., vol. 606 of Lecture Notes in Mathematics, Springer Berlin Heidelberg, (1977), pp. 292–315.
[31] T. H. Sandve, I. Berre, and J. M. Nordbotten, *An efficient multi-point flux approximation method for discrete fracture-matrix simulations*, J. Comput. Phys., 231 (2012), pp. 3784–3800.
[32] N. Schwenck, B. Flemisch, R. Helmig, and B. I. Wohlmuth, *Dimensionally reduced flow models in fractured porous media: crossings and boundaries*, Computational Geosciences, 19 (2015), pp. 1219–1230.

[33] X. Tunc, I. Faille, T. Gallouët, M.C. Cacas, and P. Havé, *A model for conductive faults with non-matching grids*, Computational Geosciences, 16 (2012), pp. 277–296.

Paper B

Stable Mixed Finite Elements for Linear Elasticity with Thin Inclusions

W.M. Boon, J.M. Nordbotten

In preparation.

Paper C

Modeling, Structure and Discretization of Mixed-dimensional Partial Differential Equations

J.M. Nordbotten, W.M. Boon

Domain Decomposition Methods in Science and Engineering XXIV, Lecture Notes in Computational Science and Engineering. In review.

arXiv:1705.06876 [math.NA]

Proceedings of 24th International Conference on Domain Decomposition Methods, Svalbard,
Lecture Notes in Computational Science and Engineering

Modeling, Structure and Discretization of Hierarchical Mixed-dimensional Partial Differential Equations

J. M. Nordbotten and W. M. Boon
Department of Mathematics
University of Bergen
Norway

Abstract

Mixed-dimensional partial differential equations arise in several physical applications, wherein parts of the domain have extreme aspect ratios. In this case, it is often appealing to model these features as lower-dimensional manifolds embedded into the full domain. Examples are fractured and composite materials, but also wells (in geological applications), plant roots, or arteries and veins.

In this manuscript, we survey the structure of mixed-dimensional PDEs in the context where the sub-manifolds are a single dimension lower than the full domain, including the important aspect of intersecting sub-manifolds, leading to a hierarchy of successively lower-dimensional sub-manifolds. We are particularly interested in partial differential equations arising from conservation laws. Our aim is to provide an introduction to such problems, including the mathematical modeling, differential geometry, and discretization.

1. Introduction

Partial differential equations (PDE) on manifolds are a standard approach to model on high-aspect geometries. This is familiar in the setting of idealized laboratory experiments, where 1D and 2D representations are used despite the fact that the physical world is 3D. Similarly, it is common to consider lower-dimensional models in applications ranging from geophysical applications. Some overview expositions for various engineering problems can be found in [1, 2, 3].

Throughout this paper we will consider the ambient domain to be 3D, and our concern is when models on 2D submanifolds are either coupled to the surrounding domain, and/or intersect on 1D and 0D submanifolds. Such models are common in porous media, where the submanifolds may represent either fractures (see e.g. [4]) or thin porous strata (see [1]), but also appear in materials [3]. In all these examples, elliptic differential equations representing physical conservation laws are applicable on all subdomains, and the domains of different dimensionality are coupled via discrete jump conditions. These systems form what we will consider as mixed-dimensional elliptic PDEs, and we will limit the exposition herein to this case.

In order to establish an understanding for the physical setting, we will in section 2 present a short derivation of the governing equations for fractured porous media, emphasizing the conservation

structure and modeling assumptions. This derivation will lead to familiar models from literature (see e.g. [4, 5, 6, 7] and references therein).

We develop a unified treatment of mixed-dimensional differential operators on submanifolds of various dimensionality, using the setting of exterior calculus, and thus recast the physical problem in the sense of differential forms. We interpret the various subdomains as an imposed structure on the original domain, and provide a decomposition of differential forms onto the mixed-dimensional structure. By introducing a suitable inner product, we show that this mixed-dimensional space is a Hilbert space. On this decomposition we define a semi-discrete exterior derivative, which leads to a de Rham complex with the same co-homology structure as the original domain. It is interesting to note that the differential operators we define were independently considered by Licht who introduced the concept of discrete distributional differential forms [8]. A co-differential operator can be defined via the inner product, and it is possible to calculate an explicit expression for the co-differential operator. This allows us to establish a Helmholtz decomposition on the mixed-dimensional geometry. We also define the mixed-dimensional extensions of the familiar Sobolev spaces.

Having surveyed the basic ingredients of a mixed-dimensional calculus, we are in a position to discuss elliptic minimization problems. Indeed, the mixed dimensional minimization problems are well-posed with unique solutions based on standard arguments, and we also state the corresponding Euler equations (variational equations). With further regularity assumptions, we also give the strong form of the minimization problems, corresponding to conservation laws and constitutive laws for mixed-dimensional problems.

This paper aims to provide a general overview and roadmap for the concepts associated with hierarchical mixed-dimensional partial differential equations, more complete and detailed analysis will necessarily due to space be considered in subsequent publications.

2. Fractured porous media as a mixed-dimensional PDE

This section gives the physical rationale for mixed-dimensional PDE. As the section is meant to be motivational, we will omit technical details whenever convenient. We will return to these details in the following sections.

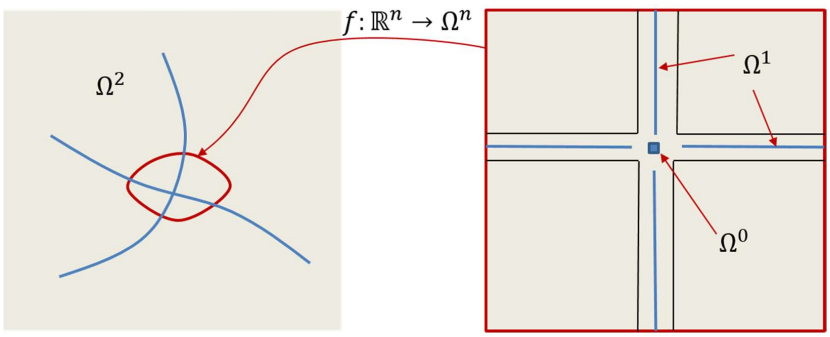

Figure 1: Example geometry of two intersecting fractures in 2D, and the logical representation of the intersection after mapping to a local coordinate system.

We consider the setting of a domain $D \in \mathbb{R}^n$. In sections 3 and onwards we will consider arbitrary n, however in this section we will for simplicity of exposition consider only $n = 3$. We consider a fractured media, where we are given explicit knowledge of the fractures, thus we consider the domains Ω_i^d as given, where $i \in I$ is an index and $d = d(i)$ represents the dimensionality of the domain. We denote by $i \in I^d$ the subset of indexes in I for which $d(i) = d$. In particular, intact material lies in domains of $d = 3$, while $d = 2$ represents fracture segments, and $d = 1$ represents intersections, see Figure 1. For each domain Ω_i^d we assign an orientation based on $n - d$ outer normal vectors $\boldsymbol{\nu}_{ij}$.

In order to specify the geometry completely, we consider the index sets $\hat{S}_i$ and $\check{S}_i$ as the $d + 1$ dimensional and $d - 1$ dimensional neighbors of a domain i. Thus for $d = 2$, the set $\hat{S}_i$ contains the domain(s) Ω_l^3 which are on the positive (and negative) side of Ω_i^2. On the other hand, the set $\check{S}_i$ contains the lines that form (parts of) the boundary of Ω_i. Additionally, the set of all lower-dimensional neighbors is defined as $\mathfrak{S}_i = \left[\check{S}_i, \check{S}_{\check{S}_i}, \dots\right]$ We will define $\Omega^d = \sum_{i \in I^d} \Omega_i^d$ as all subdomains of dimension d, while similarlty $\Omega = \sum_{d=0}^{n} \Omega^d$ is the full mixed-dimensional stratification. Note that since the superscript indicating dimension is redundant when the particular domain is given, we will (depending what offers more clarity) use $\Omega_i = \Omega_i^d$ interchangeably.

For steady-state flows in porous media, the fluid satisfies a conservation law, which for intact rock and an n-dimensional fluid flux vector $\boldsymbol{u}$ takes the form

$$\nabla \cdot \boldsymbol{u} = \phi \qquad \text{on} \qquad D \tag{2.1}$$

We wish to express this conservation law with respect to our geometric structure. To this end, let us first define the mixed-dimensional flux $\mathbf{u}$, which is simply a d-dimensional vector field on each Ω_i^d. We write $\mathbf{u} = \left[\boldsymbol{u}_i^d\right]$ when we want to talk about specific components of $\mathbf{u}$. We similarly define other mixed-dimensional variables, such as the source-term f̃.

Now clearly, for $d = n$, we recover equation (2.1). Now consider $d = n - 1$, and a fracture Ω_1 of variable Lipschitz-continuous aperture (illustrated for $d(1) = 1$ in figure 2).

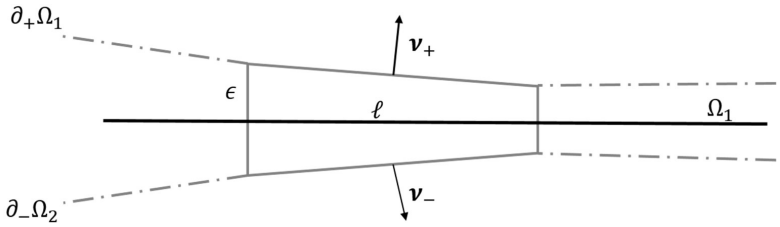

Figure 2: Example of local geometry for derivation of mixed-dimensional conservation law.

Here the dashed lines indicate a fracture boundary, the solid black line is the lower-dimensional representation, and the solid gray line indicates the region of integration, ω, of length ℓ and width $\epsilon(x)$. Evaluating the conservation law over ω leads to

$$\int_\omega \nabla \cdot \boldsymbol{u} \; da = \int_{\partial\omega} \boldsymbol{u} \cdot \boldsymbol{\nu} \; ds = \int_\omega \phi$$

where $\boldsymbol{\nu}$ are the external normal vectors. Since our integration area is in the limiting case of $\ell \to 0$ a quadrilateral, we split the last integral into parts where $\boldsymbol{\nu}$ is constant,

$$\int_{\partial\omega} \boldsymbol{u}\cdot\boldsymbol{\nu}\ ds = \boldsymbol{\nu}_+ \cdot \int_{\partial_+\omega} \boldsymbol{u}_{l_1}\ ds + \boldsymbol{\nu}_- \cdot \int_{\partial_-\omega} \boldsymbol{u}_{l_2}\ ds + \int_{\partial_R\omega} \boldsymbol{\tau}\cdot\boldsymbol{u}\ ds - \int_{\partial_L\omega} \boldsymbol{\tau}\cdot\boldsymbol{u}\ ds$$

where $[l_1, l_2] \in \hat{S}_i$ is the domain on the "+" and "-" side of Ω_1, respectively, and denote the Left and Right side of the integration boundary by subindexes. The notation $\boldsymbol{\tau}$ is the tangential vector to Ω_1. Clearly, letting the length ℓ be infinitesimal, the last two terms satisfy

$$\lim_{\ell\to 0} \frac{\int_{\partial\omega_R} \boldsymbol{\tau}\cdot\boldsymbol{u}\ ds - \int_{\partial\omega_L} \boldsymbol{\tau}\cdot\boldsymbol{u}\ ds}{\ell} = \nabla_{\Omega_1}\cdot \int_{\partial_-\omega}^{\partial_+\omega} \boldsymbol{\tau}\cdot\boldsymbol{u}\ ds = \nabla_{\Omega_1}\cdot(\epsilon\boldsymbol{u}_1)$$

where $\nabla_{\Omega_1}\cdot$ is the in-plane divergence and

$$\boldsymbol{u}_1 \equiv \tfrac{1}{\epsilon}\textstyle\int_{\partial_-\omega}^{\partial_+\omega} \boldsymbol{\tau}\cdot\boldsymbol{u}\ ds \tag{2.3}$$

Considering similarly the limits of $\ell \to 0$ for the two first terms, we obtain for the positive side

$$\lim_{\ell\to 0} \boldsymbol{\nu}_+\cdot\ell^{-1}\int_{\partial_+\omega} \boldsymbol{u}_{l_1}^{d(l_1)}\ ds = \left(1+\left|\frac{d}{dx}\nabla_{\Omega_1}(\partial_+\omega)\right|^2\right)^{1/2} \boldsymbol{\nu}_+\cdot\boldsymbol{u}_{l_1}^{d(l_1)}$$

Combining the above, we thus have

$$\lim_{\ell\to 0} \ell^{-1}\textstyle\int_\omega \nabla\cdot\boldsymbol{u}\ da = \lambda_{l_1} + \lambda_{l_2} + \nabla_{\Omega_1}\cdot(\epsilon\boldsymbol{u}_1) = [\![\lambda]\!]_i + \nabla_{\Omega_1}\cdot(\epsilon\boldsymbol{u}_1) \tag{2.4}$$

where λ is defined as

$$\lambda_{l_1} = \left(1+\left|\frac{d}{dx}\nabla_{\Omega_1}(\partial_+\omega)\right|^2\right)^{1/2} \boldsymbol{\nu}_+\cdot\boldsymbol{u}_{l_1}^{d(l_1)} \tag{2.5}$$

and (using the analogous definition for λ_{l_2})

$$[\![\lambda]\!]_i = -\textstyle\sum_{l\in\hat{S}_i}\lambda_l \tag{2.6}$$

Note that we have made no approximations in obtaining equation (2.4) – the left-hand side is an exact expression of conservation. The model approximations appear later when deriving suitable constitutive laws. Nevertheless, since the fractures have a high aspect ratio by definition, the pre-factor in equation (2.5) is in practice often approximated by identity, for which (2.5) simplifies to

$$\lambda_l \approx \boldsymbol{\nu}_\pm\cdot\boldsymbol{u}_l \tag{2.7}$$

The derivation above (including the definition in equation (2.4)), generalizes in the same way to intersection lines and intersection points, thus we find that for all $d < n$ it holds that

$$[\![\hat{\epsilon}\lambda]\!]_i + \nabla_{\Omega_i}\cdot(\epsilon_i\boldsymbol{u}_i) = \phi_i \tag{2.8}$$

Here the hat again denotes the next higher-dimensional domains, so that $\hat{\epsilon} = \epsilon_l$. Since $\hat{S}_i = \emptyset$ for $i \in I^n$, equation (2.8) reduces to (2.1) for $d = n$, and thus it represents the mixed-dimensional conservation

law for all Ω_i^d. In this more general setting, ϵ denotes the cross-sectional width (2D), area (1D) and volume (0D) for successively lower-dimensional intersections.

For porous materials, the conservation law (2.1) is typically closed by introducing Darcy's law as a modeling assumption, stated in terms of a potential p on the domain D as

$$\boldsymbol{u} = -K\nabla p \tag{2.9}$$

The coefficient K is in general a tensor. Unlike for the conservation law, it is not possible to derive an exact expression for the mixed-dimensional constitutive law, but by making some (reasonable) assumptions on the structure of the solution, it is usually accepted that Darcy's law is inherited for each subdomain (see extended discussion in [1], but also [9]), i.e.

$$\boldsymbol{u}_i = -K_i\nabla_{\Omega_i} p_i \tag{2.10}$$

To close the model, it is also necessary to specify an additional constraint, where the two most common choices are that either the potential is continuous (see discussion in [10])

$$\hat{p}_+ = \hat{p}_- \tag{2.11}$$

or, more generally, that the pressure is discontinuous but related to the normal flux above

$$\lambda_l = -2\hat{K}_{i,\pm}\frac{p_i - \hat{p}_\pm}{(\epsilon_i)^{\frac{1}{n-d}}} \tag{2.12}$$

The model equations (2.8-2.12) are typical of those used in practical applications [11]. However, to the authors' knowledge, our work is the first time they are explicitly treated as a mixed-dimensional PDE (see also [12, 13]).

3. Exterior calculus for mixed-dimensional geometries

We retain the same geometry as in the previous section, but continue the exposition in the language of exterior calculus (for introductions, see [14, 15, 16]). Throughout the section, we will assume that all functions are sufficiently smooth for the derivatives and traces to be meaningful. We also point out that similar structures to those discussed in this section have been considered previously by Licht in a different context [8].

First, we note that the components of the mixed-dimensional flux discussed in section 2 all correspond to $d-1$ forms, $\boldsymbol{u}_i^d \in \Lambda^{d-1}(\Omega_i^d)$, while the components of pressure all correspond to d-forms, $p_i^d \in \Lambda^d(\Omega_i^d)$. This motivates us to define the following mixed-dimensional k-form

$$\mathfrak{Q}^k(\Omega) = \prod_{i\in I}\Lambda^{k-(n-d(i))}(\Omega_i^d) \tag{3.1}$$

From here on, it is always assumed that $\mathfrak{Q}^k$ is defined over Ω, and the argument is suppressed.

Moreover, we note that equation (2.7) is (up to a sign) the trace with respect to the inclusion map of the submanifold, thus for a mixed-dimensional variable $\mathfrak{a} \in \mathfrak{Q}^k$ the jump operator is naturally written as

$$(\mathbb{d}\mathfrak{a})_i^d = (-1)^{d+k}\sum_{j\in\hat{S}_i}\varepsilon(\Omega_i^d, \partial_i\Omega_j^{d+1})\mathrm{Tr}_{\Omega_i^d}\, a_j^{d+1} \tag{3.2}$$

Here we have exchanged the bracket notation of equation (2.5b), which is common in applications, with a simpler notation, $\mathbb{d}$, which more clearly emphasizes that this is a (discrete) differential operator, in the normal direction(s) with respect to the submanifold. We use the notation $\varepsilon\left(\Omega_i^d, \partial_i \Omega_j^{d+1}\right)$ to indicate the relative orientation (positive or negative) of the arguments.

We obtain a mixed-dimensional exterior derivative, which we denote $\mathfrak{d}$, by combining the jump operator with the exterior derivative on the manifold, such that for $\mathfrak{a} \in \mathfrak{L}^k$

$$(\mathfrak{d}\mathfrak{a})_i^d = d a_i^d + (\mathbb{d}\mathfrak{a})_i^d \tag{3.3}$$

This expression is meaningful, since both $d a_i^d, (\mathbb{d}\mathfrak{a})_i^d \in \Lambda^{k-(n-d)+1}\left(\Omega_i^d\right)$, and thus clearly $\mathfrak{d}\mathfrak{a} \in \mathfrak{L}^{k+1}$. A straight-forward calculation shows that $d(\mathbb{d}\mathfrak{a})_i^d = -(\mathbb{d} d\mathfrak{a})_i^d$, thus for all $\mathfrak{a}$

$$\mathfrak{d}\mathfrak{d}\mathfrak{a} = 0 \tag{3.4}$$

and it can furthermore be shown that if $\mathfrak{a} = 0$, and if D is contractible, then there exists $\mathfrak{b} \in \mathfrak{L}^{k-1}$ such that $\mathfrak{a} = \mathfrak{d}\mathfrak{b}$. Thus the mixed-dimensional exterior derivative forms a de Rham complex,

$$0 \to \mathbb{R} \xrightarrow{\subset} \mathfrak{L}^0 \xrightarrow{\mathfrak{d}} \mathfrak{L}^1 \xrightarrow{\mathfrak{d}} \dots \xrightarrow{\mathfrak{d}} \mathfrak{L}^n \to 0 \tag{3.5}$$

which is exact (for the proof of this, and later assertions, please confer [13]).

Due to the jump terms in the differential operators, the natural inner product for the mixed-dimensional geometry must take into account the traces on boundaries, and thus takes the form for $\mathfrak{a}, \mathfrak{b} \in \mathfrak{L}^k$

$$(\mathfrak{a}, \mathfrak{b}) = \sum_{i \in I} \left(\left(a_i^d, b_i^d\right) + \sum_{l \in \breve{\Xi}_i^d} \left(\mathrm{Tr}_{\Omega_l^{d(l)}} a_i^d, \mathrm{Tr}_{\Omega_l^{d(l)}} b_i^d \right) \right) \tag{3.6}$$

Note that $\Lambda^k\left(\Omega_i^d\right) = \emptyset$ whenever $k \notin [0, d]$, thus many of the terms in (3.6) are void. It is easy to verify that equation (3.6) indeed defines an inner product, and thus forms the norm on $\mathfrak{L}^k$

$$\|\mathfrak{a}\| = (\mathfrak{a}, \mathfrak{a})^{1/2} \tag{3.7}$$

The codifferential $\mathfrak{d}^*: \mathfrak{L}^k \to \mathfrak{L}^{k-1}$ is defined as the dual of the exterior derivative with respect to the inner product, such that for $\mathfrak{a} \in \mathfrak{L}^k$

$$(\mathfrak{d}^*\mathfrak{a}, \mathfrak{b}) = (\mathfrak{a}, \mathfrak{d}\mathfrak{b}) + (\mathrm{Tr}\,\mathfrak{b}, \mathrm{Tr}^*\mathfrak{a})_{\partial \mathrm{D}} \qquad \text{for all } \mathfrak{b} \in \mathfrak{L}^{k-1} \tag{3.8}$$

It follows from the properties of inner product spaces that the codifferential also forms an exact de Rham sequence. Thus, when D is contractible, we have the following Helmholtz decomposition: For all $\mathfrak{a} \in \mathfrak{L}^k$, there exist $\mathfrak{a}_\mathfrak{b} \in \mathfrak{L}^{k-1}$ and $\mathfrak{a}_{\mathfrak{d}^*} \in \mathfrak{L}^{k+1}$ such that

$$\mathfrak{a} = \mathfrak{d}\mathfrak{a}_\mathfrak{b} + \mathfrak{d}^*\mathfrak{a}_{\mathfrak{d}^*} \tag{3.9}$$

In view of the uncertainty in the modeling community of the correct constitutive laws for mixed-dimensional problems (as per the discussion of equation (2.11) and (2.12)), it is of great practical utility to be able to explicitly calculate the co-differential, since this will have the structure of the constitutive law. Utilizing equations (3.6) and (3.8), we obtain

$$(\mathfrak{d}^*\mathfrak{b})_i^d = d^* b_i^d \qquad \text{on } \Omega_i^d \tag{3.10}$$

and

$$\mathrm{Tr}_{\partial_l\Omega_i^d}\,(\mathfrak{d}^*\mathfrak{b})_i^d = d^*\mathrm{Tr}_{\partial_l\Omega_i^d}\,b_i^d + \left(\mathrm{Tr}^*_{\partial_l\Omega_i^d}\,b_i^d - \sum_{j\in\xi_i^d}(-1)^{d+k}\varepsilon\left(\Omega_j^{d-1},\partial_j\Omega_i^d\right)b_j^{d-1}\right) \qquad \text{on } \partial\Omega_i^d \tag{3.11}$$

We close this section by noting that the differential operators provide the basis for extending Hilbert spaces to the mixed-dimensional setting. In particular, we are interested in the first order differential spaces, and therefore the norms of $H\mathfrak{L}^k$ and $H^*\mathfrak{L}^k$ by

$$\|\mathfrak{a}\|_H = \|\mathfrak{a}\| + \|\mathfrak{d}\mathfrak{a}\| \qquad \text{and} \qquad \|\mathfrak{a}\|_{H^*} = \|\mathfrak{a}\| + \|\mathfrak{d}^*\mathfrak{a}\| \tag{3.12}$$

from which we obtain the spaces

$$H\mathfrak{L}^k := \{\mathfrak{a}\in\mathfrak{L}^k \,|\, \|\mathfrak{a}\|_H < \infty\} \qquad \text{and} \qquad H^*\mathfrak{L}^k := \{\mathfrak{a}\in\mathfrak{L}^k \,|\|\mathfrak{a}\|_{H^*} < \infty\} \tag{3.13}$$

We use the convention that a circle above the function space denotes homogeneous boundary conditions, i.e. $\mathring{H}\mathfrak{L}^k$: $\{\mathfrak{a}\in H\mathfrak{L}^k \,|\mathrm{Tr}_{\partial D}\,\mathfrak{a}=0\}$ and $\mathring{H}^*\mathfrak{L}^k$: $\{\mathfrak{a}\in H^*\mathfrak{L}^k \,|\mathrm{Tr}^*_{\partial D}\,\mathfrak{a}=0\}$. The spaces $H\mathfrak{L}^k$ and $H^*\mathfrak{L}^k$ can be characterized in terms of product spaces of functions defined on domains Ω_i^d and its boundary components $\partial_j\Omega_i^d$, see e.g. [13, 12].

Then, the Poincaré inequality holds for contractible domains in the mixed-dimensional setting for either $\mathfrak{a}\in\mathring{H}\mathfrak{L}^k\cap H^*\mathfrak{L}^k$ or $\mathfrak{a}\in H\mathfrak{L}^k\cap\mathring{H}^*\mathfrak{L}^k$:

$$\|\mathfrak{a}\| \le C_\Omega(\|\mathfrak{d}\mathfrak{a}\| + \|\mathfrak{d}^*\mathfrak{a}\|) \tag{3.14}$$

4. Mixed-dimensional elliptic PDEs

Based on the extension of the exterior derivative and its dual to the mixed-dimensional setting, we are now prepared to define the generalization of elliptic PDEs. We start by considering the minimization problem equivalent to the Hodge Laplacian for $\mathfrak{a}\in\mathfrak{L}^k$

$$\mathfrak{a} = \arg\inf_{\mathfrak{a}\in\mathring{H}\mathfrak{L}^k\cap H^*\mathfrak{L}^k} J_{\mathfrak{K}}(\mathfrak{a}') \tag{4.1}$$

where we define the functional by

$$J_{\mathfrak{K}}(\mathfrak{a}') = \frac{1}{2}(\mathfrak{K}\mathfrak{d}^*\mathfrak{a}',\mathfrak{d}^*\mathfrak{a}') + \frac{1}{2}(\mathfrak{K}^*\mathfrak{d}\mathfrak{a}',\mathfrak{d}\mathfrak{a}') - (\mathfrak{f},\mathfrak{a}') \tag{4.2}$$

The material coefficients $\mathfrak{K}$ are spatially variable mappings from $\Lambda^{k-(n-d(i))}\left(\Omega_i^d\right)$ onto itself, defined independently for all terms in the inner product (3.6). In particular, with reference to section 2, $\mathfrak{K}$ contains all instances of the proportionality constants K appearing in (2.9), (2.10) and (2.12).

For equation (4.1) to be well-posed and have a unique solution, we need $(\mathfrak{K}\mathfrak{d}^*\mathfrak{a}',\mathfrak{d}^*\mathfrak{a}') + (\mathfrak{K}^*\mathfrak{d}\mathfrak{a}',\mathfrak{d}\mathfrak{a}')$ to be continuous and coercive, i.e. we need to impose constraints on $\mathfrak{K}$ and $\mathfrak{K}^*$. Indeed, by reverting to the definition of the inner product, we define the ellipticity constant $\alpha_{\mathfrak{K}}$ as the minimum eigenvalue of $\mathfrak{K}$, and similarly for $\alpha_{\mathfrak{K}^*}$. We require both these constants to be bounded above zero, such that

$$(\mathfrak{K}\mathfrak{d}^*\mathfrak{a}',\mathfrak{d}^*\mathfrak{a}') + (\mathfrak{K}^*\mathfrak{d}\mathfrak{a}',\mathfrak{d}\mathfrak{a}') \ge \min(\alpha_{\mathfrak{K}},\alpha_{\mathfrak{K}^*})\,(1+C_\Omega)^2\|\mathfrak{a}'\|^2$$

The minimum of equation (4.1) must satisfy the Euler-Lagrange equations, thus $\mathfrak{a} \in \mathring{H}\mathfrak{L}^k \cap H^*\mathfrak{L}^k$ satisfies

$$(\mathfrak{K}\mathfrak{d}^*\mathfrak{a}, \mathfrak{d}^*\mathfrak{a}') + (\mathfrak{K}^*\mathfrak{d}\mathfrak{a}, \mathfrak{d}\mathfrak{a}') = (\mathfrak{f}, \mathfrak{a}') \qquad \text{for all } \mathfrak{a}' \in \mathring{H}\mathfrak{L}^k \cap H^*\mathfrak{L}^k \tag{4.3}$$

From the perspective of applications, and mirroring the distinctions between conservation laws and constitutive laws discussed in Section 2, we will be interested in the mixed formulation of equation (4.3) obtained by introducing the variable $\mathfrak{b} = \mathfrak{K}\mathfrak{d}^*\mathfrak{a}$, where $\mathfrak{b}$ is the generalization of the various fluxes $\boldsymbol{u}$. Then we may either consider a constrained minimization problem derived from equation (4.1), or for the sake of brevity, proceed directly to the Euler-Lagrange formulation: Find $(\mathfrak{a}, \mathfrak{b}) \in H\mathfrak{L}^k \times H\mathfrak{L}^{k-1}$ which satisfy

$$(\mathfrak{K}^{-1}\mathfrak{b}, \mathfrak{b}') - (\mathfrak{a}, \mathfrak{d}\mathfrak{b}') = 0 \qquad \text{for all } \mathfrak{b}' \in H\mathfrak{L}^{k-1} \tag{4.4}$$

$$(\mathfrak{d}\mathfrak{b}, \mathfrak{a}') + (\mathfrak{K}^*\mathfrak{d}\mathfrak{a}, \mathfrak{d}\mathfrak{a}') = (\mathfrak{f}, \mathfrak{a}') \qquad \text{for all } \mathfrak{a}' \in H\mathfrak{L}^k \tag{4.5}$$

The saddle-point formulation is well-posed subject to Babuška-Aziz inf-sup condition. Due to the presence of a Helmholtz decomposition, this follows by standard arguments. From equations (4.4) and (4.5) we deduce the strong form of the Hodge Laplacian on mixed form, corresponding to the equations

$$\mathfrak{b} = \mathfrak{K}\mathfrak{d}^*\mathfrak{a} \qquad \text{and} \qquad \mathfrak{d}\mathfrak{b} + \mathfrak{d}^*(\mathfrak{K}^*\mathfrak{d}\mathfrak{a}) = \mathfrak{f} \tag{4.6}$$

Of the various formulations, equations (4.4) and (4.5) are particularly appealing from the perspective of practical computations, as they do not require the coderivative.

An important remark is that the relative simplicity of the well-posedness analysis for the mixed-dimensional equations relies on the definition of the function spaces and norms. In particular, due to the definition of $H\mathfrak{L}^k$ via the mixed-dimensional differential $\mathfrak{d}$, the norm on the function space is inherently also mixed-dimensional, and cannot simply be decomposed into, say norms on the function spaces $H\Lambda^{k-(n-d)}(\Omega_i^d)$. For this reason, analysis in terms of "local norms" becomes significantly more involved [17, 18, 11].

5. Finite-dimensional spaces

In order to exploit the mixed-dimensional formulations from the preceding section, and in particular equations (4.4-4.5) we wish to consider finite-dimensional subspaces of $H\mathfrak{L}^k$. These spaces should be constructed to inherit the de Rham structure of equation (3.5), and with bounded projection operators. A natural approach is to consider the polynomial finite element spaces as a starting point [15].

From the finite element exterior calculus (FEEC - [15]), we know that on the highest-dimensional domains Ω_i^d, we may choose any of the finite element de Rham sequences, and in particular, we may consider the standard spaces from applications for a simplicial tessellation $\mathcal{T}_i^n = \mathcal{T}(\Omega_i^n)$

$$\mathcal{P}_r\Lambda^k(\mathcal{T}_i^n) \qquad \text{and} \qquad \mathcal{P}_r^-\Lambda^k(\mathcal{T}_i^n) \tag{5.1}$$

These correspond to the full and reduced polynomial spaces of order r, respectively, in the sense of [15]. In order to build a finite element de Rham sequence, we recall that (while still commuting with bounded projection operators) the full polynomial spaces reduce order

$$\mathcal{P}_r\Lambda^k(\mathcal{T}^n) \xrightarrow{d} \mathcal{P}_{r-1}\Lambda^{k+1}(\mathcal{T}^n) \tag{5.2}$$

while the reduced spaces preserve order

$$\mathcal{P}_r^-\Lambda^k(\mathcal{T}^n) \xrightarrow{d} \mathcal{P}_r^-\Lambda^{k+1}(\mathcal{T}^n) \tag{5.3}$$

Thus, any of these combinations of spaces are acceptable for Ω_i^n, and consider therefore the choice as given, and denoted by $\Lambda_h^{k,n}$ and $\Lambda_h^{k+1,n}$.

For $d < n$, we must consider not only the continuous differential operator d, but also the discrete jump operator $\mathbb{d}$. It is therefore clear that for i.e. $d = n - 1$, we must consider the traces of the finite element spaces of higher dimensions. In particular, we require for all pairs of dimensions $0 \leq e < d \leq n$,

$$\mathrm{Tr}_{\Omega_i^e}\, \Lambda_h^k(\mathcal{T}^d) \subseteq \Lambda_h^{k+(n-e)}(\mathcal{T}^e) \tag{5.4}$$

In contrast to the continuous differential order, the discrete differential operator preserves order for both the full and reduced spaces, since [15]:

$$\mathrm{Tr}_{\Omega^e}\, \mathcal{P}_r\Lambda^k(\mathcal{T}^d) = \mathcal{P}_r\Lambda^{k+(n-e)}(\mathcal{T}^e) \qquad \text{and} \qquad \mathrm{Tr}_{\Omega^e}\, \mathcal{P}_r^-\Lambda^k(\mathcal{T}^d) = \mathcal{P}_r^-\Lambda^{k+(n-e)}(\mathcal{T}^e) \tag{5.5}$$

We now define the polynomial subspaces $\mathcal{P}_{\mathfrak{r}}^{\mathfrak{m}}\mathfrak{Q}^k \in H\mathfrak{Q}^k$ as

$$\left(\mathcal{P}_{\mathfrak{r}}^{\mathfrak{m}}\mathfrak{Q}^k\right)_i^d = \mathcal{P}_{r_i^d}^{p_i^d}\Lambda^{k-(n-d)}(\mathcal{T}_i^d) \tag{5.6}$$

where the multi-indexes $\mathfrak{r}$ and $\mathfrak{m}$ have values $r_i^d \in \mathbb{P}$ and $m_i^d \in [\,, -]$, respectively. When the multi-indexes are chosen to satisfy both (5.2-5.3) as well as (5.4), we obtain the discrete de Rham complex

$$0 \to \mathbb{R} \hookrightarrow \mathcal{P}_{\mathfrak{r}}^{\mathfrak{m}}\mathfrak{Q}^0 \xrightarrow{\mathfrak{d}} \mathcal{P}_{\mathfrak{r}}^{\mathfrak{m}}\mathfrak{Q}^1 \xrightarrow{\mathfrak{d}} \dots \xrightarrow{\mathfrak{d}} \mathcal{P}_{\mathfrak{r}}^{\mathfrak{m}}\mathfrak{Q}^n \to 0 \tag{5.7}$$

Due to the existence of stable projections for all finite element spaces in $\mathcal{P}_{\mathfrak{r}}^{\mathfrak{m}}\mathfrak{Q}^k$, the discrete de Rham sequence can be shown to be exact, thus equations (4.4) and (4.5) have stable approximations.

The discrete spaces for $H^*\mathfrak{Q}^k$ must satisfy similar properties. Equations (5.2-5.3) hold in the dual sense, i.e. we write $\mathcal{P}_r^*\Lambda^k(\mathcal{T}_i^d) = \mathcal{P}_r^*\Lambda^k(\mathcal{T}_i^d) =\star (\mathcal{P}_r\Lambda^{d-k}(\mathcal{T}_i^d)$, and $d^*\mathcal{P}_r^*\Lambda^k(\mathcal{T}_i^d) \subset \mathcal{P}_r^{-*}\Lambda^{k-1}(\mathcal{T}_i^d) \subset \mathcal{P}_{r-1}^*\Lambda^{k-1}(\mathcal{T}_i^d)$. Furthermore, the coderivative $\mathfrak{d}^*$ imposes the inverted condition $\Lambda_h^{k+(n-e)}(\mathcal{T}^e) \subseteq \mathrm{Tr}_{\Omega_i^{n-1}}^*\, \Lambda_h^k(\mathcal{T}^d)$ on boundaries.

6. Implications in terms of classical calculus

We take a moment to untangle the notation from Sections 3-5 in order to extract insight into modeling and discretization for the original physical problem.

Our initial task is to express simplest form of the mixed-dimensional Hodge Laplacian in terms of conventional notation. We limit the discussion to the case where $k = n$, the function spaces $H^*\mathfrak{Q}^n$ and $H\mathfrak{Q}^{n-1}$ correspond to H_1 scalars and $H(div)$ vectors on each dimension $d \geq 1$. For $d = 0$, only the scalars are defined. Furthermore, the term $\mathfrak{d}\mathfrak{a} \in \mathfrak{Q}^{n+1} = \emptyset$, and thus we arrive from (4.6) to the simpler problem

$$\mathfrak{b} = \mathfrak{K}\mathfrak{d}^{*}\mathfrak{a} \qquad \text{and} \qquad \mathfrak{d}\mathfrak{b} = \mathfrak{f} \tag{6.1}$$

In this case, the exterior derivative is the negative divergence plus jumps for each domain, while the codifferential is the gradient parallel to each domain, and the difference from boundaries perpendicular. As such, we arrive exactly at the model equations of Section 2, with the second choice of modeling assumption (2.12).

Turning our attention to the finite element spaces, the lowest order spaces for discretizing (4.4-4.5) are the reduced spaces obtained by choosing $r_i^d = 1$ and $m_i^d = -$, from which we obtain piecewise constants for $\mathfrak{a}$ on all domains, while we obtain for $\mathfrak{b}$ the Nedelec 1st kind (div) – Raviart-Thomas – continuous Lagrange elements for domains with dimensions $d = 3,2,1$, respectively – all of the lowest order [12] (this method will be referred to as "Mixed Reduced" in the next section). Interestingly, if we choose Nedelec 2nd kind (div) elements of lowest order for $d = 3$, equations (5.2) and (5.5) implies that we should increase the order in the lower-dimensional domains, obtaining dG elements of order $n - d$ for pressure, with BDM (2nd order) – continuous Lagrange (3rd order) for fluxes in domains with $d = 2,1$. This is a new method resulting from the analysis herein. We refer to this method as "Mixed Full".

The mixed finite element discretization has the advantage of a strong conservation principle, and may be hybridized to obtain a cheaper numerical scheme (see [12] for a direct approach in this context, but also [6, 5] for direct constructions in the finite volume setting). Alternatively, we consider discretizing the Euler-variation of the unconstrained minimization problem, equations (4.3). The natural finite element spaces are $\mathcal{P}_{\mathrm{r}}^{\mathfrak{m},*}\mathfrak{L}^n$, with $r_i^d = 1$ and $\mathfrak{m}$ does come into play, corresponding to 1st-order continuous Lagrange elements in all dimensions. From an engineering perspective, a similar formulation has been described in [19], we refer to this method as "Primal" in the next section.

7. Computational example

In order to illustrate the concepts discussed in the preceding sections, we will continue to consider $k = n$, and thus fractured porous media as a computational example, using the three numerical methods obtained using the lowest-order elements of the families described in the previous section.

The example consists of the unit square with two fractures crossing through the domain, intersecting at a right angle, as illustrated in figures 3. We impose unit permeability in the surroundings, set the normal and tangential permeability of the fractures to 100 and assume the apertures of both fractures as $\epsilon = 10^{-3}$. The boundary conditions are chosen as zero pressure at the bottom and no-flux conditions on the sides. Moreover, a boundary pressure of one is imposed on the fracture crossing the top boundary. All computations were performed with the use of FEniCS [20].

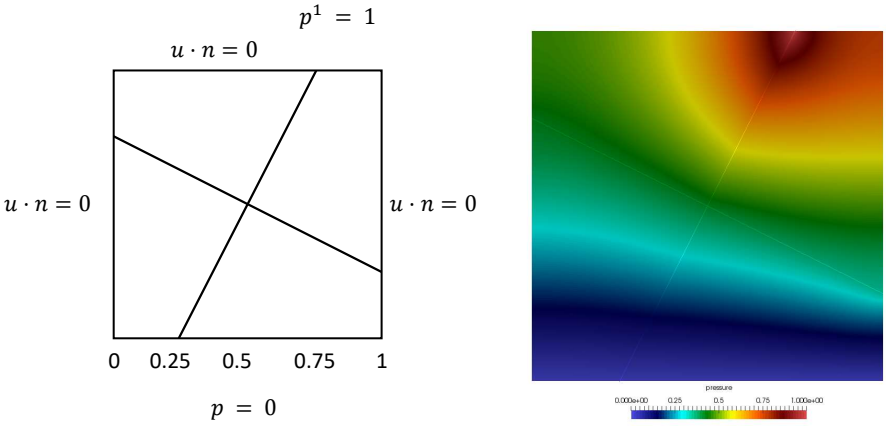

Figure 3: (Left) Domain of computation and associated boundary conditions. The pressure boundary condition is only imposed on the fracture pressure. (Right) Example of calculated solution (pressure).

The results show that all three methods are stable and convergent (Table 1). The relative errors and L^2-convergence rates after four consecutive refinements (identified by the characteristic grid size h) are given in the following table. Here, we compare the results to a fine-scale solution, obtained after a fifth refinement. In this example, all grids are matching.

		Primal		Mixed Reduced				Mixed Full			
Domain	Grid size	Pressure		Pressure		Flux		Pressure		Flux	
	h	Error	Rate	Error	Rate	Error	Rate	Error	Rate	Error	Rate
Ω^0	2^{-4}	2.66e-03	1.53	2.21e-03	1.52			2.89e-04	1.61		
	2^{-5}	8.45e-04	1.65	7.18e-04	1.62	N/A	N/A	8.99e-05	1.69	N/A	N/A
	2^{-6}	2.15e-04	1.97	1.87e-04	1.94			2.26e-05	1.99		
Ω^1	2^{-4}	2.54e-03	1.46	1.89e-02	1.01	6.32e-03	1.22	3.01e-04	1.71	1.84e-03	1.28
	2^{-5}	9.57e-04	1.41	9.22e-03	1.04	2.49e-03	1.34	8.99e-05	1.74	7.44e-04	1.30
	2^{-6}	3.23e-04	1.57	4.12e-03	1.16	7.82e-04	1.67	2.37e-05	1.92	2.61e-04	1.51
Ω^2	2^{-4}	4.25e-03	1.53	1.89e-02	1.02	8.21e-02	0.74	1.86e-02	1.01	3.16e-02	0.75
	2^{-5}	1.36e-03	1.64	9.17e-03	1.05	4.75e-02	0.79	9.11e-03	1.03	1.87e-02	0.75
	2^{-6}	3.60e-04	1.92	4.08e-03	1.17	2.47e-02	0.94	4.07e-03	1.16	1.04e-02	0.86

Table 1: Convergence rates for the three FE and MFEM discussed for the fracture problem in Section 6. With reference to Figure 3, the domain Ω^0 is the intersection point, Ω^1 represents the four fracture segments, while Ω^2 is the remaining ambient geometry.

Each method captures the intersection pressure well, with second order convergence over all. In the surroundings, the pressure convergence with second order for the primal formulation and first order for both mixed formulations, as expected. The Mixed Full method has higher-order elements in the fracture, and this is reflected in higher convergence rates for both pressure and flux.

Acknowledgments

The authors wish to thank Gunnar Fløystad, Eirik Keilegavlen, Jon Eivind Vatne and Ivan Yotov for valuable comments and discussions on this topic. The authors also with to thank the two anonymous reviewers who provided helpful comments on the initial version of this manuscript. This research is funded in part by the Norwegian Research Council grants: 233736 and 250223.

References

[1] J. M. Nordbotten and M. A. Celia, Geological Storage of CO2: Modeling Approaches for Large-Scale Simulation, Hoboken, N. J.: Wiley, 2012.

[2] J. Bear, Hydraulics of Groundwater, McGraw-Hill, 1979.

[3] P. G. Ciarlet, Mathematical Elasticity Volume II: Theory of Plates, Amsterdam: Elsevier, 1997.

[4] C. Alboin, J. Jaffré, J. E. Roberts and C. Serres, "Domain decomposition for flow in porous media with fractures," in *14th conference on Domain Decomposition Methods in Sciences and Engineering*, Cocoyoc, Mexico, 1999.

[5] T. H. Sandve, I. Berre and J. M. Nordbotten, "An efficient multi-point flux approximation method for discrete fracture-matrix simulations," *Journal of Computational Physics,* vol. 231, pp. 3784-3800, 2012.

[6] M. Karimi-Fard, L. J. Durlofsky and K. Aziz, "An effcient discrete-fracture model applicable for general-purpose reservoir simulations," *SPE Journal,* pp. 227-236, 2004.

[7] V. Martin, J. Jaffré and J. E. Roberts, "Modeling fractures and barriers as interfaces for flow in porous media," *SIAM Journal of Scientiffic Computing,* vol. 26, pp. 1557-1691, 2005.

[8] M. W. Licht, "Complexes of discrete distributional differential forms and their homology theory," *Foundations of Computational Mathematics,* 2016.

[9] Y. C. Yortsos, "A theoretical analysis of vertical flow equilibrium," *Transport in Porous Media,* vol. 18, pp. 107-129, 1995.

[10] N. Schwenk, B. Flemisch, R. Helmig and B. I. Wohlmuth, "Dimensionally reduced flow models in fractured porous media," *Computational Geosciences,* vol. 16, pp. 277-296, 2012.

[11] L. Formaggia, A. Fumagalli, A. Scotti and P. Ruffo, "A Reduced Model for Darcy's Problem in Networks of Fractures," *ESAIM: Mathematical Modelling and Numerical Analysis,* vol. 48, pp. 1089-1116, 2014.

[12] W. M. Boon, J. M. Nordbotten and I. Yotov, "Robust discretization of flow in fractured porous media," in preparation.

[13] W. M. Boon, J. M. Nordbotten and J. E. Vatne, "Exterior calculus for mixed-dimensional partial differential equations," in preparation.

[14] M. Spivak, Calculus on Manifolds, Reading, Massachusetts: Addison-Wesley Publishing Company, 1965.

[15] D. N. Arnold, R. S. Falk and R. Winther, "Finite element exterior calculus, homological techniques, and applications," *Acta Numerica,* vol. 15, pp. 1-155, 2006.

[16] R. Hiptmair, "Finite elements in computational electromagnetism," *Acta Numerica,* vol. 11, pp. 237-339, 2002.

[17] C. D'Angelo and A. Scotti, "A Mixed Finite Element Method for Darcy Flow in Fractured Porous Media with Non-Matching Grids," *ESAIM: Mathematical Modelling and Numerical Analysis,* pp. 465-489, 2012.

[18] N. Frih, V. Martin, J. E. Roberts and A. Saada, "Modeling Fractures as Interfaces with Nonmatching Grids," *Computational Geosciences,* vol. 16, pp. 1043-10060, 2012.

[19] R. Helmig, C. Braun and M. Emmert, "MUFTE: A Numerical Model for Simulation of Multiphase Flow Processes in Porous and Fractured Porous Media," Universität Stuttgart, 1994.

[20] A. Logg, K.-A. Mardal, G. N. Wells and e. al, Automated Solution of Differential Equations by the Finite Element Method, Springer, 2012.

[21] X. Tunc, F. I., T. Gallouët, M. C. Cacas and P. Havé, "A model for conductive faults with non-matching grids," *Computational Geosciences,* vol. 16, pp. 277-296, 2012.

[22] X. Claeys and R. Hiptmair, "Integral equations on multi-screens," *Integral Equations and Operator Theory,* 2013.

Paper D

Benchmarks for Single-phase Flow in Fractured Porous Media

B. Flemisch, I. Berre, W.M. Boon, A. Fumagalli, N. Schwenck, A. Scotti, I. Stefansson, A. Tatomir

Advances in Water Resources 111, (2018), p. 239–258.

doi: 10.1016/j.advwatres.2017.10.036

Advances in Water Resources 111 (2018) 239–258

Contents lists available at ScienceDirect

Advances in Water Resources

journal homepage: www.elsevier.com/locate/advwatres

Benchmarks for single-phase flow in fractured porous media

Bernd Flemisch[*,a], Inga Berre[b], Wietse Boon[b], Alessio Fumagalli[b], Nicolas Schwenck[a], Anna Scotti[c], Ivar Stefansson[b], Alexandru Tatomir[d]

[a] Department of Hydromechanics and Modelling of Hydrosystems, University of Stuttgart, Pfaffenwaldring 61, Stuttgart 70569, Germany
[b] Department of Mathematics, University of Bergen, Allégaten 41, Bergen 5007, Norway
[c] Laboratory for Modeling and Scientific Computing MOX, Politecnico di Milano, p.za Leonardo da Vinci 32, Milano 20133, Italy
[d] Department of Applied Geology, Geosciences Center, University of Göttingen, Goldschmidtstrasse 3, Göttingen 37077, Germany

ARTICLE INFO

Keywords:
Fractured porous media
Discretization methods
Benchmark

ABSTRACT

This paper presents several test cases intended to be benchmarks for numerical schemes for single-phase fluid flow in fractured porous media. A number of solution strategies are compared, including a vertex and two cell-centred finite volume methods, a non-conforming embedded discrete fracture model, a primal and a dual extended finite element formulation, and a mortar discrete fracture model. The proposed benchmarks test the schemes by increasing the difficulties in terms of network geometry, e.g. intersecting fractures, and physical parameters, e.g. low and high fracture-matrix permeability ratio as well as heterogeneous fracture permeabilities. For each problem, the results presented are the number of unknowns, the approximation errors in the porous matrix and in the fractures with respect to a reference solution, and the sparsity and condition number of the discretized linear system. All data and meshes used in this study are publicly available for further comparisons.

1. Introduction

In porous-media flow applications, the domains of interest often contain geometrically anisotropic inclusions and strongly discontinuous material coefficients that can span several orders of magnitude. If the size of these heterogeneities is small in normal direction compared to the tangential directions, these features are called fractures. Fractures can act both as conduits and barriers and affect flow patterns severely. Target applications concerning fractured porous-media systems in earth sciences include groundwater resource management, renewable energy storage, recovery of petroleum resources, radioactive waste reposition, coal bed methane migration in mines, and geothermal energy production.

The analysis and prediction of flow in fractured porous media systems are important for all the aforementioned applications. Many different conceptual and numerical models of flow in fractured porous-media systems can be found in the literature. Even though fractured porous-media systems have been of interest to modelers for a long time, they still present challenges for simulators. During the last 70 years, different modeling approaches have been developed and gradually improved. Comprehensive reviews can be found in Berkowitz (2002), Dietrich et al. (2005), Hoteit and Firoozabadi (2008), Neumann (2005), Sahimi (2011) and Singhal and Gupta (2010). Roughly, the fractured porous media systems are classified in two broad categories: discrete fracture-matrix (DFM) models and continuum fracture models. Within this paper, we will only consider DFM models.

The DFM models consider flow occurring in both the fracture network and the surrounding rock matrix. They account explicitly for the effects of individual fractures on the fluid flow. An efficient way to represent fractures in DFMs is the hybrid-dimensional approach, see e.g. Helmig (1997), Flauraud et al. (2003), Bogdanov et al. (2003), Firoozabadi and Monteagudo (2004), Karimi-Fard et al. (2004), Martin et al. (2005) and Reichenberger et al. (2006). Fractures in the geometrical domain are then discretized with elements of co-dimension one with respect to the dimension of the surrounding matrix, such as one-dimensional elements in two-dimensional settings. Due to the similarities in these models, the gradient scheme framework (Brenner et al., 2016; 2017) allows for a unified analysis of a number of DFM models. The aforementioned classical DFM approaches all rely on matching fracture and matrix grids in the sense that a fracture element coincides geometrically with co-dimension-one mesh entities, i.e. faces of matrix grid elements. In addition to the classical models, several so-called non-conforming DFM models have been developed in recent years, such as EDFM (Hajibeygi et al., 2011; Moinfar et al., 2014), XFEM-based approaches (D'Angelo and Scotti, 2012; Huang et al., 2011; Schwenck et al., 2015), or mortar-type methods (Frih et al., 2012).

* Corresponding author.
E-mail address: bernd.flemisch@iws.uni-stuttgart.de (B. Flemisch).

https://doi.org/10.1016/j.advwatres.2017.10.036
Received 5 January 2017; Received in revised form 27 October 2017; Accepted 30 October 2017
Available online 31 October 2017
0309-1708/

Benchmarking represents a methodology for verifying, testing and comparing the modeling tools. Various codes have been developed by academic institutions or companies based on different conceptual, mathematical, and numerical models. Even though benchmarking studies are increasing in all fields of engineering and workshops have been organized around specific problems (e.g. Class et al., 2009), there are still only a limited number of studies. Some are related to a specific application and are flexible as to how the problem is modeled in terms of assumptions regarding the physics and the selection of the domain, see Class et al. (2009), Nordbotten et al. (2012), Caers (2013) and Kolditz et al. (2015). Others De Dreuzy et al. (2013) and Caers (2013), like ours, focus on the comparison of numerical schemes.

One of the common requirements when selecting the test problems for comparing numerical schemes is that they allow the examination of the capabilities of each of the compared methods. Therefore, our benchmark study proposes a set of problems starting from simple geometries and then gradually increasing the geometrical complexity. The test problems are specifically selected to make clear distinctions between the different methods. They consist of existing and new computational benchmarks for fluid flow in fractured porous media and allow for comparison of several DFM-based numerical schemes in a systematic way.

We would like to invite the scientific community to follow up on this study and evaluate further methods by means of the proposed benchmarks. In order to facilitate this, the paper is accompanied by grid and result files in the form of a Git repository at https://git.iws.uni-stuttgart.de/benchmarks/fracture-flow.

The remainder of this paper is organized as follows. In Section 2, we formulate the model problem in terms of the partial differential equation to be solved. The participating DFM models are described in Section 3. The central Section 4 proposes the benchmarks and compares the results of the different methods. Finally, Section 5 concludes with a summary and outlook.

2. The model problem

We consider an incompressible single-phase flow through a porous medium, assumed to be described by Darcy's law, resulting in the governing system of equations

$$\mathbf{u} = -\mathbb{K}\,\mathbf{grad}\,p, \tag{1a}$$

$$div\,\mathbf{u} = q, \tag{1b}$$

in an open bounded domain $\mathscr{D} \subset \mathbb{R}^N$, subject to boundary conditions

$$p = p_D \quad \text{on } \partial\mathscr{D}_D, \tag{1c}$$

$$\mathbf{u}\cdot\mathbf{n} = q_N \quad \text{on } \partial\mathscr{D}_N, \tag{1d}$$

with $\partial\mathscr{D} = \overline{\partial\mathscr{D}_D \cup \partial\mathscr{D}_N}$ and $\partial\mathscr{D}_D \cap \partial\mathscr{D}_N = \emptyset$. In Eq. (1) $\mathbf{u}$ denotes the macroscopic fluid velocity whereas $\mathbb{K}$ and p stand for absolute permeability and pressure.

Let us assume that $\mathscr{D}$ contains several fractures, that all together constitute a single domain Γ of spatial dimension N such that $\Gamma \subset \mathscr{D}$, which is a possibly unconnected, open subset of $\mathscr{D}$. The surrounding porous rock, namely, the remaining part of $\mathscr{D}$, is called $\Omega = \mathscr{D}\backslash\overline{\Gamma}$. Assuming that the fracture aperture ε at each point of Γ is small compared to other characteristic dimensions of the fractures, the full-dimensional domain Γ can be reduced to the $(N-1)$-dimensional fracture network γ. This reduction involves modeling choices resulting in different hybrid-dimensional problem formulations that form the basis for the methods presented in the following section.

3. Participating discretization methods

Within this section, the discretization methods participating in this benchmark study are described. The purpose of this article is the comparison of well-known, established and/or at least published methods. Therefore, only the most significant aspects of each method are summarized. We do not show a comparison against analytical solutions here. The analysis of the methods and theoretical results such as proofs of optimal convergence can be found in the corresponding references. A summary of all participating methods is provided in Table 1. In the sequel, we will denote with *d.o.f.* the degrees of freedom associated to a specific method. We indicate also the type of conformity required to the computational grid with respect to the fractures and the assumption that the pressure is considered continuous across the fractures. With the exception of P-XFEM, all considered methods are locally conservative by construction.

Table 1
Participating discretization methods.

Method	d.o.f.	frac-dim	conforming	*p*-cont
Box	p (vert)	dim-1	yes	yes
TPFA	p (elem)	dim-1	yes	no
MPFA	p (elem)	dim-1	yes	no
EDFM	p (elem)	dim-1	no	yes
Flux-Mortar	p (elem), $\boldsymbol{u}$ (faces)	dim-1	geometrically	no
P-XFEM	p (vert)	dim-1	no	no
D-XFEM	p (elem), $\boldsymbol{u}$ (faces)	dim-1	no	no
MFD	p (faces)	dim	geometrically	no

The lower-dimensional representation of fractures allows for easier mesh generation for both conforming and non-conforming methods in comparison to the equi-dimensional approach, as it circumvents the appearance of very small elements when discretizing the interior of the fracture (i.e., within the fracture width). Conform meshing implies that the fractures are discretized with a set of line elements (in a 2D domain) that are also the edges of the triangular finite elements.

3.1. Vertex-centred, continuous-pressure, conforming lower-dimensional DFM (Box)

The Box method is a vertex-centred finite-volume method proposed in e.g. Helmig (1997) which combines the advantages of finite element and finite volume grids, allowing unstructured grids and guaranteeing a locally conservative scheme (Reichenberger et al., 2006). Fig. 1 illustrates a two-dimensional representation of the dual-grid with two finite elements E_1 and E_5 sharing the same edge $(ij)_1$ that represents a lower-dimensional fracture with the aperture ε_{ij_1}. The main characteristic in terms of the fractured system is that the pressure is required to be continuous, in particular in those vertices whose control volumes overlap both fracture and matrix regions.

The Box method used for this paper is implemented in the open-source numerical simulator DuMu^x. A detailed description of the conceptual, mathematical and numerical model and code implementation is published in Tatomir (2012). The simulation code used for the benchmark studies is publicly available under https://git.iws.uni-stuttgart.de/dumux-pub/Flemisch2016a.git.

3.2. Cell-centred, discontinuous-pressure, conforming DFM (TPFA)

The control volume finite difference method uses a two-point flux approximation (TPFA) based on the cell-centre pressure values for the evaluation of the face fluxes. The method is a widely applied and standard method for simulation of flow in porous media. The domain is partitioned with fractures coinciding with the interior faces between matrix cells just as described at the beginning of Section 3. The flux over the face between matrix cells i and j is approximated by

$$\mathbf{u}_{ij} = T_{ij}(p_i - p_j), \tag{2}$$

where p_i and p_j are the pressures in the neighbouring cells and T_{ij} is the face transmissibility, computed as the harmonic average of the two half

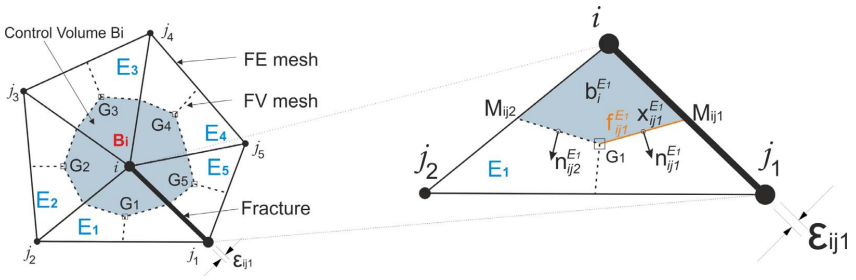

Fig. 1. Conceptual representation of the Box method: (left-hand side) The dual finite element and finite volume mesh from which the control volume B_i around node i is created. Node i is surrounded by nodes $\{j_1, j_2, j_3, j_4, j_5\}$, where segment ij_1 represents both a fracture and a shared FE edge; (right-hand side) Sub-control volume (SCV) $b_i^{E_1}$ in element E_1 has barycentre G_1 and the mid-points of the edges ij_1 and ij_2 are M_{ij1}, respectively M_{ij2}. The SCV face $f_{ij1}^{E_1}$ is the segment $\overline{G_1 M_{ij1}}$ which contains the integration point $x_{ij1}^{E_1}$ where the normal vector $\mathbf{n}_{ij1}^{E_1}$ is applied.

transmissibilities corresponding to the face and the two cells. The half transmissibility of cell-face pair i is in turn given as

$$\alpha_i = \frac{A_i \mathbf{n}_i^\top \mathbb{K}_i}{\mathbf{d}_i^\top \mathbf{d}_i} \cdot \mathbf{d}_i, \tag{3}$$

where A_i and $\mathbf{n}_i$ are the area and unit normal vector of the face, $\mathbb{K}_i$ is the permeability assigned to the cell and $\mathbf{d}_i$ is the distance vector from cell centre to face centroid.

In addition to the unknowns given at the centroids of the matrix cells, unknowns are associated to the centroids of the fracture cells. The fracture cells are associated with apertures, which multiplied with the length give the volume of these cells. The aperture is also used to construct hybrid faces for the matrix-fracture interfaces. These faces, parallel to the fracture but displaced half an aperture to either side, enable us to compute the half transmissibilities between the fracture cell and the matrix cells on the two sides. These faces are indicated by the dashed blue lines in Fig. 2, where the computational domain is superimposed on the geometrical grid. The result is a hybrid grid with fractures which are lower dimensional in the grid, but equi-dimensional in the computational domain at the cost of a small matrix volume error corresponding to the overlap of the matrix cells with the fracture cells.

Following the method proposed by Karimi-Fard et al. (2004), the intermediate fracture intersection cell drawn with dashed red lines in Fig. 2 is removed, leading to direct coupling of the fracture cells neighbour to the intersection. The purpose of this is both to obtain a smaller condition number and to avoid severe time-step restrictions associated with small cells in transport simulations. To each new face between cell i and j, face transmissibilities are assigned, calculated using the star delta transformation as described in Karimi-Fard et al. (2004):

$$T_{ij} = \frac{\alpha_i \alpha_j}{\sum_{k=1}^{n} \alpha_k}, \tag{4}$$

with n denoting the number of fracture cells meeting at the intersection.

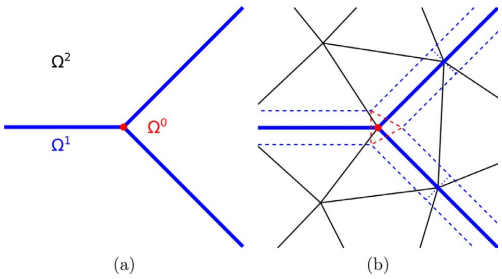

Fig. 2. (a) Conceptual decomposition of the domain according to element dimension with the matrix depicted in black, fractures in blue and their intersections in red. (b) The computational domain of the TPFA method. Dashed lines are faces of the fracture cells. (For interpretation of the references to colour in this figure legend, the reader is referred to the web version of this article.)

As this elimination disregards all information on the permeability of the intersection, it should be used with caution in cases of crossing fractures of different permeability. We encounter this feature in Section 4.3, and include results both with and without the elimination for one of the test cases presented in that section.

3.3. Cell-centred, discontinuous-pressure, conforming DFM (MPFA)

Inspired by the TPFA method presented above, a method based on the multi-point flux approximation has been developed (Sandve et al., 2012), see also e.g. Ahmed et al. (2015). The MPFA variant of the method reduces errors associated with the TPFA approach for grids that are not close to K-orthogonal, and avoids errors related to the splitting of the fluxes in the star-delta transformation. The method is constructed letting each face flux depend on the pressures of several of the neighbouring cells. Specifically, an interaction region defined by cell centroids and continuity points at the faces around each node is constructed (see Fig. 3) and the pressure is assumed to be linear within each cell of the region. Intermediate pressure unknowns are introduced at the continuity points and express the flux over each half face in terms of the weighted pressures of all cell centre and continuity point pressures of the region. Continuity of the flux over each face allows for elimination of the continuity point pressures and a relationship between flux and pressure of the form

$$\mathbf{u}_i = \mathbb{T}_i \mathbf{p} \tag{5}$$

for each half face i is obtained. Here, $\mathbf{p}$ denotes the pressures at the cell centres of the interaction region and $\mathbb{T}_i$ accounts for the effect of geometry and permeability of those same cells. For a detailed description of the method, see, e.g., Aavatsmark (2002).

The handling of the fractures is similar to the one described for the TPFA. For the fracture intersections, the pressure is assumed to be

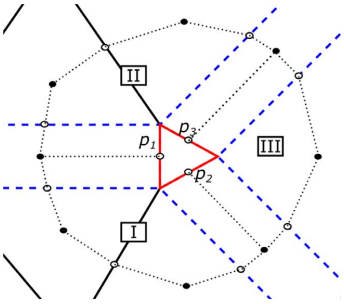

Fig. 3. The three interaction regions (dotted lines) around one fracture intersection for the MPFA consisting of four (I and II) and three (III) sub cells each. The continuity points are marked by circles and the cell centres by black dots. Fracture-matrix faces are depicted by blue dashed lines and the intermediate intersection cell in red. Figure adapted from Sandve et al. (2012). (For interpretation of the references to colour in this figure legend, the reader is referred to the web version of this article.)

constant within the intersection and continuous over the hybrid faces. After elimination of the intermediate pressures (p_1, p_2 and p_3 in Fig. 3), there are no unknowns directly associated to the intersection cells and these are removed from the computational grid. The Eq. (5) type equations are assembled for each cell and the resulting linear system solved for the cell centre pressures.

We refer to Sandve et al. (2012) for a thorough comparison of the TPFA and MPFA approaches. The implementations of both methods are available in the open-source Matlab Reservoir Simulation Toolbox, http://www.sintef.no/projectweb/mrst/ (Lie et al., 2012). An extension of control volume methods to non-matching grids across fractures may be found in Tunc et al. (2012).

3.4. Continuous-pressure, non-conforming embedded DFM (EDFM)

Recently, non-conforming methods for the treatment of lower-dimensional fractures have been developed, for example in Moinfar et al. (2011); 2014) and Hajibeygi et al. (2011), to avoid the time-consuming construction of complex matrix grids which explicitly represent the fractures. They are mostly used in the context of single and multi-phase flow simulations for petroleum engineering applications and require the normal fracture permeability to be orders of magnitude higher than the matrix permeability, as in the case of fractured petroleum reservoirs. In this field of applications corner-point grids are normally employed to describe the geological layers, e.g. different rock type, of the reservoir. An adaptation of such computational grids to the fractures could be unaffordable for real cases. The numerical method belongs to the family of two-point schemes, where a one-to-one connection between the degrees of freedom is considered through the transmissibility concept (Eymard et al., 2000). References on the embedded discrete fracture method (EDFM) can be found, for example, in Li and Lee (2008), Panfili et al. (2013), Moinfar et al. (2014), Panfili and Cominelli (2014), de Araujo Cavalcante Filho et al. (2015) and Fumagalli et al. (2016).

In practice, the mesh of the fractures is generated on top of the rock grid so that each rock cell cut by fractures contains exactly one fracture cell per fracture. Intersections between fractures are computed without affecting the creation of the grids of fractures and rock and used to compute approximate transmissibilities between different fracture cells. See Fig. 4 as an example. A degree of freedom that represents a pressure or a saturation value is assigned to each matrix cell and to each fracture cell. This means that transmissibilities between matrix and fracture cells, as well as those between different fracture cells, need to be computed. We compute the transmissibility between a fracture cell and a matrix cell T_{fm} and the half-transmissibility T_i between two intersecting fracture cells (related to the fracture i) through the following approximate expressions:

$$T_{fm} = A\frac{\mathbf{n}_f^T[\mathbf{K}\cdot\mathbf{n}_f}{d_{f,m}} \quad \text{and} \quad T_i = s\frac{k_i\varepsilon_i}{d_{i,s}}.$$

Here A is the measure of the fracture cell in the current rock cell, $\mathbf{n}_f$ is the normal of the fracture cell and $d_{f,m}$ is an average distance between the fracture cell and the matrix cell, see Li and Lee (2008). For the fracture-fracture transmissibility, s indicates the measure of the intersecting segment, k_i the scalar permeability of the fracture, ε_i the aperture and $d_{i,s}$ is the average distance between the fracture cell and the intersecting segment. The standard harmonic average is considered to compute the transmissibility between the two fracture cells. Standard formulae for fracture-fracture as well as matrix-matrix transmissibilities are computed by means of a two-point flux approximation. It is worth to notice that the recent extension of EDFM called Projection-based EDFM (pEDFM), proposed in Tene et al. (2017), is also able to handle low permeable fractures. Finally, even if the proposed benchmark cases are two-dimensional the method can be extended to three dimensions without any additional constraints.

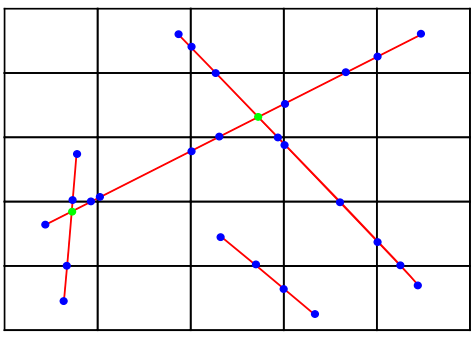

Fig. 4. Example of meshes, for both fractures and rock matrix, suited for EDFM. The rock matrix is considered as a background mesh. Each fracture cell is represented by two blue dots and the green dots are the non-matching intersection among fractures. (For interpretation of the references to colour in this figure legend, the reader is referred to the web version of this article.)

3.5. Cell-centred, discontinuous-pressure, geometrically-conforming mortar DFM (Flux-Mortar)

The key concept behind the Flux-Mortar, as described more thoroughly in Boon et al. (2016), is the idea that fractures can be considered as interfaces between different sub-domains. This has been explored previously by Martin et al. (2005) and Frih et al. (2012), among others. In this context, we consider the domain decomposition technique known as the mortar method to model flow through the fractured porous medium.

The mortar method is generally used to couple equations in different sub-domains by introducing a so-called mortar variable, defined on the interface. In case of modeling fracture flow, a well-explored choice of the mortar variable is the fracture pressure (Martin et al., 2005). The method considered here, however, uses the flux between matrix and fracture domains as the mortar variable, which leads to a stronger imposition of mass conservation. One of the main advantages of the close relationship to mortar methods is the capability to handle non-matching grids. In particular, two sub-domains bordering a fracture can be meshed independently on both sides, as illustrated in Fig. 5. The difficulty in mesh generation is then relieved significantly since only the geometry of the fractures needs to be respected.

By construction, the Flux-Mortar is applicable to problems in arbitrary dimensions. The governing equations in the matrix and the fractures (as well as fracture intersections in 3D) are identical and thus all fractures, intersections and tips are handled in a unified manner. Consequently, although only two-dimensional problems are considered in this study, the discretization scheme also applies to problems in three dimensions.

Due to a slightly different derivation of the reduced model, the scheme handles spatially varying apertures. Moreover, the apertures may be arbitrarily close, or even equal to zero which naturally eliminates the possibility of flow in the tangential direction.

With the use of mixed finite elements, mass is conserved locally in the matrix, fractures, and fracture intersections. The flux $\mathbf{u}$ in the matrix and fractures are modeled using the lowest-order Raviart–Thomas elements and linear Lagrange elements, respectively. The pressure p is then given by piecewise constants in the matrix, as well as the fractures and intersection points. Additionally, the mortar variable is given by piecewise constants on a separately generated, lower-dimensional, mortar grid on the matrix-fracture interface. This grid matches with the surrounding grids in case of matching grids and is coarser otherwise.

The resulting mixed finite element formulation is a saddle-point problem, which may be challenging to solve numerically. To relieve

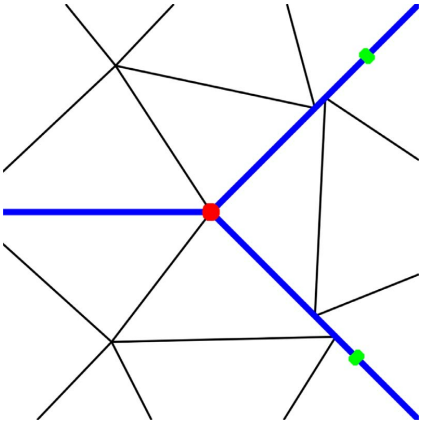

Fig. 5. The Flux-Mortar method allows for non-matching grids along fracture interfaces. Fracture and matrix flows are coupled using a mortar variable, defined on a coarser grid (green dots). (For interpretation of the references to colour in this figure legend, the reader is referred to the web version of this article.)

this, the flux variables may be eliminated through hybridization, which leads to a less computationally expensive scheme containing solely the cell-centre pressures.

Two implementations of the method have been developed, both of which are used in this benchmark study. The first version, implemented in MATLAB, is suited for simpler geometries in 2D, containing relatively few fractures, such as those considered in Benchmarks 1–3. The second version has been implemented for 3D problems and higher-order spaces on matching grids using the open-source finite element library FEniCS (Logg et al., 2012). This code is more efficient for complex cases such as Benchmark 4.

3.6. Discontinuous-pressure, non-conforming primal XFEM (P-XFEM)

The primal XFEM method participating in this benchmarking study is described in detail in Schwenck (2015), see also Flemisch et al. (2016) and Schwenck et al. (2015). The method is based on the hybrid-dimensional problem formulation investigated in Martin et al. (2005), where conditions for the coupling between fracture and matrix are derived:

$$\{\mathbf{u}_\mathrm{m}\cdot\mathbf{n}\}_\gamma = k_{\mathrm{f,n}}/\varepsilon[[p_\mathrm{m}]]_\gamma \tag{6a}$$

$$\xi_0[[\mathbf{u}_\mathrm{m}\cdot\mathbf{n}]]_\gamma = k_{\mathrm{f,n}}/\varepsilon\left(\{p_\mathrm{m}\}_\gamma - p_\mathrm{f}\right) \tag{6b}$$

Here, the subscripts “m” and “f” indicate matrix and fracture quantities, while $\{\{\cdot\}\}_\gamma$ and $[[\cdot]]_\gamma$ denote the average and the jump of a matrix quantity over the fracture γ, respectively.

The coupling conditions (6) can be used to define a source term for the fracture flow problem, while they yield an interface problem for the matrix domain. For the discretization of this interface problem, the methodology presented in Hansbo and Hansbo (2002) is used, which amounts to applying the eXtended Finite Element Method (XFEM). Together with an independent standard discretization of the lower-dimensional fracture problem, this yields a hybrid-dimensional, non-conforming primal XFEM-based method. The XFEM space is built enriching the standard Lagrangian $\mathbb{P}_1$ (or $\mathbb{Q}_1$ for quads) finite-element spaces, whose degrees of freedom are located at the vertices of the full-dimensional grid of the matrix Ω and the lower-dimensional grid of the fracture γ. A representative example of matrix and fracture grids is illustrated in Fig. 6. Unlike the EDFM method, see Fig. 4, the fracture grid

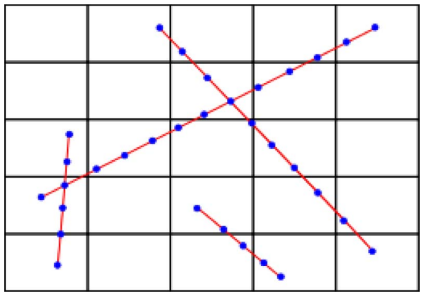

Fig. 6. Example of meshes, for both fractures and rock matrix, suited for P-XFEM. The fracture grid vertices are indicated by the blue dots. (For interpretation of the references to colour in this figure legend, the reader is referred to the web version of this article.)

vertices can be placed arbitrarily without taking into account the matrix grid. On the other hand, the method requires matching fracture branch grids in the form of vertices placed at the fracture intersections. In particular, special care has to be taken of intersecting and immersed fractures (Schwenck et al., 2015).

The method is implemented on top of the DUNE framework (Bastian et al., 2008) and the discretization module DUNe-PDELab (Bastian et al., 2010). For the enrichment of the finite-element spaces in the context of XFEM, the modules DUNe-Multidomain and DUNe-Multidomaingrid are employed (Müthing, 2015). The simulation code for the XFEM approach and for the benchmarks studied here is publicly available under https://git.iws.uni-stuttgart.de/dumux-pub/Flemisch2016a.git. Currently, the method is only implemented in 2D. Conceptually, no difficulties arise for extending it to 3D. However, the possibly multiple enrichment of the function spaces for matrix elements intersected by fracture elements can become a very tedious task for complex fracture networks.

3.7. Discontinuous-pressure, non-conforming dual XFEM (D-XFEM)

The dual XFEM method participating in his benchmark is based on D’Angelo and Scotti (2012). The method, originally derived for a domain cut by one fracture, was further developed in Formaggia et al. (2014) and Fumagalli and Scotti (2014) to account for intersecting fractures with different permeabilities. The same equations and coupling conditions as for the primal XFEM are used, but in a dual formulation where Darcy law and mass conservation give rise to a saddle-point problem for the fluid mean velocity and pressure, both in the fracture and in the surrounding medium. Moreover, unlike the previous method, this method employs triangular/tetrahedral grids. The usual lowest order $\mathbb{RT}_0 - \mathbb{P}_0$ pair for velocity and pressure is enriched following (Hansbo and Hansbo, 2002) in the elements of the porous medium cut by a fracture, or in the elements of a fracture at the intersection with other fractures. Indeed, triangular/tetrahedral grids are arbitrarily cut by triangulated lines/surfaces in 2D and 3D respectively. These surfaces can, in turn, intersect each other in a non-conforming way, as shown in Fig. 7.

In the current implementation of the method no special enrichment is added in the bulk elements containing the fracture tips. Instead, fractures are artificially extended up to the boundary of the domain, and in the extension we prescribe the same permeability of the surrounding porous medium to obtain a “virtual” fracture with no effects on the flow.

The method has been implemented on the basis of the Getfem++ library, http://download.gna.org/getfem/html/homepage/ , which provides support for the computation of the intersections and the quadrature on sub-elements thanks to an interface with QHull, http://www.qhull.org/.

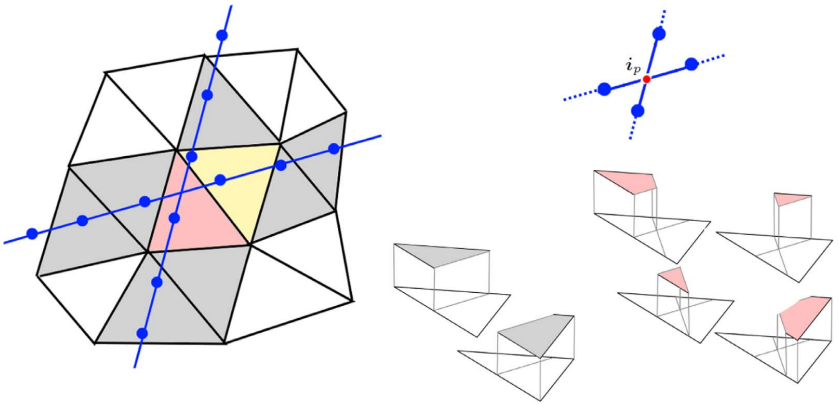

Fig. 7. A portion of the grid cut by two fractures: in the two dimensional case they can split the elements in two (grey), three (yellow), or four (red) independent parts, where the restrictions of the basis functions are defined. The fracture grids are irrespective of the bulk grid and of each other, i.e. the intersection point i_p is not a point of the grid. (For interpretation of the references to colour in this figure legend, the reader is referred to the web version of this article.)

3.8. Reference solutions calculated with mimetic finite differences (MFD)

The reference solutions are computed on very fine grids that discretize both matrix and fractures by full-dimensional triangular or quadrilateral elements. A mimetic finite difference method, see Brezzi et al. (2005) and Flemisch and Helmig (2008), is used to discretize problem (1). The method is employed as it is implemented in DuMu^{x} 2.7 (Flemisch et al., 2011). In particular, a mixed-hybrid approach is used to transform the discrete saddle point problem in terms of cell pressures and face fluxes into a symmetric positive definite formulation with face-pressure degrees of freedom.

4. Benchmark problems

This is the main section, which compares the methods described above by means of four benchmark cases. The first benchmark case, considered in Section 4.1, is based on Geiger et al. (2013) and shows a regular fracture network. Second, in Section 4.2, we present a well established benchmark for groundwater flow from Swedish Nuclear Power Inspectorate (SKI) (1987) that contains two crossing, highly permeable fractures and a non-straight top surface. After that, a small but complex fracture network exhibiting immersed fractures and intersections at different angles is investigated in Section 4.3. Finally, a case synthesized from a real application is considered in Section 4.4.

For each benchmark case, a description of the computational domain is provided, including boundary conditions, the geometrical information about the corresponding fracture network and the associated material parameters such as aperture and permeability. For some of the cases, the reference solution on the complete domain is visualized. This is followed by illustrations of the grids used by the participating methods. Since the methods pose different grid requirements, the grid could be chosen arbitrarily for each method, provided that the number of grid cells or vertices is roughly the same. If a reference solution is available (Benchmarks 1–3), the results of the different methods are compared by evaluating the errors with respect to the reference in the matrix domain as well as in the fracture network, indicated by err_m and err_f, respectively. The errors are calculated according to the formulas

$$err_m^2 = \frac{1}{|\Omega|(\Delta p_{ref})^2} \sum_{f=K_{ref,m}\cap K_m} |f| \left(p_m|_{K_m} - p_{ref}|_{K_{ref,m}} \right)^2, \tag{7a}$$

$$err_f^2 = \frac{1}{|\gamma|(\Delta p_{ref})^2} \sum_{e=K_{ref,f}\cap K_f} |e| \left(p_f|_{K_f} - p_{ref}|_{K_{ref,f}} \right)^2, \tag{7b}$$

where $|\Omega|$ and $|\gamma|$ indicate the size of the full-dimensional matrix and the lower-dimensional fracture domain, respectively, and $\Delta p_{ref} = \max_{\mathscr{D}} p_{ref} - \min_{\mathscr{D}} p_{ref}$. The sum is taken over all intersections of (full-dimensional) elements $K_{ref,\,m}$ and $K_{ref,\,f}$ of the grid employed for the reference solution with full-dimensional matrix elements K_m in case of err_m and lower-dimensional fracture elements K_f in case of err_f. The quantities $|f|$ and $|e|$ indicate the area of a full-dimensional intersection f and a lower-dimensional intersection e, respectively. We stress the fact that for the calculation of the matrix error err_m, only elements $K_{ref,\,m}$ in the matrix part of the equi-dimensional grid are considered. In other words, the full-dimensional fracture domain Γ is excluded from this calculation. In addition to errors in matrix and fracture, the densities and condition numbers of the resulting linear system matrices are provided. Moreover, a comparison is performed by means of plots along specific lines through the domain for some benchmark cases. Each case is concluded by a short discussion of the results.

4.1. Benchmark 1: regular fracture network

This test case is based on an article presenting a new dual continuum model, Geiger et al. (2013), with slightly modified boundary conditions and material properties. The computational domain including the fracture network and boundary conditions is shown in Fig. 8. The matrix permeability is set to $\mathbb{K}_m = \mathbb{I}$, all fractures have a uniform aperture $\varepsilon = 10^{-4}$. For the fracture permeability we consider two cases: a highly conductive network with $k_{f,n} = k_{f,t} = 10^4$, as worked out in Section 4.1.1, and a case with blocking fractures by setting $k_{f,n} = k_{f,t} = 10^{-4}$, as described in Section 4.1.2. The reference solutions are computed on a grid which resolves every fracture with 10

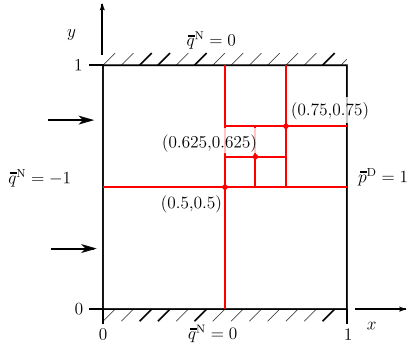

Fig. 8. Benchmark 1: Domain and boundary conditions.

Table 2
Grids for Benchmark 1.

Method	d.o.f.	♯-matr	♯-frac
Box	577	1078 triangles	74
TPFA	1481	1386 triangles	95
MPFA	1439	1348 triangles	91
EDFM	1501	1369 quads	132
Flux-Mortar	3366	1280 triangles	75
P-XFEM	1650	961 quads	164
D-XFEM	4474	1250 triangles	126
MFD	2,352,280	1,136,456 quads	38,600

elements in its normal direction and becomes coarser away from the fractures. It has a total of 1,175,056 elements.

The first distinction between the different schemes are given in Table 2, where the number of degrees of freedom, matrix elements (♯-matr) and fracture elements (♯-frac) for all the participating methods are listed. The corresponding grids are visualized in Fig. 9.

4.1.1. Conductive fracture network

First, we consider a highly conductive network by setting $k_{f,n} = k_{f,t} = 10^4$. The pressure distribution of the corresponding reference solution is shown in Fig. 10. The pressure distributions given by the different methods are first compared along two lines, one horizontal at $y = 0.7$ and one vertical at $x = 0.5$. As shown in Fig. 11, all results are relatively close to the reference solution. Qualitatively, we observe that P-XFEM produces a more diffuse pressure profile in the vertical fracture.

Table 3 lists the errors with respect to the equi-dimensional reference solution for the different methods; particularly, the error for the matrix domain and the one along the two fractures. Moreover, it provides the density of the associated matrix and its condition number for each method. The performance of the methods is comparable as shown by both the matrix and the fracture errors. In fact, since the degree of sparsity does not differ significantly either, the only notable differences between the methods are the number of degrees of freedom and the condition numbers, as shown in the last column of Table 3. In that context, the Flux-Mortar and D-XFEM are clear outliers, containing a large number of degrees of freedom due to the incorporated flux variable and resulting in high condition numbers. Nevertheless, the P-XFEM scheme exhibits the highest condition number, although it has significantly fewer degrees of freedom than Flux-Mortar and D-XFEM.

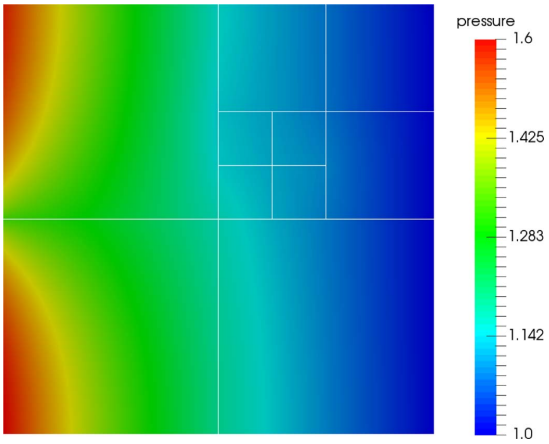

Fig. 10. Benchmark 1 with conductive fractures: pressure reference solution.

In addition to evaluating each method on a single grid, we perform a convergence study by choosing the grids above as initial ones and refining them twice. The results are shown in Fig. 12, detailed numbers are provided in Appendix A. For each method, the matrix error err_m and fracture error err_f is plotted against the square root of the number of matrix cells and against the number of fracture cells, respectively. As suggested by the numbers for the initial grids from Table 3, all methods exhibit a similar behaviour. For the matrix error in particular, the methods are very close to each other and all of them show a linear error decay. Concerning the fracture error, the XFEM methods perform a bit worse than the other ones in terms of absolute numbers. An obvious positive outlier is the fracture error for Box, which stagnates at a level much lower than all other methods. An explanation for this behaviour is still lacking. All other methods exhibit a linear error decay also for the fracture error.

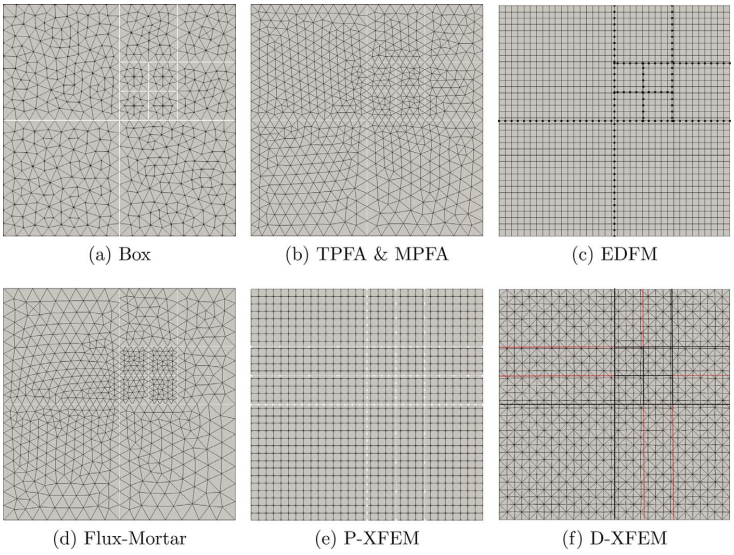

Fig. 9. Benchmark 1: the grids used by the different methods. In the D-XFEM grid the red lines indicate the virtual extension of the fractures up to the boundary. The fracture network has also been virtually extended for the application of P-XFEM. (For interpretation of the references to colour in this figure legend, the reader is referred to the web version of this article.)

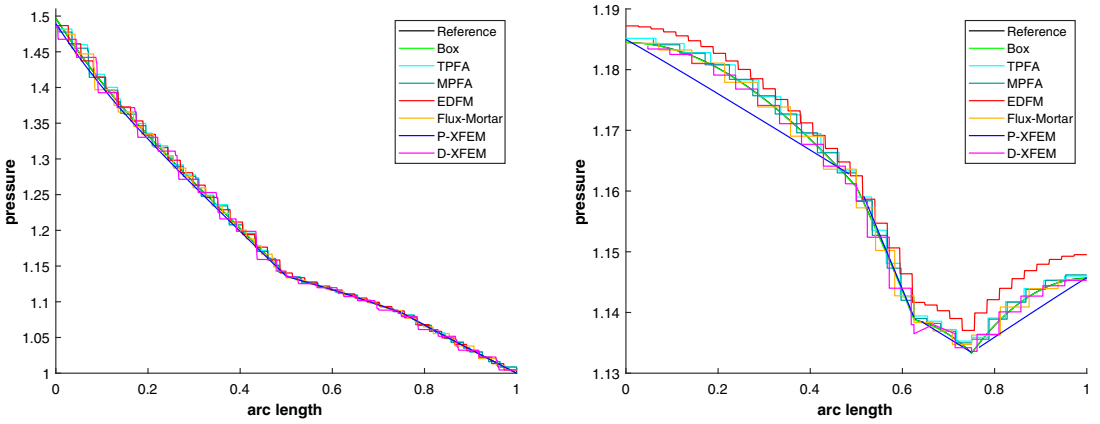

(a) Horizontal line at $y = 0.7$. (b) Longest vertical fracture at $x = 0.5$.

Fig. 11. Benchmark 1 with conductive fractures: comparison of values along two lines. The reference solution is hidden by the Box solution.

Table 3
Errors and matrix characteristics for Benchmark 1 with conductive fractures.

Method	err_m	err_f	nnz/size^2	$\|\cdot\|_2$-cond
Box	1.1e−2	1.9e−4	1.1e−2	2.2e3
TPFA	1.1e−2	4.4e−3	2.7e−3	4.8e4
MPFA	1.1e−2	4.5e−3	8.0e−3	5.8e4
EDFM	6.5e−3	4.0e−3	3.3e−3	5.6e4
Flux-Mortar	1.0e−2	6.9e−3	1.8e−3	2.4e6
P-XFEM	9.3e−3	7.3e−3	8.0e−3	9.3e9
D-XFEM	9.6e−3	8.9e−3	1.3e−3	1.2e6

4.1.2. Blocking fracture network

We now assume a blocking fracture network by setting $k_{f,n} = k_{f,t} = 10^{-4}$. The pressure distribution of the corresponding reference solution is shown in Fig. 13. The results clearly show the pressure discontinuities reminiscent of the low fracture permeability.

Fig. 14 compares the results of the different methods along a diagonal line crossing the whole domain from (0.0, 0.1) to (0.9, 1.0). The errors, sparsity densities, and condition numbers for the different methods are given in Table 4.

In the case of blocking fractures, the distinction between the

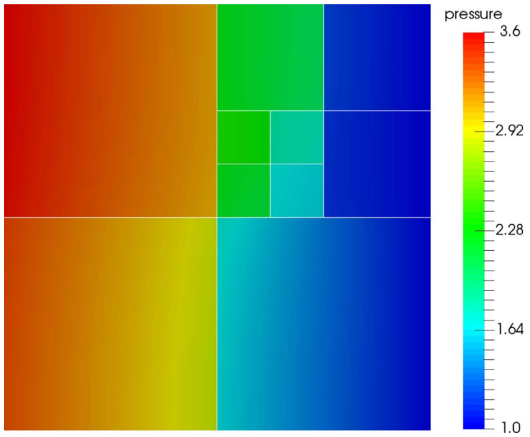

Fig. 13. Benchmark 1 with blocking fractures: pressure reference solution.

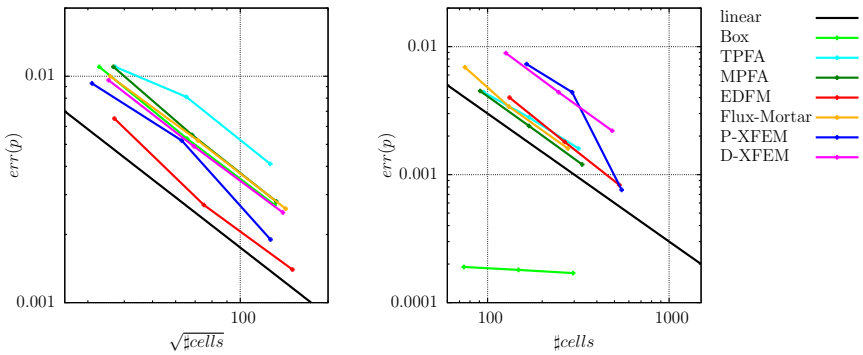

(a) Matrix error err_m. (b) Fracture error err_f.

Fig. 12. Benchmark 1 with conductive fractures: evolution of the matrix and fracture errors over grid refinement.

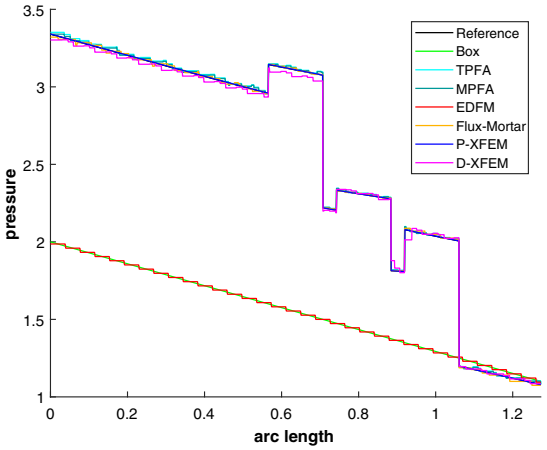

Fig. 14. Benchmark 1 with blocking fractures: values along the line (0.0, 0.1) − (0.9, 1.0). The reference solution is hidden by the P-XFEM solution.

Table 4
Errors and matrix characteristics for Benchmark 1 with blocking fractures.

Method	err_m	err_f	nnz/size^2	$\|\cdot\|_2$-cond
Box	4.1e−1	3.2e−1	1.1e−2	1.3e3
TPFA	5.6e−3	4.4e−3	2.7e−3	2.6e4
MPFA	4.4e−3	3.6e−3	2.7e−3	6.3e4
EDFM	2.9e−1	3.2e−1	3.3e−3	9.2e3
Flux-Mortar	4.3e−3	4.6e−3	1.6e−3	9.0e2
P-XFEM	2.7e−3	2.0e−2	6.9e−3	1.3e7
D-XFEM	1.0e−2	1.8e−2	1.3e−3	2.2e6

different methods is more apparent. As mentioned above, the Box and EDFM schemes are unable to capture the resulting pressure discontinuities. As a result, these methods show large errors in both the matrix and the fracture domains. The remaining methods, which are capable of handling discontinuities, differ a bit more among each other in terms of fracture and matrix errors. The condition numbers have improved significantly for the Flux-Mortar and P-XFEM schemes. Conversely, for TPFA, MPFA and D-XFEM, condition numbers for the blocking fractures case are similar to those obtained for the permeable fractures case.

We investigate the error decays also for the variant of blocking fractures. The decays are illustrated in Fig. 15. The spread between the different methods becomes very explicit here. As to be expected, the errors for Box and EDFM do not improve with grid refinement. Concerning the matrix error, TPFA, MPFA, Flux-Mortar and P-XFEM exhibit a linear decay, while D-XFEM appears to converge with an inferior order. This is due to the fact that in this method fractures are artificially extended to the boundary with a permeability that is the same of the surrounding matrix: the “T” type intersections become “X” intersections with severe permeability jumps between the two branches of the same fractures, causing numerical problems that affect convergence. Although P-XFEM shows the best numbers for the matrix error, both XFEM methods result in considerably higher fracture errors than TPFA, MPFA and Flux-Mortar. For the convergent methods, the rate of convergence for the fracture error between the second and third refinement stage is measured between 0.45 and 0.64.

4.2. Benchmark 2: Hydrocoin

Within the international Hydrocoin project, (Swedish Nuclear Power Inspectorate (SKI), 1987), a benchmark for heterogeneous groundwater flow problems was presented. The domain setup is shown in Fig. 16. We point out that we have slightly modified the original domain such that equi-dimensional and hybrid-dimensional models can be run on exactly the same domain. This allows for an easier comparison of the solution values over the whole domain. The exact modifications are described in Appendix B.

For this case, we keep the original formulation in terms of the piezometric head and the hydraulic conductivity instead of pressure and permeability. In particular, the boundary conditions are Dirichlet piezometric head on the top boundary and Neumann no flow on the other three boundaries. The permeability is 10^{-6} m/s in the fracture zones and 10^{-8} m/s in the rock matrix respectively.

Table 5 lists the number of degrees of freedom, matrix elements and fracture elements for all the participating methods.

The corresponding grids are visualized in Fig. 17.

The original benchmark shows the piezometric head distribution along five horizontal lines through the modeled domain. Here, we first show in Fig. 18 the plot at a depth of 200 m, as indicated by the dashed line in Fig. 16. All participating methods show a good agreement with the reference solution. Only the EDFM method is a bit off. We remark that the plots for the methods employing cell-wise constant solution values exhibit staircase-like patterns corresponding to these values.

Table 6 lists the errors for the different methods. The uniform behaviour exhibited in Fig. 18 is reflected by the error values. Especially the errors in the matrix domain are within very narrow bounds, while the fracture errors show a larger variation. Just like for Benchmark 1,

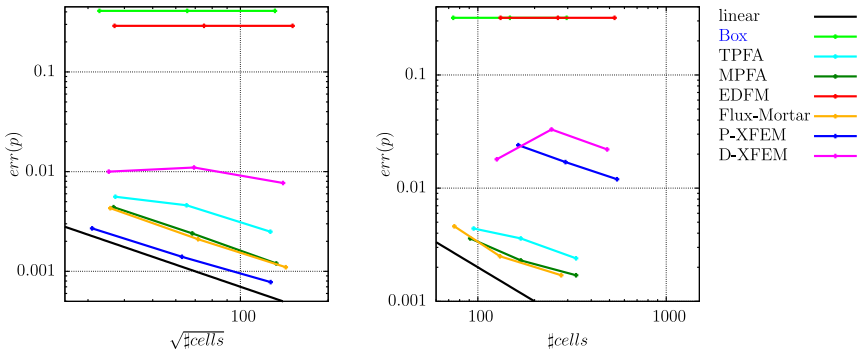

(a) Matrix error err_m. (b) Fracture error err_f.

Fig. 15. Benchmark 1 with blocking fractures: evolution of the matrix and fracture errors over grid refinement.

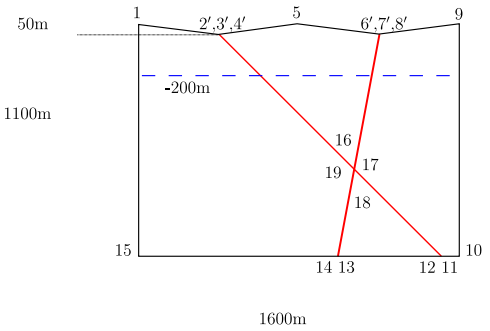

Fig. 16. Geometry of the modeled domain of the Hydrocoin test case 2, Swedish Nuclear Power Inspectorate (SKI) (1987). Modified node locations are indicated by numbers superscripted with ′. Boundary conditions are hydraulic head on top and Neumann no-flow on the other three sides of the domain.

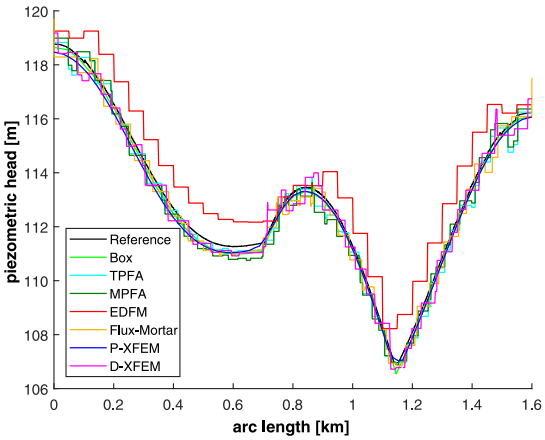

Fig. 18. Benchmark 2: head values along a horizontal line at a depth of 200 m.

Table 5
Grids for Benchmark 2.

Method	d.o.f.	♯-matr	♯-frac
Box	1496	2863 triangles	74
TPFA	1459	1416 triangles	43
MPFA	1532	1416 triangles	43
EDFM	1044	960 quads	84
Flux-Mortar	3647	1384 triangles	63
P-XFEM	1667	1320 quads	68
D-XFEM	3514	1132 triangles	160
MFD	889,233	424,921 mixed	19,287

Table 6
Errors and matrix characteristics for Benchmark 2.

method	err_m	err_f	nnz/size^2	$\|\cdot\|_2$-cond
Box	9.2e−3	3.3e−3	4.5e−3	5.4e3
TPFA	1.1e−2	1.1e−2	2.7e−3	3.5e4
MPFA	9.3e−3	6.8e−3	8.2e−3	6.6e4
EDFM	1.5e−2	8.3e−3	4.7e−3	3.9e4
Flux-Mortar	1.0e−2	7.2e−3	1.5e−3	9.0e12
P-XFEM	1.2e−2	3.2e−3	6.5e−3	2.7e9
D-XFEM	1.2e−2	6.9e−3	1.7e−3	6.2e12

remarkably high differences can be observed for the matrix condition numbers. While the ones for Box, TPFA, MPFA and EDFM are on the order of 10^4, the one for P-XFEM is five orders and the ones for Flux-Mortar and D-XFEM are even seven orders of magnitude larger, due to their saddle-point nature.

We remark that the fracture apertures are, with around 10m, rather high in relation to the dimensions of the computational domain (~ 1000 m) and the element sizes (~ 50 m) employed in the calculations above. Therefore, the assumption of a negligible aperture that justifies the usage of hybrid-dimensional methods is questionable. This is confirmed by the fact that no convergence can be observed for the considered methods when refining the grids depicted in Fig. 17. The total error is already dominated by the modeling error rather than the discretization error. Since our focus is on comparing different DFM methods that all rely on this assumption, we refrain from performing a more detailed analysis in this direction.

We would like to point out that an aperture of 10 m and more is often encountered in real field problems. The original intention of the Hydrocoin groups was to have a representation of a highly conductive fault zone: “The problem is an idealisation of the hydrogeological conditions encountered at a potential site for a deep repository in bedrock” (Swedish Nuclear Power Inspectorate (SKI), 1987). Some examples on modeling the impact of hydraulic fracturing on groundwater where the fault widths range between 10 and 30 m are provided in

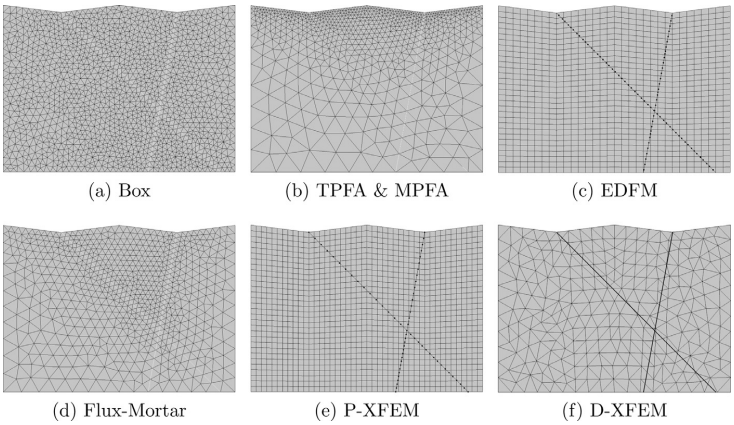

Fig. 17. Benchmark 2: the grids used by the different methods.

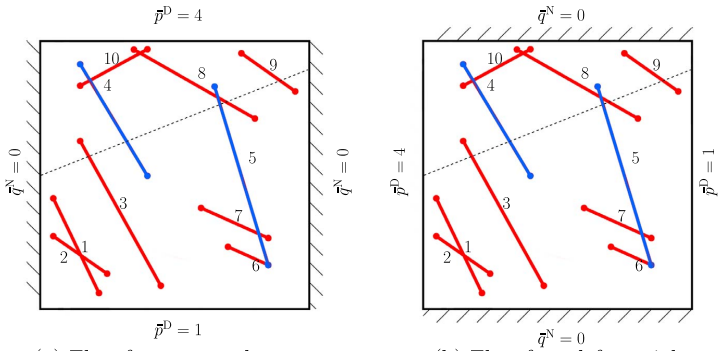

(a) Flow from top to bottom. (b) Flow from left to right.

Fig. 19. Benchmark 3: Domain and boundary conditions for cases (a) and (b). The red fractures are conductive, the blue ones are blocking. The dashed line is chosen to compare pressure profiles across both blocking and permeable fractures. (For interpretation of the references to colour in this figure legend, the reader is referred to the web version of this article.)

Gassiat et al. (2013), Pfunt et al. (2016) and Taherdangkoo et al. (2017). It is common practice and, depending on the geometrical complexity, often the only efficient possibility to treat such fault zones with lower-dimensional models. A modeler parametrizing a real field problem will often face the question of how to consider the fractures in the model. Despite the fact that the assumption of a negligible aperture is not justified, the accuracy of a hybrid-dimensional approach might still be acceptable, as is also indicated by our results.

4.3. Benchmark 3: complex fracture network

This test case considers a small but complex fracture network that includes permeable and blocking fractures. The domain and boundary conditions are shown in Fig. 19. The exact coordinates for the fracture positions are provided in Appendix C. The fracture network contains ten straight immersed fractures, grouped in disconnected networks. The aperture is $\varepsilon = 10^{-4}$ for all fractures, and the permeability is $k_{\mathrm{f,n}} = k_{\mathrm{f,t}} = 10^{4}$ for all fractures except for fractures 4 and 5, which are blocking fractures with $k_{\mathrm{f,n}} = k_{\mathrm{f,t}} = 10^{-4}$. The matrix permeability is again set to $\mathbb{K}_{\mathrm{m}} = \mathbb{I}$. Note that we are considering two sub-cases, a) and b). with a pressure gradient which is predominantly vertical and horizontal, respectively, to better highlight the impact of the blocking fractures. The corresponding reference solutions are depicted in Fig. 20.

Table 7 lists the number of degrees of freedom, matrix elements and fracture elements for all the participating methods. The corresponding grids are visualized in Fig. 21.

The P-XFEM method could not participate in this benchmark example. Its current implementation requires that each matrix element face is cut by at most one fracture branch. While it would be possible to construct a matrix grid that satisfies this requirement, this would contradict the promised advantage of admitting independent fracture and matrix grids.

Table 7
Grids for Benchmark 3.

Method	d.o.f.	♯-matr	♯-frac
Box	1373	2664 triangles	152
TPFA	1420	1332 triangles	88
TPFA*	1425	1332 triangles	93
MPFA	1500	1332 triangles	88
EDFM	1572	1369 quads	203
Flux-Mortar	3349	1230 triangles	89
D-XFEM	7180	1922 triangles	199
MFD	3,471,040	2,260,352 triangles	52,608

4.3.1. Flow from top to bottom

We first consider the setup depicted in Fig. 19(a), resulting in the reference solution visualized in Fig. 20(a). Table 8 lists the errors for this first variant, namely, the flow from top to bottom.

The pressure profiles along the line $(0, 0.5) - (1, 0.9)$, computed by the different methods, are represented in Fig. 22: one can observe that most methods are in good agreement with the reference solution, except for EDFM and the Box method that cannot represent the behaviour of the blocking fractures. Even though this is still a synthetic case, we can see that the geometry of the network starts to be an issue: relatively small intersection angles are present, for instance, between fractures 1 and 2. Another difficulty consists in the coexistence of permeable and blocking fractures which intersect each other: on one hand, some of the methods are not well suited to describe a blocking behaviour, on the other hand, the coupling conditions at the intersection become less trivial in these cases. All the participating methods that account explicitly for the effect of permeability at the fracture intersections have adopted the harmonic average in the case of a permeable and a

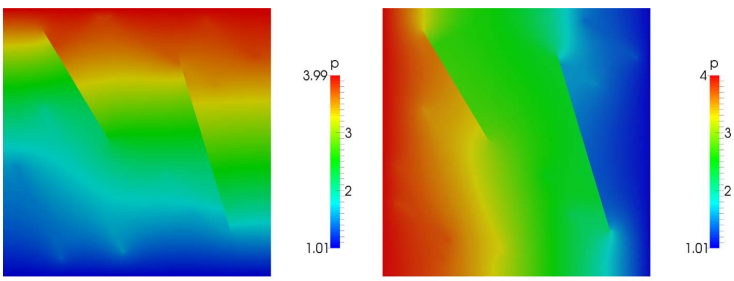

(a) Flow from top to bottom. (b) Flow from left to right.

Fig. 20. Benchmark 3: reference solution for cases a) and b).

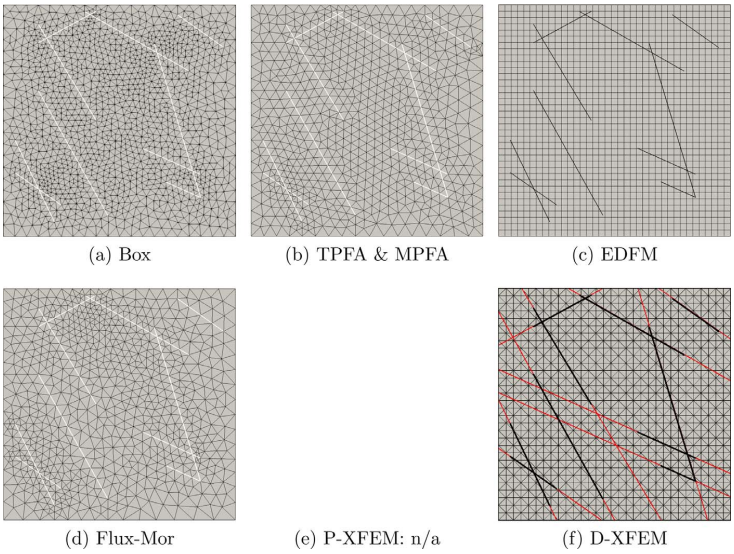

Fig. 21. Benchmark 3: the grids used by the different methods. In the DXFEM grid the red lines indicate the virtual extension of the fractures up to the boundary. (For interpretation of the references to colour in this figure legend, the reader is referred to the web version of this article.)

Table 8
Errors and matrix characteristics for the first variant of Benchmark 3.

Method	err_m	err_f	nnz/size^2	$\|\cdot\|_2$-cond
Box	4.9e−2	3.4e−2	4.9e−3	4.3e3
TPFA	2.7e−2	2.9e−2	2.8e−3	2.6e4
TPFA*	1.3e−2	1.1e−2	2.8e−3	7.9e4
MPFA	2.5e−2	2.8e−2	8.5e−3	2.5e4
EDFM	3.8e−2	4.5e−2	3.1e−3	1.2e6
Flux-Mortar	1.0e−2	8.2e−3	1.6e−3	1.3e4
D-XFEM	1.9e−2	2.9e−2	8.2e−4	8.1e3

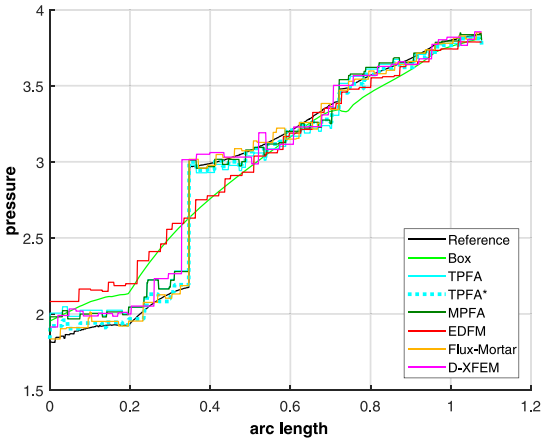

Fig. 22. Benchmark 3, first variant: pressure values along the line (0.0, 0.5) − (1.0, 0.9).

blocking fracture crossing each other. The errors reported in Table 8 show that the methods requiring the continuity of pressure (EDFM and the Box) exhibit slightly higher errors in the matrix. However, the difference is not particularly sharp, since in this sub-case the average pressure gradient is almost parallel to the blocking fractures. The elimination of the fracture intersection cells in the TPFA and MPFA methods is ill-suited for cases where fractures of different permeability cross. Therefore, we include a solution TPFA* in which we have not performed the removal. The corresponding results show a far smaller error compared to the TPFA with elimination, but also demonstrate that the elimination significantly increases the condition number.

Like for Benchmark 1, we investigate the errors in the matrix and in the fracture network, see Fig. 23 and detailed numbers in Appendix D. We have not considered Box and EDFM, since the corresponding errors stagnate due to the presence of blocking fractures, as already discussed in Section 4.1.2. Surprisingly at first sight, now also TPFA and MPFA do not converge. This is an implication of the facts mentioned above, namely, that the intersection cells are removed for both methods together with the appearance of intersecting conductive and blocking fractures. When these cells are included, convergence can be achieved. Only TPFA* and Flux-Mortar exhibit a linear decay of the matrix error, while D-XFEM shows considerably higher absolute numbers and an inferior convergence rate. As already observed for the blocking variant of Benchmark 2, linear convergence cannot be achieved for the fracture error.

4.3.2. Flow from left to right

We now investigate the more challenging setup from Fig. 19(b) and its corresponding reference solution depicted in Fig. 20(b). The errors for this second variant are summarized in Table 9. The pressure profiles along the line (0, 0.5) − (1, 0.9), computed by the different methods for are represented in Fig. 24. As in the previous sub-case EDFM and the Box method are not able to capture the pressure jumps across the blocking fractures. Moreover, the D-XFEM method underestimates the second pressure jump. This behaviour will also reflect in a poor convergence rate (see Fig. 25). In this second case, since we impose pressure on the sides of the square domain, the solution is more challenging. As we can observe from Fig. 20, the gap between continuous and discontinuous methods increases.The errors remain of the same order of magnitude, indicating that all the methods capture the overall trend of the solution. Nevertheless, the difference between TPFA/MPFA and TPFA* becomes larger, indicating that it is even more important to treat

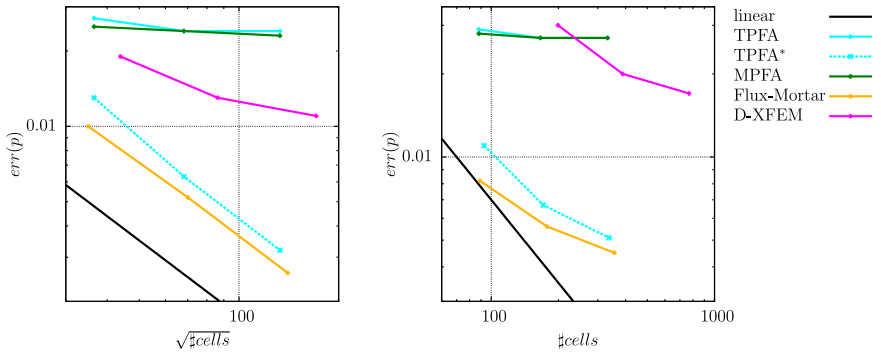

(a) Matrix error err_{m}. (b) Fracture error err_{f}.

Fig. 23. Benchmark 3, flow from top to bottom: evolution of the matrix and fracture errors over grid refinement.

Table 9
Errors and matrix characteristics for the second variant of Benchmark 3.

method	err_{m}	err_{f}	nnz/size^2	$\|\cdot\|_2$-cond
Box	7.5e−2	6.3e−2	4.9e−3	5.3e3
TPFA	5.1e−2	6.7e−2	2.8e−3	3.1e4
TPFA*	1.3e−2	1.1e−2	2.8e−3	2.0e5
MPFA	5.1e−2	6.7e−2	8.5e−3	3.1e4
EDFM	5.8e−2	8.9e−2	3.1e−3	1.2e6
Flux-Mortar	1.4e−2	1.3e−2	1.6e−3	1.4e4
D-XFEM	2.2e−2	3.6e−2	8.2e−4	8.1e3

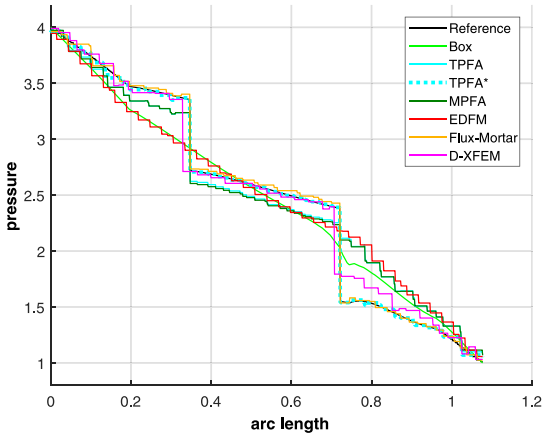

Fig. 24. Benchmark 3, second variant: pressure values along the line (0.0, 0.5) − (1.0, 0.9).

properly the intersections of conductive and blocking fractures.

The error plots associated with this second variant are shown in Fig. 25. They are very similar to the first variant, the only remarkable difference being the stagnation in the numbers for D-XFEM. This is once again caused by the intersections between fractures with different permeabilities, particularly in the "virtual" extensions of the fractures to the boundary.

4.4. Benchmark 4: a realistic case

In this last test case we consider a real set of fractures from an interpreted outcrop in the Sotra island, near Bergen in Norway. The set is composed of 64 fractures grouped in 13 different connected networks, ranging from isolated fractures up to tens of fractures each. In the interpretation process two fractures were composed by more than one segment. However, since the implementation of some methods relay on the fact that one fracture is represented by a single geometrical object, we substitute them by a single segment. It is worth to notice that we are changing the connectivity of the system, nevertheless our goal is to make a comparison of the previous schemes on a complex and realistic set of fractures. The interpreted outcrop and the corresponding set of fractures are represented in Fig. 26. The size of the domain is 700 m × 600 m with uniform matrix permeability $\mathbb{K}_{\mathrm{m}} = 10^{-14}\mathbb{I}\,\mathrm{m}^2$. For simplicity all the fractures have the same scalar permeability $k_{\mathrm{f,n}} = k_{\mathrm{f,t}} = 10^{-8}\ \mathrm{m}^2$, and aperture 10^{-2} m. We consider no-flow boundary condition on top and bottom, pressure 1013250 Pa on the left, and pressure 0 Pa on the right of the boundary of the domain. Due to the high geometrical complexity of the fracture network not all involved numerical schemes/simulators could be used. Nevertheless, it is worth to point out that for the others the main difficulty in handling such geometry is an implementation issue rather than a limitation of the scheme. It is also a very tedious task to create a full-dimensional description of the fracture network and a corresponding equi-dimensional grid of the whole computational domain. Therefore, we refrain from calculating a reference solution with the MFD method and perform a direct comparison of the hybrid-dimensional methods. Since all fractures are conductive and their aperture is negligibly small, we consider all participating methods to be verified by means of the benchmark cases above.

Table 10 lists the number of degrees of freedom, the density of the associated matrix, and its condition number for the different methods. Due to the geometrical difficulties of the network the request of having a similar number of degrees of freedom among the methods is relaxed, as Table 10 indicates. Considering Fig. 27, the solutions are reported for the four methods. We notice that, except for the top right part of the domain in the Box method, the solutions are similar and comparable, which is an indication of their correctness. Compared to the previous test cases the mesh generation is the main concern and some of the methods require a fine tuning to avoid non-physical connections among

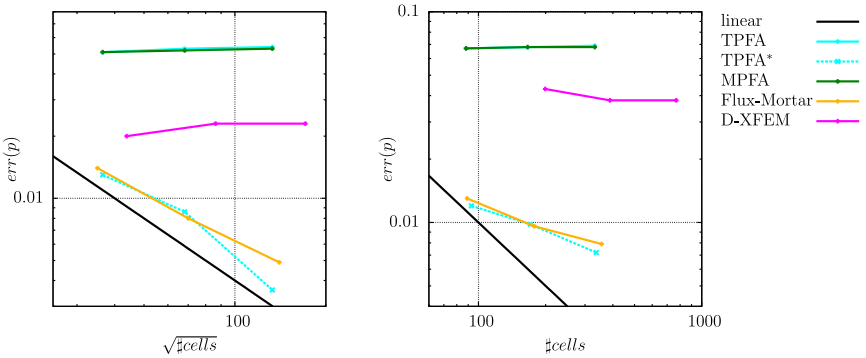

(a) Matrix error err_{m}. (b) Fracture error err_{f}.

Fig. 25. Benchmark 3, flow from left to right: evolution of the matrix and fracture errors over grid refinement.

elements where the fracture are close. An example can be found in the middle of the domain and reported in Fig. 28. Only EDFM is more robust with respect to this constraint. To present a more detailed comparison among the methods, Fig. 29 represents the pressure solution along two different lines: for $y = 500$ m and for $x = 625$ m. We note that the methods behave similarly, and the Box slightly overestimates some peaks. The oscillation of the methods are related to mesh effects.

Table 10
Discretization and matrix characteristics for Benchmark 4.

Method	d.o.f.	♯-matr	♯-frac	nnz/size^2	$\|\cdot\|_2$-cond
Box	5563	10,807 triangles	1386	1.2e−3	9.3e5
TPFA	8481	7614 triangles	867	4.9e−4	5.3e6
MPFA	8588	7614 triangles	867	1.6e−3	4.9e6
EDFM	3599	2491 quads	1108	1.4e−3	4.7e6
Flux-Mortar	25,258	8319 triangles	1317	2.0e−4	2.2e17

5. Summary and outlook

Four benchmark cases for single-phase flow in fractured porous media have been proposed and employed to compare the performances of several state-of-the-art hybrid-dimensional discrete-fracture-matrix models. If we consider the cases where all the methods are employed within the applicability range for which they were originally developed, the results are in quite good agreement. In particular, fracture networks exhibiting a larger permeability than the surrounding matrix can be accurately described by all methods. On the other hand, not all methods are capable of modeling blocking fractures. In this case, some methods fail to predict the correct flow patterns for the corresponding scenarios. These observations are confirmed by investigating the behaviour of the errors with respect to the equi-dimensional reference solution under mesh refinement. For purely conductive fracture networks, all methods exhibit a linear decay for both the error in the matrix and the fractures, and the total numbers are very similar. The fact that some methods cannot deal with blocking fractures is reflected by a stagnation of the corresponding errors. In the presence of blocking fractures, the order of convergence for the fracture error decreases for all methods. Moreover, the fracture error for the XFEM methods has been observed to be considerably larger than for the other convergent methods. Even if a method can handle conductive and blocking fractures, the intersection of a conductive with a blocking fracture branch poses additional challenges. In this case, a method may not converge if it doesn't treat these intersections carefully enough. Of the eight participating methods, only two, TPFA* and Flux-Mortar, proved to be convergent through all considered cases.

Apart from the discretization error, another component of the total error is the modeling error resulting from the assumption that the fracture apertures are negligibly small. For the Hydrocoin benchmark, this component obviously dominated the measured error. More detailed

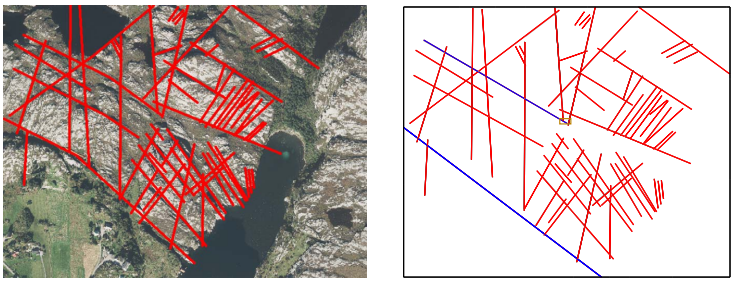

Fig. 26. In the left the interpretation of the set of fractures superimposed to the map. In the right the geometry used in the simulations. The rectified fractures are depicted in blue. (For interpretation of the references to colour in this figure legend, the reader is referred to the web version of this article.)

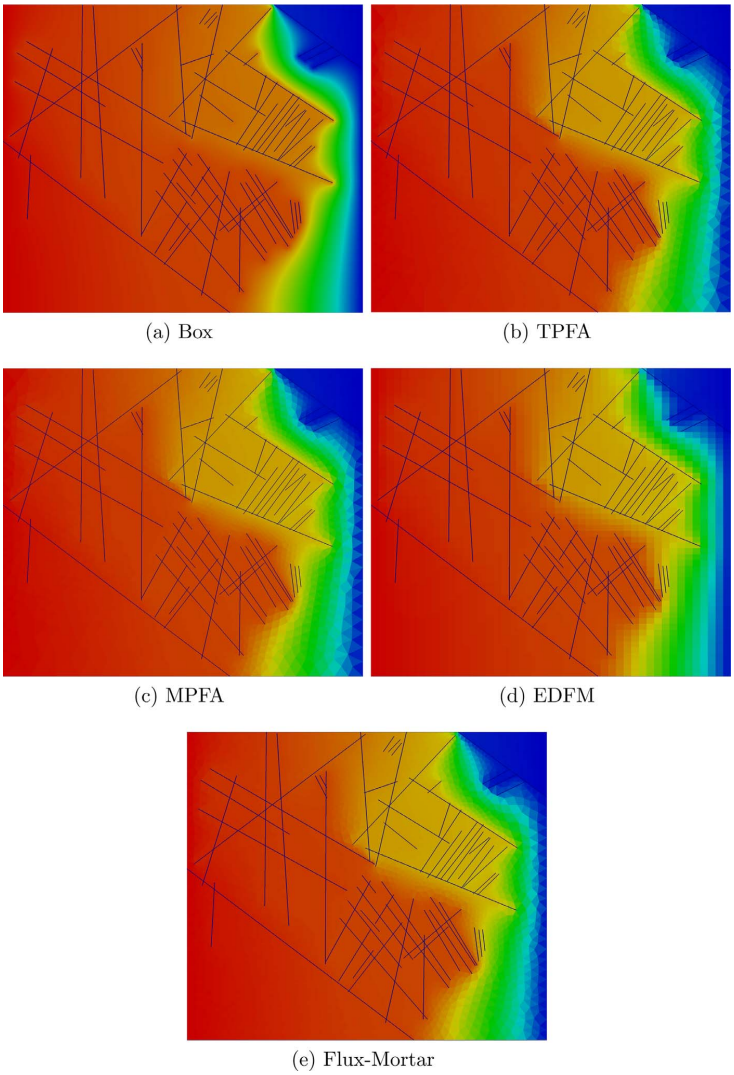

Fig. 27. Representation of the matrix pressures field for the realistic case. The solution values range between 0 and 1013250 Pa.

investigations on the relation between these two components is an interesting topic for future work.

Especially noteworthy are the large differences in the condition numbers of the associated system matrices. The effect of these differences on the behaviour of linear solvers is difficult to quantify in a comparable manner, since the different methods pose different requirements for such solvers.

In principle, all participating methods should have been able to run all proposed cases. However, due to implementation restrictions, some methods could not perform the cases with more complex fracture network geometries. Even if the methodology is general enough, technical difficulties can become crucial obstacles to tackling realistic scenarios.

All the investigated benchmarks are restricted to simple physics and two-dimensional computational domains. This should give other researchers developing DFM models the chance to perform comparison studies for their methods. We encourage the scientific community to contribute their results for the benchmarks to a corresponding Git repository at https://git.iws.uni-stuttgart.de/benchmarks/fracture-flow.

Further benchmark cases may be developed in the near future. In particular, we are very interested in enhancing the purely single-phase single-component flow physics by adding transport, deformation and/or reaction processes. We aim to carry out these efforts in a broader context by means of international workshops. A first such workshop "Modeling and benchmarking of fractured porous media: flow, transport and deformation" was organized by the authors and held in June 2017 at the University of Bergen. First future steps already have been discussed there.

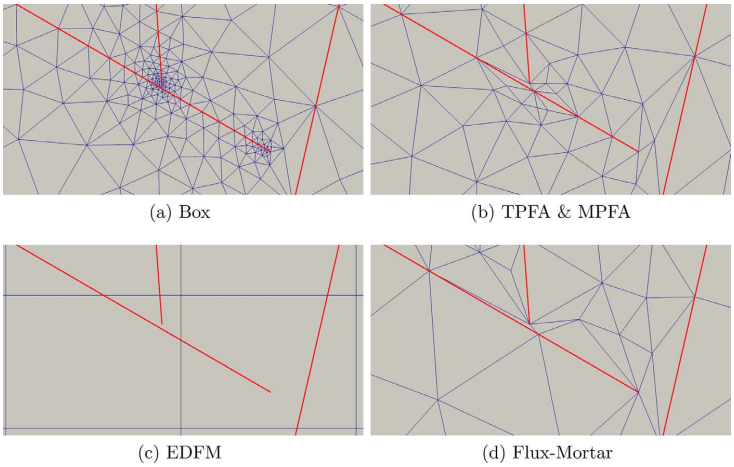

(a) Box (b) TPFA & MPFA

(c) EDFM (d) Flux-Mortar

Fig. 28. Benchmark 4: Representation of mesh in the middle of the domain. The size of the picture is approximately 30 m × 15 m centred in (360, 350). It is represented by the small rectangle in the centre of Fig. 26 left.

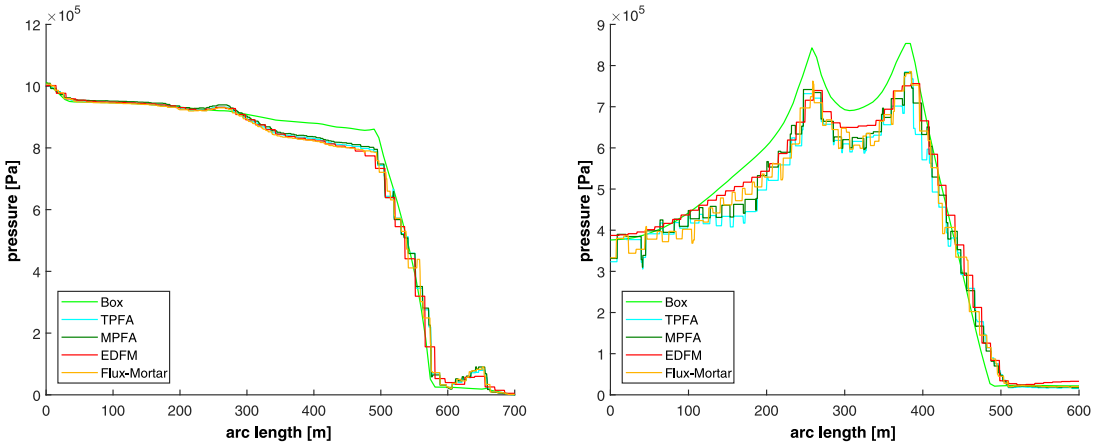

(a) $y = 500\,\mathrm{m}$ (b) $x = 625\,\mathrm{m}$

Fig. 29. Benchmark 4: Pressure solutions of the 4 methods plotted over lines (a) $y = 500$ m, and (b) $x = 625$ m.

Acknowledgement

The authors warmly thank Luisa F. Zuluaga, from University of Bergen, for constructing and providing the real fracture network for the example in Section 4.4. The authors wish to thank also Luca Pasquale and Stefano Zonca.

The second author acknowledges financial support from the GeoStim project from the Research Council of Norway (project no. 228832) through the ENERGIX program. The third author was supported by Norwegian Research Council grant 233736. The fourth author acknowledges financial support from the ANIGMA project from the Research Council of Norway (project no. 244129/E20) through the ENERGIX program.

Appendix A. Details for the convergence study in Benchmark 1

Detailed numbers for the convergence studies carried out in Section 4.1 are provided by means of tables for the errors in matrix and fracture, calculated according to (7). In particular, the index k in $err_{\mathrm{m},\,k}$ and $err_{\mathrm{f},\,k}$ refers to the refinement level. The number of elements is indicated correspondingly by $n_{\mathrm{m},\,k}$ and $n_{\mathrm{f},\,k}$ for matrix and fracture, respectively. The experimental orders of convergence $eoc_{\mathrm{m},\,k}$ and $eoc_{\mathrm{f},\,k}$ are calculated by

$$eoc_{\mathrm{m},k} = 2\frac{\log \dfrac{err_{\mathrm{m},k}}{err_{\mathrm{m},k-1}}}{\log \dfrac{n_{\mathrm{m},k-1}}{n_{\mathrm{m},k}}}, \qquad eoc_{\mathrm{f},k} = \frac{\log \dfrac{err_{\mathrm{f},k}}{err_{\mathrm{f},k-1}}}{\log \dfrac{n_{\mathrm{f},k-1}}{n_{\mathrm{f},k}}}.$$

A1. Conductive fracture network

Method	$n_{m,0}$	$err_{m,0}$	$n_{m,1}$	$err_{m,1}$	$eoc_{m,1}$	$n_{m,2}$	$err_{m,2}$	$eoc_{m,2}$
Box	1078	1.1e−02	4312	5.3e−03	1.05	17,248	2.7e−03	0.97
TPFA	1386	1.1e−02	4269	8.1e−03	0.54	14,866	4.1e−03	1.09
TPFA*	–	–	–	–	–	–	–	–
MPFA	1348	1.1e−02	4673	5.5e−03	1.12	17,632	2.8e−03	1.02
EDFM	1369	6.5e−03	5625	2.7e−03	1.24	22,801	1.4e−03	0.94
Flux-Mortar	1280	1.0e−02	5120	5.2e−03	0.94	20,480	2.6e−03	1.00
P-XFEM	961	9.3e−03	3969	5.2e−03	0.82	16,129	1.9e−03	1.44
D-XFEM	1250	9.6e−03	4802	4.9e−03	1.00	19,602	2.5e−03	0.96

Method	$n_{f,0}$	$err_{f,0}$	$n_{f,1}$	$err_{f,1}$	$eoc_{f,1}$	$n_{f,2}$	$err_{f,2}$	$eoc_{f,2}$
Box	74	1.9e−04	148	1.8e−04	0.08	296	1.7e−04	0.08
TPFA	95	4.4e−03	169	2.8e−03	0.78	317	1.6e−03	0.89
TPFA*	–	–	–	–	–	–	–	–
MPFA	91	4.5e−03	169	2.4e−03	1.02	332	1.2e−03	1.03
EDFM	132	4.0e−03	266	1.8e−03	1.14	532	8.3e−04	1.12
Flux-Mortar	75	6.9e−03	131	3.4e−03	1.27	277	1.6e−03	1.01
P-XFEM	164	7.3e−03	292	4.4e−03	0.88	548	7.6e−04	2.79
D-XFEM	126	8.9e−03	246	4.4e−03	1.05	486	2.2e−03	1.02

A2. Blocking fracture network

Method	$n_{m,0}$	$err_{m,0}$	$n_{m,1}$	$err_{m,1}$	$eoc_{m,1}$	$n_{m,2}$	$err_{m,2}$	$eoc_{m,2}$
Box	1078	4.1e−01	4312	4.1e−01	0.00	17,248	4.1e−01	0.00
TPFA	1386	5.6e−03	4269	4.6e−03	0.35	14,866	2.5e−03	0.98
TPFA*	–	–	–	–	–	–	–	–
MPFA	1348	4.4e−03	4673	2.4e−03	0.98	17,632	1.2e−03	1.04
EDFM	1369	2.9e−01	5625	2.9e−01	0.00	22,801	2.9e−01	0.00
Flux-Mortar	1280	4.3e−03	5120	2.1e−03	1.03	20,480	1.1e−03	0.93
P-XFEM	961	2.7e−03	3969	1.4e−03	0.93	16,129	7.8e−04	0.83
D-XFEM	1250	1.0e−02	4802	1.1e−02	−0.14	19,602	7.7e−03	0.51

Method	$n_{f,0}$	$err_{f,0}$	$n_{f,1}$	$err_{f,1}$	$eoc_{f,1}$	$n_{f,2}$	$err_{f,2}$	$eoc_{f,2}$
Box	74	3.2e−01	148	3.2e−01	0.00	296	3.2e−01	0.00
TPFA	95	4.4e−03	169	3.6e−03	0.35	317	2.4e−03	0.64
TPFA*	–	–	–	–	–	–	–	–
MPFA	91	3.6e−03	169	2.3e−03	0.72	332	1.7e−03	0.45
EDFM	132	3.2e−01	266	3.2e−01	0.00	532	3.2e−01	0.00
Flux-Mortar	75	4.6e−03	131	2.6e−03	1.02	277	1.7e−03	0.57
P-XFEM	164	2.4e−02	292	1.7e−02	0.60	548	1.2e−02	0.55
D-XFEM	126	1.8e−02	246	3.3e−02	−0.91	486	2.2e−02	0.60

Appendix B. Domain modifications for Benchmark 2

Table B.11 provides the exact coordinates of the points from Fig. 16.

In comparison to the original setup, the plateaus close to the upper left and right corners 1 and 9 have been omitted. Moreover, the upper ends of the two fractures have been modified according to Fig. B.30 which amounts to the changes of nodes 2–4 and 6–8.

Finally, the position of nodes 16–19 has been recalculated with higher precision. The hybrid-dimensional models do not take into account nodes 2,4,6,8 and 16–19 and combine nodes 11,12 and 13,14, since the two-dimensional fracture regions have been reduced to two intersecting straight lines.

Table B.11
Coordinates of the numbered points in the modeled region of the problem depicted in Fig. 16.

pt	x (m)	z (m)	pt	x (m)	z (m)
1	0	150	11	1505	−1000
2′	394.285714286	100.714285714	12	1495	−1000
3′	400	100	13	1007.5	−1000
4′	404.444444444	100.555555556	14	992.5	−1000
5	800	150	15	0	−1000
6′	1192.66666667	100.916666667	16	1071.34615385	−566.346153846
7′	1200	100	17	1084.03846154	−579.038461538
8′	1207.6744186	100.959302326	18	1082.5	−587.5
9	1600	150	19	1069.80769231	−574.807692308
10	1600	−1000			

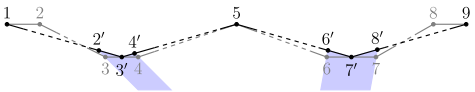

Fig. B.30. Modifications of the Hydrocoin model domain compared to the original formulation (Swedish Nuclear Power Inspectorate (SKI), 1987). The original upper boundary is drawn with grey thin lines, while thick black lines are used for the modified boundary. Modified node locations are indicated by numbers superscripted with ′. The shaded regions show the upper parts of the two slightly extended equi-dimensional fractures.

Appendix C. Fracture coordinates for Benchmark 3

The coordinates are listed in Table C.12.

Table C.12
Benchmark 3: Fracture coordinates

Nf	xA	yA	xB	yB
1	0.0500	0.4160	0.2200	0.0624
2	0.0500	0.2750	0.2500	0.1350
3	0.1500	0.6300	0.4500	0.0900
4	0.1500	0.9167	0.4000	0.5000
5	0.6500	0.8333	0.849723	0.167625
6	0.7000	0.2350	0.849723	0.167625
7	0.6000	0.3800	0.8500	0.2675
8	0.3500	0.9714	0.8000	0.7143
9	0.7500	0.9574	0.9500	0.8155
10	0.1500	0.8363	0.4000	0.9727

Appendix D. Details for the convergence study in Benchmark 3

Detailed numbers for the convergence studies carried out in Section 4.3 are provided by means of tables for the errors in matrix and fracture, analogously to Appendix A.

D1. Flow from top to bottom

Method	$n_{m,0}$	$err_{m,0}$	$n_{m,1}$	$err_{m,1}$	$eoc_{m,1}$	$n_{m,2}$	$err_{m,2}$	$eoc_{m,2}$
Box	2664	4.9e−02	10,656	5.0e−02	−0.03	42,624	5.0e−02	0.00
TPFA	1332	2.7e−02	4650	2.4e−02	0.19	17,690	2.4e−02	0.00
TPFA*	1332	1.3e−02	4650	6.3e−03	1.16	17,690	3.2e−03	1.01
MPFA	1332	2.5e−02	4650	2.4e−02	0.07	17,690	2.3e−02	0.06
EDFM	–	–	–	–	–	–	–	–
Flux-Mortar	1230	1.0e−02	4920	5.2e−03	0.94	19,680	2.6e−03	1.00
P-XFEM	–	–	–	–	–	–	–	–
D-XFEM	1922	1.9e−02	7442	1.3e−02	0.56	29,282	1.1e−02	0.24

Method	$n_{f,0}$	$err_{f,0}$	$n_{f,1}$	$err_{f,1}$	$eoc_{f,1}$	$n_{f,2}$	$err_{f,2}$	$eoc_{f,2}$
Box	152	3.4e−02	292	3.5e−02	−0.04	576	3.6e−02	−0.04
TPFA	88	2.9e−02	166	2.7e−02	0.11	332	2.7e−02	0.00

TPFA*	93	1.1e−02	171	6.7e−03	0.81	337	5.1e−03	0.40
MPFA	88	2.8e−02	166	2.7e−02	0.06	332	2.7e−02	0.00
EDFM	–	–	–	–	–	–	–	–
Flux-Mortar	89	8.2e−03	178	5.6e−03	0.55	356	4.5e−03	0.32
P-XFEM	–	–	–	–	–	–	–	–
D-XFEM	199	3.0e−02	388	2.0e−02	0.61	769	1.7e−02	0.24

D2. Flow from left to right

Method	$n_{m,0}$	$err_{m,0}$	$n_{m,1}$	$err_{m,1}$	$eoc_{m,1}$	$n_{m,2}$	$err_{m,2}$	$eoc_{m,2}$
Box	2664	7.4e−02	10,656	7.6e−02	−0.04	42,624	7.7e−02	−0.02
TPFA	1332	5.1e−02	4650	5.3e−02	−0.06	17,690	5.4e−02	−0.03
TPFA*	1332	1.3e−02	4650	8.6e−03	0.66	17,690	3.6e−03	1.30
MPFA	1332	5.1e−02	4650	5.2e−02	−0.03	17,690	5.3e−02	−0.03
EDFM	–	–	–	–	–	–	–	–
Flux-Mortar	1230	1.4e−02	4920	8.0e−03	0.81	19,680	4.9e−03	0.71
P-XFEM	–	–	–	–	–	–	–	–
D-XFEM	1922	2.0e−02	7442	2.3e−02	−0.21	29,282	2.3e−02	0.00

Method	$n_{f,0}$	$err_{f,0}$	$n_{f,1}$	$err_{f,1}$	$eoc_{f,1}$	$n_{f,2}$	$err_{f,2}$	$eoc_{f,2}$
Box	152	6.3e−02	292	6.7e−02	−0.09	576	6.9e−02	−0.04
TPFA	88	6.7e−02	166	6.8e−02	−0.02	332	6.9e−02	−0.02
TPFA*	93	1.2e−02	171	9.8e−03	0.33	337	7.2e−03	0.45
MPFA	88	6.7e−02	166	6.8e−02	−0.02	332	6.8e−02	0.00
EDFM	–	–	–	–	–	–	–	–
Flux-Mortar	89	1.3e−02	178	9.6e−03	0.44	356	7.9e−03	0.28
P-XFEM	–	–	–	–	–	–	–	–
D-XFEM	199	4.3e−02	388	3.8e−02	0.19	769	3.8e−02	0.00

References

Aavatsmark, I., 2002. An introduction to multipoint flux approximations for quadrilateral grids. Computat. Geosci. 6 (3), 405–432.

Ahmed, R., Edwards, M.G., Lamine, S., Huisman, B.A., Pal, M., 2015. Control-volume distributed multi-point flux approximation coupled with a lower-dimensional fracture model. J. Comput. Phys. 284, 462–489.

de Araujo Cavalcante Filho, J.S., Shakiba, M., Moinfar, A., Sepehrnoori, K., 2015. Implementation of a preprocessor for embedded discrete fracture modeling in an IMPEC compositional reservoir simulator. SPE Reservoir Simulation Symposium, 23–25 February, Houston, Texas, USA. Society of Petroleum Engineershttp://dx.doi.org/10.2118/173289-MS.

Bastian, P., Blatt, M., Dedner, A., Engwer, C., Klöfkorn, R., Kornhuber, R., Ohlberger, M., Sander, O., 2008. A generic grid interface for parallel and adaptive scientific computing. part II: implementation and tests in DUNE. Computing 82 (2–3), 121–138.

Bastian, P., Heimann, F., Marnach, S., 2010. Generic implementation of finite element methods in the distributed and unified numerics environment (DUNE). Kybernetika 46 (2), 294–315.

Berkowitz, B., 2002. Characterizing flow and transport in fractured geological media: a review. Adv. Water Resour. 25 (8–12), 861–884.

Bogdanov, I., Mourzenko, V., Thovert, J.-F., Adler, P., 2003. Two-phase flow through fractured porous media. Phys. Rev. E 68 (2), 026703.

Boon, W. M., Nordbotten, J. M., Yotov, I., 2016. Robust discretization of flow in fractured porous media. ArXiv:1601.06977 [math.NA].

Brenner, K., Groza, M., Guichard, C., Lebeau, G., Masson, R., 2016. Gradient discretization of hybrid dimensional darcy flows in fractured porous media. Numerische Mathematik 134 (3), 569–609.

Brenner, K., Hennicker, J., Masson, R., Samier, P., 2017. Gradient discretization of hybrid-dimensional darcy flow in fractured porous media with discontinuous pressures at matrixfracture interfaces. IMA J. Numer. Anal. 37 (3), 1551–1585. http://dx.doi.org/10.1093/imanum/drw044.

Brezzi, F., Lipnikov, K., Simoncini, V., 2005. A family of mimetic finite difference methods on polygonal and polyhedral meshes. Math. Mod. Meth. Appl. S. 15 (10), 1533–1551.

Caers, J., 2013. A special issue on benchmark problems, datasets and methodologies for the computational geosciences. Comput. Geosci. 50, 1–3. http://dx.doi.org/10.1016/j.cageo.2012.11.001.

Class, H., Ebigbo, A., Helmig, R., Dahle, H.K., Nordbotten, J.M., Celia, M.A., Audigane, P., Darcis, M., Ennis-King, J., Fan, Y., Flemisch, B., Gasda, S.E., Jin, M., Krug, S., Labregere, D., Naderi Beni, A., Pawar, R.J., Sbai, A., Thomas, S.G., Trenty, L., Wei, L., 2009. A benchmark study on problems related to CO2 storage in geologic formations: summary and discussion of the results. Computat. Geosci. 13 (4), 409–434.

D'Angelo, C., Scotti, A., 2012. A mixed finite element method for darcy flow in fractured porous media with non-matching grids. ESAIM: Math. Modell. Numer. Anal. 46 (2), 465–489.

De Dreuzy, J.-R., Pichot, G., Poirriez, B., Erhel, J., 2013. Synthetic benchmark for modeling flow in 3d fractured media. Comput. Geosci. 50, 59–71.

Dietrich, P., Helmig, R., Sauter, M., Hötzl, H., Köngeter, J., Teutsch, G., 2005. Flow and Transport in Fractured Porous Media. Springer.

Eymard, R., Gallouët, T., Herbin, R., 2000. Finite Volume Methods. In: Ciarlet, P.G., Lions, J.L. (Eds.), Solution of Equation in $\mathscr{R}^n$ (Part 3), Techniques of Scientific Computing (Part 3). Handbook of Numerical Analysis 7. Elsevier, pp. 713–1018. http://dx.doi.org/10.1016/S1570-8659(00)07005-8.

Firoozabadi, A., Monteagudo, J.E.P., 2004. Control-volume method for numerical simulation of two-phase immiscible flow in two- and three-dimensional discrete-fractured media. Water Resour. Res. 40, W07405. http://dx.doi.org/10.1029/2003WR002996.

Flauraud, E., Nataf, F., Faille, I., Masson, R., 2003. Domain decomposition for an asymptotic geological fault modeling. Comptes Rendus Mécanique 331 (12), 849–855.

Flemisch, B., Darcis, M., Erbertseder, K., Faigle, B., Lauser, A., Mosthaf, K., Müthing, S., Nuske, P., Tatomir, A., Wolff, M., Helmig, R., 2011. DuMu^x: DUNE for multi-{phase, component, scale, physics, ...} flow and transport in porous media. Adv. Water Resour. 34 (9), 1102–1112. http://dx.doi.org/10.1016/j.advwatres.2011.03.007.

Flemisch, B., Fumagalli, A., Scotti, A., 2016. A review of the xfem-based approximation of flow in fractured porous media. In: Ventura, G., Benvenuti, E. (Eds.), Advances in Discretization Methods: Discontinuities, Virtual Elements, Fictitious Domain Methods. Springer International Publishing, Cham, pp. 47–76. http://dx.doi.org/10.1007/978-3-319-41246-7_3.

Flemisch, B., Helmig, R., 2008. Numerical investigation of a mimetic finite difference method. In: Eymard, R., Hérard, J. (Eds.), Finite Volumes for Complex Applications V – Problems and Perspectives. Wiley - VCH, pp. 815–824.

Formaggia, L., Fumagalli, A., Scotti, A., Ruffo, P., 2014. A reduced model for Darcy's problem in networks of fractures. ESAIM: Math. Modell. Numer. Analysis 48, 1089–1116. http://dx.doi.org/10.1051/m2an/2013132.

Frih, N., Martin, V., Roberts, J.E., Saâda, A., 2012. Modeling fractures as interfaces with nonmatching grids. Computat. Geosci. 16 (4), 1043–1060.

Fumagalli, A., Pasquale, L., Zonca, S., Micheletti, S., 2016. An upscaling procedure for fractured reservoirs with embedded grids. Water Resour. Res. 52 (8), 6506–6525. http://dx.doi.org/10.1002/2015WR017729.

Fumagalli, A., Scotti, A., 2014. An efficient XFEM approximation of Darcy flows in fractured porous media. Oil Gas Sci. Technol. - Revue d'IFP Energies Nouvelles 69.4, 555–564.

Gassiat, C., Gleeson, T., Lefebvre, R., McKenzie, J., 2013. Hydraulic fracturing in faulted sedimentary basins: numerical simulation of potential contamination of shallow aquifers over long time scales. Water Resour. Res. 49 (12), 8310–8327. http://dx.doi.org/10.1002/2013WR014287.

Geiger, S., Dentz, M., Neuweiler, I., 2013. A novel multi-rate dual-porosity model for improved simulation of fractured and multiporosity reservoirs. SPE J. 18 (4), 670–684.

Hajibeygi, H., Karvounis, D., Jenny, P., 2011. A hierarchical fracture model for the iterative multiscale finite volume method. J. Comput. Phys. 230 (24), 8729–8743.

Hansbo, A., Hansbo, P., 2002. An unfitted finite element method, based on Nitsche's method, for elliptic interface problems. Comput. Methods Appl. Mech. Eng. 191 (47–48), 5537–5552.

Helmig, R., 1997. Multiphase Flow and Transport Processes in the Subsurface: A Contribution to the Modeling of Hydrosystems, 1 ed. Springer.

Hoteit, H., Firoozabadi, A., 2008. Numerical modeling of two-phase flow in heterogeneous permeable media with different capillarity pressures. Adv. Water Resour. 31 (1), 56–73.

Huang, H., Long, T.A., Wan, J., Brown, W.P., 2011. On the use of enriched finite element method to model subsurface features in porous media flow problems. Computat. Geosci. 15 (4), 721–736.

Karimi-Fard, M., Durlofsky, L.J., Aziz, K., 2004. An efficient discrete-fracture model applicable for general-purpose reservoir simulators. SPE J. 9 (2), 227–236.

Kolditz, O., Shao, H., Wang, W., Bauer, S., 2015. Thermo-Hydro-Mechanical-Chemical Processes in Fractured Porous Media: Modelling and Benchmarking. Springer.

Li, L., Lee, S.H., 2008. Efficient field-scale simulation of black oil in a naturally fractured reservoir through discrete fracture networks and homogenized media. SPE Reservoir Eval. Eng 11, 750–758. http://dx.doi.org/10.2118/103901-PA.

Lie, K.-A., Krogstad, S., Ligaarden, I.S., J. R. Natvig, H.M.N., Skaflestad, B., 2012. Open source matlab implementation of consistent discretisations on complex grids. Computat. Geosci. 16 (2), 297–322.

Logg, A., Mardal, K.-A., Wells, G.N., et al., 2012. Automated Solution of Differential Equations by the Finite Element Method. Springerhttp://dx.doi.org/10.1007/978-3-642-23099-8.

Martin, V., Jaffré, J., Roberts, J.E., 2005. Modeling fractures and barriers as interfaces for flow in porous media. SIAM J. Sci. Comput. 26 (5), 1667–1691.

Moinfar, A., Narr, W., Hui, M.-H., Mallison, B.T., Lee, S.H., 2011. Comparison of discrete-fracture and dual-permeability models for multiphase flow in naturally fractured reservoirs. SPE Reservoir Simulation Symposium. Society of Petroleum Engineers.

Moinfar, A., Varavei, A., Sepehrnoori, K., Johns, R.T., 2014. Development of an efficient embedded discrete fracture model for 3d compositional reservoir simulation in fractured reservoirs. SPE J. 19 (2), 289–303.

Müthing, S., 2015. A Flexible Framework for Multi Physics and Multi Domain PDE Simulations. University of Stuttgart Ph.D. thesis.

Neumann, S.P., 2005. Trends, prospects and challenges in quantifying flow and transport through fractured rocks. Hydrogeol. J. 13, 124–147.

Nordbotten, J., Flemisch, B., Gasda, S., Nilsen, H., Fan, Y., Pickup, G., Wiese, B., Celia, M., Dahle, H., Eigestad, G., Pruess, K., 2012. Uncertainties in practical simulation of CO2 storage. Int. J. Greenhouse Gas Control 9, 234–242. http://dx.doi.org/10.1016/j.ijggc.2012.03.007.

Panfili, P., Cominelli, A., 2014. Simulation of miscible gas injection in a fractured carbonate reservoir using an embedded discrete fracture model. Abu Dhabi International Petroleum Exhibition and Conference, 10–13 November, Abu Dhabi, UAE. Society of Petroleum Engineershttp://dx.doi.org/10.2118/171830-MS.

Panfili, P., Cominelli, A., Scotti, A., 2013. Using Embedded Discrete Fracture Models (EDFMs) to simulate realistic fluid flow problems. Second EAGE Workshop on Naturally Fractured Reservoirs, Muscat, Oman.

Pfunt, H., Houben, G., Himmelsbach, T., 2016. Numerical modeling of fracking fluid migration through fault zones and fractures in the north german basin. Hydrogeol. J. 24 (6), 1343–1358. http://dx.doi.org/10.1007/s10040-016-1418-7.

Reichenberger, V., Jakobs, H., Bastian, P., Helmig, R., 2006. A mixed-dimensional finite volume method for two-phase flow in fractured porous media. Adv. Water Resour. 29 (7), 1020–1036. http://dx.doi.org/10.1016/j.advwatres.2005.09.001.

Sahimi, M., 2011. Flow and Transport in Porous Media and Fractured Rock: From Classical Methods to Modern Approaches. John Wiley & Sons.

Sandve, T.H., Berre, I., Nordbotten, J.M., 2012. An efficient multi-point flux approximation method for discrete fracture-matrix simulations. J. Comput. Phys. 231 (9), 3784–3800. http://dx.doi.org/10.1016/j.jcp.2012.01.023.

Schwenck, N., 2015. An XFEM-Based Model for Fluid Flow in Fractured Porous Media. University of Stuttgart Ph.D. thesis.

Schwenck, N., Flemisch, B., Helmig, R., Wohlmuth, B., 2015. Dimensionally reduced flow models in fractured porous media: crossings and boundaries. Computat. Geosci. 19 (6), 1219–1230. http://dx.doi.org/10.1007/s10596-015-9536-1.

Singhal, B.B.S., Gupta, R.P., 2010. Applied Hydrogeology of Fractured Rocks. Springer Science & Business Media.

Swedish Nuclear Power Inspectorate (SKI), 1987. The International Hydrocoin Project–Background and Results. Paris, France: Organization for Economic Co-operation and Development.

Taherdangkoo, R., Tatomir, A., Taylor, R., Sauter, M., 2017. Numerical investigations of upward migration of fracking fluid along a fault zone during and after stimulation. Energy Procedia 125, 126–135. http://dx.doi.org/10.1016/j.egypro.2017.08.093.

Tatomir, A.-B., 2012. From Discrete to Continuum Concepts of Flow in Fractured Porous Media. Ph.D. thesis. University of Stuttgart.

Tene, M., Bosma, S.B., Kobaisi, M.S.A., Hajibeygi, H., 2017. Projection-based embedded discrete fracture model (pEDFM). Adv. Water Resour. 105, 205–216. http://dx.doi.org/10.1016/j.advwatres.2017.05.009.

Tunc, X., Faille, I., Gallouët, T., Cacas, M.C., Havé, P., 2012. A model for conductive faults with non-matching grids. Computat. Geosci. 16 (2), 277–296.

Paper E

Unified Approach to Discretization of Flow in Fractured Porous Media

J.M. Nordbotten, W.M. Boon, A. Fumagalli, E. Keilegavlen

Computational Geosciences. In review.

arXiv:1802.05961 [math.NA]

Unified approach to discretization of flow in fractured porous media

J. M. Nordbotten[1,2], W. M. Boon[1], A. Fumagalli[1], E. Keilegavlen[1]

[1] Department of Mathematics, University of Bergen, N-5020 Bergen, Norway
[2] Department of Civil and Environmental Engineering, Princeton University, Princeton, NJ 08544, USA

In celebration the 60th birthday of Professor Rainer Helmig

Abstract

In this paper, we introduce a mortar-based approach to discretizing flow in fractured porous media, which we term the mixed-dimensional flux coupling scheme. Our formulation is agnostic to the discretizations used to discretize the fluid flow equations in the porous medium and in the fractures, and as such it represents a unified approach to integrated fractured geometries into any existing discretization framework. In particular, several existing discretization approaches for fractured porous media can be seen as special instances of the approach proposed herein.

We provide an abstract stability theory for our approach, which provides explicit guidance into the grids used to discretize the fractures and the porous medium, as dependent on discretization methods chosen for the respective domains. The theoretical results are sustained by numerical examples, wherein we utilize our framework to simulate flow in 2D and 3D fractured media using control volume methods (both two-point and multi-point flux), Lagrangian finite element methods, mixed finite element methods, and virtual element methods. As expected, regardless of the ambient methods chosen, our approach leads to stable and convergent discretizations for the fractured problems considered.

Key words: discretization methods, mixed-dimensional, flux mortars

1. Introduction

Flow in porous media with thin inclusions is an important process both within subsurface and industrial materials. Our main focus herein is on the subsurface, where the thin inclusions represent fractures, and the fracture space can be either open or filled. We will thus simply refer to fractured porous media in what follows. However, thin inclusions may also be engineered in artificial porous media for the purpose of fluid flow control.

Fluid flow in fractured porous media is a dominating process in several subsurface applications, ranging from geothermal energy production, shale gas recovery and nuclear waste deposits. As such, accurate and reliable numerical representations have been an important topic of research, and Rainer Helmig has been a major contributor to the field for more than three decades. Existing discrete representations of

fractured porous media fall in two major categories, depending on whether the fractures conform to the underlying discrete grid representing the porous materials. So-called “unfitted” discretizations, wherein the fractures are allowed to be arbitrary with respect to the grid, have seen significant research and developments in recent years (see e.g. [1, 2]). Our focus herein is in contrast on discretizations the discrete grid resolves the fractures, which are conceptually simpler than unfitted discretizations.

Early research into numerical simulation and conforming discretization of fractured porous media was spear-headed by among others Rainer Helmig and his collaborators [3]. This early work was centered around lowest-order finite element discretizations. Later, it was understood that local conservation properties were important for discretization methods for flow in porous media, and conforming discretizations of fractured porous media were developed based on control volume approaches [4, 5], mixed finite element methods [6, 7], mimetic finite differences [8] and virtual element methods [9]. See also [10] for a comparison study.

A recent development in the mathematical representation of fractured porous media is the modeling and interpretation of fractures as lower-dimensional manifolds [11, 7]. This concept allows for the introduction of mixed-dimensional partial differential equations (md-PDEs), wherein partial differential equations are defined, in a coupled sense, both in the porous material, lower-dimensional fractures, and yet lower-dimensional intersections. In this abstraction, it can be shown that the mathematical models for fractured porous media, can be cast in a rich functional-analysis framework, ensuring well-posedness, and thus existence and uniqueness, of solutions [12].

In this manuscript, we revisit conforming discretizations of fractured porous media within the context of md-PDEs. We show, by introducing explicit coupling variables in the spirit of mortar methods [13, 11, 7, 14], an abstract framework for constructing a conforming fracture discretization from any discretization of non-fractured porous media. We term this approach the mixed-dimensional flux-coupling (MDFC) method. Viewed from the discretization within each dimension, the coupling between dimensions takes the form of standard boundary value problems, thus any implementation that can account for Dirichlet and Neumann boundary data can be applied to fractured media with minimal adaptations. Our approach thus unifies the various previous developments reviewed above.

We concretize the abstract framework by applying it to well-known discretizations from literature, establishing (in some cases for the first time) that these discretizations are well-posed. To illustrate the versatility of the framework, we provide numerical examples showing how five different discretization methods for non-fractured porous can be applied as discretization methods for fractured porous media. Our examples, which include a 2D case where we use non-matching grids between the dimensions and a relatively complex 3D case, highlight the convergence properties and stability of MDFC even for degenerating parameters.

The remaining manuscript honors the following structure: We first review the modeling of fractured porous media. Thereafter, in section 3, we introduce our novel approach to unifying discretization methods for fractured media. We show the stability of the approach theoretically, which emphasizes the conditions required between the (in principle non-matching) grids discretizing the matrix and fractures. Numerical examples and verification are presented before concluding the paper.

2. Modeling fractured porous media

In this section we introduce our model for fractured media, first by a single fracture, and then extended to general fracture networks.

2.1. Domain with a single fracture

Flow in (fractured) porous media can lead to complex and non-linear governing equations. However, at the heart usually lies a second-order partial differential equation, which upon linearization (i.e. within a Newton iteration) thus takes the classical form for a pressure p^3 and flux q^3

$$\nabla \cdot q^3 + \psi^3 = 0 \quad \text{on} \quad \Omega^3 \tag{2.1}$$

$$-\kappa \nabla p^3 = q^3 \quad \text{on} \quad \Omega^3 \tag{2.2}$$

$$q^3 \cdot n^3 = \lambda^2_+ \quad \text{on} \quad \partial_{\Omega^2_+}\Omega^3 \tag{2.3}$$

$$q^3 \cdot n^3 = \lambda^2_- \quad \text{on} \quad \partial_{\Omega^2_-}\Omega^3 \tag{2.4}$$

$$q^3 \cdot n^3 = g^3 \quad \text{on} \quad \partial_N\Omega^3 \tag{2.5}$$

$$\operatorname{tr} p^3 = 0 \quad \text{on} \quad \partial_D\Omega^3 \tag{2.6}$$

Here we denote by Ω^3 the (3-dimensional) porous medium, and by ∂_N and ∂_D its Neumann and Dirichlet boundaries, respectively. We denote by $\partial_{\Omega^2_\pm}\Omega^3$ the boundary of Ω^3 as seen from the positive (resp. negative) side of Ω^2, and the outer normal vector is always denoted n. The Dirichlet boundary data is set to zero for notational convenience. We emphasize the structure of the governing equations as composed of a conservation law (2.1), and a constitutive (Darcy) law (2.2). In equations (2.1-2.6) we have marked variables by a superscript '3' to emphasize that they belong in 3 dimensions, the necessity of the precision will be clear below. Note that the flux from the (2-dimensional) Neumann boundary is denoted by a superscript '2'. Throughout the manuscript, we will use ψ to denote right-hand sides, which with the chosen sign convention represents fluid extraction.

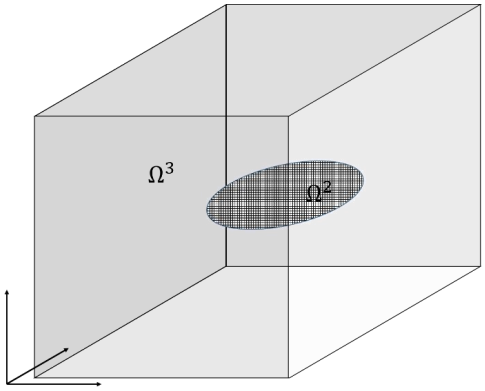

Figure 1: Illustration of a 3D-domain with a single 2D-fracture, see Section 4 for more examples.

Similarly, we may consider a single fracture as a (2-dimensional) manifold Ω^2, whereon the governing equations can in the linearized case be expressed as [15]

$$\nabla_2 \cdot q^2 - (\lambda_+^2 + \lambda_-^2) + \psi^2 = 0 \quad \text{on} \quad \Omega^2 \tag{2.7}$$

$$-\kappa_{||}^2 \nabla_2 p^2 = q^2 \quad \text{on} \quad \Omega^2 \tag{2.8}$$

$$q^2 \cdot n^2 = g^d \quad \text{on} \quad \partial_N \Omega^2 \tag{2.9}$$

$$\operatorname{tr} p^2 = 0 \quad \text{on} \quad \partial_D \Omega^2 \tag{2.10}$$

In equations (2.7-2.8), we denote by a double-strike the tensor operating tangentially (parallel) to the manifold, and emphasized that the differential operators are 2-D by a subscript. We note that in equation (2.7), two extra terms arise. These represent the outflow from the fracture into the porous medium on the two sides of the fracture (denoted + and -). As above, fracture variables are indicated by a superscript '2' for clarity.

Considering still the case of a single fracture, equations (2.1-2.10) lead to a system of equations where λ^2 is a variable internal to the system. We thus complete the model with a constitutive law for λ^2, which takes the Darcy-like form (see e.g. [7])

$$\lambda_\pm^3 = -\kappa_\perp \left(p^2 - \operatorname{tr} p_\pm^3\right) \tag{2.11}$$

We remark that the within-fracture permeability $\kappa_{||}$ and the transverse permeability $\kappa_\perp$ will in practice scale with the aperture and its inverse, respectively.

Equations (2.1-2.11) form a closed and well-posed system of equations for a porous medium including a fracture (see e.g. [8]). More generally, we note that we write these equations in a unified way, in that for $d = \{2,3\}$

$$\nabla_d \cdot q^d - \textstyle\sum_{j \in \pm} \lambda_j^d + \psi^d = 0 \quad \text{on} \quad \Omega^d \tag{2.12}$$

$$-\kappa_{||}^d \nabla_d p^d = q^d \quad \text{on} \quad \Omega^d \tag{2.13}$$

$$q^d \cdot n^d = \lambda^{d-1} \quad \text{on} \quad \partial_{\Omega^{d-1}} \Omega^d \tag{2.14}$$

$$\lambda_j^d = -\kappa_\perp^d \left(p^d - \operatorname{tr} p_j^{d+1}\right) \quad \text{on} \quad \partial_{\Omega^{d-1}} \Omega^d \tag{2.15}$$

$$q^d \cdot n^d = g^d \quad \text{on} \quad \partial_N \Omega^d \tag{2.16}$$

$$p^d = 0 \quad \text{on} \quad \partial_D \Omega^d \tag{2.17}$$

Equations (2.12-2.17) make sense with the convention that since there is no 4-dimensional domain in the model, the terms $\lambda^3 = 0$.

From physical considerations, it is customary to consider all boundaries of the fracture as Neumann boundaries with $g^d = 0$, except where the boundary coincides with an outer boundary of the full domain. However, these restrictions are not necessary from a mathematical or numerical perspective, and we will retain the slightly more general formulation in order to avoid extra notation for distinguishing between internal and external boundaries of fractures.

2.2. Extension to general fracture configurations

Equations (2.12-2.17) are written in a way that naturally generalizes also to fracture intersections, both the 1-D line intersections as well as the 0-D point intersections of three fractures [16, 6]. We introduce some extra notation to this end. Let each domain (matrix, fracture, or intersection) be indexed by number and dimension, i.e. Ω_i^d is domain number $i \in I$, having dimensionality d. We consider a total of m subdomains of various dimensionality. This subdivision is illustrated in Figure 2.

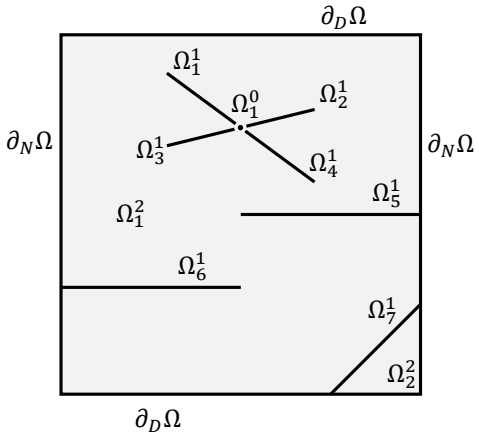

Figure 2: Illustration of a domain in 2D containing four fractures and an intersection, and its logical representation with two 2D-domains, seven 1D-domains, and one 0D domain.

Furthermore, let $\hat{S}_i$ be the set of neighbors of domain i of dimension $d+1$, and conversely let $\check{S}_i$ be the set of neighbors of i with dimension $d-1$. Then we can write for all $d = \{0,1,2,3\}$ and all $i \in I$ the equations

$$\nabla_d \cdot q_i^d - \textstyle\sum_{j\in\hat{S}_i} \lambda_{i,j}^d + \psi_i^d = 0 \quad \text{on} \quad \Omega_i^d \tag{2.18}$$

$$-\kappa_{i,||}^d \nabla_d p_i^d = q_i^d \quad \text{on} \quad \Omega_i^d \tag{2.19}$$

$$q_j^d \cdot n_j^d = \lambda_{i,j}^{d-1} \quad \text{on} \quad \partial_i\Omega_j^d \tag{2.20}$$

$$\lambda_{i,j}^d = -\kappa_{i,\perp}^d \left(p_i^d - \operatorname{tr} p_j^{d+1}\right) \quad \text{on} \quad \partial_i\Omega_j^d \tag{2.21}$$

$$q_i^d \cdot n_i^d = g_i^d \quad \text{on} \quad \partial_N\Omega_i^d \tag{2.22}$$

$$p_i^d = 0 \quad \text{on} \quad \partial_D\Omega_i^d \tag{2.23}$$

Note that for $d = 0$, the domain has no physical extent and no boundary such that (2.19), (2.20) and (2.22) are void, and correspondingly q_i^0 is not a variable in the system. Equations (2.18-2.23) - with some variations – are equivalent or generalize the standard equations used to model fractured porous media (see [7, 1, 6] and references therein). These equations have been identified as a second-order

system of mixed-dimensional partial differential equations, for which existence and uniqueness theory has been developed under fairly mild assumptions on the geometry [12]. In this work we will only consider planar fractures, but with no restrictions on their intersections or interaction with the boundary.

In order to simplify notation in the following, we consider the dimension associated with each subdomain, $d = d(i)$, to be specified, and introduce the compound variables $\mathfrak{p} = \left[p_1^{d(1)} \dots p_m^{d(m)}\right]$, $\mathfrak{q} = \left[q_1^{d(1)} \dots q_m^{d(m)}\right]$ and similarly for $\mathfrak{\lambda} = [\lambda_{i,j}]$. We also introduce corresponding function spaces, thus we let $\mathcal{H}_1 = \prod_i \overset{\circ}{H}_1\left(\Omega_i^{d(i)}\right)$ and $\mathcal{L}^2 = \prod_i \prod_{j \in \hat{S}_i} L^2(\Omega_i^d(i))$. The Dirichlet boundary conditions implied by the notation $\overset{\circ}{H}_1$ only applies to the part of the boundary covered by equation (2.23).

2.3 Variational formulation

Before considering discretization of equations (2.18-2.23), we note that equation (2.21) is in a sense dual to the summation terms in equation (2.18), thus the system can be written as a symmetric saddle-point problem: Find $(\mathfrak{p}, \mathfrak{\lambda}) \in \mathcal{H}_1 \times \mathcal{L}^2$ such that for all $i \in I$ [from equations (2.18-2.20)]:

$$\left(\kappa_{i,||}^d \nabla_d p_i^d, \nabla_d w_i^d\right)_{\Omega_i^d} + \sum_{j \in \check{S}_i} \left(\lambda_{j,i}^{d-1}, \operatorname{tr} w_i^d\right)_{\partial_j \Omega_i^d} - \sum_{j \in \hat{S}_i^d} \left(\lambda_{i,j}^d, w_i^d\right)_{\Omega_i^d} = -(\psi_i^s, w) - \left(g_i^d, \operatorname{tr} w_i^d\right)_{\partial_N \Omega_i^d} \quad \text{for all} \quad w \in H_1(\Omega_i^d) \tag{2.24}$$

and [from (2.21)]:

$$\sum_{j \in \hat{S}_i^d} \left(p_i^d, \mu_{i,j}^d\right)_{\Omega_i} - \left(\mu_{i,j}^d, \operatorname{tr} p_j^{d+1}\right)_{\partial_i \Omega_j^{d+1}} + \left(\left(\kappa_{i,\perp}^d\right)^{-1} \lambda_{i,j}^d, \mu_{i,j}^d\right)_{\partial_i \Omega_j^{d+1}} = 0 \qquad \text{for all} \quad \mu \in L^2\left(\partial_i \Omega_j^d\right) \tag{2.25}$$

By shifting indexes on the trace term in (2.24), we identify the symmetric and coupling terms as

$$a(\mathfrak{p}, \mathfrak{\lambda}; w, \mu) = \sum_{i \in I} \left(\kappa_{i,||}^d \nabla_d p_i^d, \nabla_d w_i^d\right)_{\Omega_i^d} + \left(\left(\kappa_{i,\perp}^d\right)^{-1} \lambda_{i,j}^d, \mu_{i,j}^d\right)_{\partial_i \Omega_j^{d+1}} \tag{2.26}$$

$$b(\mathfrak{p}, \mu) = \sum_{i \in I} \left(\left(\mu_{i,j}^d, \operatorname{tr} p_j^{d+1}\right)_{\partial_i \Omega_j^{d+1}} - \sum_{j \in \hat{S}_i^d} \left(p_i^d, \mu_{i,j}^d\right)_{\Omega_i^d} \right) \tag{2.27}$$

For non-degenerate coefficients, equations (2.24-2.25) are well-posed by standard saddle-point theory [17], and in the remaining manuscript we will only consider this case. Nevertheless, we remark that, following similar arguments as exposed in [6], it can be shown that significant degeneracy of coefficients can be permitted, at the cost of introducing weighted spaces. In particular, it is of interest to also allow for blocking fractures, wherein the tangential permeability is negligible. Equations (2.24-2.25) are well-posed in this sense, since if for a given domain Ω_i^d, the permeability can degenerate in the sense of $\kappa_{i,||}^d \to 0$, as long as $\kappa_{i,\perp}^{-d}$ remains bounded from below for all $j \in \hat{S}_i^d$. However, now the pressure p_i^d is only in L^2 due to the inf-sup condition for $b(\mathfrak{p}, \mu)$ [6]. This implies that this weakly continuous formulation for fractured porous media is robust both for arbitrarily thin fractures, and can also be applied to blocking fractures. We summarize the above discussion as follows:

Let an L^2-like norm on $\mathcal{H}_1 \times \mathcal{L}^2$ be defined as

$$\|(p,\lambda)\|^2 = \sum_{i\in I}\left\|p_i^d\right\|^2_{L^2(\Omega_i^d)} + \sum_{j\in\hat{S}_i}\left\|\lambda_{i,j}^d\right\|^2_{L^2(\Omega_i^d)} \tag{2.28}$$

Furthermore, let the set of indexes be refined such that $i \in I_a$ if $\kappa_{i,||}^d > 0$ and $i \in I_b$ if $\kappa_{i,||}^d = 0$. Then we introduce space $\mathcal{P}$ as

$$\mathcal{P} = \prod_{i\in I_a} \mathring{H}_1\left(\Omega_i^{d(i)}\right) \times \prod_{i\in I_b} L^2\left(\Omega_i^{d(i)}\right) \tag{2.29}$$

Then the equations for flowing and blocking fractures can be written as find $(\mathfrak{p},\mathfrak{\lambda}) \in \mathcal{P}\times\mathcal{L}^2$ such that

$$a(\mathfrak{p},\mathfrak{\lambda};w,\mu) + b(w,\mathfrak{\lambda}) - b(\mathfrak{p},\mu) = -\sum_{i\in I}(\psi_i^s, w_i^s) - \sum_{i\in I_a}\left(g_i^d, \operatorname{tr} w_i^d\right)_{\partial_N\Omega_i^d} \qquad \text{for all } (w,\mu)\in\mathcal{P}\times\mathcal{L}^2 \tag{2.30}$$

The solution of (2.30) is characterized by the following Lemma.

Lemma 2.1

Equation (2.30) has a unique solution $(\mathfrak{p},\mathfrak{\lambda}) \in \mathcal{P}\times\mathcal{L}^2$, satisfying

$$\|(\mathfrak{p},\mathfrak{\lambda})\| \le C\|(\psi,g)\| \tag{2.31}$$

Provided that there exists constants $\kappa_{0,\perp}$ and $\kappa_{\infty,\perp}$ for all i, holds that $0 < \kappa_{0,\perp} \le \kappa_{i,\perp}^d \le \kappa_{\infty,\perp} < \infty$, and that

a) There is a lower bound $\kappa_{0,||}$ such that for all $i \in I_a$, it holds that $\kappa_{i,||}^d \ge \kappa_{0,||} > 0$, while,
b) For all $i \in I_b$ there it holds that $j \in I_a$ for all $j \in \hat{S}_i$.

Proof.

For the two cases in the proof for I_a and I_b, respectively, we indicate variables in these domains by similar subscripts. Then formally, equations (2.26) take the form

$$\begin{pmatrix} \kappa_{0,||}\Delta_a & \Sigma & \Sigma & 0 \\ -\Sigma^{\mathrm{T}} & \kappa_\perp^{-1} & 0 & 0 \\ -\Sigma^{\mathrm{T}} & 0 & \kappa_\perp^{-1} & -\Sigma^{\mathrm{T}} \\ 0 & 0 & \Sigma & 0 \end{pmatrix} \begin{pmatrix} \mathfrak{p}_a \\ \mathfrak{\lambda}_{a,a} \\ \mathfrak{\lambda}_{a,b} \\ \mathfrak{p}_b \end{pmatrix} = -\begin{pmatrix} \psi_a + g \\ 0 \\ 0 \\ \psi_b \end{pmatrix}$$

Here, Δ_a represents the H_1 bilinear forms on Ω_i^d, $\kappa_\perp$ represents the L^2 bilinear forms om $\partial_j\Omega_i^d$, while Σ are the duality pairings in (2.27). The upper-left 3x3 system is coercive due to the conditions of the proof. Furthermore, we obtain the well-posedness of the full system, since it is easy to show that the Σ terms are inf-sup stable between L^2 spaces, indeed

$$\inf_{\substack{p_i^d\in L^2(\Omega_i^d)\\ i\in I_b}} \sup_{\mu_{i,j}^d\in L^2(\Omega_i^d)} \frac{\sum_{j\in\hat{S}_i^d}\left(p_i^d, \mu_{i,j}^d\right)_{\Omega_i^d}}{\left\|p_i^d\right\|_{L^2(\Omega_i^d)}\left\|\mu_{i,j}^d\right\|_{L^2(\Omega_i^d)}} \ge 1$$

Since one may simply choose $\mu_{i,j}^d = p_i^d$. The coercivity of the upper left 3x3 system together with inf-sup for the Σ terms is sufficient for stability of the full system by abstract saddle-point theory [17]. □

Remark 2.2

Lemma 2.1 is not optimal in the sense that it is fairly easy to extract H^1 regularities on all domains $i \in I_a$, and the restrictions on $\kappa_\perp$ can be somewhat relaxed. However, as we in this contribution are primarily interested in the numerical implementation, we have chosen to keep Lemma 2.1 as simple as possible. Readers interested in the functional analysis for equations of this type are referred to the papers referenced in the introduction.

It is important to note that the main objective of exposing the equations for flow in fractured porous media on the form (2.26-2.27), is that it highlights the specific domain-decomposition like structure of the problem. Indeed, we note that on each sub-domain (be it porous media, fracture, or fracture intersections), we have a fairly standard elliptic partial-differential equation. These are coupled via interface variables, $\lambda_{i,j}^d$. This structure is key to design general and flexible discretization approaches, as introduced in the next section.

3. Discretizations for fractured porous media

Our exposition of the mathematical model for fractured porous media emphasizes two main aspects of the model, namely the second-order elliptic PDE within each domain, and the flux-coupling terms. Numerous discretization methods have been constructed for second-order elliptic differential equations – many of these are bespoke to the particular challenges associated with flow in highly heterogeneous porous media (for an introduction, see the books [18, 19, 20]). Herein, we will prove that any stable discretization for flow in (mono-dimensional) porous media can be applied to fractured porous media through the framework introduced in the preceding section.

We subdivide this section in three parts, in order to provide the MDFC discretization framework, its abstract analysis, and a concrete example using finite elements.

To be precise, we consider each domain Ω_i^d and its Neumann boundary $\Gamma_i^d = \partial_N \Omega \cup_{j \in \check{S}} \partial_j \Omega_i^d$ as endowed with a numerical discretization (note that Γ_i^d includes all boundaries to lower-dimensional manifolds). We will only consider linear discretizations, however the approach should be applicable also to non-linear discretizations (for a recent contribution in this direction from Helmig's group, see [21]). We do not require that a discrete grid be defined, however we let the discrete representation of $L^2\left(\Omega_i^d\right)$ and $L^2\left(\Gamma_i^d\right)$ as $N_h\left(\Omega_i^d\right)$ and $N_h\left(\Gamma_i^d\right)$, respectively. For domains $i \in I_a$, i.e. where the fractures are permeable with $\kappa_{i,||}^d \geq \kappa_{0,||}$, the solution operator of the numerical discretization of the heterogeneous elliptic equation on a given domain $i \in I_a$ can be stated as $\mathcal{N}_i^d : \left[N_h\left(\Omega_i^d\right), N_h\left(\Gamma_i^d\right)\right] \rightarrow \left[N_h\left(\Omega_i^d\right), N_h\left(\Gamma_i^d\right)\right]$. This solution operator maps sinks and Neumann data to pressures and pressure traces, as made precise below. Here, we recall that we for notational simplicity only consider homogeneous boundary conditions on the Dirichlet boundaries, and as such suppress the Dirichlet boundary data. For domains $i \in I_b$, the solution operator is void, as there is no differential equation on these domains.

We will use the natural requirement that the numerical discretizations provided are consistent approximations in the following sense: Let $i \in I_a$, and let $[p, t] = \mathcal{N}_i^d(\psi, \theta)$, for $(\psi, \theta) \in N_h(\Omega_i^d) \times N_h(\Gamma_i^d)$, then this quadruplet of variables approximates the solution to the elliptic differential equation

$$\nabla_d \cdot \left(-\kappa_{i,||}^d \nabla_d p\right) + \psi \approx 0 \qquad \text{on} \qquad \Omega_i^d \tag{3.1}$$

$$\left(-\kappa_{i,||}^d \nabla_d p\right) \cdot n - \theta \approx 0 \qquad \text{on} \qquad \Gamma_i^d \tag{3.2}$$

$$t - \operatorname{tr} p \approx 0 \qquad \text{on} \qquad \Gamma_i^d \tag{3.3}$$

$$\operatorname{tr} p \approx 0 \qquad \text{on} \qquad \partial_D \Omega_i^d \tag{3.4}$$

The precise interpretation of $\approx$ will depend on the chosen numerical method. We note that standard methods such as finite volume, finite element, mixed-finite element and spectral methods all fall within this framework, where the approximation implied by the $\approx$ signs of equations (3.1-3-4) can for most numerical methods be characterized by grid regularity, material parameters, grid resolution, etc. By assumption, we consider only stable numerical methods, in the sense of a negative eigenvalue-spectrum for the numerical solution operators $\mathcal{N}_i^d$, with potentially a single degenerate eigenvalue for subdomains where $\partial_D \Omega_i^d = \emptyset$, and we will denote the smallest (i.e. most negative) nondegenerate eigenvalue of $\mathcal{N}_i^d$ as $-n_i^d$. Furthermore, the system (3.1-3.4) is self-adjoint, so that in many cases the numerical method $\mathcal{N}_i^d$ will be symmetric (see Section 3.3 below for the case of finite elements).

3.1 MDFC: A unified discretization of fractured porous media

To provide a discretization for fractured systems, a grid $\mathcal{T}_i^d$ is introduced on the lower-dimensional manifolds Ω_i^d on which the boundary flux variables $\lambda_{i,j}^d$ will be defined. We emphasize that this mortar-like grid $\mathcal{T}_i^d$ can be chosen independently of any grid used by the numerical methods $\mathcal{N}_i^d$ and $\mathcal{N}_{S_i^d}^{d+1}$, thus we impose a minimum of restrictions on the grids. Nevertheless, note that this construction ensures that the flux variables on either side of a fracture (or either sides of fracture intersections) are conforming with each other. The precise relationships between the admissible grids $\mathcal{T}_{i,j}^d$ as implied by the numerical methods $\mathcal{N}_i^d$, will be made clear below. For the sake of symmetry, we also define grids $\mathcal{G}_i^d$ for the Neumann data on $\partial_N \Omega_i^d$.

To formulate discrete methods for fractured porous media, we represent the flux variable as piecewise constant on the mortar grid $\mathcal{T}_i^d$, thus $\lambda_{i,j}^d \in P_0(\mathcal{T}_i^d)$ and $g_i^d \in P_0(\mathcal{G}_i^d)$ (higher-order approximations are also possible, but the regularity of the problem does not seem to justify this). We introduce projection operators in order to move between the degrees of freedom of the numerical methods $\mathcal{N}_i^d$ and the mortar grids $\mathcal{T}_i^d$. We first define the compound operator projecting from the coupling variables on the mortar grids to the subdomain degrees of freedom

$$\Pi_{N_h(\Omega_i^d)} : \left[P_0(\mathcal{T}_i^d), P_0\left(\mathcal{T}_{S_i}^{d-1}\right), P_0(\mathcal{G}_i^d)\right] \to \left[N_h(\Omega_i^d), N_h(\Gamma_i^d)\right] \tag{3.5}$$

and conversely from the numerical variables to the coupling variables

$$\Pi_{P_0(\mathcal{T}_i^d)} : \left[N_h(\Omega_i^d), N_h(\Gamma_i^d)\right] \to \left[P_0(\mathcal{T}_i^d), P_0\left(\mathcal{T}_{S_i}^{d-1}\right), P_0(\mathcal{G}_i^d)\right] \tag{3.6}$$

Now, our MDFC discretization framework for fractured porous media takes the form: For given numerical discretizations $\mathcal{N}_i^d$: Find $\lambda_{i,j}^d \in P_0(\mathcal{T}_i^d)$, for all $i \in I$ and $j \in \hat{S}_i$ such that

$$\left(p_i^d, \mu_j\right)_{\partial_i \Omega_j^{d+1}} - \left(t_{i,j}^d, \mu_j\right)_{\partial_i \Omega_j^{d+1}} + \left(\kappa_{i,\perp}^{-d} \lambda_{i,j}^d, \mu_j\right)_{\partial_i \Omega_j^{d+1}} = 0 \qquad \text{for all} \quad \mu_j \in P_0(\mathcal{T}_i^d) \tag{3.7}$$

subject to the discrete constraints:

$$\left[p_i^d, t_{l,i}^{d-1}, z_i^d\right] = \Pi_{P_0(\mathcal{T}_i^d)} \mathcal{N}_i^d \left(\psi_i^d + a_i^d, b_i^d\right) \qquad \text{for } i \in I_a \tag{3.8}$$

$$\left[a_i^d, b_i^d\right] = \Pi_{N_h(\Omega_i^d)} \left[-\sum_{j \in \hat{S}_i^d} \lambda_{i,j}^d, \lambda_{\hat{S}_i,i}^{d-1}, g_i^d\right] \qquad \text{for all } i \in I_a \tag{3.9}$$

The dummy variables a_i^d and b_i^d have the interpretations of sinks and fluxes due to the interactions with other domains, respectively. In contrast, the variables p_i^d and t_i^d are the pressure and pressure traces after projection onto the grids $\mathcal{T}_i^d$. The variable z_i^d is the pressure trace projected onto the Neumann boundaries, and is not used with the boundary conditions considered herein (but would be relevant with Robin boundary conditions).

This MDFC scheme has a particularly simple interpretation: For each subdomain $i \in I_a$, $\mathcal{N}_i^d$ can be interpreted as a generalized Neumann-Dirichlet map, in the sense that it maps boundary fluxes (which also take the apparent form of sources for neighboring domains of $d-1$) to Dirichlet data (where conversely, for $d < n$, the internal values are considered Dirichlet data for neighboring domains of dimension $d+1$). As such, equation (3.8) resolves the internal differential equations in each subdomain, equations (3.9) is the projection of variables from the flux grids to the numerical boundary (and source) data, while equation (3.7) simply states that the flux $\lambda_{i,j}$ between a fracture and its surroundings should satisfy a form of Darcy's law, depending on the difference in pressure p of the fracture and the pressure t at the boundary of the surroundings. Equations (3.7-3.9) are thus a Schur-complement formulation of the discrete problem.

3.2 Abstract analysis

Let the discretization methods corresponding to the solution operators $\mathcal{N}_i^d$ be collected in a linear system, i.e. we state equation (3.8) on the form:

$$[\mathfrak{p}, \mathfrak{t}] = \mathcal{N}[\psi + \mathfrak{a}, \mathfrak{b}] \tag{3.10}$$

Similarly, we denote the compound projection operators $\Pi_{\mathcal{T}}$ and $\Pi_{\mathcal{N}}$. Furthermore, denote by D the discrete divergence operators from equation (3.9), which sums flux variables associated with a fracture while retaining Neumann boundary data i.e.

$$D\mathfrak{l}|_i = \begin{pmatrix} -\sum_{j \in \hat{S}_i^d} \lambda_{i,j}^d \\ \lambda_{i,k}^{d-1} \end{pmatrix} \tag{3.11}$$

Finally, let the diagonal mass matrix associated with the inner product $\left(\left(\kappa_{i,\perp}^d\right)^{-1} \lambda_i^d, \mu\right)$ appearing in equation (3.9) be denoted κ^{-1}. Then we can eliminate the subdomain variables from the discrete system (3.7-3.9) to obtain a Schur-complement system only in terms of the flux variables, i.e.

$$\left(\kappa^{-1} + D^{\mathrm{T}}\Pi_{\mathcal{T}}\mathcal{N}\Pi_{\mathcal{N}}D\right)\mathfrak{l} = D^{T}\Pi_{\mathcal{T}}\mathcal{N}[\psi, \Pi_{\mathcal{N}}g] \tag{3.12}$$

From the Schur complement form, we immediately obtain the following result:

Lemma 3.1

Let all subdomain discretization methods $\mathcal{N}_i^d$ be negative definite for $i \in I_a$ (i.e. $\partial_D\Omega_i^d \neq \emptyset$ for all $i \in I_a$), and furthermore let the assumptions of Lemma 2.1 hold. Then if the projection operators are negative transposes, such that $\Pi_{\mathcal{T}}^{\mathrm{T}} = -\Pi_{\mathcal{N}}$, the Schur-complement system (3.12) is stable, with no degenerate eigenvalues.

Proof: By the choice of $\lambda_{i,j} \in P_0\left(\mathcal{T}_i^d\right)$, the κ^{-1} matrix is diagonal, and has positive eigenvalues bounded below by $\kappa_{0,\perp}^{-1}$. Thus, it is sufficient to show that the remaining term has non-negative eigenvalues. But since $\mathcal{N}$ is negative definite by the assumption of the lemma, then $D^{\mathrm{T}}\Pi_{\mathcal{T}}\mathcal{N}\Pi_{\mathcal{N}}D = -(\Pi_{\mathcal{N}}D)^{\mathrm{T}}\mathcal{N}\Pi_{\mathcal{N}}D$ will be non-negative definite. The result follows since the right-hand side operator is bounded by the assumption of the Lemma. □

In order to allow for fractures (and intersections, etc.) which do not have a Dirichlet boundary, the arguments of Lemma 3.1 must be refined. To this end, let $\bar{I}_a$ be the subset of I_a which do not have a Dirichlet boundary. For these domains, we have a pure Neumann problem, and equations (3.8) are expected to constrain the solutions up to a constant (pressure). For the analysis, we therefore introduce an auxiliary constant pressure $\bar{p}_i^d$ for each domain $i \in \bar{I}_a$, and introduce the modified numerical methods $\widetilde{\mathcal{N}}_i^d : \left[N_h\left(\Omega_i^d\right), N_h\left(\Gamma_i^d\right)\right] \setminus \mathbb{R} \to \left[N_h\left(\Omega_i^d\right), N_h\left(\Gamma_i^d\right)\right] \setminus \mathbb{R}$, i.e., the solution corresponding to equations (3.1-3.4) with a compatibility condition (fluxes and sinks must sum to zero), and the additional constraint that the pressure has mean value zero. For $i \neq I_a \setminus \bar{I}_a$, the solution operator is unaltered, $\widetilde{\mathcal{N}}_i^d = \mathcal{N}_i^d$.

Equation (3.10) is then restated as

$$[\mathfrak{p}, \mathfrak{t}] = \widetilde{\mathcal{N}}[\psi + \mathfrak{a}, \mathfrak{b}] + \bar{\mathfrak{p}} \tag{3.13}$$

Inserting

$$\left(\kappa^{-1} + D^{\mathrm{T}}\Pi_{\mathcal{T}}\widetilde{\mathcal{N}}\Pi_{\mathcal{N}}D\right)\mathfrak{l} + \left(D^{\mathrm{T}}\Pi_{\mathcal{T}}\right)_{I,\bar{I}_a}\bar{\mathfrak{p}} = D^{T}\Pi_{\mathcal{T}}\mathcal{N}[\psi, \Pi_{\mathcal{N}}g] \tag{3.14}$$

With the compatibility constraint that

$$(\Pi_{\mathcal{N}}D)_{\bar{I}_a,I}\mathfrak{l} = 0 \tag{3.15}$$

Lemma 3.2

Let all subdomain discretization methods $\widetilde{\mathcal{N}}_i^d$ be negative definite for $i \in I_a$, and furthermore let the assumptions of Lemma 2.1 hold. Furthermore, let $I_a \setminus \bar{I}_a$ contain at least one domain. Then if the projection operators are negative transposes, such that $\Pi_{\mathcal{T}}^{\mathrm{T}} = -\Pi_{\mathcal{N}}$, the saddle-point system (3.14-3.15) is stable, with no degenerate eigenvalues.

Proof: By the assumptions of Lemma 3.1, $\left(D^{\mathrm{T}}\Pi_{\mathcal{T}}\right)_{I,\bar{I}_a} = -(\Pi_{\mathcal{N}}D)_{\bar{I}_a,I}$. Moreover, by similar argument to Lemma 3.1, it holds that $\left(\kappa^{-1} + D^{\mathrm{T}}\Pi_{\mathcal{T}}\widetilde{\mathcal{N}}\Pi_{\mathcal{N}}D\right)$ is coercive. It remains to show inf-sup for $\left(D^{\mathrm{T}}\Pi_{\mathcal{T}}\right)_{I,\bar{I}_a}$. I.e., we must show that

$$\inf_{\bar{\mathfrak{p}}\in\mathbb{R}^{|\bar{I}_a|}} \sup_{\mathfrak{z}} \frac{(\Pi_{\mathcal{N}} D)_{\bar{I}_a,I}\mathfrak{z}\cdot\bar{\mathfrak{p}}}{\|\mathfrak{z}\|\|\bar{\mathfrak{p}}\|} \geq C \tag{3.16}$$

This result is obtained by considering (all) i such that $i \in I_a \setminus \bar{I}_a$. Construct a rooted tree(s) $\mathfrak{T}$ from i spanning all subdomains (this can always be done for connected domains). Then for leaves (i.e. terminal nodes of the tree) j we set $\lambda_{j,k} = \bar{p}_j$, where k is the parent of j (we use the sign convention that $\lambda_{j,k} = -\lambda_{k,j}$ if k is in $\check{S}_j$, and it is sufficient to consider $\lambda_{j,k}$ constant). Proceeding in this manner recursively, let j be a node in the tree and let $\lambda_{j,l}$ be determined all branches extending from j. Then set $\lambda_{j,k} = \bar{p}_j - \sum_l \lambda_{j,l}$. Proceeding until the root of the tree, we see by construction that $(\Pi_{\mathcal{N}} D)_{\bar{I}_a,I}\mathfrak{z} = \bar{\mathfrak{p}}$, and that $\|\mathfrak{z}\| \leq c\|\bar{\mathfrak{p}}\|$, where c increases with the depth of the tree(s) $\mathfrak{T}$. For a finite geometry, C is therefore bounded by the geometry of the fracture network, and independent of the discretization methods. The solvability and bounded eigenvalues of (3.14-3.15) then follows from standard theory [17]. □

In practice, it is of course also of interest to also obtain values for the discrete solutions p_a^i, and not only the flux exchanges $\mathfrak{z}$. This result is a slightly more subtle, in a similar sense as Lemma 2.1. To prepare, we write equation (3.12) in the same form as used in the proof of Lemma 2.1.

$$\begin{pmatrix} \mathcal{A}_a & (\Pi_{\mathcal{N}} D)_{a,a} & (\Pi_{\mathcal{N}} D)_{a,b} & 0 \\ (D^T\Pi_{\mathcal{T}})_{a,a} & \kappa_a & 0 & 0 \\ (D^T\Pi_{\mathcal{T}})_{b,a} & 0 & \kappa_b & (D^T\Pi_{\mathcal{T}})_{b,b} \\ 0 & 0 & (\Pi_{\mathcal{N}} D)_{b,b} & 0 \end{pmatrix} \begin{pmatrix} \mathfrak{p}_a \\ \mathfrak{z}_{a,a} \\ \mathfrak{z}_{a,b} \\ \mathfrak{p}_b \end{pmatrix} = \begin{pmatrix} \phi_a \\ 0 \\ 0 \\ \phi_b \end{pmatrix} \tag{3.17}$$

Here, the linear operators $\mathcal{A}$ are the inverses of $\mathcal{N}$, and represent the linear discretizations underlying the numerical solution. Hence, equation (3.17) is also structurally similar to the natural implementation of the methodology. It is also important to note that the form (3.17) is agnostic to whether a domain is in $\bar{I}_a$, thus from the perspective of implementation, it will in many cases not be necessary to introduce special treatment of these domains as in Lemma 3.2. We now obtain a similar result as for the continuous case, in the sense that

Theorem 3.3

Equation (3.17) is well-posed, provided that the assumptions of Lemma 2.1 and 3.1 (or 3.2) hold, and that furthermore

c) The largest eigenvalues n_i^d of the numerical methods $\widetilde{\mathcal{N}}_i^d$ are bounded from above.
d) The discrete projection operators $\Pi_{\mathcal{N}}$ satisfy discrete inf-sup conditions for all pairs i and j appearing in condition b) of Lemma 2.1.

Proof: The proof is identical to Lemma 2.1 in the continuous case. □

We make the following remarks regarding Theorem 3.3 and its implications for MDFC:

1. All standard numerical methods for elliptic partial differential equations will satisfy condition c) in the theorem, thus essentially any numerical method can be applied to fractured porous media through the MDFC approach given in Section 3.1.

2. There are no restrictions on the grids $\mathcal{T}_i^d$ in relation to the numerical methods $\mathcal{N}_i^d$ as long as the fracture permeabilities $\kappa_{i,||}^d$ do not degenerate. In particular, for grid-based numerical methods $\mathcal{N}_i^d$, non-matching grids, both coarser and finer, can be used between the external domain and $\mathcal{T}_i^d$, and furthermore into the internal domain.
3. In practice, conditions c) and d) of the theorem state that for subdomains where $\kappa_{i,||}^d$ degenerates, the discrete representation of p_i^d must not be finer than $\lambda_{i,j}^d$. This is similar to the typical conditions encountered in traditional mortar methods [14].
4. In the special case where $\mathcal{N}_i^d$ is chosen as the mixed-finite element method, analysis shows that spatially degenerating $\kappa_{i,||}^d$ can be allowed, thus circumventing the binary structure of Lemma 2.1 and Theorem 3.3 [6].

3.3 Worked example: Finite element methods

In order to make the presentation more concrete, we consider the finite element method with continuous linear Lagrange elements in the framework presented above. Thus, for each Ω_i^d let $\mathcal{U}_i^d$ be the corresponding grid, with nodal degrees of freedom.

Then for $i \in I_a$, the elements of the sub-matrices A_i^d of $\mathcal{A}$ are simply given by the inner products of $p, w \in P_1(\mathcal{U}_i^d)$

$$\left(\kappa_{i,||}^d \nabla_d p_i^d, \nabla_d w\right)_{\Omega_i^d} \tag{3.17}$$

with Neumann data implemented as natural boundary conditions through the duality pairing

$$\sum_{j \in \check{S}_i} \langle \lambda_{j,i}^{d-1}, \operatorname{tr} w \rangle_{\partial_j \Omega_i^d} \tag{3.18}$$

The Neumann boundary conditions are exactly dual to the evaluation of traces, and thus the operator $\mathcal{N}_i^d$ will be self-adjoint. Standard finite element theory further guarantees that the required bound on the eigenvalues holds independent of grid spacing with [22]

$$n_i^d \leq C\left(\kappa_{i,||}^d\right)^{-1} \tag{3.19}$$

Since the solution p_i^d and its trace live in finite-dimensional subspaces of L^2, the projection operators become defined in the standard way, i.e. for $\lambda_{i,j} \in P_0(\mathcal{T}_i^d)$ the projection $\Pi_{\mathcal{N}_i^d} \lambda_{i,j} \in P_1(\mathcal{U}_i^d)$ satisfies

$$\left(\Pi_{\mathcal{N}_i^d} \lambda_{i,j}, v\right) = \left(\lambda_{i,j}, v\right) \qquad \text{for all} \quad v \in P_1(\mathcal{U}_i^d) \tag{3.20}$$

It is therefore clear that $\Pi_{\mathcal{T}}^{\mathrm{T}} = \Pi_{\mathcal{N}}$. Thus, all the conditions of Theorem 3.3 are satisfied, provided that the grids $\mathcal{U}_i^d$ are no finer than $\mathcal{T}_i^d$ whenever $\kappa_{i,||}^d \to 0$.

We note that the finite element approximation could also be obtained directly from Section 2 by simply using the finite-dimensional spaces and the bilinear forms defined in equations (2.26-2.27). Thus equations (3.7-3.9) with the numerical methods $\mathcal{N}_i^d$ defined by equations (3.14-3.15) and projection operators defined by equation (3.15) is equivalent to the symmetric and bilinear saddle-point problem: Find $\left(p_{i,h}^d, \lambda_{i,h}^d\right) \in P_1(\mathcal{U}_i^d) \times P_0(\mathcal{T}_i^d)$ such that

$$a\left(p_{i,h}^d, \lambda_{i,h}^d, w, \mu\right) + b'\left(p_{i,h}^d, \mu\right) + b'\left(q, \lambda_{i,h}^d\right) = \left(\psi_i^s, w\right) \quad \text{for all } (w, \mu) \in P_1\left(\mathcal{U}_i^d\right) \times P_0\left(\mathcal{T}_i^d\right) \tag{3.21}$$

This implies that the discretization is consistent, and together with the stability of the method, it follow that equation (3.21), and equivalently the MDFC scheme exposed in Section 3.1 with P1 finite elements as subdomain solvers, represents a convergent numerical discretization for equations (2.18-2.23).

While the approach as stated above is sufficient, in the sense of obtaining a stable and convergent discretization, we also remark that an improved method would likely be obtained by honoring the structure of $\mathcal{P}$ from section 2.3, and thus using $p_{i,h}^d \in P_0\left(\mathcal{T}_i^d\right)$ for $i \in I_b$. In particular, this would eliminate the projection errors associated with the low-permeable fractures. This highlights the flexibility of the framework to accommodate different discretizations in the different domains, bespoke to the physical processes.

4. Example calculations

To confirm the theory derived above, we propose two synthetic test cases in which the ambient space is two- and three-dimensional, respectively. Out of the range of numerical methods to which the MDFC applies, we consider five discretization schemes, summarized below.

Two mixed methods are employed, namely the mixed finite element (RT0), and the dual virtual element method (VEM). The mixed finite element, considered in [6], is given by Raviart-Thomas elements of lowest order for the fluxes and piecewise constants for the pressure in all dimensions. On the other hand, VEM [9] employs a single degree of freedom per face for the fluxes without explicitly specifying the basis functions and represents pressures as piecewise constants. Thirdly, employing nodal-based, linear Lagrange elements in all dimensions leads to the primal formulation (P1) as presented in Section 3.3. This is the only method considered in this work which does not respect local mass conservation. Finally, two finite volume methods are considered, the two-point flux approximation (TPFA) and the multi-point flux approximation scheme (MPFA) [23].

In line with the spirit of the theory presented in this work, the coupling between dimensions employs a flux mortar variable, defined as piecewise constants on a separately generated, lower-dimensional grid. All computations are performed using the open-source simulation tool PorePy [24].

4.1 Two-dimensional fracture system

The first example, obtained from [6], consists of a unit square with five one-dimensional fractures as given in figure 2. Immersed in the top half of the domain are two intersecting, conductive fractures with permeability $\kappa_\perp = 10^4$ and $\kappa_{||} = 1$. Below are two half-immersed blocking fractures ($\kappa_\perp = 1, \kappa_{||} = 10^{-4}$) and finally, a conductive fracture separates the lower right corner. The boundary conditions are chosen as a unit pressure drop from top to bottom and no-flow conditions on the sides. The matrix permeability is set to 1.

This example is designed to contain all the elements that constitute challenges for numerical methods for fractured porous media: The two intersecting fractures represent both 1D and 0D domains which have no contact with the boundary, thus the numerical methods $\mathcal{N}_i^d$ on these domains will contain a degenerate eigenvalue (i.e. the pressure solutions are only defined up to a constant). Moreover, the low-permeable and horizontal fractures are expected to lead to singularities in the solution in the 2D domain. Finally, in the lower corner there is a domain which intersects both a Dirichlet and a Neumann boundary.

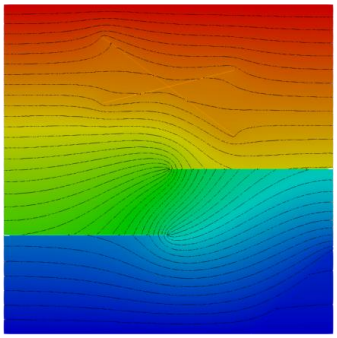

Figure 3: The contour lines and color scale of the reference solution on the domain given in Figure 2. The different qualitative aspects of the solution between the conductive and blocking fractures can be clearly seen.

In terms of mesh generation, the one-dimensional fracture grids match the trace of the adjacent two-dimensional grids. The mortar grid is then constructed at each fracture to have approximately 75% of the number of elements compared to the inner, lower-dimensional mesh.

Qualitatively, all numerical methods produce the same pressure distributions. Aside from artifacts due to the coarseness of the grid, all methods produce solutions which are visually indistinguishable from the figure 3. We turn to a more quantitative measure in order to expose differences between the discretizations. Since the only common property between the methods is the mortar variable, we compute its L^2-error with respect to a fine-scale solution obtained using the RT0 method. In case of convergence, the rate will be limited to first order with respect to the mesh size, since the mortar variable is represented by piecewise constants.

The results of this convergence test are shown in figure 4. For the one-dimensional mortar variables, very similar behavior is observed for the methods RT0, VEM, and MPFA, exhibiting stable and linear convergence. The two remaining methods show lower than first-order convergence on average. For P1, we speculate that this is due to its lack of local mass conservation, since the error is measured in a flux variable. For TPFA, this deviation is likely due to the lack of consistency in the method (i.e. the

approximation error to equations (3.1-3.4) does not necessarily go to zero with grid size). We emphasize that all methods are robust and stable from a linear algebra perspective on all grids.

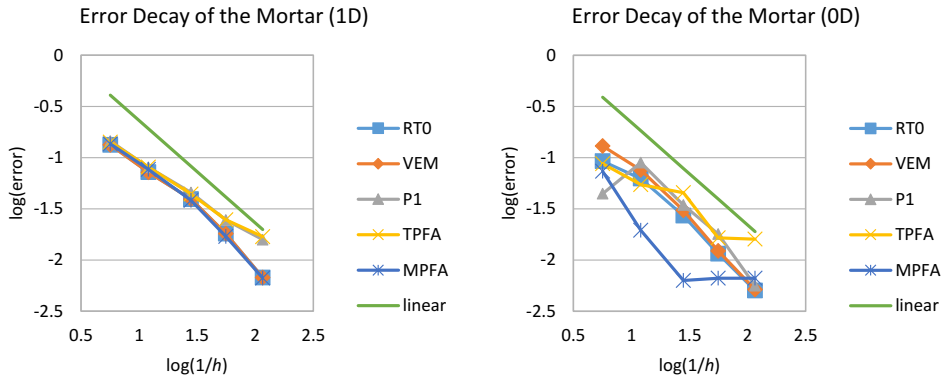

Figure 4: The errors in the mortar variable decrease with the mesh size for this range of h.

The error in the mortar variables defined at the zero-dimensional intersection is analyzed in figure (right). These results are slightly more sporadic since an accumulation of errors can occur from the higher dimensions, and since this essentially represents a point evaluation of the solution. Moreover, the grids used in the computations are not nested and mesh sensitivities of the method with may be the cause of these effects. Nevertheless, the overall trend in all methods is a decrease in error as the mesh becomes finer. It is noteworthy that the finite element methods exhibit a more monotone decay in comparison to the finite volume methods.

4.2 Stability

It is of interest to verify the claims of Theorem 3.3. In particular, we wish to address whether the discrete representation leads to a linear system which has a lower bound on condition numbers, which is independent of grid resolutions for non-degenerate parameters, and allows for degenerate parameters in the sense of conditions a)-d) in the proof.

In order to emphasize grids and parameters, we simplify the example from Section 4.1 by omitting the fractures which do not touch the boundary, and replacing the no-flow boundary conditions on the sides of the domain by a linear pressure variation. We can then consider Theorem 3.1 purely in terms of the mortar variables $\lambda_{i,j}$. Furthermore, in order to reduce the parameter space, we will let the remaining three fractures have the same parameters $\kappa_{\perp}$ and $\kappa_{||}$.

We fix the grid in the 2D domain with a resolution corresponding to the second-coarsest grid (approximately 4.5k triangles) in the convergence test of Section 4.1. Then in addition to the two fracture parameters, we introduce two grid parameters: The relative resolution of the outer grid to the mortar grid, and the relative resolution from the mortar grid to the fracture grid.

Our aim is to see how the lowest eigenvalue of the discrete Schur-complement system (3.12) depends on the fracture parameters and grid parameters. To this end, we have conducted a suite of simulations for all methods, exploring the full 4D parameter space. We observe that the results are completely independent of $\kappa_{||}$ and the ratio of the mortar grid to the inner grid. When varying the perpendicular permeability $\kappa_{\perp}$, the results depend primarily on whether the mortar grid is finer or coarser than the outer grid, and weakly depends on the ratio. These results are summarized in Figure 4.

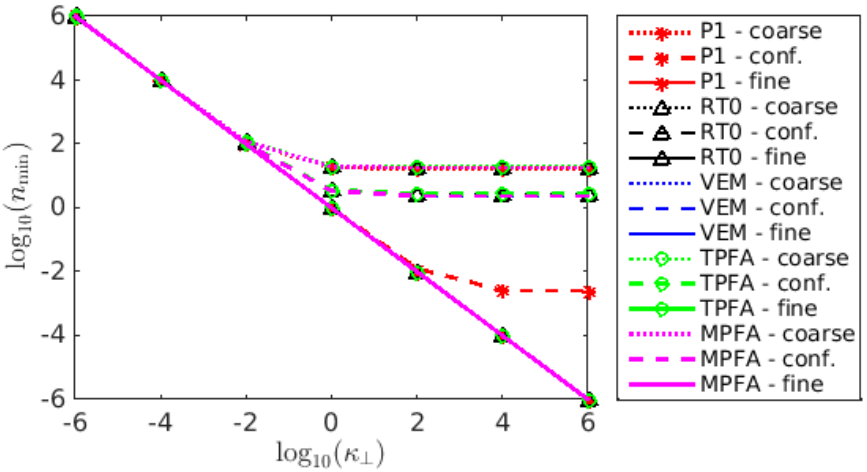

Figure 4: The minimum eigenvalue of equation (3.12) is plotted against $\kappa_{\perp}$ for all five ambient numerical methods, in the case of both a finer, conforming, and coarser mortar grid (with respect to the outer grid). In all cases, the results are independent of the coarsening/refinement ratio.

From Theorem 3.3, the expected results are that the minimum eigenvalue should scale linearly with $\kappa_{\perp}^{-1}$. Indeed, this is what is observed for all methods in the case of small values of $\kappa_{\perp}$. Moreover, all methods are also stable for coarse mortar grids for large values of $\kappa_{\perp}$. This result reflects the fact that for coarse mortar grids, the Neumann-Dirichlet maps stabilize the system, and that numerically there is an inf-sup condition on $\Pi_{\mathcal{N}} D$ such that $D^{\mathrm{T}} \Pi_{\mathcal{T}} \mathcal{N} \Pi_{\mathcal{N}} D$ has a lowest eigenvalue. We note however, that this does not hold for the continuous system given in equation (2.30), since the trace spaces for the pressure are not rich enough to control the mortar space. This, explains why stability is lost on fine mortar grids for all methods. Thus in all cases and for all grids, the MDFC method is stable, with eigenvalue bounded from below by the continuous problem.

In general, we thus conclude that for non-degenerate parameters, all discretizations lead to stable systems for the mortar variable, independent of grid resolution between matrix, flux-variable, and the fractures. For degenerate fracture flow $\kappa_{||}$, all methods remain stable. Finally, for degenerate fracture cross-flow $\kappa_{||}$, the results are in accordance with Theorem 3.3.

4.3 Three-dimensional Example

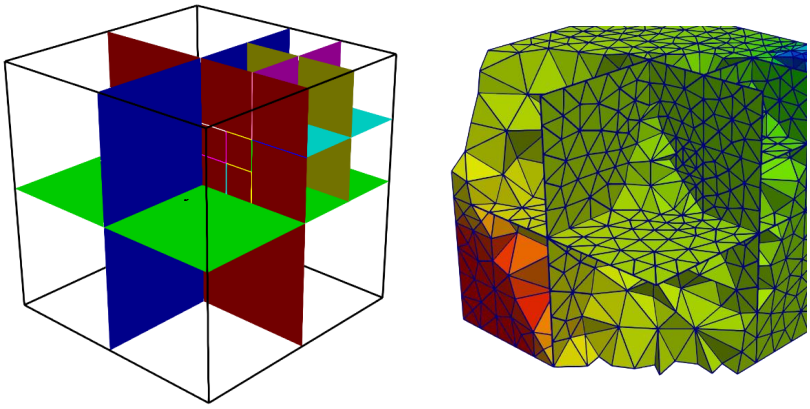

Figure 5: On the left a) the geometry of the example. On the right b) the pressure computed with RT0.

Finally, we consider simulations in a 3D problem. The computational domain is taken as the unit cube, and the fracture network for this example is reported in Figure 5a. The latter consist of 9 fractures with a structure similar to the Benchmark 1 in [Flemisch2017], extended to 3D. The matrix permeability is the identity tensor. We introduce the scaling factor $\zeta = 10^{-4(3-d)}$, for each lower dimensional object the normal permeability is given by $\kappa_{\perp} = 10^4/\zeta$ and the tangential by $\kappa_{||} = 10^4\zeta$. Flow is forced diagonally across the domain by specifying a pressure value of 1 at boundaries characterized by $(x, y, z) < 0.4$, and similarly a pressure of -1 at boundaries with $(x, y, z) > 0.8$. On all other boundaries, no-flow conditions are assigned. For illustration, the numerical solution computed using RT0 is reported in Figure 5b.

To compare the numerical schemes, we investigate numerical convergence of the mortar variables in the same way as in Section 4.1. Three simplex grids are considered, with cell counts of about 3.5k, 4.5k and 10k tetrahedrals, together with a suitable number of triangles, line elements and points. For simplicity, we consider only matching grids in this case. Errors in the mortar variables are computed relative to a reference solution obtained with RT0 on a grid with about 37k tetrahedral cells. The resulting error decay is depicted in Figure 6. The simulation confirms the findings in section 4.1: MPFA, RT0 and VEM all exhibit at least first order convergence for all dimensions, while TPFA again suffers from lack of consistency on the ambient grid, thus the low accuracy of the numerical method pollutes the flux variable.

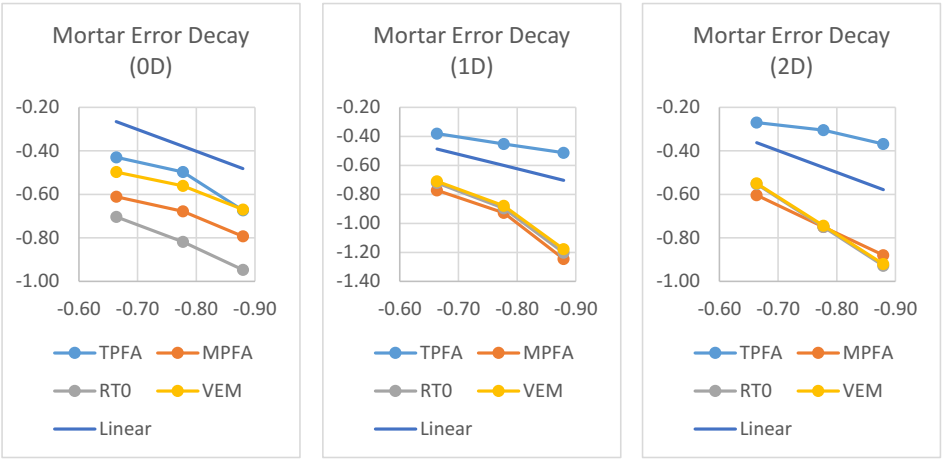

Figure 6: Error decay in the mortar variable for the 3d simulation reported in section 4.3.

5. Conclusions

We have developed a new, unified, approach to discretizing fractured porous media, termed Mixed-Dimensional Flux Coupling. The MDFC approach allows for arbitrary numerical discretizations to be used both for the porous media and the fractures. We have supported the development by both theoretical analysis, as well as numerical examples using five different numerical methods.

Several of the limitations included in this work appear to be possible to overcome. In particular, we expect that the extension to both non-linear discretizations [21] to be straight-forward in practice. Moreover, due to being agnostic of the numerical methods used, our theoretical results are not optimal nor exhaustive, and a more explicit treatment of the precise characteristics of the numerical methods chosen for the various components of the problem is known to provide more nuanced results [6].

In applications, coupled problems, are of particular interest. In particular, the fluid flow is often coupled to transport of either mass or energy. Preliminary work in this direction is ongoing, and we expect that the MDFC framework proposed herein will accommodate such coupled problems.

We conclude by noting the importance of open-source code availability. The methods developed herein have been implemented in PorePy, and both methods and the scripts used to generate the presented results are available in the public domain at time of publication.

Acknowledgements

This work has been funded in part by Norwegian Research Council grant 250223 and 244129/E20 (through the ENERGIX program).

References

[1] L. Formaggia, A. Fumagalli, A. Scotti and P. Ruffo, "A reduced model for Darcy's problem in networks of fractures," *ESAIM: Mathematical Modelling and Numerical Analysis,* vol. 48, no. 4, pp. 1089-1116, 2014.

[2] N. Schwenk, B. Flemisch, R. Helmig and B. I. Wohlmuth, "Dimensionally reduced flow models in fractured porous media," *Comutational Geosciences,* vol. 16, pp. 277-296, 2012.

[3] R. Helmig, C. Braun and M. Emmert, "MUFTE: A Numerical Model for Simulation of Multiphase Flow Processes in Porous and Fractured Porous Media," Universität Stuttgart, 1994.

[4] M. Karimi-Fard, L. J. Durlofsky and K. Aziz, "An efficient discrete-fracture model applicable for general-purpose reservoir simulations," *SPE Journal,* pp. 227-236, 2004.

[5] T. H. Sandve, I. Berre and J. M. Nordbotten, "An efficient multi-point flux approximation method for discrete fracture-matrix simulations," *Journal of Computational Physics,* vol. 231, pp. 3784-3800, 2012.

[6] W. M. Boon, J. M. Nordbotten and I. Yotov, "Robust discretization of flow in fractured porous media," *arXiv:1601.06977.*

[7] V. Martin, J. Jaffré and J. E. Roberts, "Modeling fractures and barriers as interfaces for flow in porous media," *SIAM Journal of Scientiffic Computing,* vol. 26, pp. 1557-1691, 2005.

[8] A. Scotti, L. Formaggia and F. Sottocasa, "Analysis of a mimetic finite difference approximation of flows in fractured porous media," *ESAIM: M2AN,* p. Forthcoming article, 2018.

[9] A. Fumagalli and E. Keilegavlen, "Dual Virtual Element Methods for Discrete Fracture Matrix Models," Arxiv: 1711.01818, 2018.

[10] B. Flemisch, I. Berre, W. M. Boon, A. Fumagalli, N. Schwenck, A. Scotti, I. Stefansson and A. Tatomir, "Benchmarks for single-phase flow in fractured porous media," *Advances in Water Resources,* vol. 111, pp. 239-258, 2018.

[11] N. Frih, V. Martin, J. E. Roberts and A. Saada, "Modeling Fractures as Interfaces with Nonmatching Grids," *Computational Geosciences,* vol. 16, pp. 1043-10060, 2012.

[12] W. M. Boon, J. M. Nordbotten and J. E. Vatne, "Exterior calculus for mixed-dimensional partial differential equations," in preparation.

[13] C. Bernardi, Y. Maday and A. T. Patera, "Domain Decomposition by the Mortar Element Method," in *Asymptotic and Numerical Methods for Partial Differential Equations with Critical Parameters*, Dordrecht, Springer, 1994, pp. 269-286.

[14] T. Arbogast, L. C. Cowsar, M. F. Wheeler and I. Yotov, "Mixed Finite Element Methods on Nonmatching Multiblock Grids," *SIAM Journal of Numerical Analysis,* vol. 37, no. 4, p. 1295–1315, 2000.

[15] J. M. Nordbotten and M. A. Celia, Geological Storage of CO2: Modeling Approaches for Large-Scale Simulation, Hoboken, N. J.: Wiley, 2012.

[16] J. M. Nordbotten and W. M. Boon, "Modeling, Structure and Discretization of Mixed-dimensional Partial Differential Equations," in *Domain Decomposition Methods in Science and Engineering XXIV, Lecture Notes in Computational Science and Engineering*, Svalbard, 2018.

[17] D. Boffi, F. Brezzi and M. Fortin, Mixed finite elements and applications, Heidelberg: Springer, 2013.

[18] M. A. Celia and W. G. Gray, Numerical methods for differential equations, Englewood Cliffs: Prentice Hall, 1992.

[19] R. Helmig, Multiphase flow and transport processes in the subsurface: a contribution to the modeling of hydrosystems, Berlin: Springer, 1997.

[20] Z. Chen, G. Huan and Y. Ma, Computational methods for multiphase flows in porous media, SIAM, 2006.

[21] M. Schneider, D. Gläser, B. Flemisch and R. Helmig, "Nonlinear finite-volume scheme for complex flow processes on corner-point grids," *International Conference on Finite Volumes for Complex Applications,* pp. 417-425, 2017.

[22] D. Braess, Finite Elements: Theory, Fast Solvers and Applications in Solid Mechanics, Cambridge: Cambridge University Press, 2007.

[23] I. Aavatsmark, T. Barkve, Ø. Bøe and T. Mannseth, "Discretization on non-orthogonal, quadrilateral grids for inhomogeneous, anisotropic media," *Journal of Computational Physics,* vol. 127, pp. 2-14, 1996.

[24] E. Keilegavlen, A. Fumagalli, R. Berge, I. Stefansson and I. Berre, "PorePy: An Open-Source Simulation Tool for Flow and Transport in Deformable Fractured Rocks," arXiv:1712.00460.

Paper F

Efficient Water Table Evolution Discretization using Domain Transformation

W.M. Boon, N. Balbarini, P.J. Binning, J.M. Nordbotten

Computational Geosciences 21(1) (2017), p. 3–11.

doi: 10.1007/s10596-016-9597-9

Comput Geosci (2017) 21:3–11
DOI 10.1007/s10596-016-9597-9

BRIEF COMMUNICATION

Efficient water table evolution discretization using domain transformation

W. M. Boon[1] · N. Balbarini[2] · P. J. Binning[2] · J. M. Nordbotten[1,3]

Received: 16 February 2016 / Accepted: 20 September 2016 / Published online: 2 November 2016

Abstract Domain transformation methods are useful techniques for solving problems on non-stationary domains. In this work, we consider the evolution of the water table in an unconfined aquifer. This nonlinear, time-dependent problem is greatly simplified by using a mapping from the physical domain to a reference domain and is then further reduced to a single, (nonlinear) partial differential equation. We show well-posedness of the approach and propose a stable and convergent discretization scheme. Numerical results are presented supporting the theory.

Keywords Domain transformation · Water table evolution · Finite element method

This work was supported in part by Norwegian Research Council grants 233736 and 228832 and the research project GEOCON, Advancing GEOlogical, geophysical and CONtaminant monitoring technologies for contaminated site investigation (contract 1305-00004B). The funding for GEOCON is provided by Innovation Fund Denmark.

✉ W. M. Boon
wietse.boon@uib.no

[1] Department of Mathematics, University of Bergen, Postboks 7803, Bergen 5020, Norway

[2] Department of Environmental Engineering, Technical University of Denmark, Lyngby, Denmark

[3] Department of Civil and Environmental Engineering, Princeton University, E-208 E-Quad, Princeton, NJ, 08544, USA

1 Introduction

The temporal change of the water table in an unconfined aquifer is challenging to model efficiently while maintaining a desired accuracy. Affected by natural processes including precipitation and subsurface flows combined with artificial factors such as wells and dams, this non-stationary problem emerges in a variety of engineering applications.

From a modeling perspective, the water table evolution problem is challenging because the computational domain will typically depend on the solution to the problem. Specifically, the hydraulic head is the unknown variable, yet it defines the elevation of the water table and thereby the upper boundary of the saturated region. As a result, the domain of computation and the variables of interest cannot be considered independently. Several methods have been developed to solve this problem, which we review concisely in the following summary.

A first approach to describe the non-stationary domain is to use a moving mesh. This way, the computational domain is able to follow the dynamic geometry of the saturated region [6]. However, this approach can be computationally demanding for three-dimensional problems and furthermore, large deformations of the domain may cause instabilities [3]. The primary reason for this is that significant stretching of the mesh may lead to undesirable aspect ratios in the elements and cause oscillations in the solution. For the problem considered here, it is imperative that the solution method is able to handle such large deformations and gradients, for example, those occurring in the vicinity of wells.

Alternatively, it is possible to expand the domain of computation towards the surface and treat this problem as saturated-unsaturated flow governed by Richards' equation.

The solution is then obtained using, for example, finite difference [7, 8] or finite element methods [9]. A drawback with this approach is the nonlinearity of Richards' equation which results in a substantial computational cost to obtain a solution.

A third approach is to assume vertical equilibrium and integrate all equations in the z-direction. The problem is then simplified by reduction of dimensionality which allows for the derivation of analytical solutions [2]. However, this approach is only valid if vertical flows (and head gradients) are negligible. Thus, for the sake of generality, we will not make such an assumption in this work.

Finally, the use of coordinate transformations eliminates the challenges of modeling deformable domains by mapping the problem to a stationary reference domain. This has been applied successfully for saturated-unsaturated flow [1, 10]. In those works, the highly nonlinear Richards' equation is considered leading to a computationally demanding method.

Herein, we propose a discretization method by applying a mapping from the saturated region to a reference domain, therewith considering only saturated flow. We then further reduce the original system of equations to a single, nonlinear equation with a single variable, namely the hydraulic head. These two manipulations simplify the problem to such an extent that the stability and convergence of the proposed discretization follow naturally.

The structure of this paper is as follows. Section 2 introduces the governing equations and presents an explicit choice for the mapping to a reference domain. Next, the problem is reduced to a single equation in Section 3 as part of the derivation of the variational form. Sections 4 and 5 are devoted to the discretizations in time and space, respectively, and introduce the Picard scheme used to handle the included nonlinearity. Numerical results confirming the expected stability and convergence of the scheme are presented in Section 6.

2 Model description

In this section, we introduce the water table evolution problem from a modeling perspective. Here, we state the necessary definitions and elaborate on the governing equations included in the model. First, let $\Omega(t)$ denote the d-dimensional spatial domain representing the saturated region with d equal to 2 or 3. In particular, the time-dependent top boundary, $\Gamma(t)$ is of interest since it represents the water table.

The governing equations for the problem are the mass balance equation, Darcy's law and the water table boundary condition. For the mass conservation equation, we assume incompressibility of both the fluid and the surrounding matrix. This allows us to reformulate mass conservation as volume conservation given by the equation

$$S_s \frac{\partial h}{\partial t} + \nabla \cdot \mathbf{u} = 0, \tag{1}$$

in which S_s represents the specific storativity $[\frac{1}{L}]$, h is the hydraulic head $[L]$, and $\mathbf{u}$ represents the volumetric flux $[\frac{L}{T}]$. Secondly, we assume that the flux is governed by Darcy's law, i.e., it satisfies

$$\mathbf{u} = -\mathbf{K}\nabla h. \tag{2}$$

Here, $\mathbf{K}$ represents the conductivity tensor $[\frac{L}{T}]$ which is assumed to be symmetric and positive definite. Finally, a key component of this problem is that the top boundary represents the water table and thus, it is time dependent. To incorporate this in the model, we parametrize the boundary $\Gamma(t)$ by $x_3 = \zeta(\mathbf{x}_{||}, t)$. Here, and later, we use the parallel stroke to indicate the horizontal spatial components of a vector, e.g., $\mathbf{x}_{||} = (x_1, x_2)$ in the 3D case and $\mathbf{x}_{||} = x_1$ in the 2D case. In the following, we will continue with dimensionality $d = 3$. The description in two dimensions is analogous.

The newly introduced variable ζ which represents the elevation of the water table is then subject to the evolution equation [13]

$$\phi \frac{\partial \zeta}{\partial t} = I(t) + u_3 - \mathbf{u}_{||} \cdot \nabla_{||} \zeta, \tag{3}$$

in which ϕ represents the porosity, $I(t)$ is a function representing the infiltration, and u_3 is the third component of the flux. $I(t)$ is positive for a downward flux. To close the model, we impose boundary conditions on the boundary $\partial\Omega$. For unconfined aquifers, the elevation of the water table is equal to the hydraulic head at the water table [13]. Thus, our first boundary condition becomes

$$h = \zeta \quad \text{on } \Gamma(t). \tag{4}$$

The remaining boundaries are split up into two parts, namely Γ_D and Γ_N. On Γ_D, we assume that the hydraulic head is given by a known function f. On the other hand, we assume no flow is possible on Γ_N. These two conditions are:

$$h = f, \qquad \text{on } \Gamma_D(t), \tag{5a}$$

$$\mathbf{n} \cdot \mathbf{u} = 0, \qquad \text{on } \Gamma_N(t). \tag{5b}$$

Here, $\mathbf{n}$ is the outward pointing, unit normal vector on the boundary $\partial\Omega$.

2.1 Transformation to reference space

The problem introduced up to this point may be difficult to solve since the spatial domain is not fixed in time. Therefore, we transform the problem to a stationary domain $\hat{\Omega} = \Omega_{||} \times [0, 1]$, i.e., a domain with unit height. In the subsequent derivation of the transformed governing equations,

the hat notation will consistently refer to variables in the transformed domain.

Let $\Psi(t) : \hat{\Omega} \rightarrow \Omega$ denote any invertible transformation and let $\Phi(t)$ denote its inverse. For simplicity, we will require that $\Psi(t)$ leaves horizontal components unchanged. In particular, this means that $\Psi\left([\hat{\mathbf{x}}_{||}, 1], t\right) = [\mathbf{x}_{||}, \zeta(\mathbf{x}_{||}, t)]$. The specific choice of $\Psi(t)$ is discussed in Section 2.2, and an illustration of these definitions is shown in Fig. 1. We continue with the transformation on the variables included in the model to the reference domain. The hydraulic head in reference space $\hat{h}$ will be defined such that $h(\mathbf{x}, t) = \hat{h}(\Phi(\mathbf{x}, t), t)$. For the flux vector $\hat{\mathbf{u}}$, we will use the Piola transform in order to preserve the divergence structure of the original problem [4]. In particular, we define $\hat{\mathbf{u}}$ such that

$$\mathbf{u} = \frac{\hat{\nabla}\Psi}{J}\hat{\mathbf{u}}, \tag{6}$$

with $J = \det\left(\hat{\nabla}\Psi\right)$. The transformed version of Eq. 1 then becomes

$$S_s \frac{\partial \hat{h}}{\partial t} + \hat{\nabla} \cdot \hat{\mathbf{u}} = 0. \tag{7}$$

Secondly, we reformulate Darcy's law given by Eq. 2 for the reference domain. Substitution of $h(\mathbf{x}, t) = \hat{h}(\Phi(\mathbf{x}, t), t)$ leads us to

$$\mathbf{u}(\mathbf{x}, t) = -\mathbf{K}\nabla\hat{h}(\Phi(\mathbf{x}, t), t). \tag{8}$$

Next, we use Eq. 6 and the chain rule to obtain the following formulation in transform space

$$\frac{\hat{\nabla}\Psi}{J}\hat{\mathbf{u}} = -\mathbf{K}(\nabla\Phi)^T\hat{\nabla}\hat{h}. \tag{9}$$

It follows that we may write Darcy's law in transform space as

$$\hat{\mathbf{u}} = -\hat{\mathbf{K}}\hat{\nabla}\hat{h}, \tag{10}$$

in which the transformed conductivity $\hat{\mathbf{K}}$ is given by

$$\hat{\mathbf{K}} = J(\hat{\nabla}\Psi)^{-1}\mathbf{K}(\hat{\nabla}\Psi)^{-T}. \tag{11}$$

Here, we have made the final substitution $\nabla\Phi = (\hat{\nabla}\Psi)^{-1}$.

Following the same procedure, we aim to find the equation for the water table evolution in reference space, i.e., the equivalent to Eq. 3. First, we note that since Ψ leaves horizontal components unchanged, we can express Ψ in terms of only the third component Ψ_3

$$\Psi(\hat{\mathbf{x}}) = [\hat{\mathbf{x}}_{||}, \Psi_3(\hat{x}_3, \zeta)]. \tag{12}$$

This allows us to derive the Jacobian matrix

$$\hat{\nabla}\Psi = \begin{bmatrix} I_2 & 0 \\ \nabla_{||}^T\zeta & \frac{\partial}{\partial\hat{x}_3}\Psi_3 \end{bmatrix} \text{ at } \hat{x}_3 = 1. \tag{13}$$

We now continue by rewriting Eq. 3 in the reference space. First, we note that

$$u_3 = \mathbf{e}_3 \cdot \frac{\hat{\nabla}\Psi}{J}\hat{\mathbf{u}} = \frac{[\nabla_{||}^T\zeta, \frac{\partial}{\partial\hat{x}_3}\Psi_3]}{J}\hat{\mathbf{u}}. \tag{14}$$

Secondly, the last term of Eq. 3 is rewritten using Eqs. 6 and 13 as

$$\mathbf{u}_{||} \cdot \nabla_{||}\zeta = \left(\mathbf{e}_{||}^T\frac{\hat{\nabla}\Psi}{J}\hat{\mathbf{u}}\right) \cdot \nabla_{||}\zeta = \left(\frac{[I_2, 0]}{J}\hat{\mathbf{u}}\right) \cdot \nabla_{||}\zeta. \tag{15}$$

With $J = \frac{\partial}{\partial\hat{x}_3}\Psi_3$, the water table evolution (3) is reformulated as

$$\phi\frac{\partial\zeta}{\partial t} = I(t) + \hat{u}_3. \tag{16}$$

The three equations (7), (10), and (16) form our system in reference space, which we repeat here for convenience:

$$S_s\frac{\partial\hat{h}}{\partial t} + \hat{\nabla}\cdot\hat{\mathbf{u}} = 0, \tag{17a}$$

$$\hat{\mathbf{u}} = -\hat{\mathbf{K}}\hat{\nabla}\hat{h}, \qquad \text{in } \hat{\Omega}, \tag{17b}$$

$$\phi\frac{\partial\zeta}{\partial t} = I(t) + \hat{u}_3, \qquad \text{on } \hat{\Gamma}. \tag{17c}$$

The associated boundary conditions are obtained from (4) and (2):

$$\hat{h} = \zeta, \qquad \text{on } \hat{\Gamma}, \tag{18a}$$

$$\hat{h} = f, \qquad \text{on } \hat{\Gamma}_D, \tag{18b}$$

$$\mathbf{n}\cdot\hat{\mathbf{u}} = 0, \qquad \text{on } \hat{\Gamma}_N. \tag{18c}$$

2.2 A choice of transformation

The transformation $\Psi(t)$ can in principle be chosen as any monotone function. However, although certain complex choices may hold desirable properties, we aim for a computationally efficient discretization scheme. Therefore, we choose $\Psi(t)$ to be a linear transformation in the vertical coordinate, such that:

$$\mathbf{x} = \Psi(\hat{\mathbf{x}}, t) = \left[\hat{\mathbf{x}}_{||},\ \hat{x}_3\zeta(\hat{\mathbf{x}}_{||}, t)\right]. \tag{19}$$

The inverse transformation Φ is then given by

$$\hat{\mathbf{x}} = \Phi(\mathbf{x}, t) = \left[\mathbf{x}_{||},\ \frac{x_3}{\zeta(\mathbf{x}_{||}, t)}\right]. \tag{20}$$

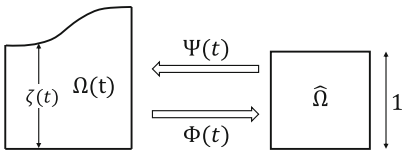

Fig. 1 The transformations between the time-dependent, physical domain $\Omega(t)$ and the stationary, reference domain $\hat{\Omega}$

Furthermore, the Jacobian matrices can be stated explicitly as follows.

$$\hat{\nabla}\Psi = \begin{bmatrix} I_2 & 0 \\ \hat{x}_3\nabla_{||}^T\zeta & \zeta \end{bmatrix} \text{ and } \nabla\Phi = \begin{bmatrix} I_2 & 0 \\ -x_3\zeta^{-2}\nabla_{||}^T\zeta & \zeta^{-1} \end{bmatrix}. \tag{21}$$

A more complex choice, adapted for layered systems, will be considered in the numerical examples.

3 Time-continuous formulation

In this section, we establish some basic properties for the time-continuous problem. We start by stating the variational form and rewrite the system (17a–17c) to a single equation with a single unknown variable. In turn, this gives us a noteworthy advantage in the consequent analysis of the well-posedness of the problem.

3.1 Variational formulation

The first step is to note that according to Eq. 18a, the variable ζ is the trace of $\hat{h}$ on $\hat{\Gamma}$. Thus, the definition of ζ as an independent variable is obsolete and it becomes convenient to discard the notation of ζ and use the variable $\hat{h}$, instead. However, it is important to note that the transformation Ψ and therewith the conductivity tensor $\hat{\mathbf{K}}$ only depend on the trace of $\hat{h}$ on $\hat{\Gamma}$ and not the whole function $\hat{h}$. To emphasize this, we will occasionally revert to the notation

$$\hat{\mathbf{K}}(\zeta) = \hat{\mathbf{K}}(\hat{h}|_{\hat{\Gamma}}). \tag{22}$$

In the following steps, we will continue to simplify the system (17a–17c). With the aim of solving this problem with the use of the finite element method, we derive the variational formulation. For this, we employ the conventional inner product notation

$$(h, g)_{\hat{\Omega}} = \int_{\hat{\Omega}} h(\hat{x})g(\hat{x})\mathrm{d}\hat{x}, \tag{23}$$

and omit hats on variables and gradients for brevity. Let us multiply Eq. 7 with a test function $g \in H^1$ and integrate over the domain $\hat{\Omega}$. We pay special attention to the second term in Eq. 7, in which we first substitute Darcy's law (10). With the application of partial integration and the associated boundary conditions, this term becomes

$$\begin{aligned} &-(\nabla\cdot(\hat{\mathbf{K}}(h)\nabla h), g)_{\hat{\Omega}} \\ &= (\hat{\mathbf{K}}(h)\nabla h, \nabla g)_{\hat{\Omega}} - (\mathbf{n}\cdot(\hat{\mathbf{K}}(h)\nabla h), g)_{\hat{\Gamma}} \\ &= (\hat{\mathbf{K}}(h)\nabla h, \nabla g)_{\hat{\Omega}} + (u_3, g)_{\hat{\Gamma}} \\ &= (\hat{\mathbf{K}}(h)\nabla h, \nabla g)_{\hat{\Omega}} + \phi\left(\frac{\partial h}{\partial t}, g\right)_{\hat{\Gamma}} - (I(t), g)_{\hat{\Gamma}}. \end{aligned} \tag{24}$$

Here, we have used Eq. 16 in order to eliminate u_3. We are now ready to write the weak form of Eq. 7 as

$$S_s\left(\frac{\partial h}{\partial t}, g\right)_{\hat{\Omega}} + (\hat{\mathbf{K}}(h)\nabla h, \nabla g)_{\hat{\Omega}} + \phi\left(\frac{\partial h}{\partial t}, g\right)_{\hat{\Gamma}} = (I(t), g)_{\hat{\Gamma}}. \tag{25}$$

Thus, we have reduced the system of equations derived in the previous section to a single equation. The advantage of this becomes evident in the next sections.

3.2 Well-posedness

Next, we analyze the well-posedness of the derived problem with the use of the following lemma.

Lemma 1 *Let the initial and boundary conditions satisfy $h_0 \geq \delta > 0$ and $f \geq 0$. Then the solution to* Eq. 25 *exists and is unique.*

Proof The proof is done by showing that the conductivity tensor $\hat{\mathbf{K}}(\zeta)$ in Eq. 25 is symmetric and positive definite under these assumptions. Then, the problem is identified as a diffusion-type problem which is known to be well-posed.

Let us start with the assumption that the physical conductivity tensor $\mathbf{K}$ is symmetric and positive definite. Equation 11 states that $\hat{\mathbf{K}}(\zeta)$ is equal to $\mathbf{K}$ which is left- and right- multiplied by transpose matrices. Thus, if ζ is bounded away from zero, it follows that $\hat{\mathbf{K}}(\zeta)$ is symmetric and positive definite as well.

In order to ensure that ζ is non-zero, it is essential that the solution to Eq. 25 is also non-zero for all time. This property can be shown by using the maximum (or rather, minimum) principle related to problem (25).

From this principle, we deduce that the solution h attains its minimum on the boundary. On this boundary, we distinguish three different cases. First, if the minimum is attained on $\hat{\Gamma}_D$, then it follows $h = f$. Since $f > 0$ by assumption, it follows that h is strictly positive as well.

Secondly, the minimum could be attained in a point $\hat{x}_0$ on $\hat{\Gamma}$. We then introduce Hopf's Lemma which states that $\frac{\partial h}{\partial \mathbf{n}}(\hat{x}_0) < 0$, yet this contradicts the homogeneous Neumann boundary condition (2) prescribed there.

Finally, if the minimum is attained on $\hat{x}_0 \in \hat{\Gamma}$, we recall that the boundary condition there is given by

$$I(t) - \mathbf{n}\cdot\hat{\mathbf{K}}(\zeta)\nabla h = \phi\frac{\partial h}{\partial t}. \tag{26}$$

Again, using Hopf's lemma, it follows that $\frac{\partial h}{\partial \mathbf{n}}(\hat{x}_0) < 0$. The prescribed boundary condition then implies that $\frac{\partial h}{\partial t} > 0$ since the infiltration is a positive function. A positive temporal derivative in combination with the assumed $h_0 \geq \delta > 0$ means that the function h remains strictly positive in time.

Thus, we conclude that the solution h is bounded away from zero. This implies positive definiteness of the conductivity tensor $\hat{\mathbf{K}}(h)$ and therewith the well-posedness of the problem. □

4 Time-discrete formulation

In this section, we continue by discretizing problem (25) in time. We show that using a Backward Euler approach is sufficient to obtain a stable discretization.

Let us introduce Δt as the time step and h_n as the solution at time t_n. Using a Backward Euler discretization scheme, we solve the following problem for h_{n+1}

$$\begin{aligned} & S_s \Delta t^{-1}(h_{n+1},\ g)_{\hat{\Omega}} + \left(\hat{\mathbf{K}}(h_{n+1})\nabla h_{n+1}, \nabla g\right)_{\hat{\Omega}} \\ & +\phi \Delta t^{-1}(h_{n+1}, g)_{\hat{\Gamma}} \\ = \ & S_s \Delta t^{-1}(h_n,\ g)_{\hat{\Omega}} + \phi \Delta t^{-1}(h_n, g)_{\hat{\Gamma}} + (I(t), g)_{\hat{\Gamma}}. \end{aligned} \tag{27}$$

Note that the nonlinearity in the diffusive term requires special attention. In order to solve the problem, we propose using a Picard iterative scheme. In this context, let the superscript k denote the iteration number. The next iterate can then be found by solving the following problem:

$$\begin{aligned} & S_s \Delta t^{-1}(h_{n+1}^{k+1}, g)_{\hat{\Omega}} + \left(\hat{\mathbf{K}}(h_{n+1}^{k})\nabla h_{n+1}^{k+1}, \nabla g\right)_{\hat{\Omega}} \\ & +\phi \Delta t^{-1}(h_{n+1}^{k+1}, g)_{\hat{\Gamma}} \\ = \ & S_s \Delta t^{-1}(h_n, g)_{\hat{\Omega}} + \phi \Delta t^{-1}(h_n, g)_{\hat{\Gamma}} + (I(t), g)_{\hat{\Gamma}}. \end{aligned} \tag{28}$$

Each iterate remains subject to the Dirichlet boundary condition

$$h_{n+1}^{k+1} = f, \text{ on } \hat{\Gamma}_D. \tag{29}$$

A natural choice as an initial guess is $h_{n+1}^{0} = h_n$, i.e., the solution at the previous time step.

We are interested in convergence of this scheme to a certain limit solution as this limit solution will solve the nonlinear problem. Therefore, a formal proof concerning the existence and uniqueness of such a limit solution is given by the following lemma.

Lemma 2 *Let the same assumptions from Lemma 1 hold and let the time step Δt be sufficiently small. Then the time-discrete problem (27) has a unique solution.*

Proof For this proof, the essential tool is the set $H_\delta^1(\hat{\Gamma})$ which contains (weakly) differentiable functions bounded away from zero. More precisely, for a given $\delta > 0$, this set is defined as follows

$$H_\delta^1(\hat{\Gamma}) = \{h \in H^1(\hat{\Gamma}) |\ h \geq \delta, \text{ a.e.}\}. \tag{30}$$

If $w \in H^1(\hat{\Omega})$ solves (28) for a given $\zeta \in H_\delta^1(\hat{\Gamma})$, then we can construct the operator $A : H_\delta^1(\hat{\Gamma}) \to H_\delta^1(\hat{\Gamma})$ given by

$$A[\zeta] = w|_{\hat{\Gamma}}. \tag{31}$$

With these definitions, the lemma states that if $f \in H_\delta^0(\hat{\Gamma}_D)$ and $h_n \in H_\delta^1(\hat{\Omega})$ for some $\delta > 0$, then the system (27) has a unique solution. The proof is done through an application of Banach's Fixed Point theorem on the introduced, nonlinear mapping A related to system (28).

Let us consider two functions $\zeta_1, \zeta_2 \in H_\delta^1(\hat{\Gamma})$ and denote the corresponding solutions to Eq. 28 by w_1 and w_2, respectively. Subtraction of these two equations leads us to

$$\begin{aligned} & (\hat{\mathbf{K}}(\zeta_1)\nabla w_1 \ - \ \hat{\mathbf{K}}(\zeta_2)\nabla w_2, \nabla g)_{\hat{\Omega}} \\ & \qquad +\Delta t^{-1}(w_1 - w_2, g)_{\hat{\Gamma}} = 0. \end{aligned} \tag{32}$$

We then set $g = w_1 - w_2$ to obtain

$$\begin{aligned} & S_s \Delta t^{-1} \|w_1 - w_2\|_{0,\hat{\Omega}}^2 + \phi \Delta t^{-1} \|w_1 - w_2\|_{0,\hat{\Gamma}}^2 \\ = & -\left(\hat{\mathbf{K}}(\zeta_1)\nabla w_1 - \hat{\mathbf{K}}(\zeta_2)\nabla w_2, \nabla(w_1 - w_2)\right)_{\hat{\Omega}} \\ = & -\frac{1}{2}\left((\hat{\mathbf{K}}(\zeta_1) - \hat{\mathbf{K}}(\zeta_2))\nabla(w_1 + w_2), \nabla(w_1 - w_2)\right)_{\hat{\Omega}} \\ & -\frac{1}{2}\left((\hat{\mathbf{K}}(\zeta_1) + \hat{\mathbf{K}}(\zeta_2))\nabla(w_1 - w_2), \nabla(w_1 - w_2)\right)_{\hat{\Omega}}. \end{aligned} \tag{33}$$

Next, we observe that $(\hat{\mathbf{K}}(\zeta_1) + \hat{\mathbf{K}}(\zeta_2))$ is positive definite. By rearranging the terms and applying the Cauchy-Schwarz-Young inequality, we derive

$$\begin{aligned} & S_s \Delta t^{-1} \|w_1 - w_2\|_{0,\hat{\Omega}}^2 + \phi \Delta t^{-1} \|w_1 - w_2\|_{0,\hat{\Gamma}}^2 \\ & +C_1 \|\nabla(w_1 - w_2)\|_{0,\hat{\Omega}}^2 \\ \leq & -\frac{1}{2}\left((\hat{\mathbf{K}}(\zeta_1) - \hat{\mathbf{K}}(\zeta_2))\nabla(w_1 + w_2), \nabla(w_1 - w_2)\right)_{\hat{\Omega}} \\ \leq & \frac{1}{2}\|\hat{\mathbf{K}}(\zeta_1) - \hat{\mathbf{K}}(\zeta_2)\|_{0,\hat{\Omega}} \|\nabla(w_1 - w_2)\|_{0,\hat{\Omega}} \|\nabla(w_1 + w_2)\|_{0,\hat{\Omega}} \\ \leq & \ \frac{1}{2}\Big(\frac{1}{2\epsilon}\|\hat{\mathbf{K}}(\zeta_1) - \hat{\mathbf{K}}(\zeta_2)\|_{0,\hat{\Omega}}^2 \\ & +\frac{\epsilon}{2}\|\nabla(w_1 - w_2)\|_{0,\hat{\Omega}}^2 \|\nabla(w_1 + w_2)\|_{0,\hat{\Omega}}^2\Big). \end{aligned} \tag{34}$$

The next step is to choose the constant ϵ. In order to do this, we form a bound for $\|\nabla(w_1 + w_2)\|_{0,\hat{\Omega}}^2$. Let us reconsider Eq. 28 and set $g = w_1 - h_n$. This choice gives us

$$\begin{aligned} & S_s \Delta t^{-1} \|w_1 - h_n\|_{0,\hat{\Omega}}^2 + \|\hat{\mathbf{K}}(\zeta_1)^{1/2}\nabla w_1\|_{0,\hat{\Omega}}^2 \\ & +\phi \Delta t^{-1} \|w_1 - h_n\|_{0,\hat{\Gamma}}^2 \\ = & \ (I(t), w_1 - h_n)_{\hat{\Gamma}} + \left(\hat{\mathbf{K}}(\zeta_1)\nabla w_1, \nabla h_n\right)_{\hat{\Omega}} \\ \leq & \ \frac{1}{2}\phi^{-1}\Delta t \|I(t)\|_{0,\hat{\Gamma}}^2 + \frac{1}{2}\phi \Delta t^{-1} \|w_1 - h_n\|_{0,\hat{\Gamma}}^2 \\ & +\frac{1}{2}\|\hat{\mathbf{K}}(\zeta_1)^{1/2}\nabla w_1\|_{0,\hat{\Omega}}^2 + \frac{1}{2}\|\hat{\mathbf{K}}(\zeta_1)^{1/2}\nabla h_n\|_{0,\hat{\Omega}}^2. \end{aligned} \tag{35}$$

Using the positive definiteness of $\hat{\mathbf{K}}$ once more, we obtain

$$\begin{aligned}\|\nabla w_1\|^2_{0,\hat{\Omega}} &\leq C_2^{-1}\|\hat{\mathbf{K}}(\zeta_1)^{1/2}\nabla w_1\|^2_{0,\hat{\Omega}} \\ &\leq C_2^{-1}\left(\phi^{-1}\Delta t\|I(t)\|^2_{0,\hat{\Gamma}} + \|\hat{\mathbf{K}}(\zeta_1)^{1/2}\nabla h_n\|^2_{0,\hat{\Omega}}\right). \quad (36)\end{aligned}$$

A bound on $\|\nabla w_2\|^2_{0,\hat{\Omega}}$ is formed analogously. This allows us to construct the desired bound on $\|\nabla(w_1 + w_2)\|^2_{0,\hat{\Omega}}$ which takes the following form:

$$\begin{aligned}\|\nabla(w_1+w_2)\|^2_{0,\hat{\Omega}} &\leq 2\left(\|\nabla w_1\|^2_{0,\hat{\Omega}} + \|\nabla w_2\|^2_{0,\hat{\Omega}}\right) \\ &\leq C_3\Delta t + C_4. \quad (37)\end{aligned}$$

Note that if $C_3\Delta t + C_4 = 0$, then $\nabla(w_1 + w_2) = 0$ as well. Consequently, we obtain $w_1 = w_2$ from inequality (34) and conclude that A is a contraction.

Otherwise, we set $\epsilon = C_1(C_3\Delta t + C_4)^{-1}$ and derive

$$\begin{aligned}\Delta t^{-1}\|w_1 - w_2\|^2_{0,\Gamma} &\leq \frac{C_3\Delta t + C_4}{4C_1\phi}\|\hat{\mathbf{K}}(\zeta_1) - \hat{\mathbf{K}}(\zeta_2)\|^2_{0,\hat{\Omega}} \\ &\leq (C_5\Delta t + C_6)\|\zeta_1 - \zeta_2\|^2_{0,\hat{\Gamma}}. \quad (38)\end{aligned}$$

Here, we used the property that $\hat{\mathbf{K}}(\zeta)$ is Lipschitz continuous when ζ is bounded away from zero. (Note, however, that the values of C_5 and C_6 depend on $\delta > 0$.) After multiplication with the time step Δt, we obtain

$$\|w_1 - w_2\|^2_{0,\Gamma} \leq (C_5\Delta t^2 + C_6\Delta t)\|\zeta_1 - \zeta_2\|^2_{0,\hat{\Gamma}}. \quad (39)$$

Substitution of $A[\zeta] = w|_{\hat{\Gamma}}$ and taking the square root leads us to the main result

$$\|A[\zeta_1] - A[\zeta_2]\|_{0,\Gamma} \leq (C_5\Delta t^2 + C_6\Delta t)^{1/2}\|\zeta_1 - \zeta_2\|_{0,\hat{\Gamma}}. \quad (40)$$

Thus, A is a contraction if we choose the time step Δt sufficiently small. Since we are considering the continuous problem, this constraint is independent of grid size. Now, by Banach's Fixed Point Theorem, it follows that A has a unique, fixed point $\zeta \in H^1_\delta(\hat{\Gamma})$ satisfying

$$A[\zeta] = \zeta. \quad (41)$$

The unique solution h can then be obtained by solving problem (28) with ζ as the trace value. □

5 Finite element formulation

The analytical results shown up to this point all concern the continuous case. The next step is to discretize the problem spatially using the finite element method leading to a discrete problem. First, the domain $\hat{\Omega}$ is partitioned using a Delaunay triangulation.

The Galerkin method is then applied to approximate the solution by a combination of N known basis functions $\varphi_j(\hat{\mathbf{x}})$ with $j = 1, ..., N$. In particular, we assume that the solution can be written as follows:

$$h(\hat{\mathbf{x}}) = \sum_j^N h_j\varphi_j(\hat{\mathbf{x}}), \quad (42)$$

with h_j constants representing the values of h at node $\hat{\mathbf{x}}_j$. These values are collected in a vector denoted by $\mathbf{h}$. Finally, the test functions g will be chosen as φ_i and the system (28) is rewritten to the following matrix-vector multiplication.

$$A(\mathbf{h}^k)\mathbf{h}^{k+1} = \mathbf{b}. \quad (43)$$

The elements in the matrix A and vector $\mathbf{b}$ can be computed as follows

$$\begin{aligned}A_{i,j}(\mathbf{h}^k) &= S_s\Delta t^{-1}(\varphi_i,\varphi_j)_{\hat{\Omega}} + \left(\hat{\mathbf{K}}(\mathbf{h}^k)\nabla\varphi_i, \nabla\varphi_j\right)_{\hat{\Omega}} \\ &\quad + \phi\Delta t^{-1}(\varphi_i,\varphi_j)_{\hat{\Gamma}}, \quad (44) \\ b_i &= S_s\Delta t^{-1}(h_n,\varphi_i)_{\hat{\Omega}} + \phi\Delta t^{-1}(h_n,\varphi_i)_{\hat{\Gamma}} + (I(t),\varphi_i)_{\hat{\Gamma}}. \quad (45)\end{aligned}$$

Here, in an abuse of notation, $\hat{\mathbf{K}}$ acts upon the function h^k given by the vector $\mathbf{h}^k$.

During the transition to a discrete problem, it is not trivial that the resulting, discrete problem is also well-posed. We therefore present the following, separate lemma concerning the discrete problem.

Lemma 3 *Let the the assumptions from Lemma 1 hold and let the spatial discretization be linear Lagrange elements on a Delaunay triangulation. If, furthermore, a sufficiently small time step is chosen, then the solution to the fully discrete problem* (43) *exists and is unique.*

Proof The choice of linear Lagrange elements on a Delaunay triangulation ensures that the matrix A is an M-matrix [11, 14]. In turn, the discrete maximum principle holds [5, 14]. Thus, following the same arguments from the proofs of Lemmas 1 and 2, we obtain the result. □

Finally, we note that Eq. 43 is a diffusion-type problem and Lagrangian finite elements are a classic choice to obtain a stable discretization. Together with the well-posedness from the Lemma 3, quadratic convergence of the hydraulic head and linear converge of its gradient are to be expected.

6 Numerical results

In this section, we introduce a model problem in order to demonstrate the theoretical results concerning stability and convergence. To capture the importance of vertical flows, we base our example on the water table evolution in the vicinity of an extraction well. A broader comparison to

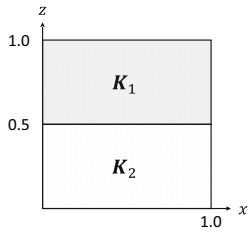

Fig. 2 The computational domain is split into two layers with (possibly different) permeabilities

existing numerical techniques and application to field data is forthcoming.

As an initial condition, we will assume that the hydraulic head is equal to one uniformly, i.e.,

$$h_0 \equiv 1. \tag{46}$$

The extraction well is incorporated as a Neumann boundary condition and starts to operate at time $t = 0$. We will assume no flow conditions on the bottom boundary and a constant unit head on the boundaries far from the well, i.e. $f = 1$. Furthermore, the top boundary is governed by the water table evolution as prescribed by Eq. 16.

The (dimensionless) parameters are as follows, $\mathbf{K} = \mathbf{I}$ where $\mathbf{I}$ is the $d \times d$ identity tensor, $S_s = 0.1$, $\phi = 0.1$, and we introduce a small, constant infiltration $I(t) = 10^{-3}$. As a result of the previous analysis, the magnitude of the extraction rate may not be too large in order to ensure that the hydraulic head remains strictly positive. Thus, we set this rate to -0.3 in the 2D case and to -1.0 for the 3D equivalent.

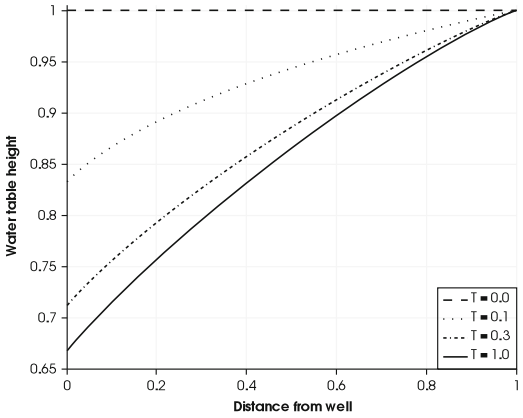

Fig. 3 Water table evolution for the two-dimensional, homogeneous case at different times. The solution is monotone, approaching an equilibrium state at $t = 1.0$

Table 1 Convergence results for the 2D, homogeneous test case showing the expected quadratic convergence of the hydraulic head and linear converge of its gradient

	h		∇h	
h_{mesh}	error	rate	error	rate
1/2	7.02E-03		1.04E-01	
1/4	1.89E-03	1.89	5.57E-02	0.90
1/8	4.86E-04	1.96	2.90E-02	0.94
1/16	1.21E-04	2.00	1.48E-02	0.97
1/32	2.91E-05	2.06	7.38E-03	1.01
1/64	6.13E-06	2.25	3.35E-03	1.14

Although these values may not coincide with physical values, this choice suffices to demonstrate the performance of the scheme. All computations are implemented within the open-source environment FEniCS [12]. In the following subsections, the model problem is considered on a two-dimensional domain followed by a 3D equivalent.

6.1 2D test case

Let us introduce the two-dimensional, reference domain $\hat{\Omega}$, which we define as the unit square. Heterogeneity is incorporated by defining two permeability tensors $\mathbf{K}_1$ and $\mathbf{K}_2$ (Fig. 2). We emphasize that radial symmetry is not assumed here and therefore the left boundary can be viewed as an infinite strip sink rather than an extraction well.

The problem is solved on a uniform, triangular mesh using a fixed time step $\Delta t = 0.1$. Adaptive time stepping or local grid refinement may hold certain advantages, but this exceeds the focus of this work.

Let us first consider the homogeneous case, i.e., $\mathbf{K}_1 = \mathbf{K}_2 = \mathbf{I}$. As depicted in Fig. 3, the solution obtained is stable in space and time, showing no sign of oscillations. Furthermore, the water table evolves rapidly to a steady state, which is to be expected.

Table 2 The scheme remains convergent when heterogeneities are included with a slight deterioration in the rates

	h		∇h	
h_{mesh}	error	rate	error	rate
1/2	7.70E-03		3.44E-01	
1/4	4.88E-03	0.66	2.48E-01	0.47
1/8	3.24E-03	0.59	1.66E-01	0.58
1/16	5.34E-04	2.60	7.96E-02	1.06
1/32	1.67E-04	1.68	5.20E-02	0.62
1/64	6.86E-05	1.28	3.25E-02	0.68

Table 3 The convergence rates can be recovered in the heterogeneous case by only applying the coordinate transformation in the upper part of the domain

	h		∇h	
h_{mesh}	error	rate	error	rate
1/2	3.28E-03		8.30E-02	
1/4	8.84E-04	1.89	4.45E-02	0.90
1/8	2.31E-04	1.94	2.32E-02	0.94
1/16	5.90E-05	1.97	1.19E-02	0.97
1/32	1.49E-05	1.99	5.93E-03	1.00
1/64	3.60E-06	2.05	2.70E-03	1.14

Next, we consider the convergence of the discretization. Due to the nonlinearity of the problem, an analytical solution is not at our disposal. Instead, the relative error is computed with respect to a solution obtained on a fine mesh at time $t = 1.0$. The results in Table 1 show that the scheme is convergent with rates as expected from linear finite elements, namely second-order convergence of the L^2-error in h and first-order convergence of its gradient.

The incorporation of heterogeneity is done by choosing a higher permeability in the upper domain. Specifically, we set $\mathbf{K}_1 = 4\mathbf{K}_2 = 4\mathbf{I}$. As the numerical results show in Table 2, the scheme remains convergent with a moderate decrease in the convergence rates. The deterioration is mainly due to the fact that the heterogeneities are not stationary in the reference domain. Nevertheless, the results show that convergence is maintained despite the unresolved heterogeneities.

If the water table remains within the upper region, a full recovery of the convergence rates from the homogeneous problem can be achieved by choosing a transformation which allows the heterogeneity to be stationary in the computational domain. For this purpose, the transformation is chosen such that it only applies to the upper layer. The recovered convergence rates are shown in Table 3.

We emphasize that this choice of coordinate transformation gives rise to a natural coupling with the saturated region situated below. This is an advantage compared to approaches with Richards' equation where the coupling with deeper, saturated layers is typically less trivial.

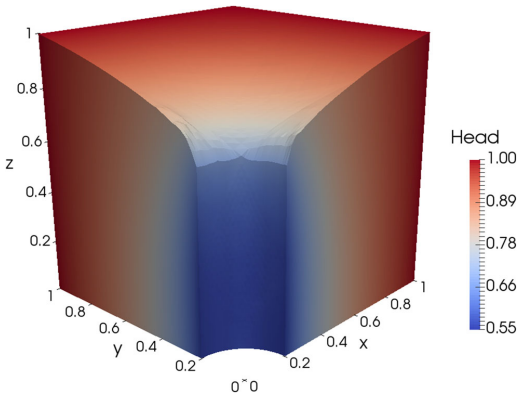

Fig. 4 The hydraulic head in the 3D test case represented in the physical domain at time $t = 1.0$

Table 4 Convergence results for the 3D test case. The observed rates approach the rates expected from the theory

	h		∇h	
h_{mesh}	error	rate	error	rate
1	3.62E-02		6.45E-01	
1/2	1.66E-02	1.13	4.61E-01	0.48
1/4	6.30E-03	1.40	2.87E-01	0.68
1/8	1.95E-03	1.69	1.60E-01	0.84

6.2 3D test case

In the 3D case, we consider $\hat{\Omega}$ to be a unit cube. The well, positioned along the z-axis with radius 0.2 is removed from the domain and is incorporated as a Neumann boundary condition.

As shown in Fig. 4, the scheme once again produces a stable solution. Qualitatively, a decrease in the water table can be seen in the vicinity of the well, as expected. The equilibrium state, depicted in Fig. 4, is attained at time $t = 1.0$.

Table 4 shows that the convergence rates approach the asymptotic rates as the nonlinearities are resolved. These numerical results therefore support the theory presented in previous sections.

References

1. An, H., Ichikawa, Y., Tachikawa, Y., Shiiba, M.: Three-dimensional finite difference saturated-unsaturated flow modeling with nonorthogonal grids using a coordinate transformation method. Water Resour. Res. **46**(11) (2010)
2. Bear, J.: Dynamics of Fluids in Porous Media. Dover Civil and Mechanical Engineering Series. Dover (1972)

3. Bresciani, E., Davy, P., Dreuzy, J.R.: A finite volume approach with local adaptation scheme for the simulation of free surface flow in porous media. Int. J. Numer. Anal. Methods Geomech. **36**(13), 1574–1591 (2012)
4. Ciarlet, P.G.: Mathematical Elasticity: Three-Dimensional Elasticity, vol. 1. Elsevier (1993)
5. Ciarlet, P.G., Raviart, P.A.: Maximum principle and uniform convergence for the finite element method. Comput. Methods Appl. Mech. Eng. **2**(1), 17–31 (1973)
6. Darbandi, M., Torabi, S., Saadat, M., Daghighi, Y., Jarrahbashi, D.: A moving-mesh finite-volume method to solve free-surface seepage problem in arbitrary geometries. Int. J. Numer. Anal. Methods Geomech. **31**(14), 1609–1629 (2007)
7. Dogan, A., Motz, L.H.: Saturated-unsaturated 3d groundwater model. i: development. J. Hydrol. Eng. **10**(6), 492–504 (2005)
8. Freeze, R.A.: Three-dimensional, transient, saturated-unsaturated flow in a groundwater basin. Water Resour. Res. **7**(2), 347–366 (1971)
9. Keating, E., Zyvoloski, G.: A stable and efficient numerical algorithm for unconfined aquifer analysis. Ground Water **47**(4), 569–579 (2009)
10. Kinouchi, T., Kanda, M., Hino, M.: Numerical simulation of infiltration and solute transport in an s-shaped model basin by a boundary-fitted grid system. J. Hydrol. **122**(1), 373–406 (1991)
11. Křížek, M., Qun, L.: On diagonal dominance of stiffness matrices in 3D. East-West J. Numer. Math. **3**(1), 59–69 (1995)
12. Logg, A., Mardal, K.A., Wells, G.N., e.t.al.: Automated Solution of Differential Equations by the Finite Element Method. Springer (2012) doi:10.1007/978-3-642-23099-8
13. Nordbotten, J.M., Celia, M.A.: Geological Storage of CO2: Modeling Approaches for Large-Scale Simulation. Wiley (2011)
14. Xu, J., Zikatanov, L.: A monotone finite element scheme for convection-diffusion equations. Mathematics of Computation of the American Mathematical Society **68**(228), 1429–1446 (1999)

Paper G

A 3-D Model of the Influence of Meanders on Groundwater Discharge to a Gaining Stream in an Unconfined Sandy Aquifer

N. Balbarini, W.M. Boon, P.L. Bjerg, J.M. Nordbotten, P.J. Binning

Journal of Hydrology 552 (2017), p. 168–181.

doi: 10.1016/j.jhydrol.2017.06.042

Journal of Hydrology 552 (2017) 168–181

Contents lists available at ScienceDirect

Journal of Hydrology

journal homepage: www.elsevier.com/locate/jhydrol

Research papers

A 3-D numerical model of the influence of meanders on groundwater discharge to a gaining stream in an unconfined sandy aquifer

Nicola Balbarini [a,*], Wietse M. Boon [b], Ellen Nicolajsen [a], Jan M. Nordbotten [b,c], Poul L. Bjerg [a], Philip J. Binning [a]

[a] Department of Environmental Engineering, Technical University of Denmark, Kgs. Lyngby, Denmark
[b] Department of Mathematics, University of Bergen, Bergen, Norway
[c] Department of Civil and Environmental Engineering, Princeton University, Princeton, NJ, USA

ARTICLE INFO

Article history:
Received 15 February 2017
Received in revised form 22 June 2017
Accepted 23 June 2017
Available online 24 June 2017
This manuscript was handled by Corrado Corradini, Editor-in-Chief, with the assistance of Dongmei Han, Associate Editor

Keywords:
Numerical model
3-D
Meander
Stream geometry
Spatial and temporal variability
Reach scale

ABSTRACT

Groundwater discharge to streams depends on stream morphology and groundwater flow direction, but are not always well understood. Here a 3-D groundwater flow model is employed to investigate the impact of meandering stream geometries on groundwater discharge to streams in an unconfined and homogenous sandy aquifer at the reach scale (10–200 m). The effect of meander geometry was examined by considering three scenarios with varying stream sinuosity. The interaction with regional groundwater flow was examined for each scenario by considering three groundwater flow directions. The sensitivity of stream morphology and flow direction to other parameters was quantified by varying the stream width, the meander amplitude, the magnitude of the hydraulic gradient, the hydraulic conductivity, and the aquifer thickness. Implications for a real stream were then investigated by simulating groundwater flow to a stream at a field site located in Grindsted, Denmark. The simulation of multiple scenarios was made possible by the employment of a computationally efficient coordinate transform numerical method. Comparison of the scenarios showed that the geometry of meanders greatly affect the spatial distribution of groundwater flow to streams. The shallow part of the aquifer discharges to the outward pointing meanders, while deeper groundwater flows beneath the stream and enters from the opposite side. The balance between these two types of flow depends on the aquifer thickness and meander geometry. Regional groundwater flow can combine with the effect of stream meanders and can either enhance or smooth the effect of a meander bend, depending on the regional flow direction. Results from the Grindsted site model showed that real meander geometries had similar effects to those observed for the simpler sinuous streams, and showed that despite large temporal variations in stream discharge, the spatial pattern of flow is almost constant in time for a gaining stream.

1. Introduction

An understanding of the interaction between groundwater and streams is needed to map water fluxes and the transport of contaminants from groundwater into streams (Cey et al., 1998; Derx et al., 2010; Anibas et al., 2012; Karan et al., 2013; Ou et al., 2013; Freitas et al., 2015). This interaction is governed by several factors such as the hydraulic gradient between the aquifer and the stream, the stream channel geometry, and the hydraulic conductivity distribution of the aquifer and the streambed (Larkin and Sharp, 1992; Cey et al., 1998; Krause et al., 2007; Anibas et al., 2012; Binley et al., 2013; Fernando, 2013; Flipo et al., 2014). Furthermore, flow processes between groundwater and streams are scale dependent and so must be investigated at different scales (Dahl et al., 2007; Anibas et al., 2012; Flipo et al., 2014; Poulsen et al., 2015).

At the reach scale (10–200 m), groundwater flow to streams is both vertical and horizontal; thus, an analysis in three-dimensions is required (Harvey and Bencala, 1993; Modica et al., 1998; Flipo et al., 2014). Reach scale groundwater flow paths to streams are not adequately resolved at the larger regional or catchment scales considered by Toth (1963) and many other later larger scale studies (e.g. Larkin and Sharp, 1992; Wroblicky et al., 1998; Modica et al., 1998; Anibas et al., 2012; Aisopou et al., 2015a; Flipo et al., 2014; Gomez-Velez et al., 2015).

* Corresponding author at: Department of Environmental Engineering, Technical University of Denmark, Bygningstorvet, Building 115, DK – 2800 Kgs. Lyngby, Denmark.
E-mail address: nbal@env.dtu.dk (N. Balbarini).

http://dx.doi.org/10.1016/j.jhydrol.2017.06.042
0022-1694/

Studies investigating reach scale groundwater flow to streams have generally considered straight streams, and have not accounted for the effect of meander bends (Derx et al., 2010; Guay et al., 2013; Miracapillo and Morel-Seytoux, 2014, see also overview in Table S1). Thus, a better understanding of how groundwater flow varies in space because of stream meanders is needed (Modica et al., 1998; Diem et al., 2014; Krause et al., 2014; Boano et al., 2014). This is particularly important when investigating contaminant plume discharge to a stream system, where insight is needed to improve site investigations, data interpretation and to design more efficient monitoring campaigns (Harvey and Bencala, 1993; Conant et al., 2004; Anibas et al., 2012; Weatherill et al., 2014). The appropriate scale for contaminant plume studies will often be similar to the stream reach scale (Conant et al., 2004; Byrne et al., 2014; Weatherill et al., 2014; Freitas et al., 2015).

Only a few studies have analyzed groundwater flow to meandering streams (e.g. Dahl et al. (2007), Nalbantis et al. (2011), Flipo et al. (2014), and Boano et al. (2014)). A literature review is shown in Table S1 and shows that the majority of research on meandering stream-aquifer interaction has focused on the hyporheic exchange processes (Wroblicky et al., 1998; Salehin et al., 2004; Cardenas et al., 2004; Revelli et al., 2008; Cardenas, 2008, 2009a,b; Boano et al., 2006; Stonedahl et al., 2010; Boano et al., 2009, 2010; Brookfield and Sudicky, 2013; Gomez-Velez et al., 2014, 2015). Hyporheic exchange processes take place in the hyporheic zone just under the stream bed, where stream water mixes with groundwater, before returning to the stream. For example, Boano et al. (2010) applied an analytical approach to examine 3-D groundwater flows directly under a streambed, but did not consider the surrounding groundwater flow system.

For many problems, it is necessary to move beyond the hyporheic zone, and consider larger scale groundwater flows at the reach scale. Thus, the focus of this paper is groundwater flow to meandering streams at the reach scale.

This study analyses the spatial variability of the groundwater flow discharge to streams along meander bends in a full 3-D system at the reach scale. The first aim is to simulate the groundwater flow paths to streams and investigate how those paths are affected by stream meanders and groundwater flow direction in an unconfined sandy aquifer. A 3-D numerical model is presented simulating the discharge to streams for a synthetic gaining sinuous stream with three scenarios of sinuosity: a straight stream, a moderately sinuous stream, and a highly sinuous stream. For each scenario, three groundwater flow directions are assumed with the dominant groundwater flow being: perpendicular to the stream; along the stream; and diagonally across the stream. The resulting groundwater flow to the stream for different sinuosities was quantified for different stream widths, meander geometries, aquifer thicknesses, homogenous hydraulic conductivities, and hydraulic gradients in order to assess the combined effects and the robustness of the results. All numerical models were designed to simulate the groundwater flow to the stream, disregarding the hyporheic flow. The second aim is to apply the 3-D numerical model to a meandering stream at Grindsted in Denmark in order to assess the effects in a field scale system (unconfined, sandy aquifer) with a real geometry and time varying stream water levels. Finally, the implications for our current understanding of discharges to streams are discussed.

To address these aims, the 3-D numerical model employed a novel coordinate transformation method developed by Boon et al. (2016). This method solves the equation for groundwater flow in a transformed domain, which is constant in time, while the coordinate system changes depending on the groundwater free surface variations. The application of the linear transformation allows the transformed domain geometry to be simpler than the original problem; thus, the method is computationally efficient and can be applied to complex geometries. Boon et al. (2016) employs the method to simulate groundwater flow to wells, but it has not been applied to other relevant groundwater systems. Since the application of the coordinate transform method to groundwater/surface water interaction is new, it was first tested and compared to existing approaches (the moving mesh and the saturated-unsaturated groundwater flow method). It is shown that the coordinate transform method is far more computationally efficient than the other methods (see Supporting Information, Section S1).

2. Method

2.1. Sinusoidal stream model

In this study, the effect of the stream sinuosity on the groundwater flow to streams is analyzed by extending the two-dimensional steady state model developed by Cardenas (2009a,b) to three dimensions. The stream is assumed to be sinusoidal with a constant wavelength (λ) of 40 m and amplitude (α), which is varied in order to reproduce different levels of sinuosity. The sinuosity (S) is calculated by dividing the sinuous stream length along the channel by the straight valley length (300 m in this study). Three sinuosity scenarios (Fig. 1) are considered: a) straight stream ($S = 1$, $\alpha = 0$ m), b) moderately sinuous stream ($S = 1.14$, $\alpha = 5$ m), and c) a highly sinuous stream ($S = 1.74$, $\alpha = 13.5$ m). The choices of sinuosity, wavelength, and amplitude are the same as those of Cardenas (2009a,b).

The spatial variability of the groundwater flow to the stream is affected by the stream morphology, the groundwater flow direction, and the distribution of hydraulic conductivities (Krause et al., 2012; Gomez-Velez et al., 2014). In order to isolate and analyze the effect of the stream morphology and the groundwater flow direction, the aquifer is assumed to be homogenous and isotropic with a hydraulic conductivity of 40 m/d. The stream cross section is a half-ellipsoidal with a depth of 3 m and a width of 5 m. The stream-aquifer interface is a constant-head boundary where the head varies linearly along the channel with a gradient determined by dividing the overall gradient in the x-direction (0.001) by the sinuosity. Thus, the stream is a gaining stream along the entire length. The top and bottom boundary, except for the stream boundary, are no-flow boundaries and the remaining boundaries are constant-head boundaries. The head gradient is assumed to change linearly depending on the direction.

In order to simulate different groundwater flow directions, the head gradient on the boundary in the x-direction and in the z-direction are constant (0.001 and 0 respectively) while the y-direction gradient is 0.004 for simulating regional groundwater directed laterally toward the stream and 0.0005 for regional groundwater flowing in the direction of stream flow. These values were selected based on Cardenas (2009a,b). The third groundwater flow scenario assumes groundwater directed south-west diagonally across the stream, with a boundary gradient in the y-direction of 0.0005 in the area north of the stream and 0.0001 south of the stream.

The effect of the hydraulic gradient on the x-direction (Fig. 1) was tested by comparing results for a low gradient of 0.0005 and a high gradient of 0.01. The effect of the 40 m constant aquifer thickness was tested by modeling aquifer with thicknesses of 5 m and 80 m. Similarly, different stream morphologies were tested by varying the stream width between 2 and 10 m, and the meander wavelength between 30 ($S = 1.94$) and 60 m ($S = 1.39$). The effect of the constant hydraulic conductivity was investigated by varying the hydraulic conductivity between 20 and 80 m/d.

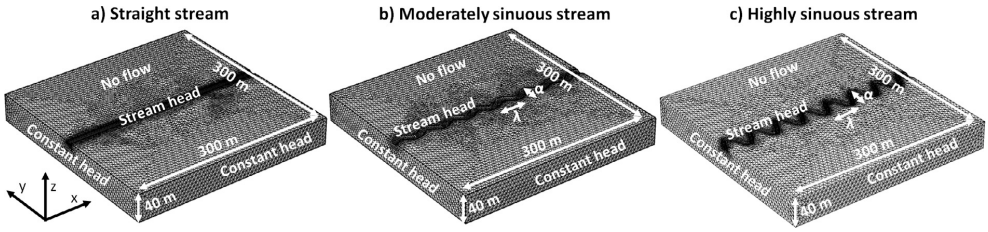

Fig. 1. Model domain, finite element mesh, and boundary conditions for the three scenarios of the synthetic stream model: straight stream (a), the moderately sinuous stream (b), and the highly sinuous stream (c) models.

These scenarios were simulated for the highly sinuous stream with groundwater flow directed laterally toward the stream.

2.2. Grindsted stream field site

To examine the implications of findings for real streams with more complex geometries with time varying boundary conditions, a 500 m reach scale numerical model of a field site in southern Jutland, Denmark (Fig. 2) was constructed. Grindsted stream has a catchment area of approximately 200 km^2, is 1–2.5 m deep and 8–12 m wide. The unconfined aquifer is 80 m thick and is in hydraulic contact with the stream. The geology is composed of a Quaternary sand formation for the first 10–15 mbgs and, below that, a Tertiary sand formation. The aquifer is underlain by a thick and extensive Tertiary clay layer at 80 mbgs (Barlebo et al., 1998; Heron et al., 1998). Two contaminated sites are present in the surrounding area: Grindsted factory located 1.5 km north of the stream, and Grindsted landfill located 2 km south of the stream (Kjeldsen et al., 1998). From these sites, contaminant plumes discharge into the stream, as evident by examination of stream water quality (Rasmussen et al., 2016). The domain of the numerical model was designed in order to include the area where the contaminant plumes discharge to the stream. This paper focuses on an assessment of the 3D groundwater flows to the stream. The

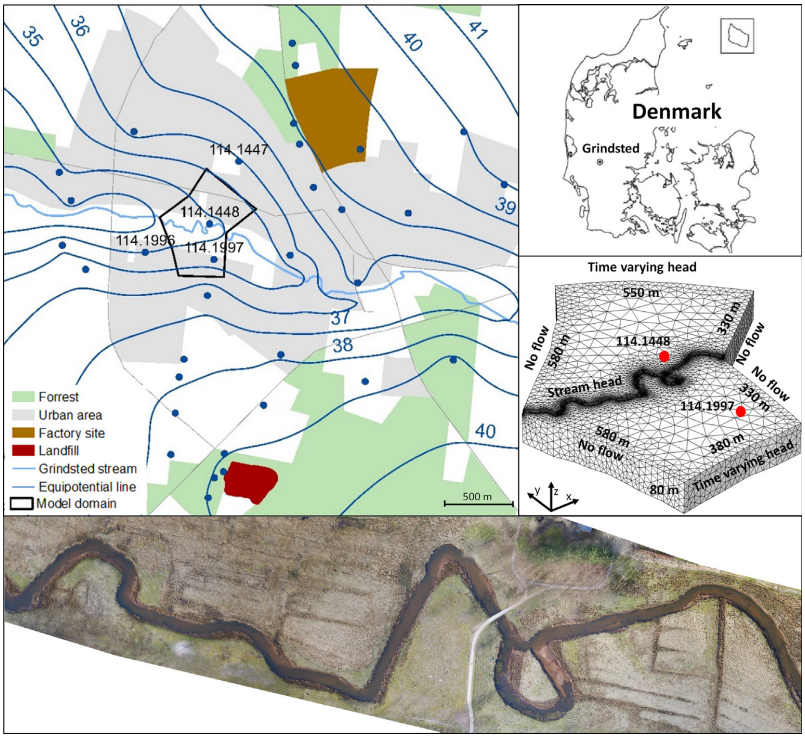

Fig. 2. Overview of the Grindsted stream study site and model set up. The blue lines indicate the equipotential lines with an interval of 1 m. The equipotential map is based on groundwater head measurements collected at the wells indicated by the blue dots. The name of the observation wells used to set up boundary conditions or for comparison with model results are shown on the map. The model domain area is defined by the black line. The bottom figure shows an orthophoto of the simulated stream reach. The middle right figure shows the model grid, the boundary conditions, the model size, and the location of boreholes in the model domain. (For interpretation of the references to color in this figure legend, the reader is referred to the web version of this article.)

analysis of the coupled contaminant transport processes is beyond the scope of this paper and will not be discussed further.

The regional equipotential map (Fig. 2) was used to define the lateral extent of the model domain and its geometry. Equipotential boundaries, where the flow is perpendicular to the boundary and the head is constant over depth, are employed (Aisopou et al., 2015b). The remaining boundaries are placed along streamlines where a no-flow condition is assumed on vertical sides. The temporal variability of groundwater flow to streams was modeled accounting for variation in precipitation, stream water level and groundwater head. Precipitation data were collected by the Danish Meteorological Institute at a measurement station at Billund Airport, 15 km from the study site (DMI, 2015). The temporal variation in groundwater heads was monitored at several wells in the Grindsted area (selected wells are shown in Fig. 2). Well 114.1996 was used to set the variable head on the southern boundary, adjusting all measured heads by 1.2 m because the well is not located exactly on the boundary. Similarly, the head at well 114.1447 was applied on the northern boundary, with an adjustment of 0.9 m. The adjustment was made as part of the model calibration in order to fit the simulated with the observed groundwater head level at the two wells located inside the model domain: 114.1448 and 114.1997. The Quaternary and the tertiary layers are both sandy and have similar hydrogeological properties. Therefore, it was decided to assume a homogenous sandy aquifer. During the model calibration, values of 30 m/d for the horizontal hydraulic conductivity and 3 m/d for the vertical hydraulic conductivity were selected. These values are being similar to the hydraulic conductivities from other field and model studies in the area (Barlebo et al., 1998; Bjerg et al., 1995; Lønborg et al., 2006).

Stream water level data was obtained at the Tingvejen gaging station, located 2.5 km upstream of the model domain, and at Eg BrO, located 8.1 km downstream of the model domain. The average water slope between the two gaging stations is 0.001. The mean annual stream discharge is 2150 l/s at Tingvejen and 2980 l/s at Eg BrO. The simulated stream reach is about 900 m long and the annual average groundwater discharge to the stream in the reach, estimated from annual average discharge measurements from the gaging stations, is 70 l/s.

Based on three measured streambed cross sections, the stream cross section is modeled using a half-ellipsoidal with depth of 3 m and width of 10 m. The depth of 3 m is larger than the stream water depth to allow for in stream head variations without overbank flow. The stream is implemented as a time varying head boundary where the head varies linearly along the channel with a gradient of 0.001, corresponding to the average water slope between the two gaging stations. The slope of the streambed is assumed to be 0.001, as to the stream water slope.

2.3. Modeling groundwater flow to streams with the coordinate transformation method

The groundwater head at the interface between groundwater and the streambed which controls the flow to/from the stream is temporally variable and is difficult to simulate with a traditional groundwater flow model employing a regular grid. Two methods have been developed to describe the variability of groundwater head in unconfined aquifers: the moving mesh (Knupp, 1996; Darbandi et al., 2007; Bresciani et al., 2011) and the saturated-unsaturated groundwater flow (Freeze, 1971; Sugio and Desai, 1987; Dogan and Motz, 2005; Keating and Zyvoloski, 2009; Camporese et al., 2010; Walther et al., 2012). A review of studies applying these methods is provided in Table S2. These methods were developed for unconfined aquifers without considering stream interaction, which introduces large local variations in groundwater head.

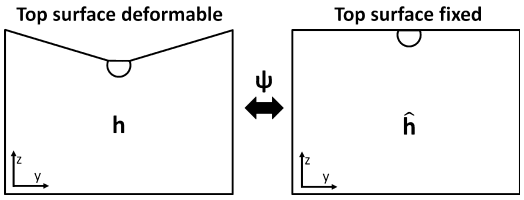

Fig. 3. The coordinate transformation method for modeling unconditioned aquifers interacting with streams of Boon et al. (2016) employs a fixed domain (right) instead of the real deformable domain (left). A coordinate transformation Ψ is used to map the governing equations between the two domains.

The moving mesh method solves the groundwater flow problem under saturated conditions and adjusts the mesh depending on the groundwater head calculated at the previous time step. The method requires re-meshing at each time step, which is very computationally demanding (Freeze, 1971; Kinouchi et al., 1991; Knupp, 1996) and can fail for large changes in the water head between time steps or for steep gradients, such as at the stream-aquifer interface (Bresciani et al., 2011; COMSOL, 2013). The saturated-unsaturated method solves the flow equation in both the saturated and unsaturated zone avoiding the problem of explicitly describing the water table surface (An et al., 2010; Kinouchi et al., 1991). However, the method is more computationally demanding than saturated flow models and is rarely justified when the main focus is the saturated flow (Keating and Zyvoloski, 2009).

The new coordinate transformation of Boon et al. (2016) was used to solve the groundwater flow equations in the model domain. The method reduces computational time by employing a coordinate transformation so that the saturated groundwater flow equations are solved on a fixed mesh (Fig. 3). For comparison purposes, the equations were also solved on a domain with a dynamically deforming mesh, and by a coupled saturated/unsaturated flow solver (Supporting information S1).

To test the three methods for the groundwater flow to streams problem, they were implemented for a two-dimensional test case and their computational accuracy and efficiency compared (Section S1 in the Supporting Information). The comparison between the methods shows (Table S4) that the coordinate transformation method is the least computationally demanding of the three methods for a 2-D test problem, requiring 32 times less computational effort than the saturated-unsaturated approach and 3 times less time than moving mesh, for a relatively coarse discretization. Differences become larger in 3-D and when the grid is refined: the computational time required by the moving mesh in a 3-D test (137 min) is 32 times more computational time than the coordinate transformation (4 min). Furthermore, the coordinate transformation method does not lead to instabilities and oscillations, problems that were encountered with the moving mesh. The coordinate transformation is a much more computationally efficient solution making it possible to simulate a variety of scenarios and properly explore the problem. Thus, the coordinate transformation method is employed for all examples in this study.

In the coordinate transformation method (Boon et al., 2016), the groundwater flow equation for saturated conditions is solved in a transformed domain $\hat{\Omega}$:

$$S_s \frac{\partial \hat{h}}{\partial t} + \nabla \cdot (-\hat{\mathbf{K}} \cdot \nabla \hat{h}) = 0 in \hat{\Omega} \quad (1)$$

Where Ss is the specific yield [1/m], $\hat{h}$ is the hydraulic head in the transformed space [m] and $\hat{K}$ is the hydraulic conductivity tensor in the transformed space [m/s]. The groundwater flow velocity in the transformed domain $\hat{\Omega}$ becomes:

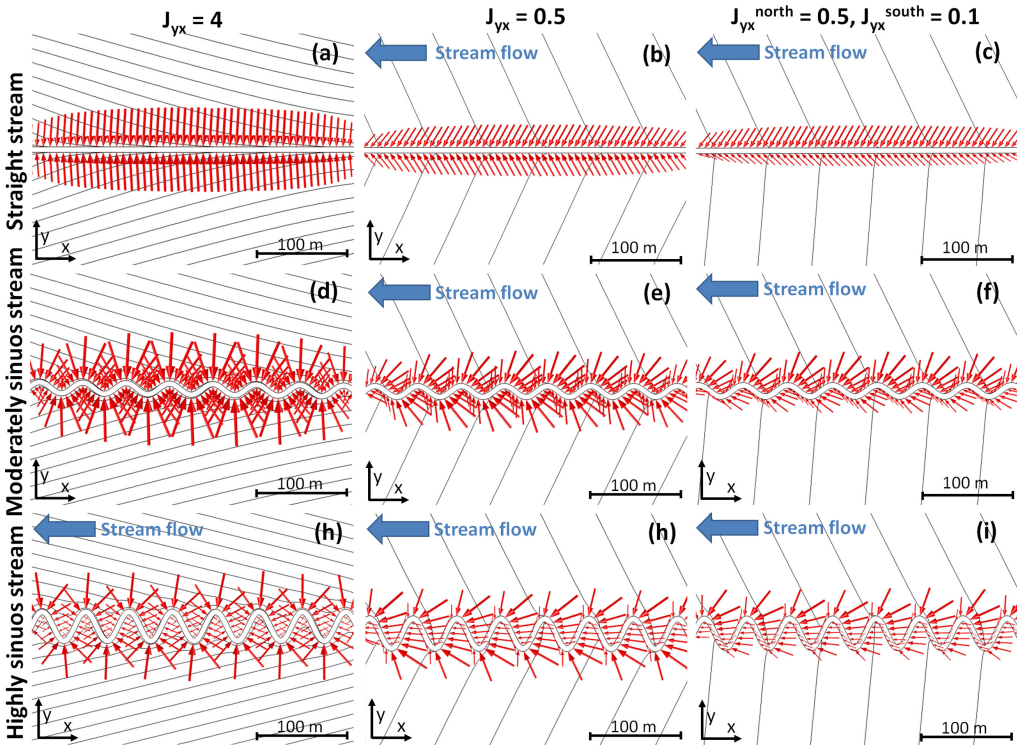

Fig. 4. Groundwater discharge to the stream at the upper edge of the stream-aquifer interface shown by the red arrows, which are proportionate to the flow. The equipotential lines are indicated by the black lines and are separated by 0.05 m interval. Jyx represent the ratio between the hydraulic gradient in the y and in x-direction. The moderately sinuous stream has sinuosity (S) of 1.14 and amplitude (α) of 5 m. The highly sinuous stream has sinuosity (S) of 1.74 and amplitude (α) of 13.5 m.

$$\hat{q} = -\hat{\mathbf{K}} \cdot \nabla \hat{h} \tag{2}$$

The conditions at the top boundary Γ are:

$$\hat{h}(\hat{x}, t) = \zeta(\hat{x}, t) \quad \text{on} \quad \Gamma \tag{3}$$

$$-\mathbf{e}_\Gamma \cdot (-\hat{\mathbf{K}} \cdot \nabla \hat{h}) = \left(I - S_y \frac{\partial \zeta}{\partial t}\right) \quad \text{on} \quad \Gamma \tag{4}$$

where S_y is the specific yield [–],ζ is the elevation for the free surface [–], and e_Γ is the unit normal to Γ. The governing equations are solved in Comsol Multiphysics, which employs a finite element numerical approximation (COMSOL, 2013). The finite element method employs the weak form of (1) with a linear polynomial Lagrange test function $g \in H^1(\hat{\Omega})$ which is combined with the boundary equation (4) and input into COMSOL Multiphysics:

$$\begin{aligned}\left(S_s \frac{\partial \hat{h}}{\partial t} + \nabla \cdot (-\hat{\mathbf{K}} \cdot \nabla \hat{h}), g\right)_{\hat{\Omega}} &= \left(S_s \frac{\partial \hat{h}}{\partial t}, g\right)_{\hat{\Omega}} + (\hat{\mathbf{K}} \cdot \nabla \hat{h}, \nabla g)_{\hat{\Omega}} \\ &+ (\mathbf{e} \cdot (-\hat{\mathbf{K}} \cdot \nabla \hat{h}), g)_\Gamma = \left(S_s \frac{\partial \hat{h}}{\partial t}, g\right)_{\hat{\Omega}} \\ &+ (\hat{\mathbf{K}} \cdot \nabla \hat{h}, \nabla g)_{\hat{\Omega}} - \left(\left(I - S_y \frac{\partial \zeta}{\partial t}\right) e_\Gamma z, g\right)_\Gamma = 0\end{aligned} \tag{5}$$

The linear transformation ψ is:

$$\mathbf{x} = \psi(\hat{x}, \hat{z}, t) = [\hat{x}, 0] + \zeta(\hat{x}, t)\hat{z}\mathbf{e_z} \tag{6}$$

$$h(x, z, t) = \hat{h}(\hat{x}, \hat{z}, t) \tag{7}$$

where e_z is the unit vector in the z-direction. The hydraulic conductivity field is a function of the elevation of the free surface ζ and can be derived from the linear transformation:

$$\begin{aligned}\hat{\mathbf{K}}(\hat{x}, \hat{z}, t) &= \det \hat{\nabla}\psi (\hat{\nabla}\psi)^{-1} \mathbf{K} (\hat{\nabla}^T \psi)^{-1} \\ &= \zeta \begin{bmatrix} K_h & -K_h \hat{z} \zeta^{-1} \hat{\nabla}\zeta \\ -K_h \hat{z} \zeta^{-1} \hat{\nabla}^T \zeta & (K_h \hat{z}^2 \hat{\nabla}^T \zeta \hat{\nabla}\zeta + K_v)\zeta^{-2} \end{bmatrix}\end{aligned} \tag{8}$$

In Eq. (8) $\zeta = \zeta(\hat{x}, t)$, $K_h = K_h(x, z)$, $K_v = K_v(x, z)$, and $\hat{K}$ depends on the linear transformation described in Eqs. (6) and (7).

Apart from the boundary condition for the top boundary (5), the boundary conditions applied in the transformed domain are: no-flow for the bottom boundary, and time-variable fixed-head for the lateral boundaries. The transform formulation, as well as its numerical implementation using lowest-order Lagrange finite elements is provably stable and convergent (Boon et al., 2016).

3. Results

In this section, the effect of meander bends on groundwater flow to streams is presented, with focus on both the vertical and horizontal variability of groundwater flow patterns. The difference between the vertical and horizontal flow could neither have been observed, nor investigated, with a 2-D model. First, the effect of sinuosity is analyzed in combination with other parameters affecting groundwater flow to streams through the synthetic sinuous stream model; then, the results from the Grindsted stream field site are described.

3.1. Horizontal variability of the groundwater flow to the stream

The groundwater discharge to the stream at the upper edge of the stream-aquifer interface is shown in Fig. 4, where the red arrows are proportional to the horizontal groundwater discharge. Table 1 shows the mean flux over one meander from both stream sides (m/s) for each scenario and the percentage of flow discharged at the outward pointing side of the meander and at the inward pointing side of the meander.

The straight stream has a constant discharge along the stream for all hydraulic gradients (Fig. 4a, b, and c), except at the boundaries, where the boundary conditions affected the results. In the moderately sinuous stream (Fig. 4d, e, and f), the groundwater discharge to the stream is not constant and changes depending on the location along the stream meander, as shown by the arrow size. The discharge is largest at the extremes of the stream meanders, with 68% and 67% of the groundwater flux entering the stream on the outward pointing side of the meanders for a J_{yx} (ratio between the hydraulic gradient in the y-direction and in the x-direction) of 4 and 0.5 respectively (Table 1). This variation in the groundwater discharge to the stream is due to the stream sinuosity and increases with the sinuosity: 85% and 82% of the groundwater flux enters at the outward pointing side of the meander for a J_{yx} of 4 and 0.5 respectively (corresponding to Fig. 4g and h). This effect can also be seen by comparing Fig. 4d and e with Fig. 4g, h.

The ratio between the hydraulic gradient in the y and x-direction (J_{yx}) and, thus, the hydraulic gradient in the y-direction affect the groundwater direction to the stream. In the straight stream, for a large J_{yx} (Fig. 4a), the groundwater direction is more perpendicular to the stream (compared with a lower J_{yx} in Fig. 4b). When two different values of J_{yx} are applied on each side of the stream (Fig. 4c), both the direction of groundwater to the stream and the magnitude of the discharge changes on each side of the stream. A lower value of J_{yx} corresponds to a lower groundwater discharge to the stream, as shown on the southern part of the stream in Fig. 4c. Therefore, the percentage of groundwater flux to the stream is lower (39%) on the southern side of the stream, where the hydraulic gradient in the y-direction is higher, compared to northern side where the gradient in the y-direction is lower (61%).

The effect of the hydraulic gradient can also be observed in the moderately (Fig. 4f) and highly sinuous stream (Fig. 4i). The highest groundwater flow to the stream is located further upstream

Table 1
Mean groundwater fluxes to the stream at a meander and percentage of the fluxes entering the stream on the outward pointing side and on the inward pointing side of the meander. The mean flux was calculated as the integral of the discharge along the meander at the stream-aquifer interface divided by the interface area.

Model	Sinuosity	Meander side	$J_{yx} = 4$	$J_{yx} = 0.5$	$J_{yx}^{north} = 0.5$ $J_{yx}^{south} = 0.1$
Straight stream	1	Northern side [%]	50	50	61
		Southern side [%]	50	50	39
		Mean flux [m/s]	0.58	0.06	0.04
Moderately sinuous stream	1.14	Outward side [%]	68	67	74
		Inward side [%]	32	33	26
		Mean flux [m/s]	0.51	0.06	0.05
Highly sinuous stream	1.74	Outward side [%]	85	82	84
		Inward side [%]	15	18	16
		Mean flux [m/s]	0.48	0.05	0.05

on the outward pointing side of the meander bend when decreasing the value of J_{yx}. Therefore, the groundwater flux on the outward pointing side increases from 67% to 74% for the moderately sinuous stream, when the flux is measured on the meander pointing north, where the gradient in the y-direction is higher. The effect of the gradient decreases when the sinuosity increases: for the highly sinuous stream the flux increases from 82% to 84%.

The results shown in Fig. 4 and Table 1 are based on simulations where all parameters are fixed, except for the amplitude of a meander which affects the stream sinuosity, and the ratio between the hydraulic gradient in the y and x-direction. The fixed parameters include the wavelength of a meander (40 m), the hydraulic gradient in the x-direction (1‰), the stream width (5 m), homogenous hydraulic conductivity (40 m/d), and the aquifer depth (40 m). In order to study how these model parameters affect the results shown in Table 1 and Fig. 4, the parameters were varied for the scenario with the highly sinuous stream and J_{yx} of 4. The results are summarized in Table 2 and Fig. S3 (Supporting Information), with bold values indicating the parameter values used for the simulations in Table 1 and Fig. 4.

The mean groundwater flux to a stream meander increases with the hydraulic gradient in the x-direction and with the hydraulic conductivity, as described by Darcy's law: from 0.24 m/s to 4.84 m/s for a hydraulic gradient of 0.5‰ and 10‰ respectively, and from 0.25 m/s to 0.94 m/s for conductivities of 20 m/d and 80 m/d respectively. However, the percentages of groundwater entering the stream on one side or the other of the meander do not change. This indicates that the magnitude of the hydraulic gradient and of hydraulic conductivity affect the magnitude of groundwater flow entering the stream, but not the direction of the groundwater flow to the stream.

The mean groundwater flux to a stream decreases when increasing the stream width, from 0.53 m/s to 0.42 m/s for, respectively, a 2 m and an 8 m wide stream, because the same discharge enters through a larger area for a larger stream. The percentage of groundwater flux entering the stream on the outward pointing side of the meanders is lower (79%) for a 2 m wide stream, compared to an 8 m wide stream (88%). In a wider stream, the stream bank on the outward pointing side is closer to the model boundary conditions, leading to a steeper hydraulic gradient and a higher groundwater flux to the stream. Even though the stream width affects the magnitude of the groundwater flux to the stream, it does not affect the direction of groundwater flow to the stream (see Supporting Information, Fig. S3).

The wavelength of the stream meanders affects both the average discharge to the stream and the percentage of groundwater entering on each side of a meander bend. The average discharge to the stream is 0.44 m/s for the scenario with the wavelength of 30 m, and 0.55 m/s with the wavelength of 60 m. The groundwater flux on the outward pointing side of a meander decreases, from 89% to 75%, by increasing the wavelength from 30 to 60 m. When the amplitude of a meander is held constant and the wavelength increases, the sinuosity of the stream decreases. Thus, the flow to the stream is also dependent on sinuosity.

The average groundwater flux increases with increasing the aquifer thickness: from 0.12 m/s to 0.64 m/s for an aquifer thickness of 5 m and 80 m respectively. This can be explained by looking at the depth of the origin of groundwater, discharging to the stream, compared to the depth of the origin of groundwater exiting the model at the downstream boundaries (as seen in Section 3.2 and Fig. 6). The percentage of water entering the stream on the outward pointing side of a meander is also affected and decreases from 99% for the 5 m thick aquifer to 83% for the 80 m thick aquifer.

Based on the model sensitivity analysis, the parameters most strongly affecting the spatial distribution of the groundwater flow to a stream are the groundwater flow direction, the stream sinuosity, and the aquifer thickness. The effect of these parameters is further analyzed in Section 3.2 where the groundwater flow to the stream in a vertical cross section is examined.

3.2. Vertical variability of the groundwater flow to the stream

In order to analyze the vertical spatial variability of the groundwater close to the stream, the groundwater flow direction on a vertical cross section perpendicular to the stream is shown in Fig. 6 with particle tracks to highlight the streamlines: blue for the particles originating south of the stream and red for particles originating from the north. The contour lines (black lines) show the equipotential lines separated by 0.005 m interval.

In the straight stream (Fig. 5a and b), the groundwater streamlines enter the stream through the stream bank closest to the boundary of streamline origin. In Fig. 5c, the hydraulic gradient in the y-direction is larger on the northern side of the stream compared to the southern side. Here, the groundwater streamlines originating from the north enter the stream on both the northern and southern side of the stream, with the discharging bank depending on the depth of origin of the groundwater flow.

In the moderately sinuous stream and in the highly sinuous stream, the cross section was placed at a point with a meander pointing south. When the hydraulic gradient in the y-direction is the same on both sides of the stream (moderately sinuous stream: Fig. 5d and e; highly sinuous stream: Fig. 5g and h), the groundwater streamlines originating from the south enter the stream on both the southern and northern side of the stream, with the discharging bank depending on the depth of the groundwater flow. This effect increases with the stream sinuosity, as can be observed by comparing Fig. 5d and g. Furthermore, a similar, but reversed situation occurs in Fig. 5c, where flow patterns are driven by the difference in hydraulic gradient in the y-direction.

In Fig. 5f and i, the effects of stream sinuosity and a change in the flow direction at the stream are combined. The two factors have an opposing effect on results; thus, the combined effect is smoothed (compare Fig. 5c, f, and i). In contrast, at meander bends

Table 2
Groundwater discharge to the stream at a meander bend. The base parameter values, shown in bold, are the same as those used for the simulation, whose results are summarized in Figs. 4, 5, and Table 1. Each parameter is then varied and results shown. The ratio between the hydraulic gradient in the y- and x-direction (J_{yx} = 4) and the meander amplitude (α = 13.5) were fixed for these simulations.

		Wavelength [m]			Hydraulic gradient in x-direction [‰]			Stream width [m]			Hydraulic conductivity [m/d]			Aquifer thickness [m]		
		30	**40**	60	0.5	**1**	10	2	**5**	8	20	**40**	80	5	**40**	80
Sinuosity	1.94	**1.74**	1.39	1.74	**1.74**	1.74	1.74	**1.74**	1.74	1.74	**1.74**	1.74	1.74	**1.74**	1.74	
Meander side	Outward side [%]	89	**85**	75	85	**85**	86	79	**85**	88	85	**85**	87	99	**85**	83
	Inward side [%]	11	**15**	25	15	**15**	14	21	**15**	12	15	**15**	13	1	**15**	17
	Mean flux [m/s]	0.44	**0.48**	0.55	0.24	**0.48**	4.84	0.53	**0.48**	0.42	0.25	**0.48**	0.94	0.12	**0.48**	0.64

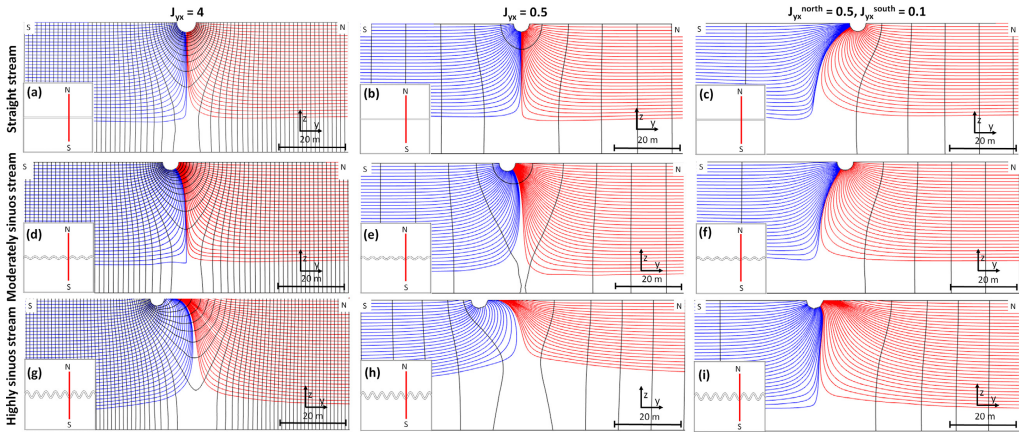

Fig. 5. Groundwater paths from the northern (red lines) and southern (blue lines) sides of the stream at a vertical cross section perpendicular the stream located at the edge of a meander pointing south. The black lines show the equipotential lines separated by 0.005 m. Jyx represent the ratio between the hydraulic gradient in the y and in x-direction. The moderately sinuous stream has sinuosity (S) of 1.14 and amplitude (α) of 5 m. The highly sinuous stream has sinuosity (S) of 1.74 and amplitude (α) of 13.5 m. (For interpretation of the references to color in this figure legend, the reader is referred to the web version of this article.)

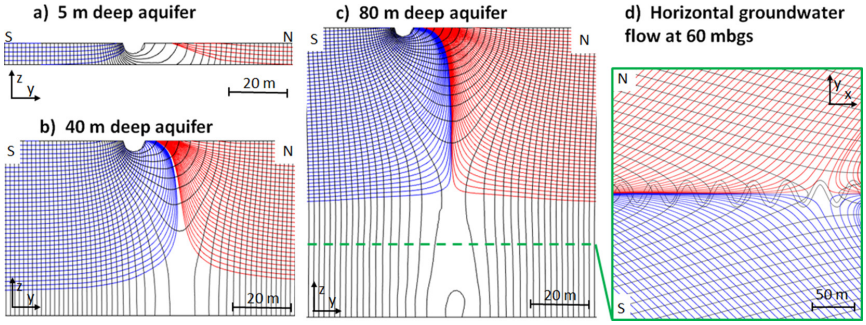

Fig. 6. Effect of the aquifer thickness on the groundwater paths from the northern side of the stream (red lines) and from the southern side of the stream (blue lines) at three vertical cross sections perpendicular the stream and located at the edge of a meander bend pointing south (a, b, and c). The black lines show the equipotential lines separated by 0.005 m interval. The green line in the 80 m deep aquifer (c) show the depth of the plan view section (d). The highly sinuous stream scenario with a J_{yx} of 4 was employed. (For interpretation of the references to color in this figure legend, the reader is referred to the web version of this article.)

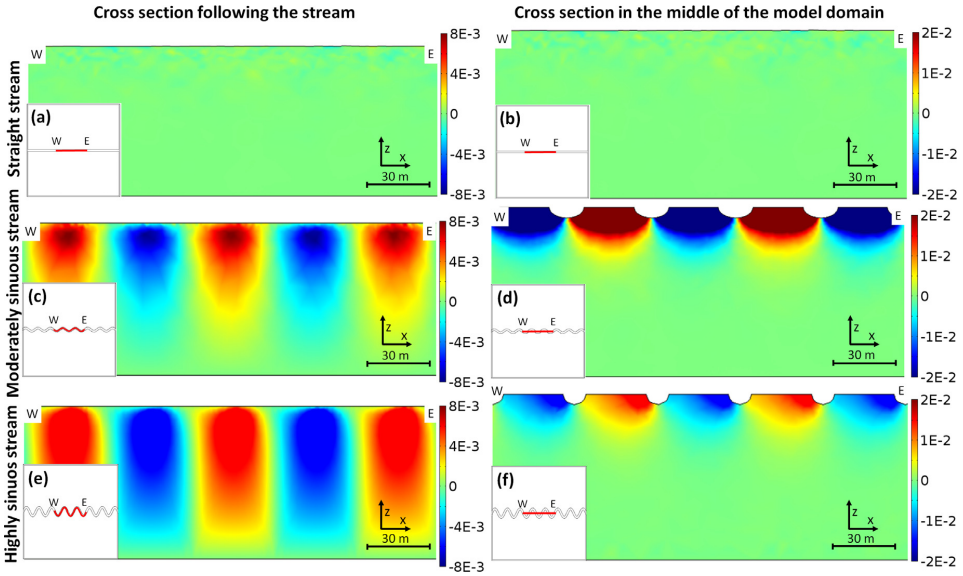

Fig. 7. Groundwater flow in the y direction (q_y) in m/s through vertical cross sections along the stream: the left panels show cross sections that follow the meandering stream path (a, c, and e), while the right hand panels show straight cross sections centered in the middle of the model domain (b, d, and f). Positive flow is directed to the north. The results are shown for the straight, the moderately sinuous and the highly sinuous stream with J_{yx} = 0.5 and an aquifer thickness of 40 m. The moderately sinuous stream has sinuosity (S) of 1.14 and amplitude (α) of 5 m while the highly sinuous stream has a sinuosity (S) of 1.74 and amplitude (α) of 13.5 m.

pointing to the north, the effects of the meander bend and the changes in hydraulic gradient reinforce each other.

The effect of the aquifer thickness on the groundwater flow to a stream is shown in Fig. 6 for the highly sinuous stream with J_{yx} of 4. In the shallow aquifer, which is 5 m thick, all groundwater discharges to the stream. However, for the 40 m thick aquifer, groundwater in the top 32 m discharges to the stream, while the deepest groundwater, in the lowest 8 m of the aquifer, flows horizontally beneath the stream and is not affected by the stream. Increasing the thickness of the aquifer, from 5 m to 40 m, results in an increase from 0.12 to 0.48 m/s of the average groundwater flux to the stream, as observed in Table 2. When further increasing the aquifer thickness to 80 m, groundwater in the deepest 32 m of the aquifer flows horizontally downstream without entering the stream, as shown by the horizontal groundwater flow paths in the plan view section 60 mbgs (Fig. 6d). The horizontal hydraulic gradient is affected by the stream in the deepest part of the aquifer, while the vertical gradient is not. This indicates that streams have a diminishing effect on groundwater discharge as aquifer thickness increases. Moreover, the area discharging to the stream does not linearly increase with the aquifer thickness. These results are based on three scenarios where the aquifer depth is varied and the stream depth is assumed to be constant. The effect of the stream depth is likely to combine with effect of the aquifer depth, when both parameters are varied. However, this is beyond the scope of this analysis.

The groundwater flow component in the y-direction is shown in Fig. 7. The figure shows two cross section: one follows the path to the stream (Fig. 7a, c, and e) while the other is centered in the middle of the model domain (Fig. 7b, d, and f). The results are shown

for the straight, the moderately, and the highly sinuous stream scenarios with a constant J_{yx} of 0.5. The green color indicates the absence of flow in the y-direction, the blue color indicates a negative flow, directed to the south, and the red color indicates a positive flow, directed to the north.

On the cross section following the stream, the straight stream (Fig. 7) shows that y-directional groundwater flow below the stream is zero. The results are presented only for a constant J_{yx} of 0.5 and a constant aquifer thickness of 40 m, but are valid whenever the hydraulic gradient and the aquifer thickness is constant. The scenario with different hydraulic gradients in the y-direction at the two sides of the stream shows groundwater flow below the stream from north to south, as shown in Fig. 7c.

The moderately sinuous stream (Fig. 7c) shows areas colored in blue, associated with a meander pointing toward north, and the areas colored in red, with a meander pointing south. For meanders pointing north, groundwater from the northern side of the stream flows beneath the stream in a southerly direction (the flow has a negative sign), while for meanders pointing south, groundwater from the southern side of the stream flows beneath the stream in a northerly direction (the flow has a positive sign). Between two meander extremes, an area with no flow in the y direction occurs (Fig. 7c). Y-directional groundwater flow under the stream is greatest for shallow depths and decreases deeper in the aquifer. The same pattern in the groundwater flows can be observed for the highly sinuous stream (Fig. 7e), but is more pronounced than for the moderately sinuous stream.

The groundwater flow between the northern and southern side of the stream is further analyzed by showing the y-direction flow on a vertical cross section centered in the middle of the model domain (Fig. 7b, d, and f). Curiously, Fig. 7d show that the greatest amount of groundwater flow across the stream centerline occurs for the moderately sinuous stream. When sinuosity increases there is less flow inside the meander bend (Fig. 4), and a lower y-directional flow across the stream centerline (Fig. 7e). This effect is related to the higher discharge to the outward pointing side of a meander bend in the highly sinuous stream, compared to the moderately sinuous stream. In the highly sinuous stream more water enters the stream at the meander bend, instead of crossing the line placed in the middle of the model domain and entering the stream in the inward pointing side of the meander.

3.3. Grindsted stream field site

The model implemented at the Grindsted stream field site was first evaluated by comparing model results with the observed groundwater head and discharge to the stream. In Fig. 8, the simulated groundwater head is compared to the observed head at wells located within the model domain: 114.1448 and 114.1997 (Fig. 2). In well 114.1448, the model describes the variation groundwater head well, except for the period May–July 2014 when the simulated head (red line) is higher than the observed (black dots). In well 114.1997, the meandering stream model properly simulates the head until June 2014, but the head is overestimated for the remaining simulation time. This is confirmed by the Nash-Sutcliffe efficiency coefficient (Nash and Sutcliffe, 1970) for the entire simulation period of 0.63 and 0.68 at the two observation wells 114.1448 and 114.1997 respectively. The simulated annual average groundwater discharge to the stream is 75 l/s, which matches well the annual averaged discharge estimated from the gaging stations (70 l/s). The inflow at the upgradient groundwater boundaries resembles the discharge to the stream, with small differences due to changes in storage in the domain and recharge.

The simulated groundwater discharge to the stream along the entire modeled stream stretch is shown in Fig. 8 (green line). The groundwater discharge to the stream varies up to 40% during the one year simulation. Despite this, the spatial patterns of the groundwater flow to the stream in the simulations are not time varying. This is because the modeled stream is always a gaining stream, and head variations are small (up to 0.4 m over a one year simulation) compared to the aquifer thickness (80 m). We carefully note, however, that the spatial patterns of groundwater flow to the stream will probably change with time for a stream that switches between being gaining and losing conditions.

The horizontal groundwater flow at the upper edge of the stream-aquifer interface is shown in Fig. 9 by the red arrows, whose length is proportionate to the magnitude of the flow. The groundwater discharge is not constant, but changes depending on the location along the stream. As for the sinusoidal stream geometries (Fig. 4), the groundwater discharge peaks at the outside extremes of the meander bends and is smallest on the inside of the meander bends.

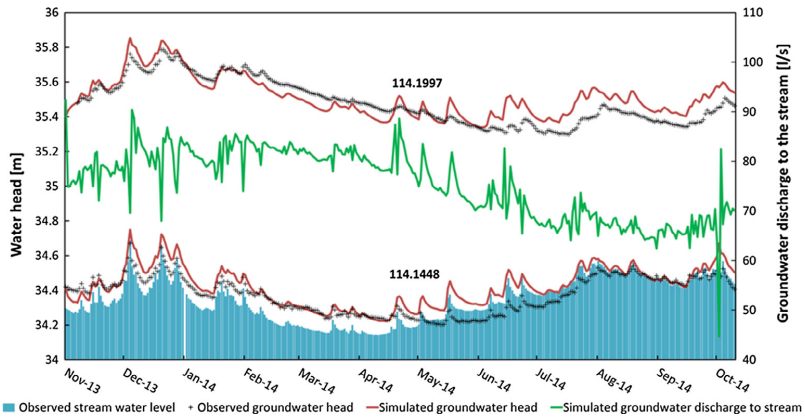

Fig. 8. Model results from Grindsted stream compared to groundwater head data from well 114.1448 and 114.1997 (Fig. 2). The stream water level at the closest location to well 114.1448 is indicated by the blue columns. The stream water level was calculated from the water level measurements at the Tingvejen station assuming a stream water slope, which was calculated at each day from the water level measurements at the Tingvejen and the Eg bro stations. The groundwater discharge to the stream (green line) is plotted to the secondary y-axes, which starts at 40 l/s, and is the integrated value of the discharges along the modeled stream stretch. (For interpretation of the references to color in this figure legend, the reader is referred to the web version of this article.)

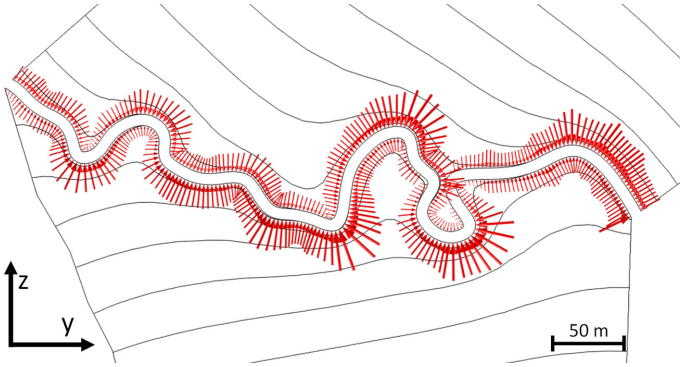

Fig. 9. Horizontal groundwater flow at the upper edge of the stream-aquifer interface. The red arrows are proportional to the fluxes. The equipotential lines are separated by 0.2 m. (For interpretation of the references to color in this figure legend, the reader is referred to the web version of this article.)

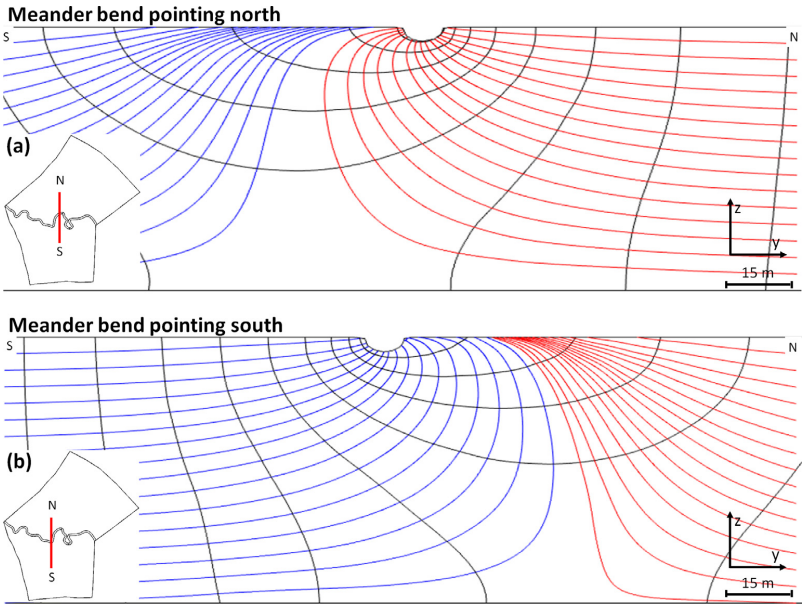

Fig. 10. Groundwater paths from the northern side of the stream (red lines) and from the southern side of the stream (blue lines) at two vertical cross sections perpendicular the stream and located at the edge of a meander bend pointing north (a) and south (b). The black lines show the equipotential lines with a 0.1 m interval. (For interpretation of the references to color in this figure legend, the reader is referred to the web version of this article.)

The groundwater flow to the stream at two vertical cross sections perpendicular to the stream is shown in Fig. 10. The cross section in Fig. 10a is placed at the location of a meander bend pointing to the north and the cross section in Fig. 10b is placed where a meander bend is pointing to the south. In Fig. 10a, the particles originating in the shallow part of the aquifer north from the stream enter the stream at the northern bank. The particles originating in the deep part of the aquifer north of the stream enter the stream on the southern bank while the particles coming from the southern side of the aquifer enter the stream on the shallow part of the southern bank. The reverse pattern is observed in Fig. 10b. This is similar to the results of the moderately sinuous stream (Fig. 5d and e) and the high sinuous stream (Fig. 5g and h).

4. Discussion

This study shows that meander bends lead to significant spatial variability in groundwater flow to streams. The results show that most of groundwater flowing to the stream enters the stream at the outward pointing side of the meander bend (85% for the highly sinuous stream with a J_{yx} of 4), just upstream of the extremities of the meander (Fig. 4 for the synthetic stream and Fig. 9 for Grindsted stream). The groundwater discharge to the stream is lowest on the inside of meander bends, where only 15% of groundwater enters the stream for the highly sinuous stream with a J_{yx} of 4. The amount of groundwater entering the stream is affected by the groundwater flow direction in the aquifer. In case of regional groundwater flowing perpendicularly to the stream direction,

85% of groundwater discharge occurs on the outward pointing side of a meander, compared to 82% for regional groundwater flowing in the direction of the stream. In this case, the largest groundwater flows occur on the upstream part of the outward pointing meander. For real streams, such as the Grindsted stream (Fig. 9) the variations in the groundwater discharge at the stream-aquifer interface are not as regular as for the synthetic streams (Fig. 4). In the synthetic streams, all meanders have the same amplitude and period and are oriented in the same way relative to the groundwater flow direction. In the Grindsted stream, the meanders have different size and are oriented differently. Thus, the spatial variability of the groundwater flow to streams is affected by the size as well as by the orientation of the meander bend.

In the field study of Weatherill et al. (2014), a high concentration of contaminants in groundwater discharge was detected at the outside of a meander bend. Our study, which indicates that the outward pointing side of the bends is the dominant location for groundwater discharge, helps explain those results.

The groundwater flow to the stream is observed to vary greatly with depth for both the synthetic (Fig. 5, 6, and 7) and Grindsted streams (Fig. 10). This confirms that groundwater flow to streams at meandering streams is three dimensional, as previously suggested by Harvey and Bencala (1993), Modica et al. (1998), and Flipo et al. (2014). The present study investigates how the vertical variability of the groundwater flow to the stream is affected by the meander bends with the discharging bank being dependent on the depth of origin of the groundwater and the stream geometry. The amount of groundwater entering the stream on the opposite bank, increases with the sinuosity (Fig. 7a and b) and amplitude of the meanders (Fig. 5). Curiously the magnitude of the flow crossing the stream center line is highest for moderately sinuous streams and decreases when increasing the sinuosity (Fig. 7d and e). Groundwater can enter the stream on the opposite bank from its origin because of difference in hydraulic gradient in the aquifer between the two sides of the stream, as occurring when the regional groundwater flow direction is across the stream. The regional groundwater flow can either enhance or smooth the effect of the stream sinuosity, depending on the direction of the regional groundwater flow and the orientation of the meander bends.

The observation that groundwater can flow below a stream and enter the stream through the opposite bank has previously been described by Aisopou et al. (2015a) and Miracapillo and Morel-Seytoux (2014). However, the factors causing groundwater to enter the stream through the opposite bank are different in those papers than here. In Aisopou et al. (2015a), the presence of a pumping well on one side of the stream creates a head gradient that forces groundwater to cross to the opposite side of the stream and enter the stream at the bank closest to the well. In Miracapillo and Morel-Seytoux (2014), the difference of the horizontal gradient between the two sides of the stream imposed by the boundary conditions, is responsible for the flow below the stream. Here we focus on the combined influence of stream geometry and groundwater flow direction on the location of groundwater discharge to a stream.

The synthetic stream and the Grindsted stream models have been implemented using different boundary conditions. In the synthetic stream, all the lateral boundary conditions (Fig. 1) are constant head and account for the head gradient in the x and y direction. In the Grindsted stream model (Fig. 2), the boundaries perpendicular to the stream are streamlines (no-flow boundaries) and the upstream groundwater boundaries are fixed-head. The constant head boundaries of the synthetic stream model assume no vertical groundwater gradients. As previously discussed, this is not the case close to a meandering stream. The streamline boundaries applied in the Grindsted stream model allow a vertical gradient. However, the streamline boundaries of the Grindsted model do not allow a horizontal flow across the stream lines in the aquifer. Thus along-stream groundwater flow is better modeled by constant head boundaries. Neither the no-flow nor the constant head boundary conditions perfectly describe conditions under streams. However, this paper has shown that the effect of meanders is similar for both types of groundwater boundary conditions (compare the sinusoidal examples with fixed head boundaries with the Grindsted model with the no flow boundaries). In addition, the results from a larger modeling domain (Fig. S4) show that the effect of stream meanders on the groundwater flow pattern to the stream do not change when the model boundaries are further from the stream (compare Fig. 5i with Fig. S4), so the conclusions are robust despite boundary condition uncertainty.

The hydraulic conductivity distribution in the aquifer and in the stream bed is one of the factors, together with the stream morphology and the hydraulic gradient, known to affect the groundwater flow to streams. Recent studies by Krause et al. (2012), Brookfield and Sudicky (2013), Gomez-Velez et al. (2014), and Poulsen et al. (2015) have focused on the effect of the hydraulic conductivity distribution on the groundwater discharge to streams. Since the aim of this study is to investigate the effect of stream meanders and groundwater flow direction on the groundwater flow to streams at the reach scale, the models assume a homogenous sandy aquifer and a constant stream hydraulic gradient. Future studies that investigate the combined effect of stream meanders, varying stream-aquifer hydraulic gradients, and heterogeneous aquifer systems (spatially varying hydraulic conductivity distributions) or layered aquifers would enhance the understanding on groundwater flow to streams.

5. Conclusions

A numerical modeling study analyzing the effect of meander bends on the spatial variability of the groundwater flow in an unconfined and homogenous sandy aquifer to a gaining stream at the reach scale is presented. Results were obtained by applying the coordinate transformation method of Boon et al. (2016) to a new problem: the groundwater flow to streams.

The results showed that presence of meander bends leads to significant spatial variability in groundwater discharge to streams. The groundwater fluxes are highest at the meander bend extremes, up to 85% of the mean fluxes to a meander with a sinuosity of 1.74, and much lower on the inside of meander bends. This effect increases with the stream sinuosity. The magnitude of the hydraulic gradient of groundwater and of the hydraulic conductivity in the aquifer affects the mean groundwater flux to the stream, while the stream width and the direction of groundwater affects the groundwater flow direction to the stream. Groundwater gradients combine with the effect of stream meanders and can either enhance or smooth the effect of a meander bend, depending on groundwater flow directions.

The location of the discharge of groundwater along the stream cross section is affected by the stream sinuosity, the direction of the groundwater flow, and the aquifer thickness. At the meander extremes, groundwater coming from the shallow part of the aquifer enters the stream at the outward pointing bank. Groundwater originating from the deep part of the aquifer often flows beneath the stream and enters the stream at the opposite bank at the inward side of a meander bend, with the amount of groundwater flow under the stream increasing with aquifer thickness.

The field site application confirmed the finding of the synthetic study case and showed that the irregular geometry of the stream meanders affects the groundwater discharge to the stream. This study improved our conceptual understanding of the groundwater flow paths to meandering streams in an unconfined homogenous

sandy aquifer and shows how stream meanders, combined with groundwater flow direction, affect the spatial variability of the groundwater flow to streams at the reach scale in both synthetic and field systems.

Acknowledgements

This study was supported by the research project GEOCON, Advancing GEOlogical, geophysical and CONtaminant monitoring technologies for contaminated site investigation (contract 1305-00004B). The funding for GEOCON is provided by Innovation Fund Denmark. Additionally, this study was supported by Norwegian Research Council grant 233736. The data used in this paper can be accessed by contacting the first author Nicola Balbarini at nbal@env.dtu.dk. The authors would like to thanks Vinni Rønde, Anne Thobo Sonne and Ursula McKnight for the field data collection and their valuable assistance in the data interpretation.

Appendix A. Supplementary data

Supplementary data associated with this article can be found, in the online version, at http://dx.doi.org/10.1016/j.jhydrol.2017.06.042.

References

Aisopou, A., Binning, P.J., Albrechtsen, H., Bjerg, P.L., 2015a. Modeling the factors impacting pesticides concentrations in groundwater wells. Groundwater 53 (5), 722–736. http://dx.doi.org/10.1111/gwat.12264.

Aisopou, A., Bjerg, P.L., Sonne, A.T., Balbarini, N., Rosenberg, L., Binning, P.J., 2015b. Dilution and volatilization of groundwater contaminant discharges in streams. J. Contam. Hydrol. http://dx.doi.org/10.1016/j.jconhyd.2014.11.004.

An, H., Ichikawa, Y., Tachikawa, Y., Shiiba, M., 2010. Three-dimensional finite difference saturated-unsaturated flow modeling with nonorthogonal grids using a coordinate transformation method. Water Resour. Res. 46, W11521. http://dx.doi.org/10.1029/2009WR009024.

Anibas, C., Verbeiren, B., Buis, K., Chormánski, J., De Doncker, L., Okruszko, T., Meire, P., Batelaan, O., 2012. A hierarchical approach on groundwater-surface water interaction in wetlands along the upper Biebrza River, Poland. Hydrology Earth System Sci. 16, 2329–2346. http://dx.doi.org/10.5194/hess-16-2329-2012.

Barlebo, H.C., Hill, M.C., Rosbjerg, D., Jensen, K.H., 1998. Concentration data and dimensionality in groundwater models: evaluation using inverse modelling. Nord. Hydrol. 29, 149–178.

Binley, A., Ullah, S., Heathwaite, A.L., Heppell, C., Byrne, P., Lansdown, K., Trimmer, M., Zhang, H., 2013. Revealing the spatial variability of water fluxes at the groundwater-surface water interface, Water Resources Research, Vol. Pages 49, 3978–3992. http://dx.doi.org/10.1002/wrer.20214.

Bjerg, P.L., Rügge, K., Pedersen, J.K., Christensen, T.H., 1995. Distribution of redox sensitive groundwater quality parameters downgradient of a landfill (Grindsted, Denmark). Environ. Sci. Technol. 29, 1387–1394.

Boano, F., Camporeale, C., Revelli, R., Ridolfi, L., 2006. Sinuosity-driven hyporheic exchange in meandering rivers. Geophys. Res. Lett. 33, L18406.

Boano, F., Revelli, R., Ridolfi, L., 2009. Quantifying the impact of groundwater discharge on the surface-subsurface exchange. Hydrol. Process. 23, 2108–2126. http://dx.doi.org/10.1002/hyp.7278.

Boano, F., Camporale, C., Revelli, R., 2010. A linear mode for the coupled surface-subsurface flow in a meandering stream. Water Resour. Res. 46, W07535. http://dx.doi.org/10.1029/2009WR008317.

Boano, F., Harvey, J.W., Marion, A., Packman, A.I., Revelli, R., Ridolfi, L., Wörman, A., 2014. Hyporheic flow and transport processes: Mechanisms, models, and biogeochemical implications. Rev. Geophys. 52, 603–679. http://dx.doi.org/10.1002/2012RG000417.

Boon, W.M., Balbarini, N., Binning, P.J., Nordbotten, J.M., 2016. Efficient water table evolution discretization using domain transformation. Comput. Geosci. http://dx.doi.org/10.1007/s10596-016-9591-2.

Bresciani, E., Davy, P., De Dreuzy, J.R., 2011. A finite volume approach with local adaptation scheme for the simulation of free surface flow in porous media. Int. J. Numer. Anal. Methods Geomech. 2. http://dx.doi.org/10.1002/nag.1065.

Brookfield, A.E., Sudicky, E.A., 2013. Implications of hyporheic flow on temperature-based estimates of groundwater/surface water interactions. J. Hydrol. Eng. 18 (10), 1250–1261.

Byrne, P., Binley, A., Heathwaite, A.L., Ullah, S., Heppel, C.M., Lansdown, K., Zhang, H., Trimmer, M., Keenan, P., 2014. Control of river stage on the reactive chemistry of hyporheic zone. Hydrol. Process. 28, 4766–4779. http://dx.doi.org/10.1002/hyp.9981.

Camporese, M., Paniconi, C., Putti, M., Orlandini, S., 2010. Surface-subsurface flow modeling with path-based runoff routing, boundary condition-based coupling, and assimilation of multisource observation data. Water Resour. Res. 46. http://dx.doi.org/10.1029/2008WR007536.

Cardenas, M.B., 2008. The effect of river bend morphology on flow and timescales of surface-groundwater exchange across pointbars. J. Hydrol. 362, 134–141. http://dx.doi.org/10.1016/j.hydrol.2008.08.018.

Cardenas, M.B., 2009a. Stream-aquifer interactions and hyporheic exchange gaining and losing sinuous streams. Water Resour. Res. 45, W06429. http://dx.doi.org/10.1029/2008WR007651.

Cardenas, M.B., 2009b. A model for lateral hyporheic flow based on valley slope and channel sinuosity. Water Resour. Res. 45, W01501. http://dx.doi.org/10.1029/2008WR007442.

Cardenas, M.B., Wilson, J.L., Zlotnik, V.A., 2004. Impact of heterogeneity, be forms, and stream curvature on subchannel hyporheic exchange. Water Resour. Res. 40, W08307. http://dx.doi.org/10.1029/2004WR003008.

Cey, E.E., Rudolph, D.L., Parkin, G.W., Aravena, R., 1998. Quantifying groundwater discharge to a small perennial stream in southern Ontario, Canada. J. Hydrol. 210, 21–37.

COMSOL, 2013. COMSOL Multiphysics Reference Manual, Version 4.4.

Conant Jr., B., Cherry, J.A., Gillham, R.W., 2004. A PCE groundwater plume discharging to a river: influence of the streambed and near-river zone on contaminant distributions. J. Contam. Hydrol. 73, 249–279. http://dx.doi.org/10.1016/j.jconhyd.2004.04.001.

Dahl, M., Nilsson, B., Langhoff, J.H., Refsgaard, J.C., 2007. Review of classification systems and new multi-scale typology of groundwater-surface water interaction. J. Hydrol. 344, 1–16. http://dx.doi.org/10.1016/j.jhydrol.2007.06.027.

Darbandi, M., Torabi, S.O., Saadat, M., Daghighi, Y., Jarrahbashi, D., 2007. A moving mesh finite-volume method to solve free-surface seepage problem in arbitrary geometries. Int. J. Numer. Anal. Meth. Geomech. 31, 1609–1629.

Derx, J., Blaschke, A.P., Blöschl, G., 2010. Three dimensional flow pattern at the river-aquifer interface-a case study at the Danube. Adv. Water Resour. 33, 1375–1387.

Diem, S., Renard, P., Schirmer, M., 2014. Assessing the effect of different river water level interpolations schemes on modeled groundwater residence times. J. Hydrol. 51, 393–402. http://dx.doi.org/10.1016/j.jhydrol.2013.12.049.

DMI, 2015. Available from: <http://www.dmi.dk/vejr/> [20 December 2015].

Dogan, A., Motz, L.H., 2005. Saturated-unsaturated 3D groundwater model. I: development. J. Hydrol. Eng. http://dx.doi.org/10.1061/(ASCE)1084-0699(2005)10:6(492).

Fernando, H.J.S., 2013. Handbook of Environmental Fluid Dynamics, vol. 2. CRC Press. Chapter 2, Pages 19–30.

Flipo, N., Mouhri, A., Labarthe, B., Biancamaria, S., Riviere, A., Weill, P., 2014. Continental hydrosystem modelling: the concept of nested stream-aquifer interfaces. Hydrol. Earth Syst. Sci. 18, 3121–3149. http://dx.doi.org/10.5194/hess-18-3121-2014.

Freeze, R.A., 1971. Three-dimensional, transient, saturated-unsaturated flow in a groundwater basin. Water Resour. Res. 7, 347–366. http://dx.doi.org/10.1029/WR007i002p00347.

Freitas, J.G., Rivett, M.O., Roche, R.S., Durrant, M., Walker, C., Tellam, J.H., 2015. Heterogeneous hyporheic zone dechlorination of a TCE groundwater plume discharging to an urban river reach. Sci. Total Environ. 505, 236–252.

Gomez-Velez, J.D., Krause, S., Wilson, J.L., 2014. Effect of low-permeability layers on spatial patterns of hyporheic exchange and groundwater upwelling. Water Resour. Res. http://dx.doi.org/10.1002/2013WR015054.

Gomez-Velez, J.D., Harvey, J.W., Cardenas, M.B., Kiel, B., 2015. Denitrification in the Mississippi River network controlled by flow through river bedforms. Nat. Geosci. http://dx.doi.org/10.1038/NGEO2567.

Guay, C., Nastev, M., Paniconi, C., Sulis, M., 2013. Comparison of two modeling approaches for groundwater-surface water interactions. Hydrol. Process. 27, 2258–2270.

Harvey, J.W., Bencala, K.E., 1993. The effect of streambed topography on surface-subsurface water exchange in mountain catchments. Water Resour. Res. 29 (1), 89–98.

Heron, G., Bjerg, P.L., Gravesen, P., Ludvigsen, L., Christensen, T.H., 1998. Geology and sediment geochemistry of a landfill leachate contaminated aquifer (Grindsted, Denmark). J. Contam. Hydrol. 29, 301–317.

Karan, S., Engesgaard, P., Looms, M.C., Laier, T., Kazmierczak, J., 2013. Groundwater flow and mixing in a wetland-stream system: Field study and numerical modeling. J. Hydrol. 488, 73–83.

Keating, E., Zyvoloski, G., 2009. Saturated-unsaturated 3D groundwater model. I: Development. Ground Water 4, 569–579. http://dx.doi.org/10.1111/j.1745-6584.2009.00555.x.

Kinouchi, T., Kanda, M., Hino, M., 1991. Numerical simulation of infiltration and solute transport in an S-shaped model basin by a boundary-fitted grid system. J. Hydrol. 122, 373–406. http://dx.doi.org/10.1016/0022-1694(91)90189-O.

Kjeldsen, P., Bjerg, P.L., Rügge, K., Christensen, T.H., Pedersen, J.K., 1998. Characterization of an old municipal landfill (Grindsted, Denmark) as a groundwater pollution source: Landfill hydrology and leachate migration. Waste Manage. Res. 16 (1), 14–22. http://dx.doi.org/10.1177/0734242X9801600103.

Knupp, P., 1996. Moving mesh algorithm for 3-D regional groundwater flow with water table and seepage face. Adv. Water Resour. 19 (2), 83–95.

Krause, S., Bronstert, A., Zehe, E., 2007. Groundwater-surface water interactions in a north German lowland floodplain – Implications for the river discharge dynamics and riparian water balance. J. Hydrol. 347, 404–417. http://dx.doi.org/10.106/j.jhdrol.2007.09.028.

Krause, S., Blume, T., Cassidy, N.J., 2012. Investigating patterns and controls of groundwater up-welling in a lowland river by combining Fibre-optic Distributed Temperature Sensing with observations of vertical hydraulic gradients. Hydorl. Hearth Syst. Sci. 16, 1775–1792. http://dx.doi.org/10.5194/hess-16-1775-2012.

Krause, S., Boano, F., Cutchbert, M.O., Fleckenstein, J.H., Lewandowski, J., 2014. Understanding process dynamics at aquifer-surface water interfaces: An introduction to the special edition section on modeling approaches and novel experimental technologies. Water Resour. Res. 50, 1847–1855. http://dx.doi.org/10.1002/2013WR014755.

Larkin, R.G., Sharp, J.M., 1992. On the relationship between river-basin geomorphology, aquifer hydraulics, and ground-water flow direction in alluvial aquifers. Geolog. Soc. Am. Bull. 104, 1608–1620.

Lønborg, M.J., Engesgaard, P., Bjerg, P.L., Rosbjerg, D., 2006. A steady state redox zone approach for modeling the transport and degradation of xenobiotic organic compounds from a landfill site. J. Contam. Hydrol. 87, 191–210.

Miracapillo, C., Morel-Seytoux, H.J., 2014. Analytical solutions for stream-aquifer flow exchange under varying head asymmetry and river penetration: Comparison to numerical solutions and use in regional groundwater models. Water Resour. Res. 50, 7430–7444. http://dx.doi.org/10.1002/2014WR015456.

Modica, E., Buxton, H.T., Plummer, L.N., 1998. Evaluating the source and residence time of groundwater seepage to streams, New Jersey Coastal Plan. Water Resour. Res. 34 (11), 2797–2810.

Nalbantis, I., Efstratiadis, A., Rozos, E., Kopsiafti, M., Koutsoyiannis, D., 2011. Holistic versus monometric strategies for hydrological modelling of human-modified hydrosystems. Hydrol. Earth Syst. Sci. 15, 743–758. http://dx.doi.org/10.5194/hess-15-743-2011.

Nash, J.E., Sutcliffe, J.V., 1970. River flow forecasting through conceptual models part I — A discussion of principles. J. Hydrol. 10 (3), 282–290. http://dx.doi.org/10.1016/0022-1694(70)90255-6.

Ou, G., Chen, X., Kilic, A., Bartelt-Hunt, S., Li, Y., Samal, A., 2013. Environ. Modell. Software 50, 132–143.

Poulsen, J.R., Sebok, E., Duque, C., Tezlaff, D., Engesgaard, P.K., 2015. Detecting groundwater discharge dynamics from point-to-catchment scale in a lowland stream: combining hydraulic and tracer methods. Hydrol. Earth Syst. Sci. 19, 1871–1886. http://dx.doi.org/10.5194/hess-19-1871-2015.

Rasmussen, J.J., McKnight, U.S., Sonne, A.T., Wiberg-Larsen, P., Bjer, P.L., 2016. Legacy of a chemical factory site: contaminated groundwater impacts stream macroinvertebrates. Arch. Environ. Contam. Toxicol. http://dx.doi.org/10.1007/s00244-015-0211-2.

Revelli, R., Boano, F., Camporale, C., Ridolfi, L., 2008. Intre-meander hyporheic flow in alluvial rivers. Water Resour. Res. 44. http://dx.doi.org/10.1029/2008WR007081.

Salehin, M., Packman, A.I., Paradis, M., 2004. Hyporheic exchange with heterogenous streambeds: Laboratory experiments and modeling. Water Resour. Res. 40, W11504. http://dx.doi.org/10.1029/2003WR002567.

Stonedahl, S.H., Harvey, J.W., Wörman, A., Salehin, M., Packman, A.I., 2010. A multistate model for integrating hyporheic exchange from rippleds to meanders. Water Resour. Manage. 46, W12539. http://dx.doi.org/10.1029/2009/WR008865.

Sugio, S., Desai, C.S., 1987. Residual flow procedure for sea water intrusion in unconfined aquifers. J. Numer. Methods Eng. 24, 1439–1450.

Toth, J., 1963. A theoretical analysis of groundwater flow in small drainage basins. J. Geophys. Res. 68 (16), 4795–4812.

Walther, M., Delfs, J.-O., Grundmann, J., Kolditz, O., Liedl, R., 2012. Saltware intrusion modeling: verification and application to an agricultural coastal arid region in Oman. J. Comput. Appl. Math. 236. http://dx.doi.org/10.1016/j.cam.2012.02.008. 4798-1809.

Weatherill, J., Krause, S., Voyce, K., Drijfhout, F., Levy, A., Cassidy, N., 2014. Nested monitoring approaches to delineate groundwater trichloroethene discharge to a UK lowland stream at multiple spatial scales. J. Contam. Hydrol. 158, 38–54.

Wroblicky, G.J., Campana, M.E., Valett, H.M., Dahm, C.N., 1998. Seasonal variation in surface-subsurface water exchange and lateral hyporheic area of two stream-aquifer systems. Water Resour. Res. 34 (3), 317–328.

Paper H

An Adaptive Penalty Method for Constrained Minimization Problems

W.M. Boon, J.M. Nordbotten

Optimization Letters In review.

Graphic design: Communication Division, UiB / Print: Skipnes Kommunikasjon AS

uib.no

ISBN: 978-82-308-3748-1